

**Ruling Out the Onset of Color
Transparency up to $Q^2 = 14.2 \text{ GeV}^2$ in
Quasielastic $^{12}C(e, e'p)$ Scattering**

John Matter

Moreno Valley, CA

B.S., University of California, Davis, 2012

A Dissertation Presented to the Graduate Faculty
of the University of Virginia in Candidacy for the Degree of
Doctor of Philosophy

Department of Physics

University of Virginia

August, 2021

Abstract

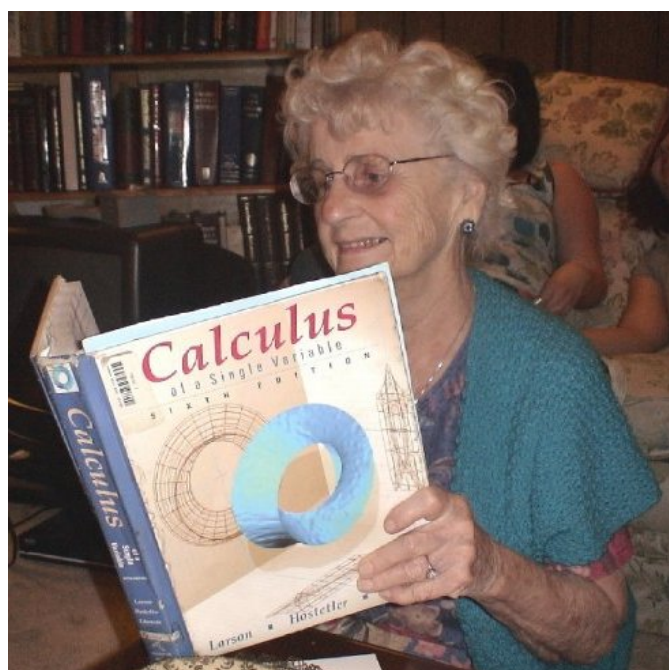
Color Transparency (CT) is a prediction of QCD that at high momentum transfer Q^2 , a system of quarks which would normally interact strongly with nuclear matter could form a small color-neutral object whose compact transverse size would be maintained for some distance, passing through the nucleus undisturbed. A clear signature of CT would be a dramatic rise in nuclear transparency T with increasing Q^2 . CT emerges as a deviation from Glauber multiple scattering theory, which predicts constant T . While a rise in nuclear transparency would provide an unequivocal validation of QCD factorization theorems, the complex nature of nuclear interactions renders its observation difficult to predict. The E12-06-107 experiment at JLab measured T in quasielastic electron-proton scattering with carbon-12 and liquid hydrogen targets, for Q^2 between 8.0 and 14.2 GeV 2 , a range over which models of CT predicted that T might differ appreciably from Glauber calculations. Supported in part by US DOE grant DE-FG02-03ER41240.

Dedication

For Mormor

Josephine Anne Binnquist

14 Feb 1917 – 3 Oct 2006



Acknowledgments

First, I would like to thank my advisor, Nilanga Liyanage, for his guidance, support, and enthusiasm. I wouldn't be here without his tireless work finding research and funding opportunities for me and his other students.

I would like to thank the members of my defense committee: Phil Arras, Simonetta Liuti, and Kent Paschke.

I would like to thank my collaborators on this experiment: Dipangkar Dutta, Holly Szumila-Vance, Carlos Ayerbe Gayoso, Latif Kabir, and Deepak Bhetuwal.

I would like to thank Krishni Wijesooriya, who I have worked with on and off over the past several years. I'm inspired by her drive to find new uses for existing information, whether clinical CT scans or stray nuclear resonance fluorescence photons.

I would like to thank my parents and siblings for their love and support over the years.

Thank you to Kathleen Larsen, for her love and patience.

Thank you to my dear friends: Hicham Benhallam, Jacob Boyd, Kim McMasters, Adam Smith, and Anney Traymany.

I would also like to thank the following people for their contributions to my research and education:

Eric Aliotta, Xinzhan Bai, Hem Bhatt, Deb Biswas, Max Bychkov, JP Chen, Eric Christy, Peter Cline, Silviu Covrig, Brad Cox, Donal Day, Danning Di, Craig Dukes, Burcu Duran, Rolf Ent, Debbie Eyer, Howard Fenker, Michael Fowler, Dave Gaskell, Kondo Gnanvo, Craig Group, Thir Gautam, Beth Guyton, Ole Hansen, Tanja Horn, Garth Huber, Sarah Jarrett, Siyu Jian, Mark Jones, Abishek Karki, Joe Kiskis, Israel Klich, Eugene Kolomeisky, Cynthia Keppel, Chuck Long, Dave Mack, Simona Malace, Rick Marshall, Beverly Martyn, Dave Meekins, Hamlet Mkrtchyan, Vladimir Nelyubin, Huong Nguyen, Brian Peter, Eric Pooser, Anuruddha Rathnayake, James Rocillo, Cass Sackett, Faye Safley, Brad Sawatzky, Dawn Shifflett, Tammie Shifflett, Greg Smith, the Spiliotis family, Larry St. John, Hank Thacker, Al Tobias, Diana Vaman, April Wilson, Bogdan Wojtsekowski, Steve Wood, Bryan Wright, Carlos Yero, Jixie Zhang, Xiaochao Zheng, Rena Zieve, and many more I'm sure I've forgotten.

Contents

1	Introduction	1
1.1	Atoms, Nuclei, and Nucleons	1
1.2	Electron scattering	3
1.3	Color Transparency	6
1.4	Nuclear Transparency	7
1.5	Plane Wave Impulse Approximation (PWIA)	9
1.6	Quasielastic Scattering and the Glauber Approximation	11
1.6.1	Pandharipande et al.	14
1.7	The Onset of Color Transparency	16
1.7.1	Frankfurt et al.	17
1.7.2	Cosyn et al.	19
1.8	Simulation	21
1.9	This Experiment: E12-06-107	22
2	Theoretical Background and Previous Experiments	24
2.1	Defining Color Transparency	24
2.1.1	Squeezing	25
2.1.2	Reduced Interaction Strength	25
2.1.3	Freezing and Expansion	26
2.1.4	Color Transparency and QCD Factorization Theorems	29
2.2	Color Transparency at High Energies	31
2.2.1	J/ψ photoproduction	31
2.2.2	Pion dissociation into two jets	32
2.2.3	Vector meson production	34
2.3	Color Transparency at Intermediate Energies	35

2.3.1	Quasielastic proton scattering	35
2.3.2	Quasielastic electron scattering	38
2.3.3	Pion photoproduction	38
2.3.4	Pion electroproduction	39
2.3.5	ρ^0 meson leptoproduction	41
2.4	Summary	46
3	Experimental Apparatus	48
3.1	Overview	48
3.2	Accelerator and Beamline	48
3.2.1	CEBAF	48
3.2.2	Hall C Arc and Beamline	50
3.3	Targets	54
3.4	Spectrometers	56
3.4.1	High Momentum Spectrometer	57
3.4.2	Super High Momentum Spectrometer	58
3.4.3	Collimators and Slit Systems	59
3.5	Detector Packages	59
3.5.1	Hodoscopes	59
3.5.2	Drift Chambers	62
3.5.3	Threshold Cherenkov Counters	65
3.5.4	Calorimeters	69
3.6	Trigger and Data Acquisition Systems	70
3.6.1	Pretriggers, TDC, and fADC Logic	71
3.6.2	Reference Times	74
4	Data Analysis	75
4.1	hcana	75
4.2	Reference Time Cuts	76
4.3	Detector Time Window Cuts	77
4.4	Detector Calibrations	79
4.4.1	Hodoscopes	79
4.4.2	Drift Chambers	83

4.4.3	Cherenkovs	85
4.4.4	Calorimeters	86
4.5	Tracking Algorithm	89
4.6	Optics	90
4.6.1	Target Variable Reconstruction Algorithm	90
4.6.2	Reconstruction Matrix Optimization	92
4.7	Efficiency	96
4.7.1	HMS Calorimeter	96
4.7.2	HMS Cherenkov	97
4.7.3	SHMS Noble Gas Cherenkov	98
4.7.4	Tracking	100
4.7.5	Luminosity Scan	101
4.7.6	Trigger	102
4.7.7	Livetime	104
4.8	Proton Absorption	105
4.9	Coincidence Time	110
4.10	Event Selection	112
4.11	Charge-normalized Yield	113
5	Results	114
5.1	Missing Energy and Missing Momentum	114
5.2	Nuclear Transparency	119
5.2.1	Systematic Uncertainty	120
6	Summary and Conclusion	123
A	SIMC	125
A.1	Spectral Functions	125
A.2	Coulomb Corrections	126
A.3	Radiative Corrections	127
A.3.1	Internal Bremsstrahlung	128
A.3.2	External Bremsstrahlung	131
A.4	Multiple Scattering	133
A.5	Energy Loss	133

List of Figures

1-1	The elementary particles of the Standard Model. Reproduced from Wikimedia [7].	3
1-2	Feynman diagram for elastic ep scattering.	4
1-3	Schematic representation of the nuclear response function.	5
1-4	Total, elastic, and inelastic pp , pn , and pd , cross sections versus lab momentum p_{lab} and center of mass energy \sqrt{s}	8
1-5	An illustration of the Q^2 dependence of nuclear transparency T for three scenarios.	9
1-6	Feynman diagram for $A(e, e'p)$ scattering in the PWIA.	10
1-7	Transparency measurements from several experiments studying quasielastic electron scattering from deuterium, carbon, iron, and gold.	16
1-8	Transparency calculations for $^{12}C(e, e'p)$ based on a model that accounts for nucleon correlations and proton knock-out from particular nuclear shells [38].	19
1-9	Transparency measurements from several experiments studying quasielastic electron scattering carbon.	22
2-1	The transverse size of a hadron with twist τ as a function of momentum transfer Q^2 , as predicted by light-front holographic QCD. .	27
2-2	Sketch of a hard exclusive process in the factorization limit.	30
2-3	Three-dimensional rendering of the pion's transverse density, as calculated in Ref [87].	33
2-4	The results of a parameterization, $\sigma = A^\alpha \sigma_0$, of the cross section for pion dissociation into two jets.	33

2-5	The results of a parameterization, $\frac{d\sigma}{dt} \propto e^{-bt}$, of the ρ and J/ψ electroproduction cross sections measured at HERA.	34
2-6	Transparency values T_{pp} versus p_{eff} for quasielastic proton scattering from carbon and aluminum	36
2-7	Fit ratio of the differential cross section $d\sigma/dt$ to the quark-counting prediction $d\sigma_0/dt$	37
2-8	Transparency measurements from several experiments studying quasielastic electron scattering from deuterium, carbon, iron, and gold.	38
2-9	Nuclear transparency for ${}^4\text{He}(\gamma, p\pi^+)$ at $\theta_{CM} = 70^\circ$ and $\theta_{CM} = 90^\circ$ as a function of 4-momentum transfer $ t $	39
2-10	Nuclear transparency T as a function of Q^2 for ${}^{12}\text{C}$, ${}^{27}\text{Al}$, ${}^{63}\text{Cu}$, and ${}^{197}\text{Au}$ targets measured by the piCT experiment [22, 23]. The inner error bars indicate statistical uncertainties and the outer error bars are the quadrature sum of statistical and point-to-point systematic uncertainties. The red dashed and solid lines are Glauber calculations from Larson et al. [110]. The green dotted and dot-dot-dashed lines are microscopic+BUU transport calculations from Kaskulov et al. [111, 112, 113]. The blue dashed and solid lines are Glauber calculations with and without CT from Cosyn et al. [40]; these calculations include the effects of short-range correlations.	40
2-11	The parameter $\alpha(Q^2)$ extracted from the form $T = A^{\alpha(Q^2)-1}$ fit to nuclear transparency measured by the piCT experiment.	42
2-12	Transparency versus Q^2 for ρ^0 lepton production.	43
2-13	Transparency versus coherence length for ρ^0 lepton production from hydrogen, helium, and nitrogen targets.	44
2-14	Transparency versus Q^2 for varying bins of coherence length.	44
2-15	Nuclear transparency as a function of l_{fr} measured by CLAS.	45
2-16	Nuclear transparency as a function of Q^2 measured by CLAS.	46
3-1	The Continuous Electron Beam Accelerator Facility	49
3-2	Pictures of the beam viewer from two positions.	50
3-3	Schematic representation of a superharp.	50
3-4	The Harp Fitter GUI.	51

3-5	A comparison of the distributions of the x and y positions of the beam on target for data taken with the old and new raster patterns.	53
3-6	The Hall C target chamber.	54
3-7	The Hall C target ladder.	55
3-8	Scheme of the system that maintains the cryotargets' temperatures.	55
3-9	High Momentum Spectrometer (HMS) side view.	58
3-10	Super High Momentum Spectrometer (SHMS) side view.	59
3-11	The two pairs of hodoscope planes that make up the SHMS hodoscope are placed on either side of Aerogel and Heavy Gas Cherenkov detectors.	60
3-12	A schematic diagram of the energy levels of an organic scintillator	61
3-13	A rendering of the SHMS drift chambers mounted in the detector hut frame.	62
3-14	CAD drawings of the drift chambers.	63
3-15	Side view of the order of planes encountered by a particle traveling through the SHMS.	64
3-16	Value of $1 - \beta$ for various particles as a function of momentum.	65
3-17	Value of $1 - \beta$ for various particles as a function of momentum. The horizontal lines represent the Cherenkov threshold for various gases at 1 atm, below which a particle will produce Cherenkov radiation.	66
3-18	The HMS Cherenkov	67
3-19	CAD rendering of the SHMS Noble Gas Cherenkov	67
3-20	CAD rendering of the SHMS Heavy Gas Cherenkov	68
3-21	A picture of the SHMS Aerogel Cherenkov	68
3-22	The HMS and SHMS calorimeters	69
3-23	Schematic diagram of the trigger system.	71
4-1	Scheme illustrating the synchronization of a detector signal with a CAEN 1190 TDC's internal 4 MHz and 10 GHz clocks.	77
4-2	The raw TDC time spectrum in channels for the trigger formed by coincidence of three of four hodoscope planes in the SHMS.	78

4-3	The difference between fADC pulse times and reference-time-subtracted TDC times for six representative PMTs on one side of one plane of the HMS calorimeter.	78
4-4	An illustration of the timewalk effect.	79
4-5	An illustration of the fADCs' CFD algorithm.	80
4-6	An illustration of the absence of timewalk in the fADCs' CFD algorithm.	80
4-7	A two dimensional histogram showing the difference between TDC and fADC pulse times as a function of fADC pulse amplitude.	81
4-8	The distribution of drift times for one card in the HMS 2x1 plane. .	85
4-9	Two dimensional histograms of wire drift times for the HMS 2x1 plane, before and after t_0 correction.	86
4-10	The distribution of pulse integrals in one PMT of the HMS Cherenkov.	87
4-11	Track-normalized energy deposition for this experiment's $Q^2 = 8.0 \text{ GeV}$ hydrogen data.	89
4-12	A two-dimensional histogram of HMS delta versus track-normalized energy deposition in the HMS calorimeter.	89
4-13	Coordinate systems and distances relevant to reconstruction.	91
4-14	A 2D histogram of SHMS track positions projected to the sieve. .	93
4-15	A picture of the broken HMS Cherenkov mirrors taken after the detector was removed from the hut for repair. The mirrors' Rohacell supports are visible where portions of the mirrors have broken off.	98
4-16	The distribution of tracks projected to the HMS Cherenkov mirrors for events that should (left) and did (right) fire the Cherenkov. . .	99
4-17	The efficiency of the HMS Cherenkov, binned by track position projected to the Cherenkov mirrors.	99
4-18	The distribution of tracks projected to the HMS Cherenkov mirrors for our $Q^2 = 8.0 \text{ GeV}^2 H(e, e'p)$ data is shown in red and lavender on top of the efficiency as a function of position in blue and yellow.	100
4-19	The distribution of tracks projected to the HMS Cherenkov mirrors for our $Q^2 = 8.0 \text{ GeV}^2 {}^{12}\text{C}(e, e'p)$ data is shown in red and lavender on top of the efficiency as a function of position in blue and yellow.	100

4-20 Histograms of the quantities used to guide the selection of cuts for selecting $H(e, e'p)$ events to estimate proton absorption.	107
4-21 Values of absorption estimated with 10% variations on cuts used to select $H(e, e'p)$ events.	109
4-22 The distribution of coincidence times for two runs.	111
 5-1 Experimental (in blue) and Monte Carlo (in red) distributions of reconstructed physics quantities for the LH_2 target at $Q^2 = 8.0 \text{ GeV}^2$	 115
5-2 Experimental (in blue) and Monte Carlo (in red) distributions of reconstructed physics quantities for the LH_2 target at $Q^2 = 9.5 \text{ GeV}^2$	115
5-3 Experimental (in blue) and Monte Carlo (in red) distributions of reconstructed physics quantities for the LH_2 target at $Q^2 = 11.5 \text{ GeV}^2$	116
5-4 Experimental (in blue) and Monte Carlo (in red) distributions of reconstructed physics quantities for the LH_2 target at $Q^2 = 14.2 \text{ GeV}^2$	116
5-5 Experimental (in blue) and Monte Carlo (in red) distributions of reconstructed physics quantities for the ^{12}C target at $Q^2 = 8.0 \text{ GeV}^2$	117
5-6 Experimental (in blue) and Monte Carlo (in red) distributions of reconstructed physics quantities for the ^{12}C target at $Q^2 = 9.5 \text{ GeV}^2$	117
5-7 Experimental (in blue) and Monte Carlo (in red) distributions of reconstructed physics quantities for the ^{12}C target at $Q^2 = 11.5 \text{ GeV}^2$	118
5-8 Experimental (in blue) and Monte Carlo (in red) distributions of reconstructed physics quantities for the ^{12}C target at $Q^2 = 14.2 \text{ GeV}^2$	118
5-9 Distributions of missing energy E_m measured in experiment (blue) and from Monte Carlo with (red) and without (black) radiative corrections. Data are for $^{12}C(e, e'p)$	119
5-10 Nuclear transparency for $H(e, e'p)$ as a function of momentum transfer.	120

5-11 Nuclear transparency for $^{12}C(e, e'p)$ as a function of momentum transfer.	121
A-1 Figure reproduced from Ref [185].	128
A-2 The angular distribution of first order single photon Bremsstrahlung for three values of momentum transfer Q^2	130
B-1 Experimental (in blue) and Monte Carlo (in red) distributions of target quantities reconstructed from the HMS for the LH_2 target at $Q^2 = 8.0 \text{ GeV}^2$	135
B-2 Experimental (in blue) and Monte Carlo (in red) distributions of target quantities reconstructed from the HMS for the LH_2 target at $Q^2 = 9.5 \text{ GeV}^2$	136
B-3 Experimental (in blue) and Monte Carlo (in red) distributions of target quantities reconstructed from the HMS for the LH_2 target at $Q^2 = 11.5 \text{ GeV}^2$	136
B-4 Experimental (in blue) and Monte Carlo (in red) distributions of target quantities reconstructed from the HMS for the LH_2 target at $Q^2 = 14.2 \text{ GeV}^2$	137
B-5 Experimental (in blue) and Monte Carlo (in red) distributions of target quantities reconstructed from the HMS for the ^{12}C target at $Q^2 = 8.0 \text{ GeV}^2$	137
B-6 Experimental (in blue) and Monte Carlo (in red) distributions of target quantities reconstructed from the HMS for the ^{12}C target at $Q^2 = 9.5 \text{ GeV}^2$	138
B-7 Experimental (in blue) and Monte Carlo (in red) distributions of target quantities reconstructed from the HMS for the ^{12}C target at $Q^2 = 11.5 \text{ GeV}^2$	138
B-8 Experimental (in blue) and Monte Carlo (in red) distributions of target quantities reconstructed from the HMS for the ^{12}C target at $Q^2 = 14.2 \text{ GeV}^2$	139

B-9 Experimental (in blue) and Monte Carlo (in red) distributions of target quantities reconstructed from the SHMS for the LH_2 target at $Q^2 = 8.0 \text{ GeV}^2$.	139
B-10 Experimental (in blue) and Monte Carlo (in red) distributions of target quantities reconstructed from the SHMS for the LH_2 target at $Q^2 = 9.5 \text{ GeV}^2$.	140
B-11 Experimental (in blue) and Monte Carlo (in red) distributions of target quantities reconstructed from the SHMS for the LH_2 target at $Q^2 = 11.5 \text{ GeV}^2$.	140
B-12 Experimental (in blue) and Monte Carlo (in red) distributions of target quantities reconstructed from the SHMS for the LH_2 target at $Q^2 = 14.2 \text{ GeV}^2$.	141
B-13 Experimental (in blue) and Monte Carlo (in red) distributions of target quantities reconstructed from the SHMS for the ^{12}C target at $Q^2 = 8.0 \text{ GeV}^2$.	141
B-14 Experimental (in blue) and Monte Carlo (in red) distributions of target quantities reconstructed from the SHMS for the ^{12}C target at $Q^2 = 9.5 \text{ GeV}^2$.	142
B-15 Experimental (in blue) and Monte Carlo (in red) distributions of target quantities reconstructed from the SHMS for the ^{12}C target at $Q^2 = 11.5 \text{ GeV}^2$.	142
B-16 Experimental (in blue) and Monte Carlo (in red) distributions of target quantities reconstructed from the SHMS for the ^{12}C target at $Q^2 = 14.2 \text{ GeV}^2$.	143

List of Tables

1.1	The kinematic settings used in the E12-06-107 experiment in Hall C at JLab.	23
2.1	Slope parameters from a fit to the Q^2 dependence of CLAS nuclear transparency data taken for carbon and iron	47
3.1	Summary of the materials and thicknesses of the cryotarget loops and dummy targets.	56
3.2	Summary of the HMS performance and design specifications for the SHMS.	57
3.3	Summary of the HMS and SHMS hodoscopes	61
4.1	List of cuts used to estimate HMS Calorimeter efficiency.	96
4.2	List of cuts used to estimate HMS Cherenkov efficiency.	97
4.3	List of cuts used to estimate SHMS Noble Gas Cherenkov efficiency.	101
4.4	List of cuts used to estimate HMS tracking efficiency.	102
4.5	List of cuts used to estimate SHMS tracking efficiency.	103
4.6	List of runs used to study target boiling and the corresponding nominal beam currents.	104
4.7	Summary of materials in the SHMS that contribute to proton absorption.	106
4.8	List of cuts used in proton absorption estimate.	108
4.9	List of cuts used to select clean $H(e, e'p)$ events.	112
4.10	List of cuts used to select clean $^{12}C(e, e'p)$ events.	112
5.1	Systematic uncertainties in our measurements of nuclear transparency.	122

Chapter 1

Introduction

1.1 Atoms, Nuclei, and Nucleons

Both the notion of the atom and the English word *atom* (from the Greek ἄτομος—átomos—“uncuttable,” itself composed of the etymological “atoms” ἀ—a—“not” and τέμνω—témnō—“I cut”) can be traced to the Presocratic Greek philosophers Leucippus and Democritus [1]. They posited that the natural world consists of two fundamental constituents—atoms and the void through which they move.

This theory was developed in response to the paradoxes of Zeno of Elea, which appear to draw contradictory conclusions about “plurality” and the possibility of motion, particularly if matter consists of infinitely divisible constituent parts [2]. Zeno argued that traversing a finite distance required first traversing infinitely many subdivisions of that distance—an apparent contradiction. Democritus’s model supposes the existence of a smallest subdivision, rendering the finite distance to be traversed a sum of finitely many parts. Various configurations of varying kinds, shapes, and sizes of Democritus’s atoms were thought to be the origins of the sensible properties of macroscopic matter. According to Democritus, these combinations of atoms collide with an animal’s sensory organs, giving rise to sensory experience.

In the early 19th century, John Dalton formulated the first modern concept of the atom as the fundamental building block of chemical compounds. His theory held that every chemical element is composed of atoms of identical type and that

different elements are composed of atoms of different size and weight. Chemical compounds are composed of whole numbers of atoms and reactions involving different compounds consist of a rearrangement of the constituent atoms.

In 1828, while studying the plant *Clarkia pulchella* immersed in water under a microscope, botanist Robert Brown noted the irregular motion of the plant's pollen on the surface of the water [3]. In 1905, Albert Einstein developed a model of this motion as arising from collisions between the pollen and individual water molecules [4]. French physicist Jean Perrin's measurements of the sedimentation of small particles in liquid confirmed Einstein's hypothesis, work for which he was awarded the Nobel Prize in 1926 [5].

Ernest Rutherford, Hans Geiger, and Ernest Marsden carried out a series of experiments between 1908 and 1913 in which they fired a beam of alpha particles at thin metal foils to study atomic-scale structure [6]. The distribution of scattered particles they observed suggested that the atom is composed of a small, dense, positively charged nucleus surrounded by a cloud of electrons.

In the century since, physicists have used other particle beams to study the substructures of nuclei as well as the nucleons (i.e. protons and neutrons) that compose nuclei. The culmination of decades of such experiments is a theory called quantum chromodynamics (QCD)—the theory that quarks and gluons are the fundamental building blocks that make up hadrons, a category of composite particles that includes protons and neutrons. QCD also describes the interactions between such particles—the *strong nuclear force*.

QCD is part of the “Standard Model” of particle physics, which holds that everything in the universe is made up of a handful of basic building blocks whose interactions are governed by a few fundamental forces. These building blocks, collectively called fermions, belong to two groups of particles—quarks and leptons. The quarks are typically found confined inside hadrons, while leptons can move about more freely. The interactions between these particles are mediated by force-carrying particles called bosons that carry discrete packages of energy and momentum between fermions.

Each of the three fundamental forces has one or more bosons associated with it. The strong nuclear force, as mentioned above, has the gluon. The electromagnetic

force (quantum electrodynamics or QED) has the photon. The weak nuclear force, responsible for beta decay among other things, has the positively and negatively charged W bosons and the neutral Z boson. There are a number of theories that have tried to incorporate the fourth fundamental force, gravity, in a way that is consistent with the Standard Model. Unfortunately, this pursuit has proven difficult and no such theory has been proven correct. Fig 1-1 displays the full list of fundamental particles in the Standard Model, along with some of their properties.

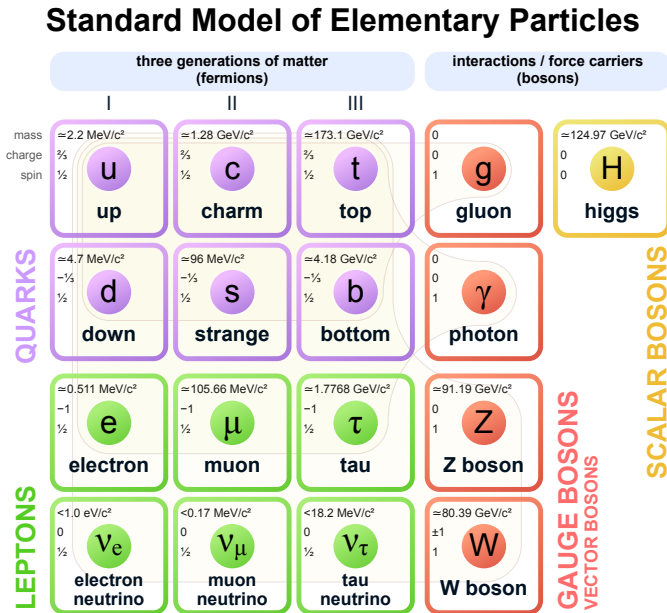


Figure 1-1: The elementary particles of the Standard Model. Reproduced from Wikimedia [7].

1.2 Electron scattering

The Thomas Jefferson National Accelerator Facility (JLab) in Newport News, VA is home to the Continuous Electron Beam Accelerator Facility (CEBAF). The CEBAF beam delivers a beam of high energy polarized electrons to four experimental halls. Most JLab experiments study the debris produced when the electron beam hits a fixed nuclear target. By studying this debris, physicists are able to obtain new insights into nuclear and nucleon structure, exotic configurations of quarks, and other features of QCD. Electron beams such as the CEBAF are powerful tools for studying nuclear structure because the processes involved

in electron-nucleus scattering experiments are governed by QED (a theory which is very well understood and calculable to high degrees of precision).

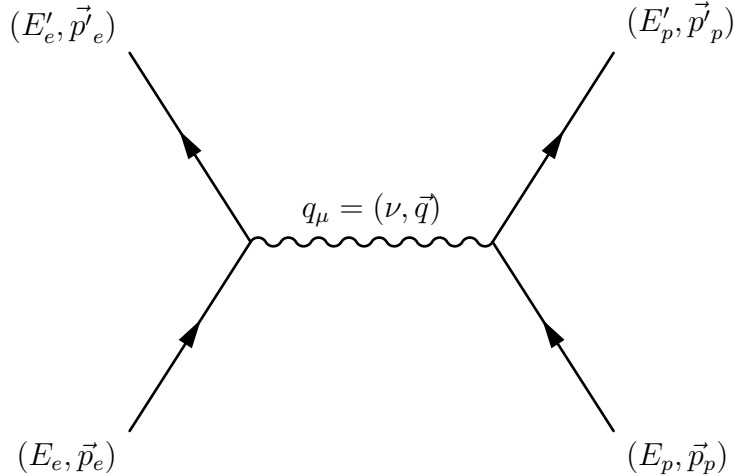


Figure 1-2: Feynman diagram for elastic ep scattering.

Consider a situation in which an electron and proton collide. The tree-level diagram for this process is shown in Fig 1-2. Let $p_e^\mu = (E_e, \vec{p}_e)$ be the incoming four-momentum of the electron and $p'^\mu = (E'_e, \vec{p}'_e)$ be its outgoing four-momentum. Similarly, let p_p^μ and p'^μ be the incoming and outgoing four-momenta of the proton. The virtual photon carries a four-momentum $q^\mu = (\nu, \vec{q}) = (E_e - E'_e, \vec{p}_e - \vec{p}'_e)$ between the two particles. An important quantity defined for such processes is the four-momentum transfer squared $Q^2 = -q^\mu q_\mu$. Similarly, $\nu = E_e - E'_e$ is the energy transfer.

Elastic scattering is a process in which an electron and proton collide, and both particles retain their identities. This process can be seen as a distinct peak at $Q^2 = 2m_p\nu$ on the bottom axis labeled “PROTON” in Fig 1-3. This figure is a schematic representation of the nuclear response function¹ as a function of Q^2 and ν .

For a fixed value of Q^2 , higher energy transfers ν result in first resonances of the proton and, as the virtual photon probes smaller and smaller distances, eventually deep inelastic scattering (DIS). DIS processes are possible because the proton is not a point-like particle without a substructure, but rather a composite particle

¹The nuclear response function can be thought of as the probability for an interaction to occur between an electron and a proton or nucleus at a given value of Q^2 and ν .

composed of quarks. The DIS region extends to electron-nucleus scattering at larger ν (see the middle axis labeled “NUCLEUS.” In DIS events, quarks can be knocked out of protons and neutrons to form other hadrons such as pions and kaons.

At lower values of ν for fixed Q^2 , there is a peak labeled quasi-free scattering, which is another term for *quasielastic scattering*. This is a process in which the struck proton retains its identity and holds onto its constituent quarks. The process “looks” more like elastic scattering involving a free proton than it does an inelastic process.

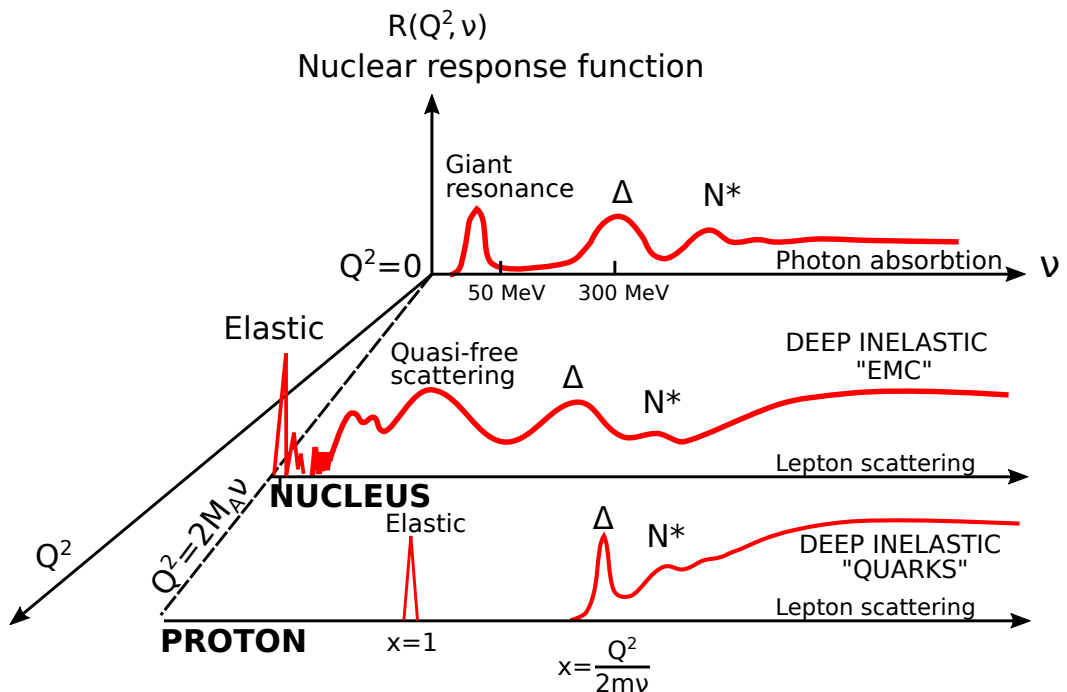


Figure 1-3: A schematic representation of the nuclear response function, illustrating the phenomena probed by electron-nucleus scattering in different regions of energy and momentum transfer. Reproduced from Ref [8].

Quasielastic scattering is one type of scattering process that can be studied in detail at JLab in Hall C using a pair of apparatuses called spectrometers. If both spectrometers are used in tandem to collect both the scattered electron and ejected proton, this is called *exclusive* quasielastic scattering. Inclusive scattering detects only one of the particles, leaving some ambiguity about exactly what process led to its being scattered into a spectrometer.

Because the ejected proton interacts with the residual nucleons via the strong

force, it will interact with the nuclear medium as it exits the nucleus. This “rescattering” process is well-described by Glauber multiple scattering theory [9]. However, there is a distinctive prediction [10, 11] arising from QCD that in exclusive processes at large Q^2 , initial and final state interactions (ISI and FSI) such as Glauber multiple scattering vanish. At sufficiently large Q^2 , a proton ejected from a nucleus in quasielastic scattering behaves as if it were a free proton participating in elastic scattering.

1.3 Color Transparency

Color transparency (CT), a characteristic prediction of QCD, refers to the reduction of initial and final state interactions between a hadron and the nuclear medium in exclusive processes at large momentum transfer Q^2 . The concept was first independently proposed by Mueller and Brodsky in the context of perturbative QCD, but was later shown to arise in nonperturbative models.

There are three requirements for the observation of CT in an experiment:

- Squeezing: the formation of a small configuration of quarks, sometimes referred to as a point-like configuration (PLC)
- Interactions between the PLC and the nuclear medium are attenuated because of its small size
- Freezing: the PLC maintains its small size over a distance comparable to or greater than the nuclear radius

There is some evidence for the existence of and onset of CT in experiments involving mesons. The results of experiments involving baryons are a mixed bag; some results are consistent with the absence of CT and others are ambiguous and cannot be attributed to CT alone. These experiments and relevant theoretical models and considerations are discussed in Chapter 2.

In experiments studying the color transparency phenomenon, a common observable is the nuclear transparency. It is generally of the form $T = \sigma_A/A\sigma_0$, the ratio of the per-nucleon cross section for some exclusive scattering process to the cross section for the same process on a free nucleon. Nuclear transparency can be

thought of as the probability that a hadron produced in a scattering process will exit the nucleus without rescattering from another nucleon.

Previous experiments have used slightly different definitions of nuclear transparency depending on the experiment's particulars. Studies of $A(p, 2p)$, quasielastic proton knockout using a proton beam, at Brookhaven National Lab (BNL) [12, 13, 14, 15] used the ratio of $\frac{d\sigma}{dt}$, where t is the four-momentum transfer squared. Studies of $A(e, e'p)$, quasielastic electron scattering, at MIT-Bates [16], SLAC [17, 18] and Jefferson Lab (JLab) [19, 20, 21] used the ratio of charge-normalized yields Y measured in experiment and from Monte Carlo simulation, $T = Y^{exp}/Y^{MC}$. Studies of $A(e, e'\pi^+)$, pion electroproduction, at JLab [22, 23] used the super-ratio of the ratio of yields from experiment and simulation for a nucleus with A nucleons in the numerator and hydrogen in the denominator, $T = (Y^{exp}/Y^{MC})_A/(Y^{exp}/Y^{MC})_H$.

Traditional Glauber multiple scattering theory predicts that T is constant as Q^2 increases. In this picture, the transparency should follow the same energy dependence of the nucleon-nucleon scattering cross sections which, as shown in Fig 1-4, are relatively constant between lab momenta of 1 GeV and 1 TeV. The reduction of initial/final state interactions predicted by CT results in an increase in nuclear transparency with Q^2 . An illustration of this behavior is shown in Fig 1-5.

1.4 Nuclear Transparency

In order to quantify the effects of final state interactions in processes like quasielastic scattering, experiments measure nuclear transparency—the ratio of the measured interaction cross section to the cross section calculated in the PWIA. The definition of transparency used in this work is the same as that used by previous experiments looking for the onset of CT in ${}^{12}C(e, e'p)$,

$$T(Q^2) = \frac{\int_V d^3p_m dE_m Y^{exp}(E_m, \vec{p}_m)}{\int_V d^3p_m dE_m Y^{PWIA}(E_m, \vec{p}_m)} \quad (1.1)$$

where Y^{exp} and Y^{PWIA} are charge-normalized yields from experiment and simulation.

The experimental yield is given by $Y = N/Q$, where N is the total number of

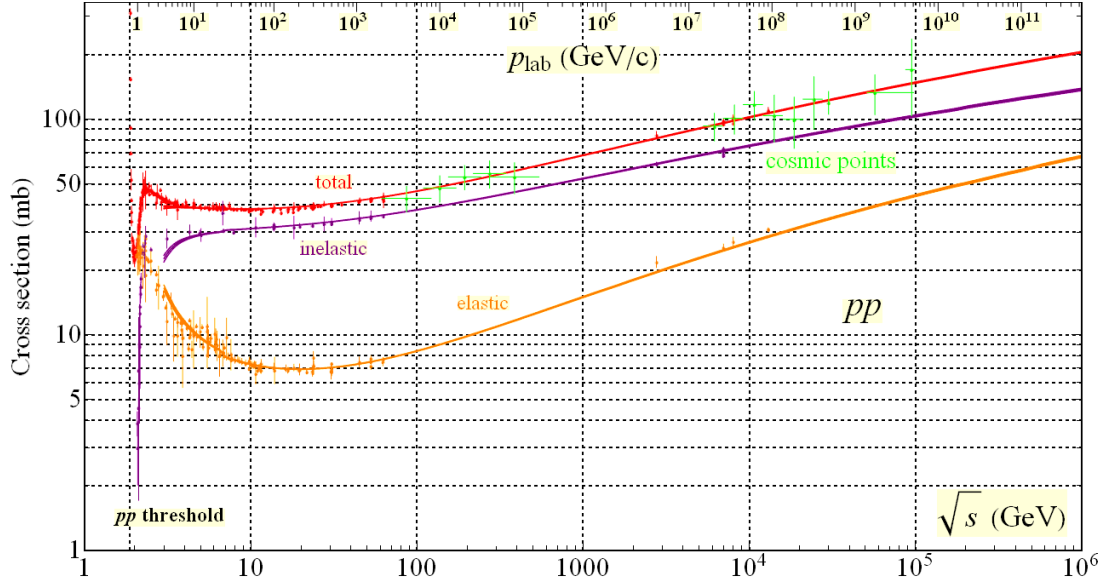
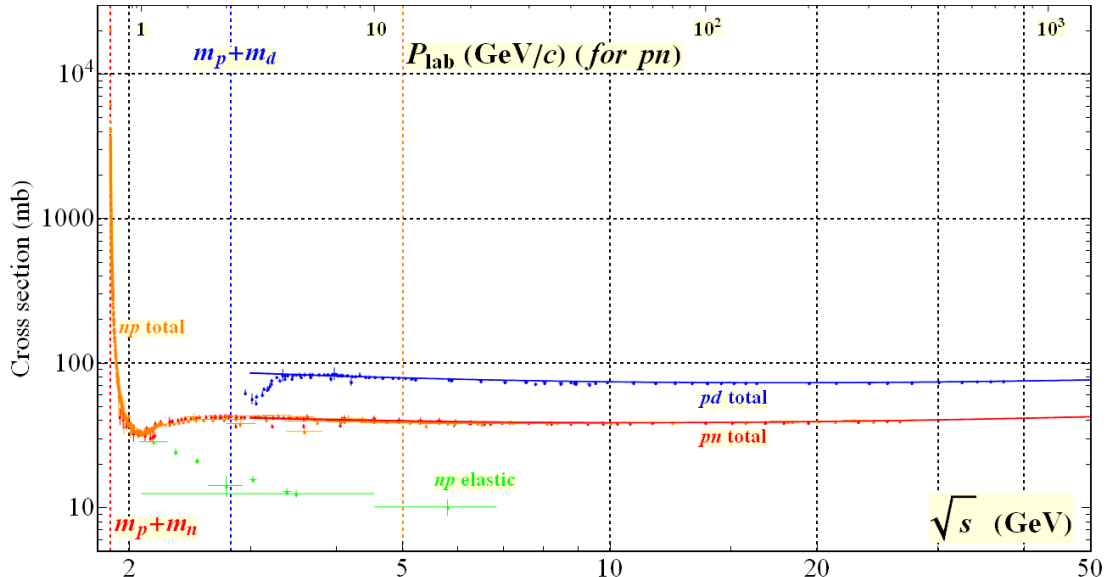
(a) Total, elastic, and inelastic pp cross sections versus p_{lab} and \sqrt{s} .(b) Total pn and pd cross sections versus p_{lab} and \sqrt{s} .

Figure 1-4: Total, elastic, and inelastic pp , pn , and pd , cross sections versus lab momentum p_{lab} and center of mass energy \sqrt{s} . Note that the total cross section is relatively constant over the range of momenta studied in E12-06-107, about 4 GeV to 10 GeV. Figure reproduced from Ref [24].

scattering events measured per integrated beam charge Q incident on the target. If the beam current is j and the target has density ρ and length l , then the total number of events is $N = \int_{t_1}^{t_2} j \rho l \sigma dt$, integrated over the total time the beam was on $t_2 - t_1$. The simulated yield is generated by SIMC, a Monte Carlo simulation of the PWIA. The details of the simulation are described in Section 1.8 and Appendix A.

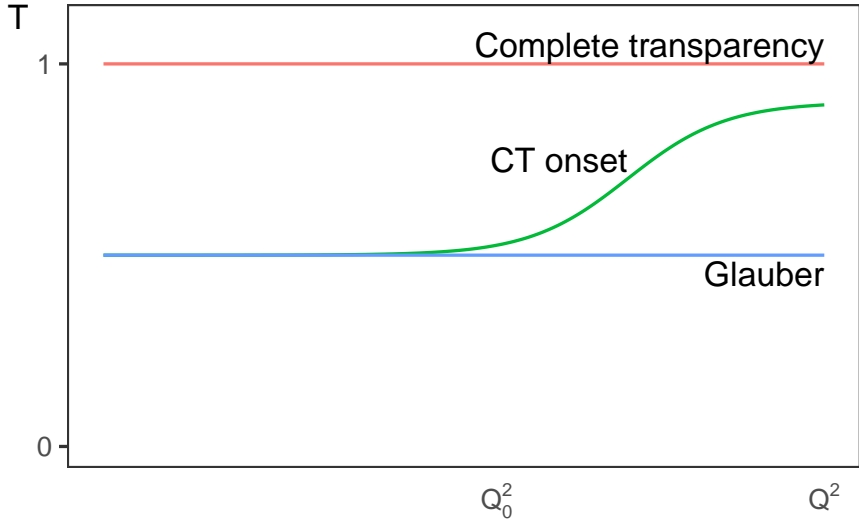


Figure 1-5: An illustration of the Q^2 dependence of nuclear transparency T for three scenarios. The blue line illustrates the prediction of the Glauber model, which has constant T as Q^2 increases. The red line illustrates that for full color transparency, $T = 1$; in this scenario there are no final state interactions between the ejected proton and the rest of the nucleus. The green line illustrates the scenario where the transparency begins to deviate from the Glauber prediction above an onset Q_0^2 and approach $T = 1$ with increasing Q^2 .

The yields are integrated over a volume of missing energy and momentum phase space V , defined by the cuts $E_m < 80\text{ MeV}$ and $|\vec{p}_m| < 300\text{ MeV}$. These cuts prevent inelastic contributions from pion production and ensure that the recoil nucleus remains in its ground state.

1.5 Plane Wave Impulse Approximation (PWIA)

Let E_e and E'_e be the incoming and outgoing energies of an electron scattering elastically from a proton. The cross section for this process, calculated for single photon exchange, is given by the Rosenbluth formula

$$\frac{d\sigma}{d\Omega} = \left(\frac{d\sigma}{d\Omega} \right)_{Mott} \frac{E'_e}{E_e} \left(\frac{G_E^2 + \tau G_M^2}{1 + \tau} + 2\tau G_M^2 \tan^2 \frac{\theta}{2} \right) \quad (1.2)$$

where G_E and G_M are the electric and magnetic form factors, $q^\mu = (\nu, \vec{q})$ is the 4-momentum transferred to the proton, $Q^2 = -q_\mu q^\mu$ is the momentum transfer squared, $\tau = Q^2/4M^2$, and $\left(\frac{d\sigma}{d\Omega} \right)_{Mott}$ is the cross section for elastic scattering off a structureless point particle,

$$\left(\frac{d\sigma}{d\Omega} \right)_{Mott} = \frac{\alpha^2 \cos^2 \frac{\theta}{2}}{4E_e^2 \sin^4 \frac{\theta}{2}} \quad (1.3)$$

Because nucleons bound in nuclear targets are off-shell and the particles involved can interact with the surrounding nuclear medium, the Rosenbluth model is not valid in this case.

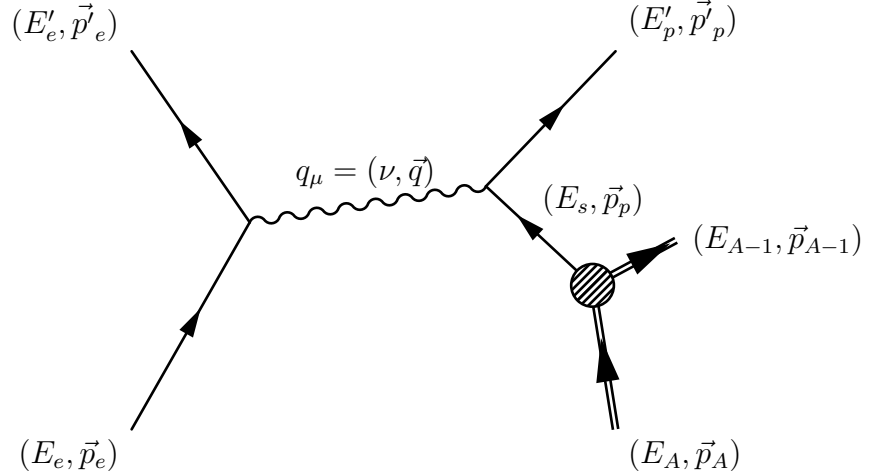


Figure 1-6: Feynman diagram for $A(e, e'p)$ scattering in the PWIA.

The plane wave impulse approximation (PWIA) incorporates these complications with the following assumptions and approximations:

1. Individual nucleons interact with the mean field generated by the rest of the nucleus, with no current exchanged between nucleons
2. Free form factors can be used to describe bound nucleons
3. The electron and proton's initial and final state wavefunctions are undistorted plane waves (meaning there are no ISI, FSI, or Coulomb distortions)
4. The outgoing proton absorbed the entire momentum transfer
5. Single photon exchange is sufficient to describe the interaction

Incorporating off-shell effects, the differential cross section can be factorized [25, 26, 27]

$$\frac{d^6\sigma}{dE'_e d\Omega'_e dE'_p d\Omega'_p} = p'_p E'_p \sigma_{ep} S(E_s, \vec{p}_p) \quad (1.4)$$

where Ω'_e and Ω'_p are the solid angles of the outgoing particles, σ_{ep} is the off-shell ep cross section, and the spectral function $S(E_s, \vec{p}_p)$ represents the probability of finding a proton in the nucleus with initial momentum \vec{p}_p and separation energy E_s . The separation energy is the energy required to remove a proton from the nucleus to infinity while leaving the recoil nucleus with zero kinetic energy $T_{A-1} = 0$. In this work, the ep cross section used is DeForest's prescription [26] σ_1^{cc} , which was initially calculated in Ref [28] for quasielastic scattering from 3He . This cross section is set by imposing momentum and energy conservation at the γp vertex. The normalization condition, given nuclear charge Z , for the spectral function is

$$\int d^3p_p dE_s S(E_s, \vec{p}_p) = Z \quad (1.5)$$

E_s and p_p can be estimated by measuring missing energy and momentum

$$E_m = \omega - T_{p'} - T_{A-1} \quad (1.6)$$

$$\vec{p}_m = \vec{p}_{p'} - \vec{q} \quad (1.7)$$

where the kinetic energy is $T = E - m$. These measured quantities differ from E_s and p_p due to FSI, radiative effects, and the spectrometers' finite resolutions.

The cross section in Equation 1.4 assumes the recoil nucleus $A-1$ remains in its ground state. Coincidence data can include events where this is not the case, for instance where the recoil nucleus is excited or one spectrometer arm is triggered by a pion. Data taken at Saclay [29] for quasielastic scattering from ^{12}C suggest that a cut on missing energy below ~ 100 MeV limits the rates of the former. Cutting on missing energy and using cuts on quantities from particle identification (PID) detectors limits coincidence events other than ep .

1.6 Quasielastic Scattering and the Glauber Approximation

Benhar et. al [30, 21] present a calculation of nuclear transparency for quasielastic scattering in the correlated Glauber approximation. What follows is a summary

of their method.

Let $\Psi_0^{(A)}$ be the ground state wave function of the A -body target nucleus, $\Psi_{\vec{p}}$ the final state wave function of the ejected proton with momentum \vec{p} , and $\Psi_f^{(A-1)}$ is the final state wave function of the residual $(A - 1)$ nucleus. Then, in terms of annihilation $\hat{a}_{\vec{k}}$ and creation operators $\hat{a}_{\vec{k}}^\dagger$ for nucleon states of momentum \vec{k} , the matrix amplitude for $A(e, e'p)$ scattering can be written

$$\mathcal{M} = \langle \Psi_{\vec{p}}^{(A-1)} | \sum_{\vec{k}} \hat{a}_{\vec{k}+\vec{q}}^\dagger \hat{a}_{\vec{k}} | \Psi_0^{(A)} \rangle \quad (1.8)$$

The Hamiltonian of the full A -body system can be rewritten to separate the final state interactions between the ejected proton and the spectator nucleons

$$\hat{H}_A = \hat{H}_0 + \hat{H}_{FSI} = (\hat{H}_{A-1} + T_1) + \hat{H}_{FSI} \quad (1.9)$$

where H_{A_1} is the Hamiltonian of the recoil nucleus T_1 is the kinetic energy operator for the ejected proton and \hat{H}_{FSI} contains the final state interactions.

Then, if the state $\Phi_{\vec{p}}$ is an eigenstate of H_0 that describes the system in the absence of FSI, there is a scattering operator $\Omega_{\vec{p}}$ such that

$$|\Psi_{\vec{p}}\rangle = \Omega_{\vec{p}} |\Phi_{\vec{p}}\rangle \quad (1.10)$$

Formally, this operator can be written

$$\Omega_{\vec{p}} = \lim_{t \rightarrow \infty} e^{-i\hat{H}_A t} e^{-i\hat{H}_0 t} \quad (1.11)$$

$$= \lim_{t \rightarrow \infty} \hat{T} e^{-\int_0^t dt' \hat{H}_{FSI}(t')} \quad (1.12)$$

where \hat{T} is the time ordering operator and

$$\hat{H}_{FSI}(t) = e^{i\hat{H}_0 t} \hat{H}_{FSI} e^{-i\hat{H}_0 t} \quad (1.13)$$

Calculating this expression for a realistic Hamiltonian is difficult, but under appropriate circumstances the Glauber approximation [9] can be used to simplify this expression. The Glauber approximation assumes that the ejected proton

moves in a straight line without rescattering (the eikonal approximation) and the spectator nucleons can be treated as fixed (the frozen approximation).

Assume the spectator nucleons are frozen at positions $\vec{r}_j = z_j \hat{z} + \vec{b}_j$ where the \hat{z} axis lies along the path of the ejected proton and \vec{b}_j are perpendicular to \hat{z} .

Let $R = \{\vec{r}_1, \vec{r}_2, \dots, \vec{r}_A\}$ be the spatial configuration of the full A -body system. In the correlated Glauber approximation, the scattering operator can be written in coordinate space

$$\Omega_{\vec{p}}(R) \equiv \langle R | \Omega_{\vec{p}} | R \rangle = \hat{P}_z \left[1 - \sum_{j=2} \theta(z_j - z_1) \Gamma(\vec{b}_j - \vec{b}) \right. \\ \left. + \sum_{j=2, k>j} \theta(z_j - z_1) \Gamma(\vec{b}_j - \vec{b}) \theta(z_k - z_1) \Gamma(\vec{b}_k) \right. \\ \left. - \dots \right] \quad (1.14)$$

where \hat{P}_z is a z -ordering operator preventing backscattering of the ejected proton and the step functions $\theta(z)$ ensure causality. The profile function $\Gamma(\vec{b})$ is a function of impact parameter \vec{b} and contains all the information about the scattering process. It is a Fourier transform of the scattering amplitude $f(\vec{k}_t)$ which can be extracted from measured cross sections.

$$\Gamma(\vec{b}) = -\frac{i}{2} \int \frac{d^2 k_t}{(2\pi)^2} e^{-\vec{k}_t \cdot \vec{b}} f(\vec{k}_t) \quad (1.15)$$

The scattering amplitude takes the parameterized form

$$f(\vec{k}_t) = i\sigma_{tot}(1 - i\epsilon)e^{-k_t^2/2B} \quad (1.16)$$

where ϵ is the ratio of the scattering amplitude's real and imaginary parts and B is a slope parameter.

Let $\rho_p(\vec{r})$ be the proton density in a target nucleus with Z protons. Then the transparency is

$$T = \frac{1}{Z} \int d^3 r \rho(\vec{r}) |\Omega_{\vec{p}}(\vec{r})|^2 \quad (1.17)$$

The integrand can be expanded in terms of n -body distribution functions $\rho_{pN\dots N}^{(n)}(\vec{r}_1, \vec{r}_2, \dots, \vec{r}_n)$ that express the joint probability of finding the ejected pro-

ton at \vec{r}_1 and the $n - 1$ spectator nucleons at positions $\{\vec{r}_2, \dots, \vec{r}_n\}$.

$$\begin{aligned} \rho_p(\vec{r}_1) |\Omega_{\vec{p}}(\vec{r})|^2 = \\ 1 - \frac{1}{\rho_p(\vec{r}_1)} \left[\int d^3\vec{r}_2 \theta(z_2 - z) \Gamma(\vec{b}_2 - \vec{b}) \rho_{pN}^{(2)}(\vec{r}_1, \vec{r}_2) \right. \\ - \int d^3\vec{r}_2 d^3\vec{r}_3 \theta(z_2 - z) \Gamma(\vec{b}_2 - \vec{b}) \theta(z_3 - z) \Gamma(\vec{b}_3 - \vec{b}) \rho_{pNN}^{(3)}(\vec{r}_1, \vec{r}_2, \vec{r}_3) \\ \left. + \int d^3\vec{r}_2 d^3\vec{r}_3 d^3\vec{r}_4 \dots \right] \end{aligned} \quad (1.18)$$

The quantity in brackets contains the effects of final state interactions, which result in a decrease in transparency from the PWIA result, $T = 1$. Each term represents contributions from $n - 1$ rescatterings. The single rescattering term can be written as $\rho_{pN}^{(2)}(\vec{r}_1, \vec{r}_2) = \rho_p(\vec{r}_1) \rho_N(\vec{r}_2) g(\vec{r}_1, \vec{r}_2)$, where the function $g(\vec{r}_1, \vec{r}_2)$ describes the correlations between nucleons [31]. At short ranges $r = \|\vec{r}_1 - \vec{r}_2\|$, $g(r) \ll 1$ because of the strongly repulsive core of the nucleon-nucleon interaction. At large r , $g(r) \rightarrow 1$ because of asymptotic freedom.

1.6.1 Pandharipande et al.

This experiment takes the work of Pandharipande and Pieper [32] as the null hypothesis against which the onset of color transparency is to be tested. This is the same model used in previous measurements of nuclear transparency in quasielastic scattering [20, 19, 21, 16].

The model starts with the assumption that the differences between cross sections for free and in-medium nucleon-nucleon scattering arise primarily from Pauli blocking of final states and effective mass corrections. Pandharipande and Pieper find good agreement between experimental results and their model's estimates of the imaginary part of the optical potential in nuclear matter. The model uses the Urbana v₁₄+TNI Hamiltonian [33, 34] and variational method [35, 36] to calculate an optical potential U for symmetric nuclear matter. This Hamiltonian includes the effect of nucleon-nucleon correlations by fitting two-body operators to phase shift data taken for neutron-proton scattering [37].

The dispersion relation $e(k, \rho)$ for nucleons in nuclear matter with density ρ

and real part of the optical potential $U(k, \rho)$ is

$$e(k, \rho) = \frac{\hbar^2 k^2}{2m} + U(k, \rho) \quad (1.19)$$

The group velocity of an in-medium nucleon with momentum k differs from that of a free nucleon. The derivative of the dispersion relation gives this velocity and a definition of the effective mass m^*

$$\frac{1}{\hbar} \frac{d}{dk} e(k, \rho) = \frac{\hbar^2 k}{m} + \frac{1}{\hbar} \frac{d}{dk} U(k, \rho) \equiv \frac{\hbar k}{m^*(k, \rho)} \quad (1.20)$$

The in-medium cross section for a proton with momentum k scattering off a nucleon $a = n, p$ is

$$\tilde{\sigma}_{pa}(k, \rho) = \frac{m^*(k, \rho)}{\hbar k \rho_a \tau_a(k)} \quad (1.21)$$

where τ_a is the life time of the two-particle-one-hole state. With this expression for the cross section, the nuclear transparency T can be calculated using a local density approximation and a wavefunction from conventional Glauber multiple-scattering theory,

$$T = \frac{1}{A} \int d^3 r' \rho_p(\vec{r}') P_T(\vec{r}') \quad (1.22)$$

where P_T , the probability that a proton struck at \vec{r}' emerges without rescattering, is

$$P_T(\vec{r}') = \exp \left\{ - \int_{z'}^{\infty} dz'' \left[g_{pn}(\vec{r}', \vec{r}'') \tilde{\sigma}_{pn} \left(k, \rho(\vec{r}'') \right) \rho_n(\vec{r}'') + g_{pp}(\vec{r}', \vec{r}'') \tilde{\sigma}_{pp} \left(k, \rho(\vec{r}'') \right) \rho_p(\vec{r}'') \right] \right\} \quad (1.23)$$

In the above expression, $g_{pa}(\vec{r}', \vec{r}'')$ is a pair distribution function [31], the joint probability to find a proton at \vec{r}' and nucleon a at \vec{r}'' .

Glauber models such as this predict that nuclear transparency T remains constant for increasing momentum transfer Q^2 , as shown by the dotted line in Fig 1-7.

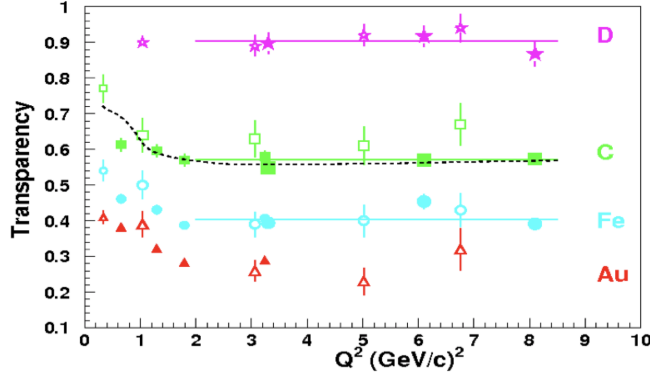


Figure 1-7: Transparency measurements from several experiments studying quasielastic electron scattering from deuterium, carbon, iron, and gold. Data taken at JLab [19, 20, 21] are shown as solid points. Data taken at SLAC [17, 18] are shown as large open symbols. Data taken at Bates [16] are shown as small open symbols. The dotted line is a Glauber calculation from [32] for carbon data. Solid lines are constant-value fits to data above 2 GeV.

1.7 The Onset of Color Transparency

The signature of the onset of CT is a rise in T with Q^2 above some threshold Q_0^2 . Previous measurements of T in $^{12}C(e, e'p)$ at SLAC, MIT-Bates, and JLab for momentum transfers between $Q^2 = 0.6$ and 8.1 GeV^2 have been consistent with the predictions of the Glauber model. This section outlines two models of color transparency whose predictions for the Q^2 dependence of T will be compared with this experiment's results in the final chapter.

The model presented by Frankfurt et al. [38] starts by calculating the amplitude \mathcal{M}_h^{*A} for quasielastic scattering of a proton from a fixed shell h in a nucleus. This amplitude includes the effects of short range nucleon-nucleon correlations, both between the ejected proton and remainder nucleons in the recoil nucleus as well as between the remainder nucleons. Using the distorted wave impulse approximation (DWIA), they derive an expression for nuclear transparency whose behavior is dependent on the form of nucleon-nucleon interactions. These interactions are determined by the choice of profile function $\Gamma(\vec{b})$ that parameterizes the interaction strength as a function of impact parameter \vec{b} . They compare two choices of profile function—one which corresponds to the absence of CT (i.e. typical pp and pn scattering) and one which includes a model of CT in which the PLC grows to the full size of a proton over a length l_h , the hadron formation length [39].

The model presented by Cosyn et al. [40, 41] uses a relativistic multiple scat-

tering Glauber approximation [42]. Glauber calculations account for final state interactions by applying a phase to the ejected proton's wavefunction². This phase is determined by a profile function $\Gamma(\vec{b})$ that parameterizes nucleon-nucleon scattering. As in the other model, this profile function is modified to either include or not include the same CT effects [39]. Short range correlations are implemented by means of an effective nucleon density [43] that enters into the calculation of the Glauber phase.

To include CT effects, both models replace the total cross section σ_{tot} with an effective cross section σ_{eff} based on a quantum diffusion model [39] that accounts for reduced interaction between the prehadron and nuclear matter over a hadron formation length l_h ,

$$\sigma_{eff} = \sigma_{tot} \left\{ \left[\frac{z}{l_h} + \frac{\langle n^2 k_t^2 \rangle}{t} \left(1 - \left(\frac{z}{l_h} \right) \right) \right] \theta(l_h - z) + \theta(z - l_h) \right\} \quad (1.24)$$

In this expression, n is the number of valence quarks (2 for mesons, 3 for baryons), $k_t \sim 1 \text{ GeV}^2/Q^2$ is the average transverse momentum of a quark inside a hadron, z is the distance the object has traveled since its creation, and $l_h = 2p/\Delta M^2$ is the hadronic formation length. This length depends on the momentum p of the outgoing hadron and the mass squared difference between the prehadron and outgoing hadron state. Frankfurt et al. use $\Delta M^2 = 0.7 \text{ GeV}^2$ for protons, while Cosyn et al. use $\Delta M^2 = 1.0 \text{ GeV}^2$.

1.7.1 Frankfurt et al.

In the DWIA, the cross section can be written

$$\frac{d^6\sigma}{dE'_e d\Omega'_e d^3p'_p} = p'_p E'_p \sigma_{eN} S(\vec{p}_p, E_M, \vec{p}'_p) \quad (1.25)$$

²Note that this phase is not a unique relativistic effect. It is part of the *eikonal approximation* employed in general by Glauber calculations. In this approximation, the outgoing wavefunction of a particle with incident momentum $\vec{k} = k\hat{z}$ and impact parameter \vec{b} (where $\vec{k} \cdot \vec{b} = 0$) interacting with a potential $V(b, z)$ can be written $\psi_{out} = e^{i\chi(b)} e^{ikz}$ where the phase is $\chi(b) \propto \int_{-\infty}^{\infty} V(b, z) dz$. This phase is implicit in the other Glauber models discussed in this chapter; it is mentioned explicitly in this section because it is the location in the derivation of Cosyn et al. that they insert the effects of CT. In contrast, Frankfurt et al.'s derivation does not explicitly mention the eikonal phase.

where σ_{eN} is the cross section for an electron scattering from a bound nucleon and $S(\vec{p}_p, E_m, \vec{p}'_p)$ is the distorted spectral function. For a fixed shell h the spectral function can be written [27],

$$S(\vec{p}_p, E_m, \vec{p}'_p) = n_h(E_m) |\Phi_h(\vec{p}_p, \vec{p}'_p)|^2 \quad (1.26)$$

where $\Phi_h(\vec{p}_p, \vec{p}'_p)$ is the distorted momentum distribution for nucleons in the h shell and $n_h(E_m)$ (proportional to the shell's occupation probability) characterizes the strength of the shell. Frankfurt et al. derive the following expression for the momentum distribution by expressing the ground state A -body wave function and $(A - 1)$ -body density matrix in terms of two-nucleon correlation functions

$$\left| \Phi_h(\vec{p}_p, \vec{p}'_p) \right|^2 = \left| \int d^3 r_1 \Psi_h(r_1) e^{-i\vec{p}_p \cdot \vec{r}_1} \exp \left\{ - \int_{z_1} \Gamma(\vec{b}_1 - \vec{b}) \tilde{\rho}(r) d^3 r \right\} \right|^2 \quad (1.27)$$

The profile function $\Gamma(\vec{b})$ takes the form

$$\Gamma(\vec{b}) = \frac{1}{2\pi i k} \int e^{i\vec{k}_t \cdot \vec{b}} f(\vec{k}_t) d^2 k_t \quad (1.28)$$

where the nucleon-nucleon scattering amplitude with CT effects is

$$f_{CT}(k_t, z, Q^2) = i \frac{k}{4\pi} \sigma_{eff}(z, Q^2) e^{Bt/2} \frac{G_N(t \sigma_{eff}(z, Q^2) / \sigma_{eff})}{G_N(t)} \quad (1.29)$$

and the amplitude without CT effects is

$$f(k_t) = \left(\frac{k_t}{4\pi} \right)^2 \sigma_{tot}^2 (1 + \epsilon^2) e^{-Bt} \quad (1.30)$$

where ϵ is the ratio of the scattering amplitude's real and imaginary parts and B is a slope parameter.

The nuclear transparency for the h shell is the ratio of the distorted momentum distributions from the DWIA and PWIA,

$$T_h = \left(\frac{\sigma^{exp}}{\sigma^{PWIA}} \right) = \frac{|\Phi_h^{DWIA}(p_p, p'_p)|^2}{|\Phi_h^{PWIA}(p_p)|^2} \quad (1.31)$$

Transparency predictions for $^{12}C(e, e'p)$ scattering from the s shell, with and

without CT, are shown in Fig 1-8.

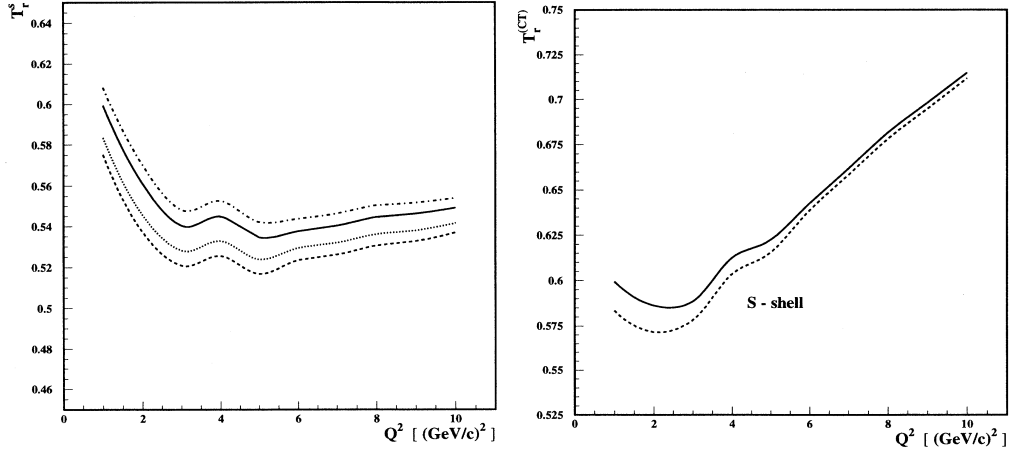


Figure 1-8: Transparency calculations for $^{12}C(e, e'p)$ based on a model that accounts for nucleon correlations and proton knock-out from particular nuclear shells [38]. The figure on the left is for a model that does not include CT. The dotted line is the calculation without correlation effects; the dashed line, with the effects of correlation between undetected nucleons; the dash-dotted line, with the effects of correlation between knocked-out proton and undetected nucleons; and solid line, with over-all correlation effects. The figure on the right includes CT. The dashed line is the calculation without correlation effects; the solid line, with correlation effects. The rise in transparency with Q^2 is the characteristic signature of the onset of CT. Note that the effect of nucleon correlations on the CT model is a correction of a few percent.

1.7.2 Cosyn et al.

Cosyn et al. derive an expression for nuclear transparency as a ratio of cross sections calculated in a relativistic multiple scattering Glauber approximation (RMSGA) and a relativistic plane wave approximation (RPWIA). They do so using the RMSGA formalism for $A(e, e'p)$ reactions developed by Ryckebusch et al. [42].

Briefly stated, the Glauber approximation consists of assigning a complex phase $\chi(\vec{r})$ the outgoing proton wavefunction ψ_{out}

$$\psi_{out}(\vec{r}) = e^{i\chi(\vec{r})}\psi_{in}(\vec{r}) \quad (1.32)$$

This phase can be parameterized as a function of impact parameter \vec{b} , momen-

tum transfer Q^2 , etc. by a profile function $\Gamma(\vec{b})$. For a single rescattering,

$$\psi_{out}(\vec{r}) = (1 - \Gamma(\vec{b}))\psi_{in}(\vec{r}) \quad (1.33)$$

Every spectator nucleon in the recoil nucleus lying in the forward path of the ejected proton contributes to the total phase. Let \vec{r} be the point at which the ejected proton absorbs the virtual photon. The total phase shift for A nucleons is a product

$$e^{i\chi(\vec{r})} = \prod_{j=2}^A \left(1 - \Gamma(\vec{b}_j)\theta(z_j - z)\right) \quad (1.34)$$

The profile function for a hadron h scattering from a nucleon N is determined by the interaction cross section σ_{tot}^{hN} , the ratio ϵ_{hN} of the scattering amplitude's real and imaginary parts, and slope parameter β_{hN} , all of which are momentum-dependent. These parameters can be estimated by interpolating data from the Particle Data Group.

$$\Gamma(\vec{b}) = \frac{\sigma_{tot}^{hN}(1 - i\epsilon_{hN})}{4\pi\beta_{hN}^2} \exp -\frac{\vec{b}^2}{2\beta_{hN}^2} \quad (1.35)$$

The slope parameter β_{hN} can be estimated using the elastic σ_{el}^{hN} and total σ_{tot}^{hN} cross sections in the following approximation

$$\beta_{pN}^2 \approx \frac{(\sigma_{tot}^{hN})^2(\epsilon_{hN}^2 + 1)}{16\pi\sigma_{el}^{hN}} \quad (1.36)$$

More rigorously, the analysis starts with an expression for the differential cross section

$$\frac{d^5\sigma}{dE'_ed\Omega'_ed\Omega'_p} = \frac{m_e^2 m_p M_{A-1}}{(2\pi)^5 M_A} \frac{p'_e p_p}{p_e} f_{rec}^{-1} \sum_{if} |\mathcal{M}_{fi}|^2 \quad (1.37)$$

where f_{rec} is a hadronic recoil factor

$$f_{rec} = \frac{E_{A-1}}{E_A} \mid 1 + \frac{E_p}{E_{A-1}} \left(1 - \frac{\vec{q} \cdot \vec{p}_p}{p_p^2}\right) \mid \quad (1.38)$$

To evaluate this expression, Ryckebusch et al. write the matrix elements of the electromagnetic current operator \hat{J}^μ in terms of solutions $\phi(\vec{r})$ of the Dirac

equation

$$\langle J^\mu \rangle = \int d\vec{r} \phi_{p_p m_s}^\dagger(\vec{r}) \mathcal{G}^\dagger(\vec{b}, z) \gamma^0 J^\mu(\vec{r}) e^{i\vec{q}\cdot\vec{r}} \phi_\alpha(\vec{r}) \quad (1.39)$$

where \mathcal{G} is the Dirac-Glauber phase

$$\mathcal{G}(\vec{b}, z) = \prod_{\alpha_{\text{occ}} \neq \alpha} \left[1 - \int d\vec{r}' |\phi_{\alpha_{\text{occ}}}(\vec{r}')|^2 \theta(z' - z) \Gamma(\vec{b}' - \vec{b}) \right] \quad (1.40)$$

The RPWIA is a special case of this phase with $\mathcal{G} = 1$. That is, the RPWIA does not include any FSI effects.

With this formalism, Cosyn et al. arrive at the following expression for nuclear transparency:

$$T = \frac{\sum_\alpha \int dq Y(q) \int d\vec{p}_m \left(\frac{d^5\sigma}{dE'_e d\Omega'_e d\Omega'_p} \right)_{\text{RMSGA}}}{\sum_\alpha \int dq Y(q) \int d\vec{p}_m \left(\frac{d^5\sigma}{dE'_e d\Omega'_e d\Omega'_p} \right)_{\text{RPWIA}}} \quad (1.41)$$

1.8 Simulation

The simulated yields in equation 1.1 come from Monte Carlo simulations of scattering processes, radiative effects, and spectrometer performance. These simulations are carried out by the FORTRAN program SIMC [44, 45].

SIMC was initially written for the NE18 experiment at SLAC [17] and subsequently adapted for the HMS and SOS spectrometers in JLab's Hall C. Further development added support for more scattering processes, the pair of HRS spectrometers in Hall A, and more recently the new SHMS spectrometer in Hall C.

SIMC generates events over a wide phase space, starting from beam and target geometry. Generating events over a region of phase space wider than the spectrometers' acceptance allows simulation of events that will be thrown into the acceptance window, for example, because of multiple scattering or energy loss. Events are then propagated through models of the spectrometers' optics, accounting for effects such as energy loss and multiple scattering in materials lying along the particles' trajectories, as well as spectrometer acceptance and resolution. Target variables are reconstructed from tracks fit at the focal plane. Then a weight is calculated based on a model cross section for the initial kinematics of each event.

Appendix A contains descriptions of some of the models and parameters used in SIMC simulations.

1.9 This Experiment: E12-06-107

Previous measurements of nuclear transparency in quasielastic electron scattering experiments have been consistent with the Glauber prediction, as shown in Fig 1-9. The goal of this experiment was to extend the range of Q^2 studied in quasielastic $^{12}C(e, e'p)$ scattering in hopes of observing the onset of CT. Data were taken in Hall C at the Thomas Jefferson National Accelerator Facility in Newport News, VA, using the High Momentum Spectrometer (HMS) and new Super High Momentum Spectrometer (SHMS) in coincidence. Data were taken with carbon foil and liquid hydrogen targets over a range of momentum transfer Q^2 from 8.0 to 14.2 GeV 2 . The spectrometer angles and central momenta for these Q^2 points are listed in Table 1.1.

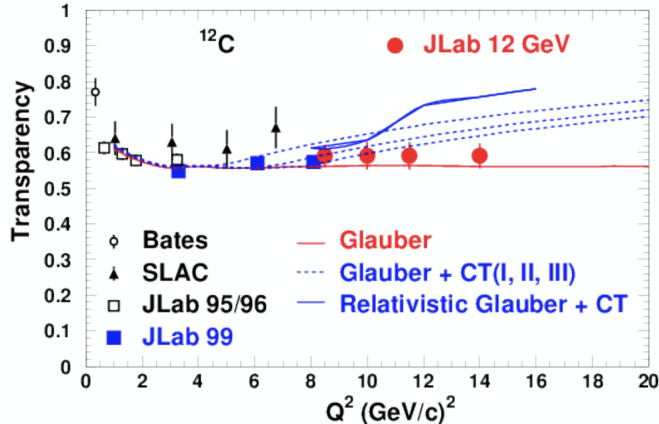


Figure 1-9: Transparency measurements from several experiments studying quasielastic electron scattering carbon. Data taken at JLab [19, 20, 21] are shown as squares. Data taken at SLAC [17, 18] are shown as solid triangles. Data taken at Bates [16] are shown as open circles. The Q^2 locations of this experiment’s measurements are shown as red circles with arbitrary T values and error bars represented expected uncertainty. The solid red line is a Glauber calculation from [32] for carbon data. The solid blue line is the prediction of Cosyn et al.’s relativistic Glauber model [41, 40]. The dashed blue lines are the predictions of Frankfurt et al.’s Glauber model [38] that includes the effects of CT for three choices of parameters.

Chapter 2 contains an overview of theoretical considerations relevant to the experiment and a brief history of previous experiments that have studied color transparency. Chapters 3 and 4 describe the experimental apparatus and data analysis procedure. Chapter 5 contains the final measurements of nuclear transparency and missing energy and momentum. Chapter 6 is a conclusion and summary.

Table 1.1: The kinematic settings used in the E12-06-107 experiment in Hall C at JLab.

Q^2 (GeV 2)	θ_{SHMS} ($^\circ$)	p_{SHMS} (GeV)	θ_{HMS} ($^{\circ\circ}$)	p_{HMS} (GeV)
8.0	17.1	5.122	45.1	2.131
9.5	21.6	5.925	23.2	5.539
11.5	17.8	7.001	28.5	4.478
14.2	12.8	8.505	39.3	2.982

Chapter 2

Theoretical Background and Previous Experiments

2.1 Defining Color Transparency

The phenomenon known as color transparency (CT) was independently proposed by Mueller [10] and Brodsky [11] in 1982. It is a distinctive feature of QCD’s quark degrees of freedom, not arising in a purely hadronic model. CT refers to vanishing initial and final state interactions (ISI and FSI) between hadrons and the surrounding nuclear medium in exclusive processes at large momentum transfer Q^2 . This is in contrast to conventional Glauber theory which assumes strong ISI/FSI and rescattering.

A QED phenomenon analogous to CT can be seen in the Chudakov effect. Several experiments have studied the decay $\pi^0 \rightarrow e^+e^-\gamma$ in photographic emulsions [46, 47, 48, 49, 50, 51]. As an electron-positron pair traveled through the emulsion, the observed ionization density increased with distance from the decay vertex, consistent with suppressed interaction between a small, slowly growing electric dipole and the surrounding medium. A small $q\bar{q}$ or qqq system or “point-like configuration” (PLC) is the QCD analogue of the QED dipole¹.

The existence of CT requires the following criteria:

- Scattering takes place by preferentially selecting point-like configurations

¹Incidentally, Bjorken used the reverse of this analogy in 1976 to illustrate why a small $q\bar{q}$ system shouldn’t create jets in hadronic final states created in electron-positron collisions [52].

(PLCs) with transverse size much smaller than a hadron’s “free” radius.

- Interactions between the PLC and the nuclear medium are reduced.
- The PLC’s compact size is maintained for a distance comparable to the size of the nucleus.

2.1.1 Squeezing

The first criterion can be thought of as “squeezing” a quark system into a PLC with transverse size smaller than the radius of the hadron detected in the final state.

An intuitive argument from Frankfurt et al. [53] is suggestive of the possibility of forming a PLC in quasielastic electron scattering from nuclei. Suppose a quark in the nucleus, after absorbing a virtual photon, is off-shell by $\Delta E = Q$. By the uncertainty principle, its lifetime should be $\tau = 1/Q$. It will decay by emitting a gluon which, if the final state is to include a proton, must be absorbed by nearby quarks in a radius $r \approx c\tau \sim 1/Q$. Thus, for large momentum transfers, the quark system formed in the scattering process should be quite small.

In 1980, Brodsky and Lepage [54, 55] showed, using perturbative QCD (pQCD), that the “squeezing” criterion is satisfied for exclusive processes at large Q^2 . In the years following, Isgur and Smith [56, 57, 58] cautioned against the use of pQCD to study exclusive processes, citing experimental evidence of significant soft contributions to pion and nucleon form factors. Experimental support for the dominance of PLCs in these processes will be discussed in Section 2.3.

2.1.2 Reduced Interaction Strength

The second criterion is a consequence of the PLC’s small size. Small configurations of quarks and gluons have small cross sections. The Low-Nussinov two-gluon exchange model [59, 60, 61] is a simple model of this phenomenon that treats baryons (mesons) as composed of only the bound states of valence quarks, $|qqq\rangle$ ($|q\bar{q}\rangle$). In this model, the hadron-hadron scattering amplitude vanishes as the transverse size of either of the hadrons vanishes—“simply put, color-singlet point particles do not radiate gluons, and cannot interact via gluon exchange” [62]. For

example, the couplings to a transferred gluon for the constituents in a small meson's $q\bar{q}$ pair contribute opposite signs. The same “color screening” effect occurs for small qqq configurations. Interactions with a hadron's $q\bar{q}$ sea components are similarly suppressed.

Holographic light-front QCD treats hadrons as a superposition of n -particle Fock states $|n\rangle$ [63]. In these states, n is constrained such that the difference between the number of quarks and antiquarks is three for baryons and zero for mesons. For example, the proton can be written

$$\begin{aligned} |p\rangle &= \sum_n \langle n|p\rangle|n\rangle \\ &= \psi_{3q/p}|uud\rangle + \psi_{3qg/p}|uudg\rangle + \psi_{4q\bar{q}/p}|uudu\bar{u}\rangle + \psi_{4q\bar{q}/p}|uudd\bar{d}\rangle + \dots \end{aligned} \quad (2.1)$$

where $\psi_{n/H}$ is the n -body light-front wavefunction for a hadron H . A hadron's form factor $F(Q^2)$ can be calculated with these wavefunctions, from which the transverse size $a_\perp^2(Q^2)$ can be calculated

$$a_\perp^2(Q^2) = -4 \frac{\frac{d}{dQ^2}F(Q^2)}{F(Q^2)} \quad (2.2)$$

In light-front holographic QCD, for a hadron of twist² τ at large Q^2 , this expression approaches [64]

$$a_\perp^2(Q^2) = \frac{4(\tau - 1)}{Q^2} \quad (2.3)$$

The value of Q^2 required to contract a hadron's valence constituents to a color-singlet of a given transverse size grows with the number of constituents as shown in Fig 2-1.

2.1.3 Freezing and Expansion

Suppose a PLC is created in the interior of a nucleus and, in its rest frame, expands to a configuration with normal size over a time τ_0 . Taking time dilation into account, it expands in a time $\tau = \tau_0 E/m$ in the rest frame of the nucleus over a distance called the coherence length l_c . For large enough energy E , l_c is

²the number of constituent quarks of the hadron's valence state

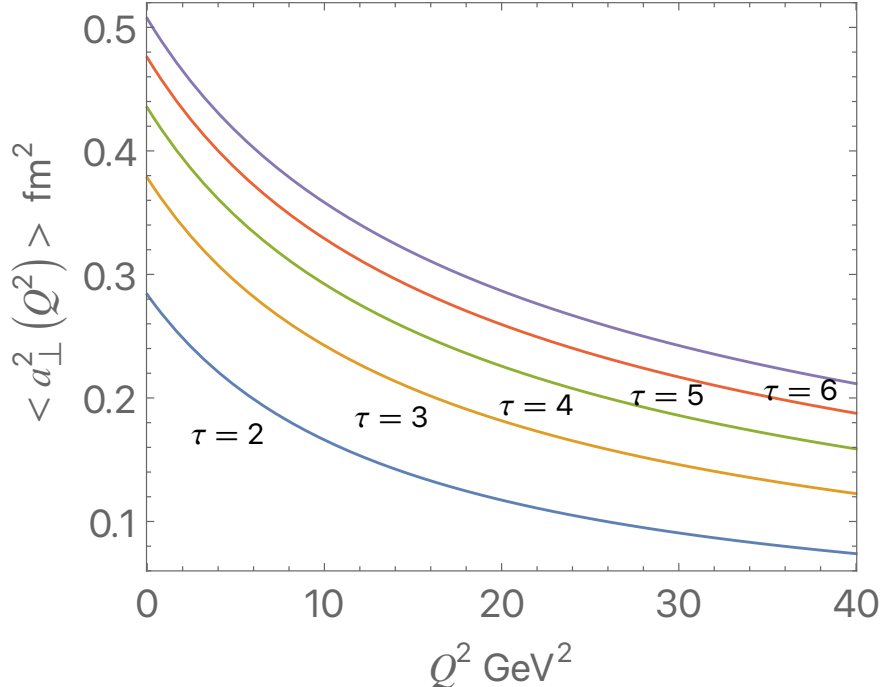


Figure 2-1: The transverse size of a hadron with twist τ as a function of momentum transfer Q^2 , as predicted by light-front holographic QCD. Figure reproduced from Ref [64].

larger than the nuclear diameter and the PLC can be described as “frozen” in its small transverse size as it escapes the nucleus. High energy processes where this is indeed the case will be discussed in Section 2.2.

At intermediate energies however, one must take into account the expansion of the PLC. Using the uncertainty principle, the decoherence time can be estimated, as in Ref [39], for an intermediate PLC state with mass m_{inter} and “normal” mass M_h :

$$\Delta E = \sqrt{p_h^2 + m_{inter}^2} - \sqrt{p_h^2 + M_h^2} \quad (2.4)$$

$$= p_h \left(\sqrt{1 + \frac{m_{inter}^2}{p_h^2}} - \sqrt{1 + \frac{M_h^2}{p_h^2}} \right) \quad (2.5)$$

$$\approx p_h \left(\frac{m_{inter}^2}{2p_h^2} - \frac{M_h^2}{2p_h^2} \right) \quad (2.6)$$

$$= \frac{\Delta M_h^2}{2p_h} \quad (2.7)$$

where $\Delta M_h^2 = m_{inter}^2 - M_h^2$. Then, in natural units, $\Delta E \Delta t = 1$ implies that the

coherence length is

$$l_c = \frac{2p_h}{\Delta M_h^2}. \quad (2.8)$$

The freezing approximation is valid if $l_c \gg R_A$ where R_A is the radius of the relevant nucleus.

Ref [39] also presents an estimate of the effective PLC-nucleon cross section as a function of propagation distance z . The model assumes that the effective cross section is scaled by the transverse size of the quark system x_t relative to the average size of the hadron $\langle x_t \rangle$. That is $\sigma_{hN}^{eff} = [x_t^2(z)/\langle x_t \rangle^2] \sigma_{hN}^{tot}$

Let n be the number of partons in the quark system, $\langle k_t \rangle$ the average transverse momentum of a parton in the hadron, and $t = -Q^2$ the momentum transfer squared. Then the transverse area occupied by the quark system is $\sigma_{hN}^{tot}(n^2 \langle k_t \rangle^2/t)$ at the point of interaction. The system expands over the coherence length l_c to its normal hadronic size.

The effective cross section is then

$$\sigma_{hN}^{eff} = \sigma_{hN}^{tot} \left\{ \left(\left(\frac{z}{l_c} \right)^\tau + \frac{\langle n^2 k_t^2 \rangle}{t} \left[1 - \left(\frac{z}{l_c} \right)^\tau \right] \right) \theta(l_c - z) + \theta(z - l_c) \right\} \quad (2.9)$$

The parameter τ distinguishes three models: non-perturbative QCD ($\tau = 0$; no reduction in cross section), pQCD ($\tau = 1$; x_t grows like \sqrt{z}), and a naive parton model ($\tau = 2$; x_t grows like z).

Another approach [65, 66, 67] expands the PLC wave function in terms of hadronic eigenstates $|\psi_i\rangle$ of the Hamiltonian. Let P be the PLC's momentum and assume each eigenstate satisfies $E_i \gg m_i$. Then

$$|\psi_{PLC}(t)\rangle = \sum_{i=1}^{\infty} a_i e^{-iE_i t} |\psi_i\rangle \quad (2.10)$$

$$= e^{-iE_1 t} \sum_{i=1}^{\infty} e^{-i\frac{(m_i^2 - m_1^2)t}{2P}} |\psi_i\rangle \quad (2.11)$$

This suggests that the loss of coherence is due to the relative phase between hadronic components. In other words, the coherence length is the length at which coherence between the lowest and first excited states is lost.

2.1.4 Color Transparency and QCD Factorization Theorems

CT is closely connected with QCD factorization theorems [68, 69, 70, 71, 72] which provide access to the generalized parton distributions (GPDs) that currently provide the most complete picture of the internal quark-gluon structure of various hadrons [73, 74, 75, 76]. These theorems assume, at sufficiently large Q^2 , that deeply inelastic exclusive processes' amplitudes are separable into two parts—a hard scattering at the parton level, and a soft part characterized by GPDs. The very possibility of calculating these processes in perturbative QCD depends on a fundamental property of QCD—the small interaction cross section between a small color singlet and other hadrons [72].

A general proof of QCD factorization theorems for exclusive DIS processes relies on showing that soft gluon interactions cancel [69, 77]. This cancellation is tied to the fact that the meson arises from a $q\bar{q}$ pair generated by the hard scattering that starts as a PLC, remains small, and only later grows to a normal hadronic size in the final state meson.

To illustrate the connection between CT and factorization, consider meson electroproduction in which a baryon such as a proton absorbs a virtual photon. In the Breit frame, the virtual photon and baryon are both initially at rest. After the quark-gluon system (which will become a meson) absorbs the photon, both it and the recoiling baryon move off in opposite directions at without any further gluon exchange between the two, provided the meson maintains a small transverse size. Qualitatively, the factorization in processes such as this is due precisely to color transparency—a virtual photon with small transverse size $b \sim 1/Q$ selects a PLC that will become the meson [72].

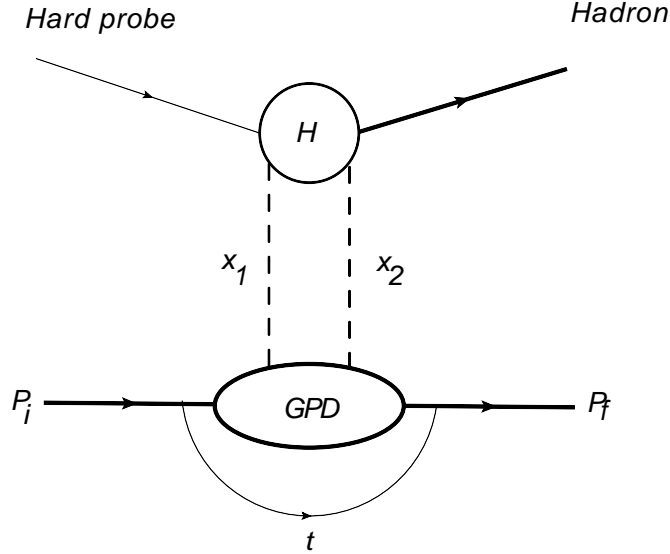


Figure 2-2: Sketch of a hard exclusive process in the factorization limit. CT ensures that additional exchanges of partons between the upper and lower blocks are suppressed by powers of Q^2 .

The amplitude of the hard exclusive process sketched in Fig 2-2 can be written in terms of three factors [78]:

1. The wave function of the PLC produced by the hard probe
2. The matrix element of the hard interaction
3. The GPD in the target $f(x_1, x_2, t, Q^2)$,

The GPD here describes the transition of the target from the initial state i to the final hadronic state when partons with light-cone fractions x_1 and x_2 are exchanged with the hard block, H , and the final state f of fixed mass and fixed $t = (p_i - p_f)^2$ is produced. CT ensures that additional exchanges of partons between the upper and lower blocks are suppressed ³ by powers of Q^2 .

The Q^2 scale at which this suppression is sufficient to ensure one is safely in the factorization regime is not well-understood. Because of the link between CT and factorization, understanding the scale at which CT “turns on” is crucial to understanding factorization. Experiments discussed in Section 2.3 suggest that

³The use of a hard probe does not necessarily guarantee the validity of a factorization theorems [78]. In the case of the exclusive meson production, factorization has only been proven for the case of longitudinally polarized photons [69]. For transversely polarized photons, only suppression of the Sudakov form factor of the unfactorized component has been demonstrated [79].

the onset of CT is on the order of a few GeV² for mesons. An unambiguous onset for baryons has not yet been observed.

2.2 Color Transparency at High Energies

For l_c greater than the nuclear radius, one can treat a PLC as a “frozen” $q\bar{q}$ dipole with transverse size d [80, 81]. Then in the leading log approximation, the dipole-nucleon cross section is given by [82, 83]

$$\sigma_{q\bar{q}N}^{inel}(d, x) = \frac{\pi^2}{3} \alpha_s(Q_{eff}^2) d^2 \left[xG_N(x, Q_{eff}^2) + \frac{2}{3}xS_N(x, Q_{eff}^2) \right]. \quad (2.12)$$

Here $Q_{eff}^2 = \lambda/d^2$, $x = Q_{eff}^2/s$, s is the invariant energy of the dipole-nucleon system, and S and G are the sea quark and gluon distributions making up the dipole. The parameter λ takes values between 4 and 10, and was estimated by matching this model with the leading log description of $\sigma_L(x, Q^2)$ [84].

2.2.1 J/ψ photoproduction

The A -dependence of J/ψ production by real photons was studied at Fermilab, providing the first experimental evidence of CT [85]. A beam of 210 GeV electrons passed through 0.53 radiation lengths of material, generating 80 GeV to 190 GeV Bremsstrahlung photons. These real photons passed through both a 1 m LH₂ target and one of three solid targets (Be, Fe, and Pb) which were alternated throughout the run period. A lead absorber shielded detectors from electromagnetic showers generated in the targets. Relative per-nucleon cross sections were computed from dimuon p_T^2 spectra measured for each target in the Tagged Photon Spectrometer.

The photoproduction process proceeds in three stages [68]; the photon converts to a small $c\bar{c}$ pair before it gets to the target, passes through the target with little expansion, and converts to J/ψ outside the target.

The measured cross section can be fit to a power law, $\sigma_{coh} = \sigma_0 A^\alpha$. A vector-meson-dominance model [86] of coherent photoproduction predicts the per-nucleon cross section grows like $A^{4/3}$ at high energies, provided interactions between J/ψ

and nucleons are small. Using more realistic nuclear wavefunctions predicts $A^{1.40}$. Consistent with this prediction, the experiment measured $\alpha_{coh} = 1.40 \pm 0.06 \pm 0.04$, which can be interpreted as a result of CT.

2.2.2 Pion dissociation into two jets

Consider a high momentum pion undergoing a coherent interaction with a nucleus. The final state consists of two jets with high transverse relative momentum k_T and the nucleus still in its ground state. This $q\bar{q}$ Fock component of the pion should dominate this process. Since momentum transfer to the nucleus is very small, the large transverse momentum k_T must originate in gluonic interactions between the quark and antiquark. In addition, this large k_T means the $q\bar{q}$ pair must be in a PLC. Indeed, a model-independent analysis of the pion form factor [87] showed that the pion's transverse charge density is sharply peaked at small distances, consistent with a PLC, as shown in Fig 2-3.

The amplitude for this process, given the cross section in equation 2.12, is

$$A(\pi N \rightarrow 2\text{jets} + N)(z, p_t, t = 0) \propto \int d^2d\psi_\pi^{q\bar{q}}(z, d)\sigma_{q\bar{q}-N(A)}(d, s)e^{ip_td} \quad (2.13)$$

The normalization is determined by the Brodsky-Lepage relation [55]:

$$\psi_\pi^{q\bar{q}}(z, d)_{d \rightarrow 0} = \sqrt{48}f_\pi z(1 - z) \quad (2.14)$$

The E791 experiment at Fermilab studied diffractive dissociation into dijets of 500 GeV pions [88, 89] scattering coherently from carbon and platinum targets. As with J/ψ photoproduction, the per-nucleon cross section can be fit to $\sigma = A^\alpha\sigma_a$. Frankfurt et al. [81] predicted that this cross section's A -dependence should depend on k_T , the transverse momentum of each jet with respect to the beam axis. The E791 experiment calculated α for three different k_T bins. Their results are shown in Fig 2-4 along with the predictions of [81]. These results differ appreciably from the Glauber prediction and are consistent with dominance of the pion's $q\bar{q}$ component. In other words, there is strong support for the existence of CT in this process.

It may seem counterintuitive that the *enhancement* of an interaction should be interpreted as a sign of CT. In the absence of CT (i.e. the presence of strong

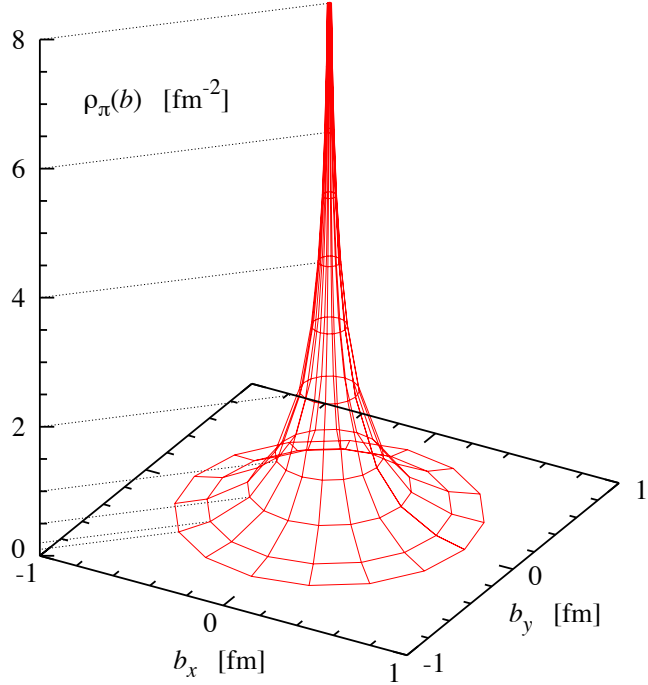


Figure 2-3: Three-dimensional rendering of the pion’s transverse density, as calculated in Ref [87].

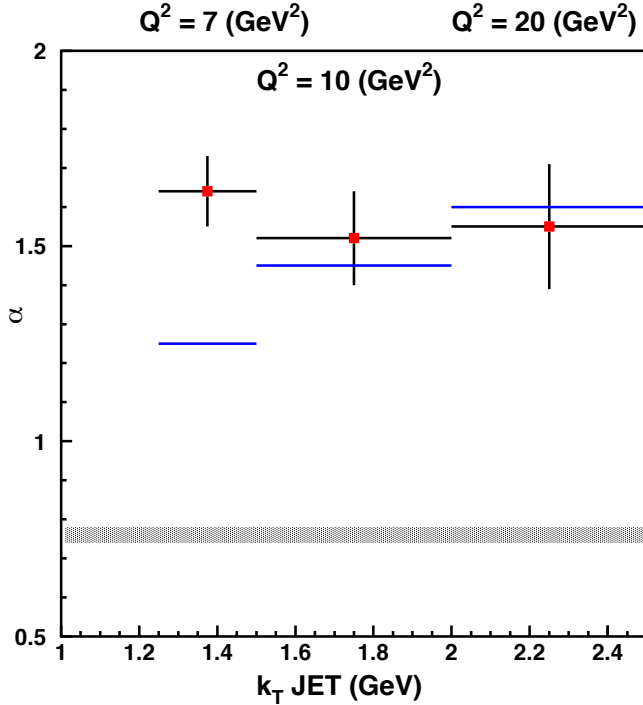


Figure 2-4: The results of a parameterization, $\sigma = A^\alpha \sigma_0$, of the cross section for pion dissociation into two jets. The values from data are shown as red points with statistical and systematic errors added in quadrature. The lines represent the CT-based predictions of [81]. The shaded band represents the value $\alpha \sim 2/3$ typical of coherent inelastic pion-nucleus interactions [90].

FSI), the pion would simply be absorbed by the nucleus. For large k_T , the pion can be assumed to have a small transverse size, which allows it to interact with only one nucleon, and diffract into jets.

2.2.3 Vector meson production

The leading twist picture [68] of vector meson production involves a longitudinally polarized photon transforming into a PLC, interacting elastically with a target, and emerging as a vector meson. This process is in some sense a mirror image of pion dissociation into two jets, and is governed by the same equation, substituting the $q\bar{q}$ component of the photon for the plane wave $q\bar{q}$.

Cross section measurements taken at HERA [91, 92] for exclusive vector meson production are consistent with the predictions of this model [93]. The differential electroproduction cross sections $\frac{d\sigma}{dt}$ can be parameterized as proportional to e^{-bt} for some Q^2 -dependent b , the results of which are shown in 2-5. The above model predicts that the values of b for the ρ and J/ψ cross sections should converge at large Q^2 to one determined by the two-gluon form factor. These results suggest that the transverse size of the ρ shrinks at large Q^2 to a PLC.

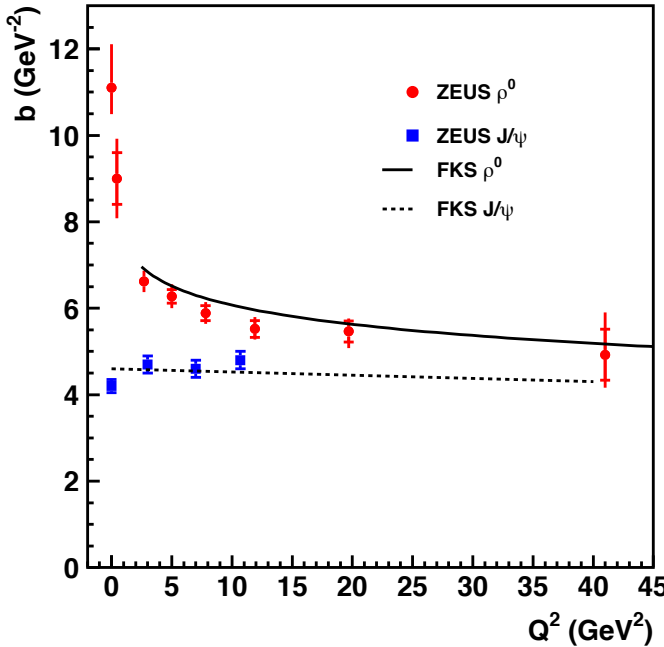


Figure 2-5: The results of a parameterization, $\frac{d\sigma}{dt} \propto e^{-bt}$, of the ρ and J/ψ electro-production cross sections measured at HERA. The curves are predictions of the Q^2 dependence of b from [94].

Taken together, the experiments discussed in this section establish the presence and dominance of small $q\bar{q}$ Fock states in mesons. The energy scales probed by this experiment correspond to coherence lengths that are greater than the nuclear radius. The next section discusses experiments in which the frozen approximation is not valid and expansion effects must be taken into account.

2.3 Color Transparency at Intermediate Energies

2.3.1 Quasielastic proton scattering

The first attempt to measure the onset of color transparency at energies where significant expansion is expected took place at BNL. These experiments measured nuclear transparency T_{pp} , the ratio of the quasielastic cross section for a given target to the free pp elastic cross section, for large-angle ($80^\circ < \theta_{cm} < 90^\circ$) elastic pp and quasielastic $A(p, 2p)$ scattering. To account for Fermi motion and the fact that the square of the invariant energy s is different in quasielastic scattering and elastic scattering from a free proton, transparency was measured as a function of the effective incident momentum p_{eff} , defined by equation 2.15.

$$s = 2m_p \sqrt{m_p^2 + p_{eff}^2} + 2m_p^2 \quad (2.15)$$

The first experiment's measurements were taken using protons with incident momenta of 6, 10, and 12 GeV scattering from carbon, lithium, aluminum, copper, and lead targets [12]. Nuclear transparency was observed to increase between p_{eff} of 5.9 and 9.5 GeV and decrease above 9.5 GeV. A follow-up experiment [13, 14] extended these carbon transparency measurements to 14.5 GeV. The results confirmed the behavior observed in the first experiment. The final transparency results from both experiments [15] are shown in Fig 2-6 as a function of p_{eff} . There are two proposed explanations for the observed rise and subsequent fall in transparency.

One explanation focuses on interference between the amplitudes of two perturbative QCD processes [95], resulting in a transparency that oscillates with s . In this model, the effect of the energy-dependent phase shift on the scattering

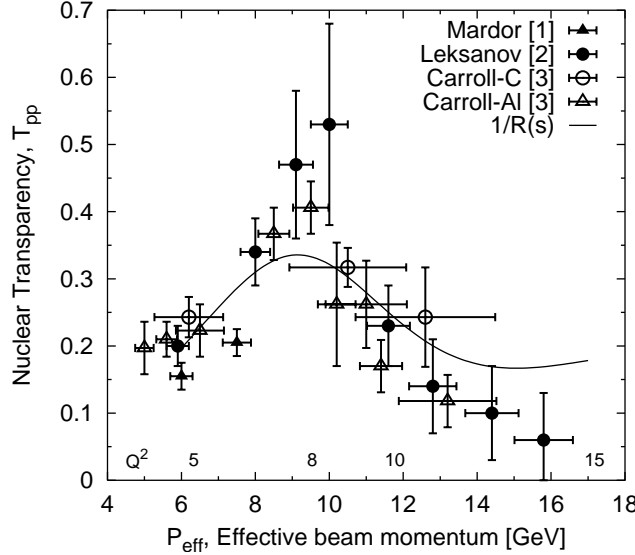


Figure 2-6: Transparency values T_{pp} versus p_{eff} for quasielastic proton scattering from carbon and aluminum (scaled by $(27/12)^{1/3}$) targets [15]. The solid curve is the inverse of $R(s)$ defined in equation 2.18.

amplitude can be represented by

$$\mathcal{M} = \mathcal{M}_{QC} + e^{i\phi(s)+i\delta_1} |\mathcal{M}_L| \quad (2.16)$$

Here δ_1 is an energy-independent phase shift and $\phi(s)$ has a known energy dependence analogous to renormalization-group evolution [96, 97, 98]

$$\phi(s) \propto \ln \left\{ \ln \left(\frac{s}{\Lambda_{QCD}^2} \right) \right\} \quad (2.17)$$

The first term \mathcal{M}_{QC} is a hard amplitude dominant at high energies, characterizing quarks separated by small transverse distances [99, 100, 101, 55]; so-called “quark counting rules” predict that the asymptotic energy dependence of pp scattering at a fixed angle θ_{cm} should look like $\frac{d\sigma}{dt} \sim s^{-10}$. The second term \mathcal{M}_L is the Landshoff mechanism—three-gluon exchange in the t-channel [102, 103]. It is suppressed at high energies, but may be significant at intermediate energies [104].

Taking the ratio of the differential cross section $d\sigma/dt$ to the quark-counting prediction $d\sigma_0/dt$ yields the following ratio, with parameters ρ_1 and K to be

determined by a fit to data:

$$R(s) = \frac{d\sigma}{dt_{pp}} / \frac{d\sigma_0}{dt_{pp}} = s^{10} \frac{d\sigma}{dt_{pp}} \quad (2.18)$$

$$\propto 1 + \rho_1 s^{1-K} \cos [\phi(s) + \delta_1] + \rho_1^2 s^{2-2k}/4 \quad (2.19)$$

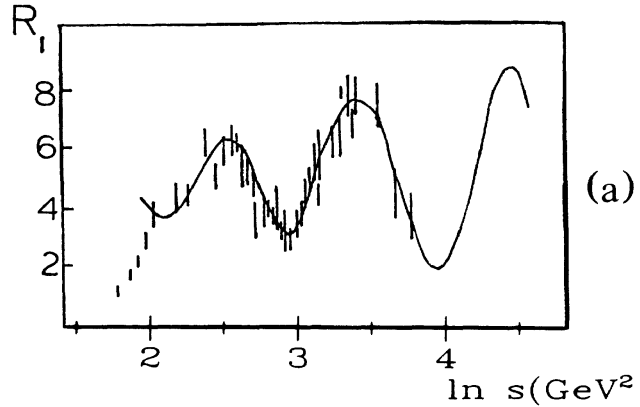


Figure 2-7: A fit of $R(s)$, defined in equation 2.18, to data taken from [105] for pp elastic scattering at fixed angle $\theta_{cm} = 90^\circ$. Figure reproduced from [96].

Similarly, this model predicts the energy dependence of the transparency T :

$$T(s) = \frac{1}{A} \frac{d\sigma(pA \rightarrow pp(A-1)) / dt}{d\sigma(pp \rightarrow pp) / dt} \quad (2.20)$$

$$\propto \frac{1 + \rho_A s^{1-K} \cos [\phi(s) + \delta_A] + \rho_A^2 s^{2-2k}/4}{1 + \rho_1 s^{1-K} \cos [\phi(s) + \delta_1] + \rho_1^2 s^{2-2k}/4} \quad (2.21)$$

For large A such that $\rho_A s^{1-K} \ll 1$, the numerator is independent of energy and transparency is approximately $1/R(s)$. Given the form of $R(s)$ in equation 2.18, the transparency should oscillate as a function of s , with another rise potentially appearing around $s \approx 20$ GeV.

A second explanation is that the energy dependence corresponds to a resonance or some threshold for new physics, such as a charm quark resonance or some multi-quark state [106]. This model also predicts an oscillatory behavior, rising again near $s \approx 16$ GeV.

A relativistic Glauber multiple scattering approximation model incorporating nuclear filtering and color transparency produced fits that are in acceptable agreement with the BNL measurements [107].

2.3.2 Quasielastic electron scattering

Looking for the onset of CT in quasielastic electron scattering is cleaner than in $A(p, 2p)$. Both the electron-proton elastic scattering cross section and spectral functions $S(p_m, E_m)$ for a variety of nuclei have been extensively measured over a wide range of kinematics. Complications involving s near a charm threshold and oscillatory s dependence mentioned in previous section are not relevant for $A(e, e'p)$; for quasielastic scattering, s is always approximately m_p^2 .

Previous transparency measurements, compiled in Fig 2-8, were taken at SLAC, MIT Bates, and JLab for several nuclear targets. These transparency measurements are independent of Q^2 between 2 and 8 GeV. This is consistent with the Glauber prediction, which is to say, an absence of color transparency.

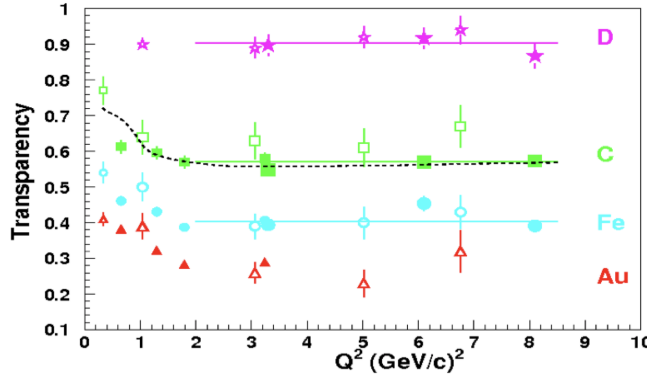


Figure 2-8: Transparency measurements from several experiments studying quasielastic electron scattering from deuterium, carbon, iron, and gold. Data taken at JLab [19, 20, 21] are shown as solid points. Data taken at SLAC [17, 18] are shown as large open symbols. Data taken at Bates [16] are shown as small open symbols. The dotted line is a Glauber calculation from [32] for carbon data. Solid lines are constant-value fits to data above 2 GeV.

2.3.3 Pion photoproduction

The onset of color transparency in pion photoproduction was studied at JLab, using Bremsstrahlung photons generated by the CEBAF beam incident on a copper radiator [108]. Transparency was measured by taking the ratio of ${}^4\text{He}$ to ${}^2\text{H}$ cross sections at two angles. These measurements are shown in Fig 2-9 along with two models. The first model is a Glauber calculation, using exact ground state wave functions [109]. The second adds CT to this model using the quantum

diffusion model's modified hN cross section [39].

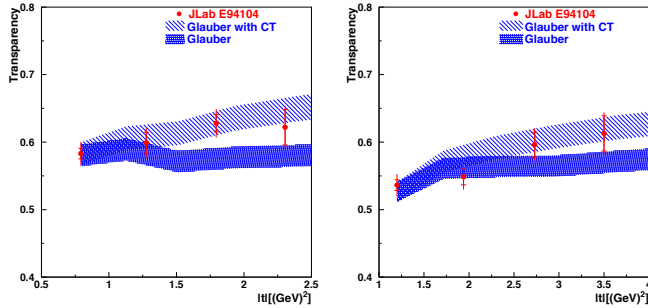


Figure 2-9: Nuclear transparency for ${}^4\text{He}(\gamma, p\pi^+)$ at $\theta_{CM} = 70^\circ$ (left) and $\theta_{CM} = 90^\circ$ (right) as a function of 4-momentum transfer $|t|$. The inner bars are statistical uncertainties only. The outer bars are the statistical and point-to-point systematic uncertainties added in quadrature. The lower shaded band represents the prediction of a traditional Glauber calculation based on ground state wave functions for ${}^4\text{He}$ [109]. The upper shaded band adds CT to this model using a modified hadron-nucleus cross section [39].

The slope of the measured transparencies' dependence on Q^2 is within 1σ (2σ) of the Glauber calculation for the $\theta_{CM} = 70^\circ (= 90^\circ)$ data. The data seem to deviate from the Glauber prediction, but a subsequent analysis using a relativistic Glauber approximation showed that these data are not conclusive evidence of the onset of CT [41].

2.3.4 Pion electroproduction

The piCT experiment at JLab measured the A and Q^2 dependence of the pion cross section for several targets (${}^1\text{H}$, ${}^2\text{H}$, ${}^{12}\text{C}$, ${}^{27}\text{Al}$, ${}^{63}\text{Cu}$, and ${}^{197}\text{Au}$) [22, 23]. Ref [22] defines nuclear transparency T as the ratio of the pion electroproduction cross section from a given nuclear target to the cross section for a free proton, while Ref [23] defines nuclear transparency T_D using the deuteron cross section in the denominator. The purpose of this definition is to reduce uncertainty stemming from the unknown pion electroproduction off a neutron and uncertainty in Fermi smearing. The deuterium nuclear transparency measurements are relatively independent of Q^2 , so both definitions show similar Q^2 dependencies in Ref [23]. The transparency results are shown in Fig 2-10 along with three model predictions described below.

Larson et al. [110] use a semiclassical formula based on the eikonal approxi-

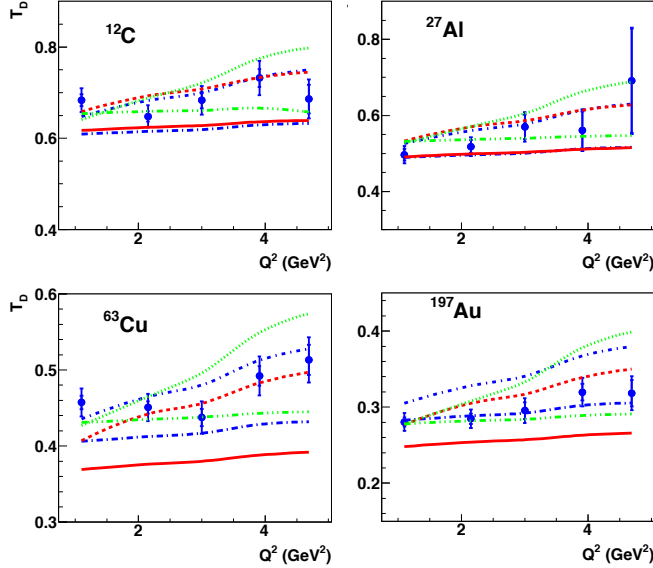


Figure 2-10: Nuclear transparency T as a function of Q^2 for ^{12}C , ^{27}Al , ^{63}Cu , and ^{197}Au targets measured by the piCT experiment [22, 23]. The inner error bars indicate statistical uncertainties and the outer error bars are the quadrature sum of statistical and point-to-point systematic uncertainties. The red dashed and solid lines are Glauber calculations from Larson et al. [110]. The green dotted and dot-dot-dashed lines are microscopic+BUU transport calculations from Kaskulov et al. [111, 112, 113]. The blue dashed and solid lines are Glauber calculations with and without CT from Cosyn et al. [40]; these calculations include the effects of short-range correlations.

mation and a parameterization of final state interactions in terms of an effective cross section based on a quantum diffusion model [39], in which the strength of the interaction is proportional to the pion's propagation distance through the nucleus. The transparency is given by a single integral over the path of the outgoing pion, where the nuclear density $\rho(r)$ is of Woods-Saxon form,

$$T = \frac{1}{A} \int d^3 r \rho(r) \exp - \int_z^\infty dz' \sigma_{eff}(z' - z, p_\pi) \rho(r') \quad (2.22)$$

Cosyn et al. [40] calculate nuclear transparency as a ratio of differential cross sections (integrated over the kinematic range of the experiment) in a relativistic multiple scattering Glauber approximation (RMSGA) to that in a relativistic plane wave impulse approximation (RPWIA). All particles are taken to be plane waves in the RPWIA, while in the RMSGA the wavefunctions of the outgoing pion and spectator nucleon are a convolution of a plane wave with an eikonal phase operator that parameterizes the final state interactions. This model implements CT in this

operator using the same quantum diffusion model's effective cross section [39] used by Larson et al. This model also includes the effects of short range correlations, which create local fluctuations in nuclear density.

Kaskulov et al. [112, 113] calculate nuclear transparency as a ratio of the differential cross sections from two variations of the same model, one with and one without final state interactions. This model is based on a microscopic description of pion electroproduction from hydrogen [111]. The nuclear reaction is broken up into hard partonic DIS and soft hadronic components. It is assumed that the beam electron interacts with a nucleon in the nucleus the way it would with a free nucleon (also taking into account Fermi motion, Pauli blocking, and nuclear shadowing). The time development of the PLC is determined by the quantum diffusion model [39], with formation and production times determined by Monte Carlo simulation of the Lund string hadronization model [114] as described in Ref [115]. The produced hadrons are then propagated through the nuclear medium using the Boltzmann-Uehling-Uhlenbeck (BUU) equation. This propagation models elastic and inelastic rescattering of outgoing hadrons.

The results of the piCT experiment are in agreement with the CT predictions of Larson et al., while Cosyn et al. and Kaskulov et al. overestimate the P_π and Q^2 dependence of the data. Nevertheless, the observed increase in nuclear transparency is consistent with CT.

In addition to studying the Q^2 dependence of nuclear transparency, piCT fit the data to the form $T = A^{\alpha(Q^2)-1}$ where A is the number of nucleons in the nucleus and $\alpha(Q^2)$ is a free parameter. The results of this fit along with the predictions of Larson et al. and Cosyn et al. are shown in Fig 2-11. These results show a clear difference from the prediction of the Glauber model without CT.

2.3.5 ρ^0 meson leptoproduction

Because of the hadronic structure of high energy photons, a virtual photon can fluctuate to a small $q\bar{q}$ state with mass $M_{q\bar{q}}$ and propagate through a nucleus. The formation length $l_{fr} = 2\nu/(Q^2 + M_{q\bar{q}}^2)$ refers to the distance over which this $q\bar{q}$ state is frozen. The coherence length $l_c = 2\nu/(m_v^2 - m_v^2)$ refers to the distance over which the small $q\bar{q}$ state grows to a normal size ρ^0 meson, where m_v is the

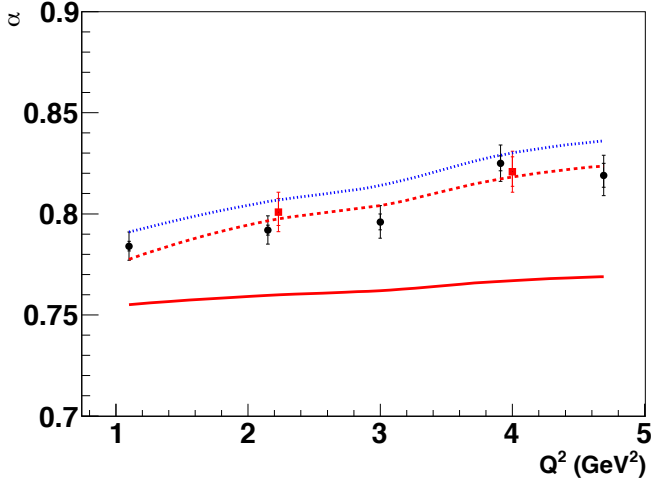


Figure 2-11: The parameter $\alpha(Q^2)$ extracted from the form $T = A^{\alpha(Q^2)-1}$ fit to nuclear transparency measured by the piCT experiment. The inner bars are statistical uncertainties only. The outer bars are the statistical, systematic, and model uncertainties added in quadrature. Red points are data taken with low transverse photon polarization ($\epsilon \approx 0.25$). Black points are data taken with high transverse photon polarization ($\epsilon \approx 0.5$). The solid, dashed and dotted lines are the predictions of the Glauber model of Ref [110], the Glauber+CT model of Ref [110], and the Glauber+CT+SRC model of Ref [41], respectively.

mass of the ρ^0 in its ground state and $m_{\nu'} \approx 1.5 \text{ GeV}$ is the mass of the lowest ρ excited state.

The results of early exclusive diffractive ρ_0 lepton production experiments in the 1990s were suggestive of the onset of CT, but had limited statistical power. Another factor complicating the study of CT in this process is the need to separate the effects of l_{fr} and l_c . If one is not careful, an increase in nuclear transparency with decreasing l_{fr} can be mistaken for an increase with Q^2 , the signature of CT.

The first measurements of nuclear transparency for incoherent diffractive ρ^0 lepton production were performed at Fermilab by the E665 collaboration [116] and at CERN by the NMC collaboration [117] using muon beams of 450 GeV and 200 GeV respectively. At these energies, the l_{fr} is comparable to the nuclear radius and the l_c is much larger than the nuclear radius; the $q\bar{q}$ state is frozen.

E665 took data with hydrogen, deuterium, carbon, calcium, and lead targets, while NMC took data with deuterium, carbon and calcium targets. The results for carbon and calcium, shown together in Fig 2-12, are consistent with each other and show a slight increase in transparency. This is only suggestive of an onset of CT due to limited statistics and substantial background.

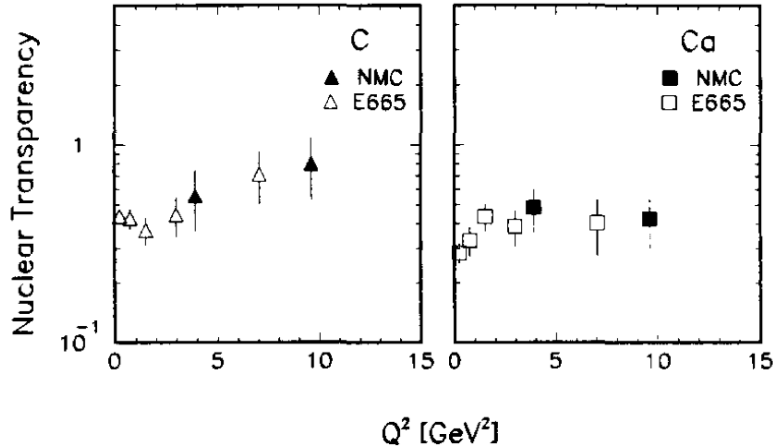


Figure 2-12: Transparency versus Q^2 for ρ^0 leptoproduction. Filled symbols are data from NMC [117]. Open symbols are data from E665 [116].

E665 also studied the A -dependence of the cross section, fitting their data for all targets to a power law, $\sigma_A = \sigma_0 A^\alpha(Q^2)$ where both σ_0 and α are free parameters. The extracted value of α at low Q^2 is consistent with soft nuclear interactions. The increase of α at higher Q^2 is again only suggestive of CT due to the large uncertainty.

The HERMES collaboration at DESY [118] measured nuclear transparency as a function of Q^2 and l_{fr} for coherent and incoherent ρ^0 leptoproduction from ^{14}N using a 27.5 GeV positron beam. Their measurements for exclusive incoherent electroproduction, shown in Fig 2-13, show an increase in transparency at lower l_{fr} consistent with an introduction of initial state interactions between the nuclear medium and the $q\bar{q}$ pair when the pair remains small for a distance smaller than mean free path of a ρ^0 meson.

Because l_{fr} is comparable the nuclear radius in this experiment, these measurements of nuclear transparency depend on l_c . This could lead to an ambiguous result, where a rise in transparency could be attributed to either decreasing l_{fr} or increasing Q^2 . As such, the collaboration studied the nuclear transparency's Q^2 -dependence while keeping l_{fr} fixed [121]. Transparencies for coherent and incoherent ρ^0 electroproduction were extracted for fixed (l_{fr}, Q^2) bins, as shown in Fig 2-14. Due to low statistics, the transparencies were fit to a form $P_0 + P_1 \cdot Q^2$, where P_0 is a free parameter for each l_{fr} bin and the slope P_1 is a common free parameter among the bins.

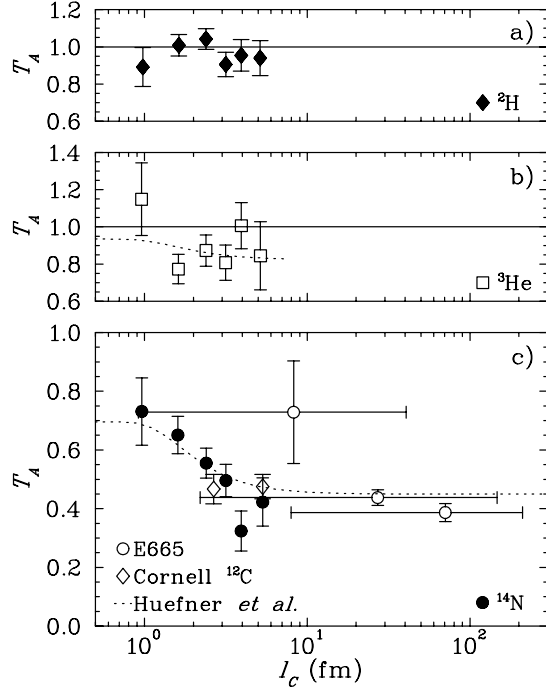


Figure 2-13: Transparency versus coherence length for ρ^0 leptoproduction from hydrogen, helium, and nitrogen targets. These results demonstrate interactions of $q\bar{q}$ states with the nuclear medium at larger coherence lengths. Open circles are data from E665 [116] taken with muons. Open diamonds are data [119] taken with photons. Filled circles are data from HERMES [118] taken with electrons. The error bars include statistical and point- to-point systematic uncertainties added in quadrature. The dashed line is the result of a Glauber model [120].

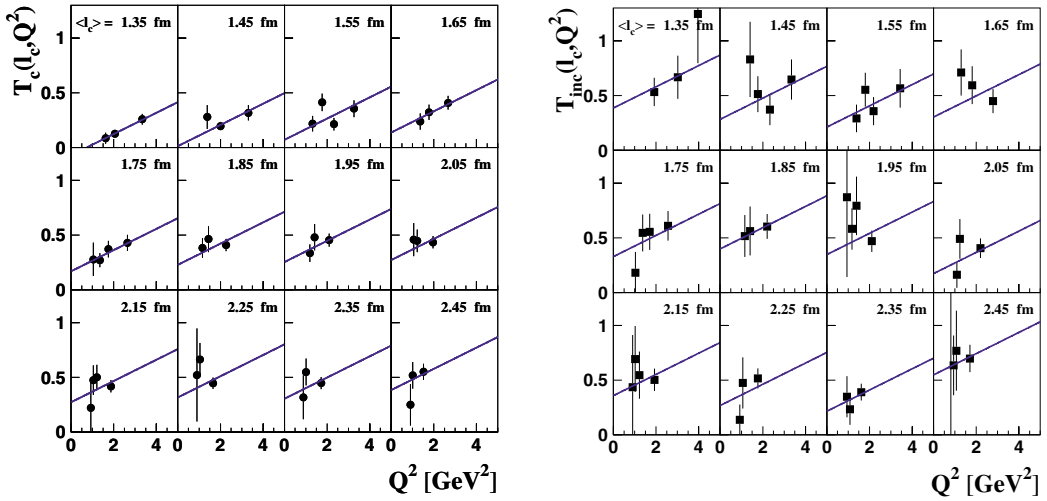


Figure 2-14: Transparency versus Q^2 for bins of coherence length indicated by a label at the top right of each panel. The straight line is the result of the fit to the Q^2 -dependence of all bins. Error bars represent statistical uncertainties.

The extracted slopes for incoherent and coherent production were 0.70 ± 0.21 and $0.089(46) \text{ GeV}^{-2}$ respectively. These slopes agree with the predictions of a model using the light cone Green function formalism, incorporating the effects of coherence length and CT [122]. As with the E665 and NMC results, the HERMES results are only suggestive of the onset of CT due to their limited statistics.

The CLAS collaboration measured nuclear transparency for exclusive incoherent ρ^0 production off carbon and iron relative to deuterium using a 5 GeV electron beam at JLab [123]. As seen in Fig 2-15, these transparencies are independent of l_{fr} because l_{fr} ($\sim 0.5 \text{ fm}$ to 0.9 fm) is smaller than the nuclear radii of carbon and iron, 2.9 fm and 4.6 fm respectively. As a result, any increase in transparency as a function of Q^2 cannot be a result of varying l_{fr} , but rather a signal of CT.

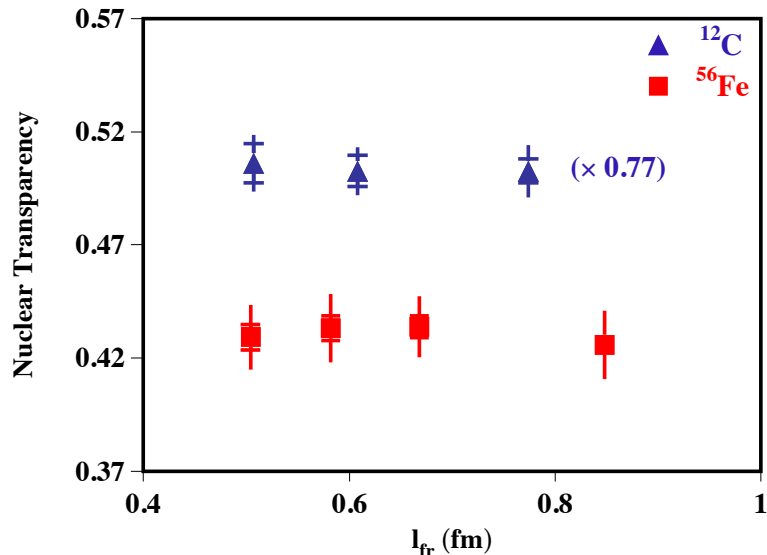


Figure 2-15: Nuclear transparency as a function of l_{fr} measured by CLAS [123]. The inner error bars are statistical uncertainties. The outer error bars are the quadrature sum of statistical and systematic uncertainties. The carbon data has been scaled by a constant to fit in the same figure with the iron data.

The Q^2 dependence of these transparency measurements is shown in Fig 2-16 along with the predictions of two models. The Frankfurt-Miller-Strikman (FMS) model [124] uses a standard Glauber calculation, using the quantum diffusion model's modified hadron-nucleus cross section [39] to implement CT. This model also includes the effects of the decay of the ρ^0 meson. The Gallmeister-Kaskulov-Mosel (GKM) model [125] is similar to Kaskulov et al.'s model [111] of pion electroproduction, which uses the BUU formalism to transport (pre)hadrons through

the nucleus. Both models predict the behavior of the CLAS carbon data quite well, but the GKM model underestimates the iron transparency.

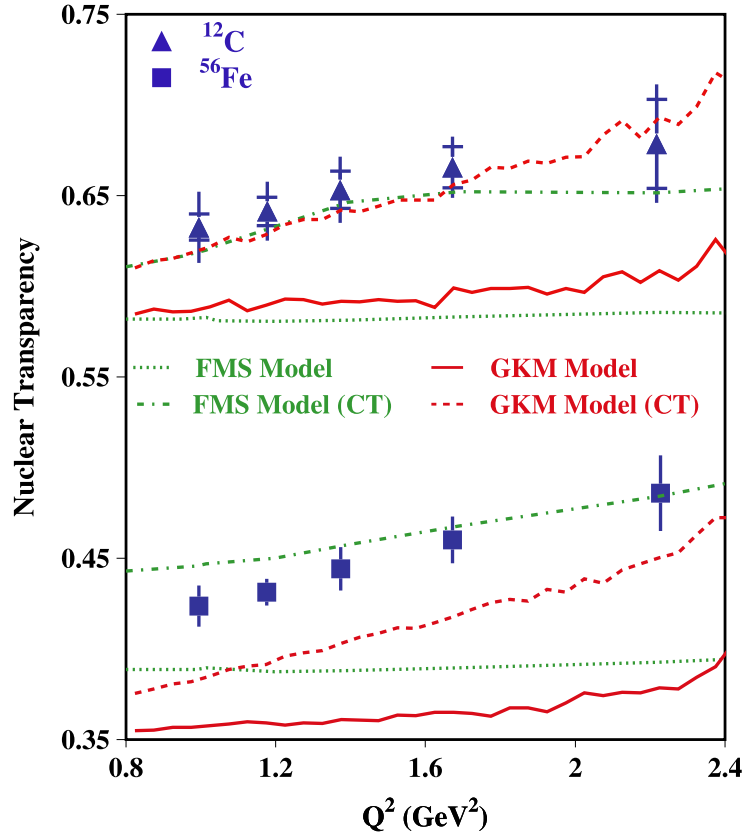


Figure 2-16: Nuclear transparency as a function of Q^2 measured by CLAS [123]. The inner error bars are statistical uncertainties. The outer error bars are the quadrature sum of statistical and systematic uncertainties. The curves are predictions of the FMS [124] (red) and GKM [125] (green) models with (dashed–dotted and dashed curves, respectively) and without (dotted and solid curves, respectively) the effects of CT. Both models include the pion absorption effect when the ρ^0 meson decays inside the nucleus.

These data were also fit to a linear form $T = aQ^2 + b$, and the slope a was compared to the predictions of the above two models as well as a third, the Kopeliovich-Nemchick-Schmidt (KNS) model [126]. The KNS model uses the same light cone Green function formalism used in the context of the HERMES ρ^0 production data. The results of these fits and the model predictions are shown in Table 2.1.

2.4 Summary

Taken together, these experiments show support for the existence of CT, as well as observation of its onset for scattering processes involving mesons. Such

Table 2.1: Slope parameters from a fit to the Q^2 dependence of CLAS nuclear transparency data taken for carbon and iron [123]. Also shown are predictions of the KNS [126], GKM [125], and FMS [124] models.

Nucleus	Measured slopes (GeV^{-2})	Model predictions		
		KNS	GKM	FMS
C	$0.044 \pm 0.015_{\text{stat}} \pm 0.019_{\text{sys}}$	0.06	0.06	0.025
Fe	$0.053 \pm 0.008_{\text{stat}} \pm 0.013_{\text{sys}}$	0.047	0.047	0.032

evidence for processes involving hadrons has not yet been demonstrated. This may be because the onset for a qqq PLC will necessarily be higher in Q^2 than that of a $q\bar{q}$ pair.

Other reviews of theoretical considerations and previous experiments can be found in the recent articles by Dutta, Hafidi, and Strikman [127, 78].

Chapter 3

Experimental Apparatus

3.1 Overview

3.2 Accelerator and Beamline

The Thomas Jefferson National Accelerator Facility (JLab), located in Newport News, VA, is home to the Continuous Electron Beam Accelerator Facility (CEBAF) which delivers a stable, high energy, high duty factor electron beam to four experimental halls. The data for the E12-06-107 experiment were taken in early 2018 in Hall C at JLab.

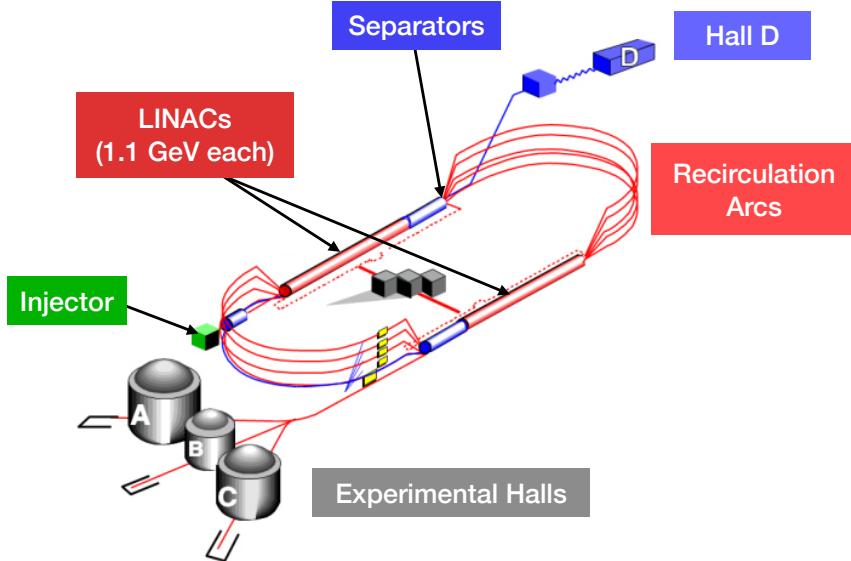
3.2.1 CEBAF

CEBAF consists of an injector that generates a beam of 123 MeV electrons, a racetrack-shaped combination of linear accelerators (linacs) and recirculation arcs, and extraction regions.

The injector consists of a 130 keV electron gun, a bunching system¹, and superconducting radiofrequency (SRF) linacs that accelerate electrons to an energy of 123 MeV before they enter the accelerator ring.

The accelerator ring consists of two linacs, each of which gives the beam an additional 1.1 GeV per pass. At the end of each linac, the beam can be extracted and

¹The prebuncher, chopper, and buncher separate the continuous beam into “bunches” of electrons that can be independently removed from the recirculating beam using radiofrequency (RF) separators, allowing simultaneous beam delivery to all four experimental halls. [128]



(a) A schematic view of the CEBAF accelerator.



(b) An aerial photograph of the CEBAF accelerator site.

Figure 3-1: The Continuous Electron Beam Accelerator Facility

delivered to an experimental hall, or sent back to be recirculated and accelerated to a maximum of 10.9 GeV for Halls A, B, and C or 12 GeV for Hall D.

Because the beam in the linacs contains bunches with different energies, different magnetic field strengths are necessary in the recirculation arcs. Dipole magnets are used to spread the beam vertically into separate arcs (consisting of bending dipoles and focusing quadrupoles) tuned to different pass energies, and then recombine them for extraction to experimental halls or additional passes through the linacs.

The injector's buncher system creates a beam that has a high duty factor but also has an internal structure consisting of 2 ps long bunches of electrons that come at a rate of 1497 MHz. RF cavities with a fundamental frequency of 499 MHz

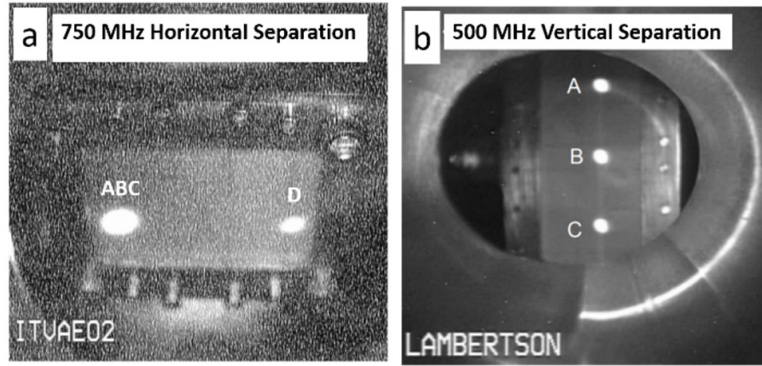


Figure 3-2: (a) Beam viewer downstream from 5th pass 748.5 MHz RF separator showing horizontal separation of Hall D's beam. (b) Beam view downstream from the 499 MHz RF separator showing vertical separation of the beams to be delivered to Halls A, B, and C.

(or 748.5 MHz for Hall D) separate these bunches spatially to allow them to be separated from the beam and delivered to the halls independently. This results in beam bunches that arrive at the Hall C target chamber every 4 ns.

3.2.2 Hall C Arc and Beamline

Once separated from recirculation through the accelerator ring, the beam passes through the Hall C arc and beamline. Along the way the beam passes through several diagnostic elements including superharps, beam position monitors (BCMs), beam current monitors (BCM), and polarimeters.

Superharps

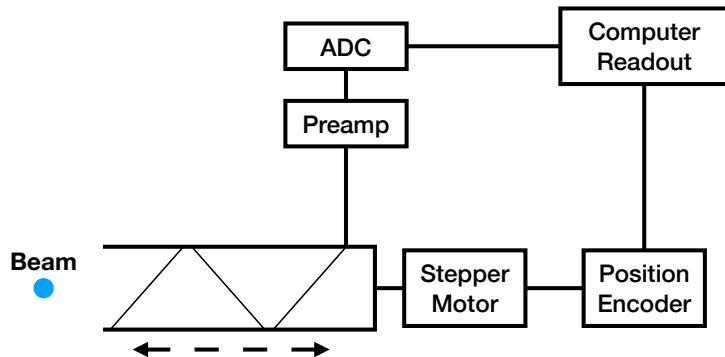


Figure 3-3: Schematic representation of a superharp. The motor moves the fork into the beam, where beam electrons interact with the wires, creating a signal registered by the ADC.

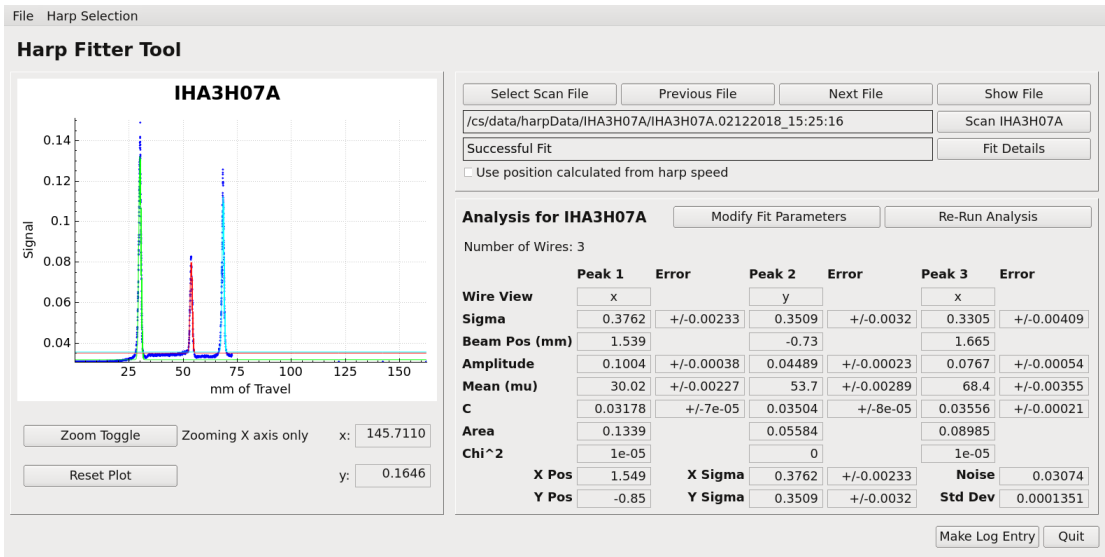


Figure 3-4: The Harp Fitter GUI, which fits the signal from a superharp and reports the estimated beam position and width.

Superharps [129] are used to measure the beam’s position, XY profile, and energy. They also provide information to the Compton and Møller polarimeters.

Each superharp consists of a fork with two vertical wires and one horizontal wire, attached to a stepper motor that allows it to be inserted and removed from the beam. A position encoder measures the position of the fork. As the wires pass through the beam, secondary electron emission creates a current in the wires, yielding a signal that can be read out by an analog-to-digital converter (ADC). The profile of the beam can be estimated by fitting the wire signals vs encoder position, as shown in 3-4.

Beam Position Monitors

Three BPMs (IPM3H07A, IPM3H07B, IPM3H07C) upstream from the target provide measurements of the relative beam position within $100\text{ }\mu\text{m}$. The BPMs’ absolute position can be calibrated with respect to the adjacent superharps, IHA3H07A and IHA3H07B.

Each BPM consists of four antennae attached to a cylindrical cavity that forms part of the beamline enclosure. Two pairs of antennae are located opposite each other, with each pair 90° from the other, forming an $X'Y'$ coordinate system rotated 45° from the X and Y axes of the EPICS (left-handed) coordinate system. The beam induces a signal in each antenna, which is tuned to 499 Hz (a subhar-

monic of the beam). The amplitude of this signal is inversely proportional to the distance from the beam to the antenna, so the relative distance can be computed by taking the ratio of the difference to the sum of the signals from pairs of antennae on opposite sides of the enclosure.

Superharp measurements of the beam position are invasive and cannot be taken during production data acquisition. BPM measurements are noninvasive and can be taken continuously. Each BPM measurement is averaged over 0.3 s and logged by EPICS every 1 s. The BPMs' raw outputs are also recorded for every event in the CODA datastream. Converting these raw values to physical outputs requires calibrating the parallel electronics chain to the EPICS data.

Beam Current Monitors

The system for monitoring beam current consists of several resonant-cavity BCMs and one parametric-current-transformer Unser monitor.

The Unser current monitor [130] consists of a toroidal pickup placed around the beam pipe. The beam's magnetic field induces a flux in the toroid, which a feedback system tries to cancel by driving a current through a compensating coil. This compensating current is proportional to the beam current.

The BCMs consist of high Q (~ 500) stainless steel cylindrical waveguides tuned to the fundamental frequency of the beam. The voltage at their output is proportional to the beam current.

The gain of the Unser is a relatively stable $4 \text{ mV } \mu\text{A}^{-1}$ but has an unstable offset that is known to drift significantly on a time scale of minutes [131]. This offset can be corrected for by intermittently taking calibration runs with no current. The Unser's gain can be precisely measured during downtime by passing a known DC current through it during downtime. The gains of the BCMs are unstable and must be calibrated relative to the Unser's. In contrast to the Unser, the BCMs have a relatively stable offset.

The output of both the Unser and BCMs² are sent to voltage-to-frequency converters whose outputs are sent to DAQ scalers as well as a VME crate for processing and integration into the EPICS stream.

²The BCMs' RF outputs must first be sent through an analog (for BCM1 and BCM2) or digital (for BCM4A, BCM4B, and BCM4C) downconverter.

Beam Rastering System

To prevent overheating and damage to solid targets and local boiling in cryogenic targets, Hall C uses a “fast raster” system [132]. The system consists of two sets horizontal and vertical steering magnets that rapidly vary the beam position. The magnets consist of bedstead air-core windings of Litz³ cables. The raster magnets are located about 20 m upstream from the center of the target chamber, a region that does not include any optical focusing elements so as decouple the raster system from beam optics tuning. The final profile of the rastered beam on the target will be a result of a combination of the beam optics and raster magnets.

Hall C used a Lissajous raster system, driven by sinusoidal magnet currents, from 1996 to 2002 that slowed down at the edges of the raster scan. This resulted in the rastered beam spending more time at the edges and corners than the central region of the raster scan. To more evenly distribute the raster scan, the fast raster system now uses a 25 kHz triangle wave to drive the raster magnets.

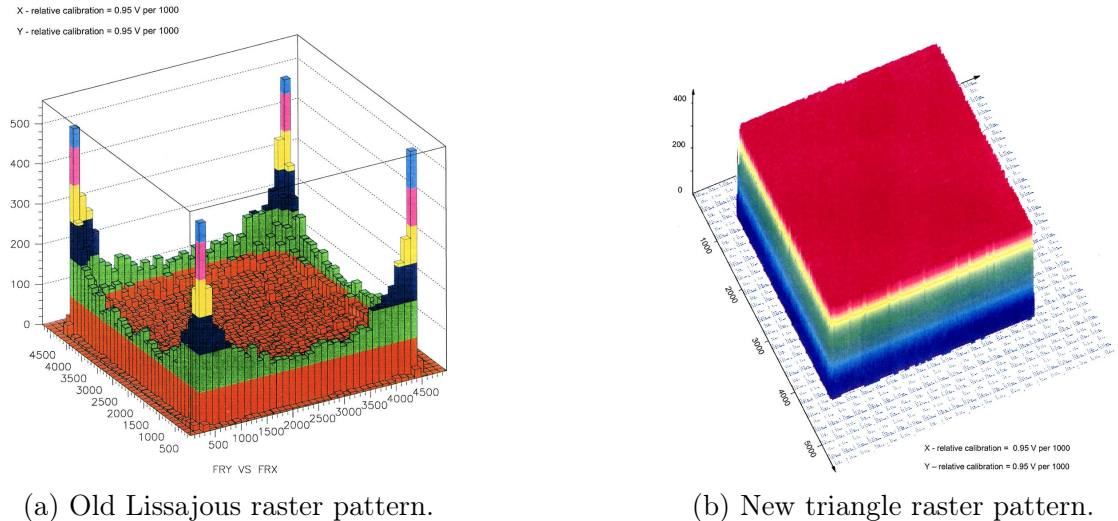


Figure 3-5: A comparison of the distributions of the x and y positions of the beam on target for data taken with the old and new (i.e. in operation since 2002) raster patterns. Figure reproduced from [132].

³“Litz is a short term used for a German word ‘Litzendraht’ that means braided wire. Litz cable consists of multiple strands and each strand is coated by insulation film. The entire cable is also subdivided into several twisted groups, which are formed by twisted basic strands. The major purpose for use of the Litz cable is to reduce power loss caused by the Eddy current.” [132]

3.3 Targets

The target chamber is a large evacuated cylinder located above the spectrometers' pivot point, designed to allow each spectrometer to rotate around it without any coupling between the beam line vacuum and the spectrometers' vacuum. Fig 3-6 is a rendering of the target chamber, viewed from the exit window and beam exit pipe. A single target ladder, a rendering of which can be found in Fig 3-7 containing solid and cryogenically cooled liquid targets can be raised or lowered via a GUI in the counting house to select a desired target.

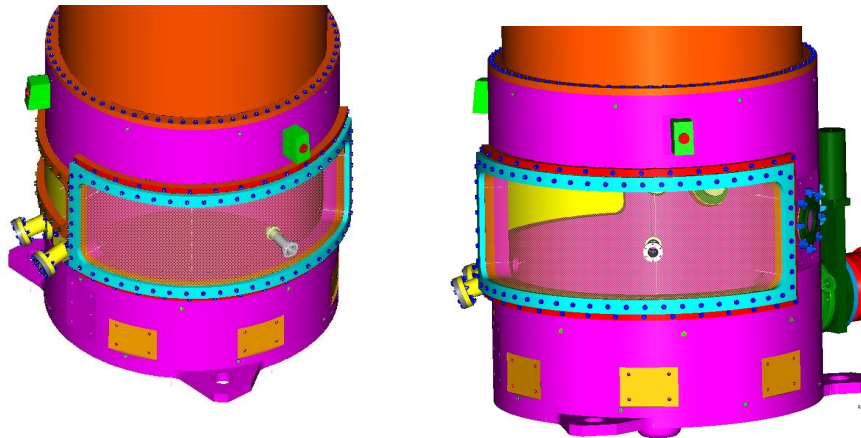


Figure 3-6: The Hall C target chamber.

The target ladder contains three cryotarget loops, two “dummy” targets consisting of two aluminum foils placed at z positions corresponding to the entrance and exit windows of the cryotargets, two optics targets, and a number of solid targets. Table 3.1 summarizes the target ladder as configured for the 2017 commissioning experiments, including our experiment, E12-06-107. During our experiment, cryotarget loop 1 was filled with LHe₃, loop 2 with LH₂, and loop 3 with LD₂. The loops can be filled with other gases depending on experimental requirements.

A detailed engineering drawing of the ladder is available online [133].

Each cryotarget loop is maintained at $\sim 3\text{K}$ below the fluid's boiling point by constantly recycling the fluid through a circuit containing the target cell and a heat exchanger.

A gas panel outside the counting house feeds a constant supply of target fluid to the heat exchanger, where the 15K liquid helium coolant from the End Stage

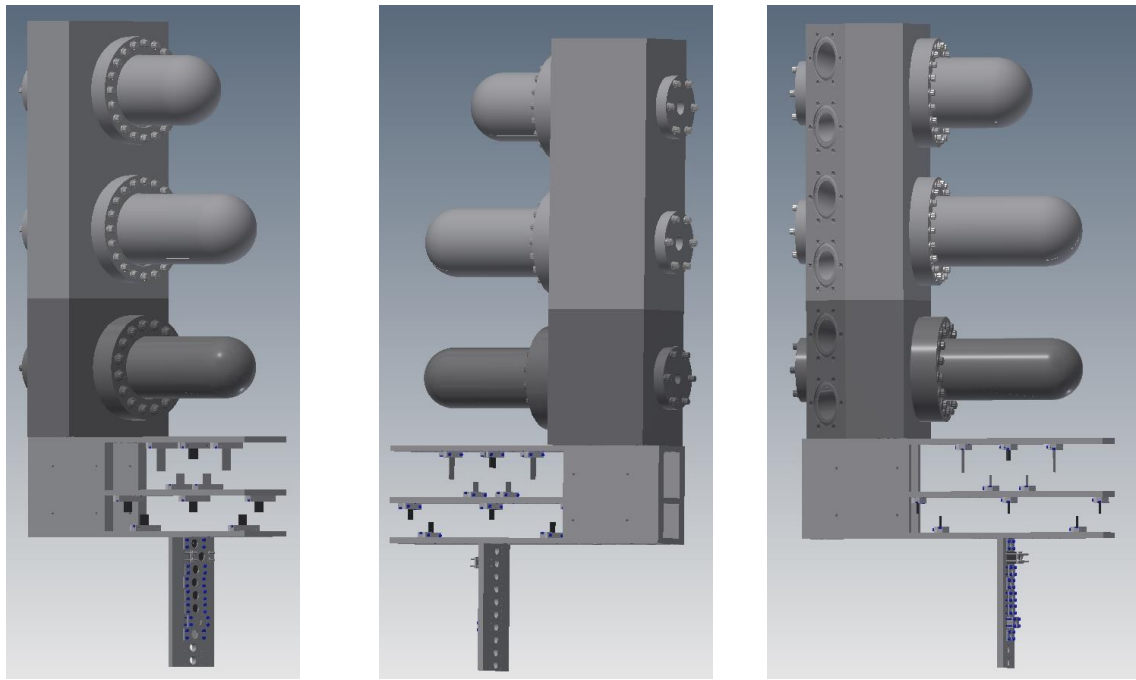


Figure 3-7: The Hall C target ladder.

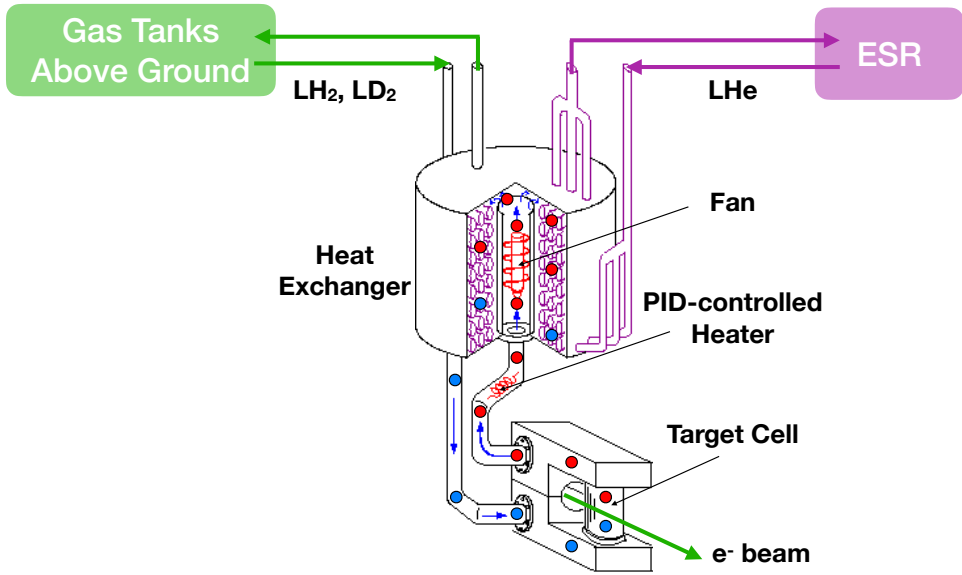


Figure 3-8: Scheme of the system that maintains the cryotargets' temperatures.

Refrigerator cools it to the target temperature of $\sim 3\text{K}$ below boiling. The fluid is then sent to the target cell which is designed to maintain uniform fluid velocity and density as the fluid makes its way from the cell's inlet to its outlet. As it leaves, the fluid will be at a higher temperature due to heat deposited by the beam in operating conditions. In the event that the beam is off, tripped, or other-

Table 3.1: Summary of the materials and thicknesses of the cryotarget loops and dummy targets.

(a) Cryotarget loops and dummy targets				
Target	Entrance Thickness [mm]	Exit thickness [mm]	Length [mm]	Material
Loop 1 (4 cm)	0.165 ± 0.0019	0.151 ± 0.0053	Tip	40 ± 0.25 Aluminum 7075
Loop 2 (10 cm)	0.104 ± 0.0025	0.133 ± 0.0096	Tip	10 ± 0.26 Aluminum 7075
Loop 3 (15 cm)	0.147 ± 0.008	0.177 ± 0.013	Tip	150 ± 0.26 Aluminum 7075
4 cm dummy	0.0789 ± 0.000148	0.0811 ± 0.00014		Aluminum 7075
10 cm dummy (with carbon foil at $z=0$, described below)	0.1816 ± 0.0003	0.1815 ± 0.0003		Aluminum 7075
(b) Optics and solid targets				
Target	Thickness [g cm^{-2}]	z position [cm]	Material	
Optics (three foils)	0.044 ± 0.001	-10, 0, +10	Aluminum 7075/Carbon 99.95%	
Optics (two foils)	0.044 ± 0.001	-5, +5	Carbon 99.95%	
Carbon on 10 cm dummy	0.4426 ± 0.0008	0	Carbon 99.95%	
Carbon Hole	0.171 ± 0.001	0	Carbon 99.95%	
Carbon 6%	2.068 ± 0.004	0	Carbon 99.95%	
Carbon 1.5%	0.5244 ± 0.001	0	Carbon 99.95%	
Carbon 0.5%	0.1749 ± 0.00035	0	Carbon 99.95%	
$^{10}\text{B}_4\text{C}$	0.5722 ± 0.001	0	$^{10}\text{B}_4\text{C}$ (99.9% Chem/95% enrichment)	
$^{11}\text{B}_4\text{C}$	0.6348 ± 0.001	0	$^{11}\text{B}_4\text{C}$ (99.9% Chem/95% enrichment)	
BeO	0.263 ± 0.001	0	BeO 99.5%	

wise interrupted, a high power heater controlled by a software PID (Proportional-Integral-Derivative) loop heats the exiting target fluid as if the beam were present. The fluid then returns to the heat exchanger, completing the circuit.

3.4 Spectrometers

The major experimental equipment in Hall C consists of two medium-resolution, large-acceptance magnetic spectrometers with similar flexible detector packages. The High Momentum Spectrometer (HMS) is designed to analyze particles with momenta up to 7.4 GeV. The Super High Momentum Spectrometer (SHMS) is designed to analyze particles with momenta up to 11 GeV. The spectrometers' detector packages are designed to analyze both electrons and hadrons in coincidence or single-arm experiments studying inclusive and exclusive reactions. Both spectrometers' magnets and detector stacks sit on independent carriages that rotate on rails around a central pivot located beneath the target chamber. A summary of the spectrometers' performance is given in table 3.2.

For E12-06-102's production data, protons were detected in the SHMS in coincidence with electrons in the HMS. Additional single-arm data were taken for the purpose of detector calibration.

Table 3.2: Summary of the HMS performance and design specifications for the SHMS.

Parameter	HMS	SHMS
Central Momentum Range	0.4 – 7.4 GeV	2 – 11 GeV
Momentum Acceptance	$\pm 10\%$	-10% to $+22\%$
Momentum Resolution	$0.1\% - 0.15\%$	$0.03\% - 0.08\%$
Scattering Angle Range	10.5° to 90°	5.5° to 40°
Target Length Accepted at 90°	10 cm	50 cm
Horizontal Angle Acceptance	± 32 mrad	± 18 mrad
Vertical Angle Acceptance	± 85 mrad	± 50 mrad
Solid Angle Acceptance	8.1 msr	> 4 msr
Horizontal Angle Resolution (yptar)	0.8 mrad	2 – 4 mrad
Vertical Angle Resolution (xptar)	1.0 mrad	1 – 2 mrad
Target resolution (ytar)	0.3 cm	0.2 – 0.6 cm
Maximum DAQ Event Rate	2000 events/second	10,000 events/second
Maximum Flux within Acceptance	~ 5 MHz	~ 5 MHz
e/h Discrimination	$> 1000:1$ at 98% efficiency	1000:1 at 98% efficiency
π/K Discrimination	100:1 at 95% efficiency	100:1 at 95% efficiency

3.4.1 High Momentum Spectrometer

The HMS is a 25° vertical bend spectrometer with superconducting magnets in a QQQD configuration. Its maximum central momentum is 7.4 GeV with an acceptance of $\sim \pm 10\%$. The HMS detector stack consisting of a hodoscope, lead glass calorimeter, Cherenkov counter, and pair of drift chambers sits in a concrete shielding hut approximately 27 m from the target chamber. A vacuum is maintained in the region between the entrance to Q1 and the dipole exit to minimize multiple scattering.

The HMS's performance is well understood from 6 GeV era experiments, but some changes have been made for the 12 GeV era. The dipole NMR probe was moved outside the dipole for more accurate measurement of central momenta. The original HMS drift chambers were replaced with a pair of drift chambers that match the design of those in the SHMS.

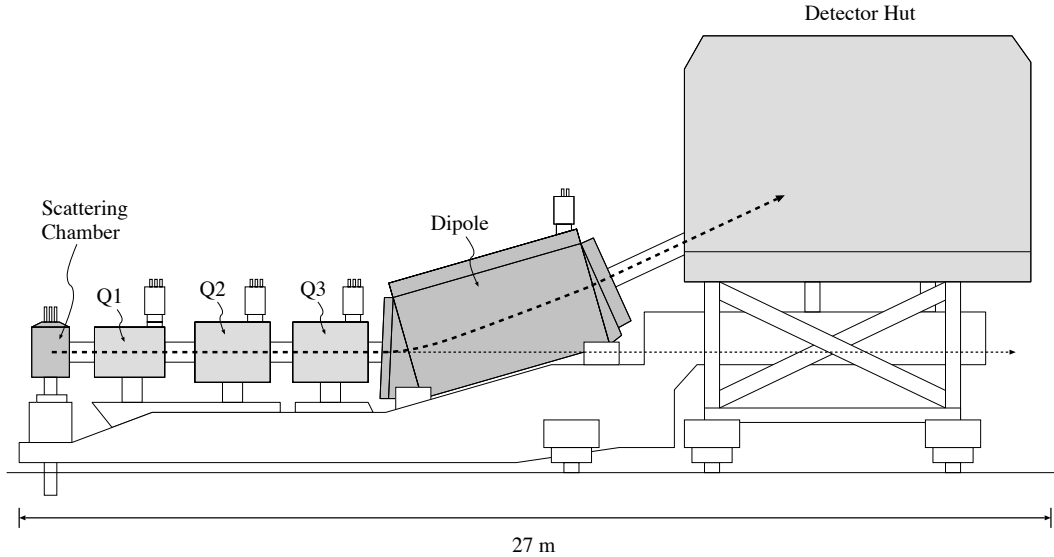


Figure 3-9: High Momentum Spectrometer (HMS) side view.

Optics calibration runs⁴ using hydrogen elastic scattering and carbon data were taken to determine central dipole field values, external NMR measurements, and corresponding magnet currents. These data were also used to characterize spectrometer mispointing and angular offsets and optimize the matrix used in projecting tracks from the focal plane to the interaction at the target. See [134] for more details.

3.4.2 Super High Momentum Spectrometer

Like the HMS, the SHMS is an 18.4° vertical bend spectrometer with superconducting magnets in a QQGD configuration. To allow it to reach smaller scattering angles, the SHMS has an additional 3° horizontal bender (HB) dipole before the first quadrupole. Its maximum central momentum is 11 GeV with an acceptance covering -10% to $+22\%$. The SHMS detector stack consisting of a hodoscope, lead glass calorimeter, three Cherenkov counters, and pair of drift chambers sits in a concrete shielding hut approximately 22 m from the target chamber.

As with the HMS, she commissioning of the SHMS magnets used hydrogen and carbon elastic scattering and the 4.4 MeV carbon excited peak to characterize spectrometer mispointing and angular offsets and optimize the track reconstruction matrix. See [135] for more details.

⁴HMS singles with run numbers 1337–1352

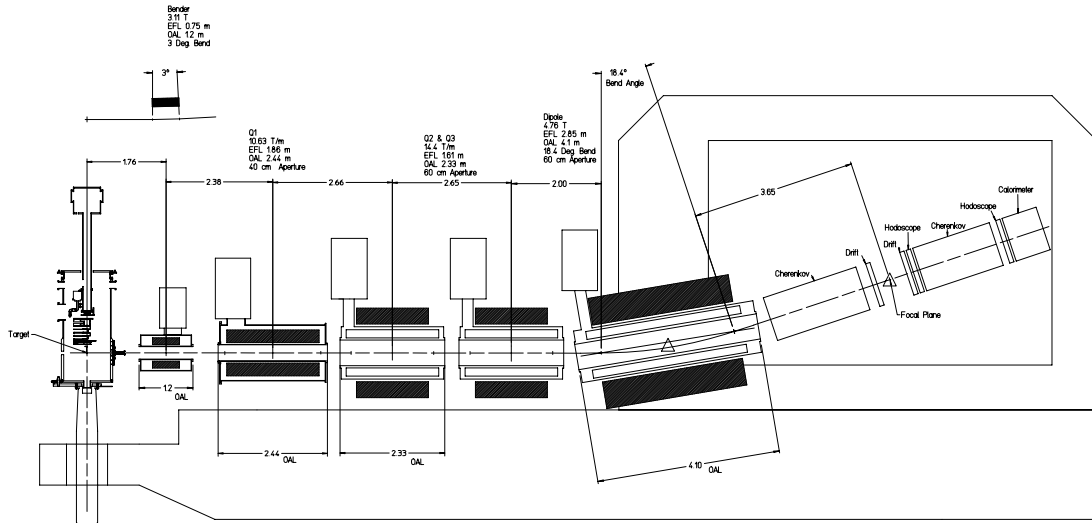


Figure 3-10: Super High Momentum Spectrometer (SHMS) side view.

3.4.3 Collimators and Slit Systems

The HMS has a remotely operated collimator ladder installed on the front face of Q1. The HMS ladder contains one sieve-slit for optics tuning and two solid-angle-defining collimators.

The SHMS has a similar system installed on the front face of Q1. The SHMS ladder contains two sieve-slits for optics tuning and one solid-angle-defining collimator. The two sieve slits consist of a lattice of holes separated by 0.6457" horizontally and 0.9843" vertically. Two holes in each sieve are missing to ensure correct orientation. To account for the HB magnet, the SHMS has an additional sieve slit ladder placed immediately upstream from the HB.

3.5 Detector Packages

The detector stacks in both spectrometers consist of a lead glass calorimeter, one or more Cherenkov counters, a hodoscope, and a pair of drift chambers. Details beyond what are covered here can be found online [131].

3.5.1 Hodoscopes

The HMS and SHMS hodoscopes consist of two pairs of X/Y planes that generate the basic trigger for the DAQ system and provide an initial estimate of

particle velocity based on time of flight (TOF). Each X (Y) plane consists of some number of horizontally (vertically) oriented paddles. All paddles except those in the SHMS S2Y are plastic scintillators. The HMS paddles are BC-404 [131, 136]. The SHMS S1X, S1Y, and S2X paddles are RP-408 [137, 138]. The SHMS S2Y paddles are quartz [139]. In both spectrometers the first pair of planes, S1X and S1Y, are about 2.2 m upstream from the second pair of planes, S2X and S2Y. Table 3.3 contains a summary of each plane.

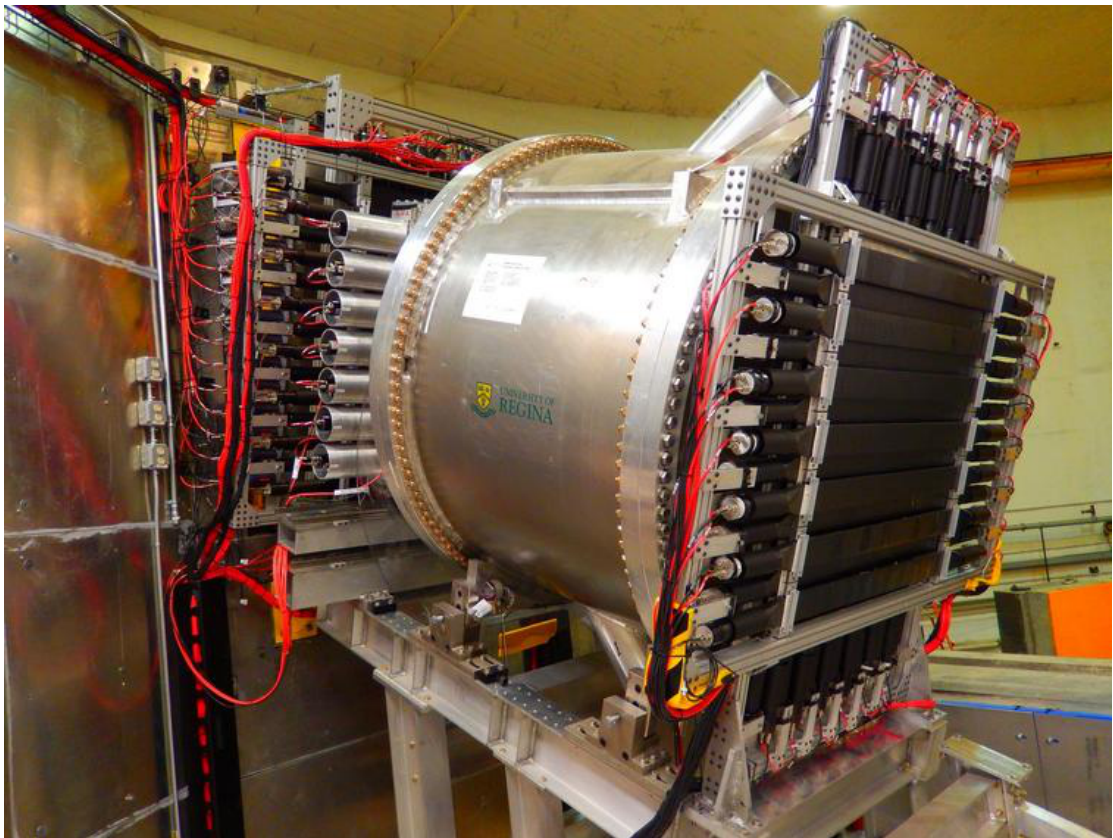


Figure 3-11: The two pairs of hodoscope planes that make up the SHMS hodoscope are placed on either side of Aerogel and Heavy Gas Cherenkov detectors.

Plastic scintillators are solid plastics that contain organic scintillating compounds: aromatic hydrocarbons containing linked or condensed benzene-ring structures [140]. Light produced in plastic scintillators is generated by transitions of free valence electrons belonging to π -molecular orbitals. When a particle passes through the material, it excites electrons to either a singlet or triplet state, as well as a vibrational mode of the molecule, as shown in figure 3-12.

An electron excited to the S^{**} state will quickly decay to S^* without radiation, and then radiatively decay to a vibrational state of the ground state S_0 within a

Table 3.3: Summary of the HMS and SHMS hodoscopes

Parameter	HMS				SHMS			
	S1X	S1Y	S2X	S2Y	S1X	S1Y	S2X	S2Y
Width (mm)	8.0	8.0	8.0	8.0	8.0	8.0	10.0	5.5
Thickness (mm)	1.0	1.0	1.0	1.0	5.0	5.0	5.0	2.5
Length (mm)	75.5	120.5	75.5	120.5	100.0	100.0	110.0	125
z-position (cm)	77.83	97.52	298.82	318.51	52.1	61.7	271.4	282.4
Pitch (cm)	7.5	7.5	7.5	7.5	7.5	7.5	9.5	5.0
δz from odd numbered to even numbered paddles	2.12	2.12	2.12	2.12	2.12	-2.12	-2.12	-5.4
Paddles per plane	16	10	16	10	13	13	14	21
Material	BC404	BC404	BC404	BC404	RP408	RP408	RP408	Quartz

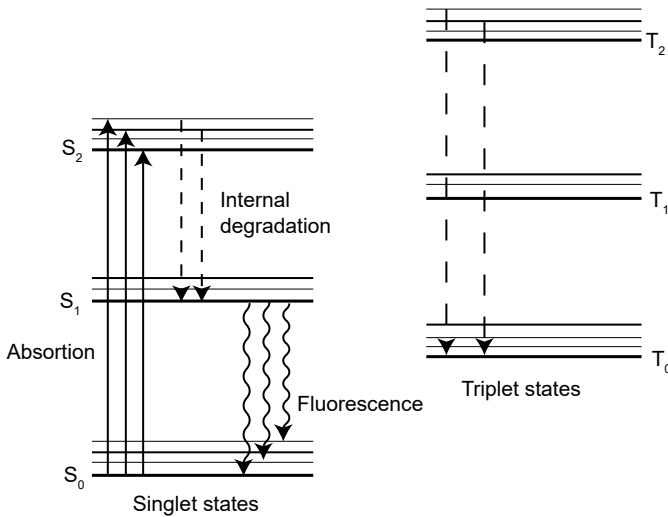


Figure 3-12: A schematic diagram of the energy levels of an organic scintillator [140]. Particles passing through the material will excite valence electrons to singlet and triplet states, decay from which will create visible light.

few nanoseconds. The energy of the radiation is less than that required to excite an electron from S_0 to S^* , so none of it will be absorbed in the process. The material is transparent to its own radiation.

The transition from a triplet state is similar. Decay from T_0 to S_0 is possible, but suppressed by selection rules. The decay typically takes place when two T_0 molecules interact with each other, resulting in one in the excited S^* state, one in the ground state, and heat dissipated in the medium. The excited S^* molecule then radiatively decays as in the singlet case.

Light produced in the SHMS quartz plane is Cherenkov radiation, which is discussed further in the subsection on Threshold Cherenkov Counters.

Both ends of each HMS paddle are read out by Philips XP2282B PMTs, with

nominal operating voltages of ~ 1800 V [141]. Similarly, the ends of each SHMS paddle are read out by a combination of ET ET9214B, ET ET9814QB, Photonis XP2262B, and Photonis XP2020QB PMTs. The operating voltages for each SHMS hodoscope PMT are available on the Hall C Wiki [142, 143].

The signals from each PMT are fed into a passive splitter, yielding two signals with amplitudes 1/3 and 2/3 of the original. The smaller signal is sent to a flash Analog-to-Digital Converter (fADC). The larger is sent to a discriminator as part the core of the trigger system, which will be discussed in the next section.

3.5.2 Drift Chambers

Both spectrometers have a pair of drift chambers [144] that provide precise tracking information. Combined with knowledge of the spectrometers' optics, this tracking information is used to calculate particle momenta, angles, and positions at the interaction point in the target.

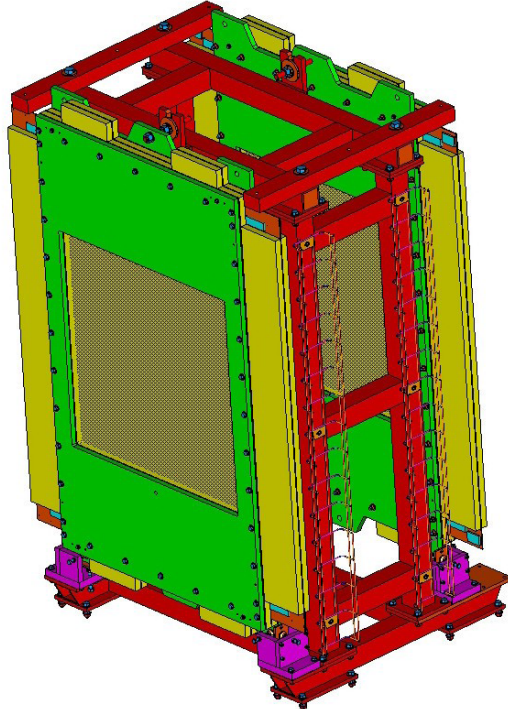


Figure 3-13: A rendering of the SHMS drift chambers mounted in the detector hut frame.

The drift chamber packages consist of a pair of identical chambers, each of consists of six wire planes. Each chamber has an active area of $80 \times 80 \text{ cm}^2$ to match

the size of the SHMS's acceptance and focal plane. Copper-coated mylar cathode planes are placed between each wire plane, before the first plane, and after the last plane. Each wire plane consists of a set of alternating 20 μm gold tungsten sense (anode) wires and 80 μm field wires, separated by 500 μm . To reduce cost, only two wire orientations were manufactured: an X plane with horizontally oriented wires and a U plane with wires oriented 60° from the X wires, both of which are shown in figure 3-14. In the SHMS, the U planes have 109 sense wires per plane and the X planes have 79. In the HMS, the U planes have 96 sense wires per plane and the X planes have 102.

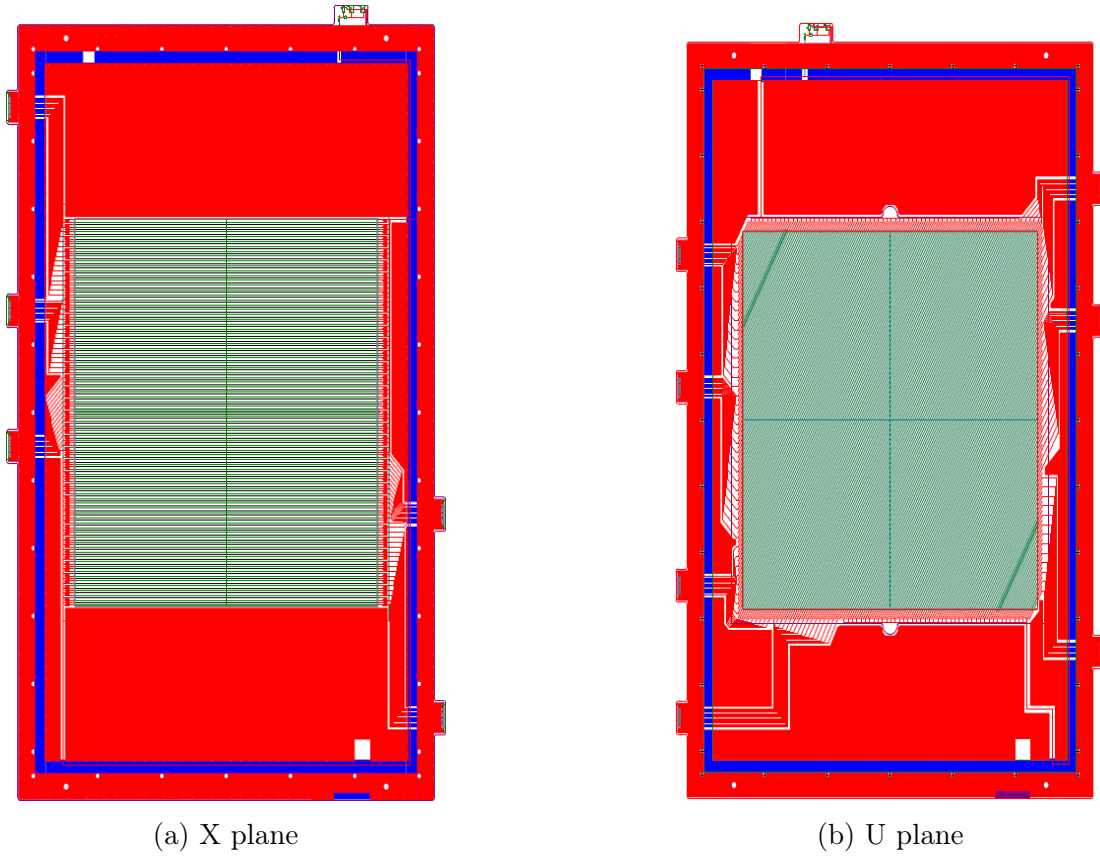


Figure 3-14: The drift chambers consist of 6 wire planes with different orientations, each of which are generated by rotating the two X and U planes.

X' and U' planes, with identical wire orientations offset by 500 μm from the unprimed planes, can be generated by rotating an X or U plane 180° such that the top becomes the bottom. V and V' planes, with wires oriented -60° from the X wires, can be generated by rotating the U and U' planes 180° around a vertical axis running through the center of the plane. The offset between the primed and

unprimed planes allows us to resolve the left-right ambiguity of each hit⁵

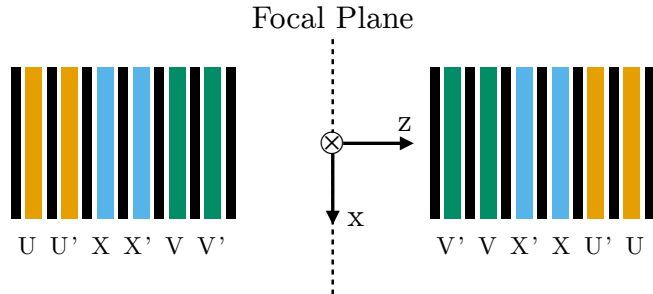


Figure 3-15: Side view of the order of planes encountered by a particle traveling through the SHMS. The focal plane of the spectrometer is roughly halfway between the two drift chambers.

As shown in figure 3-15, the order of the planes in the first chamber encountered by a particle traveling through the SHMS is (U, U', X, X', V, V') . The order in the second chamber is reversed. In the HMS, the V and V' planes in each chamber are swapped.

During operation, each chamber is filled with a 50/50 mix of argon and ethane. When a charged particle passes through the chamber, it will ionize some of the gas. The cathode planes and field wires are kept at $\sim -1900\text{ V}$ with respect to the sense wires kept at ground, creating an electric field pointing from sense wires toward field wires and cathode planes. The field accelerates these primary ionized electrons toward the sense wires, ionizing more electrons along the way. The resulting cloud of electrons drifts toward sense wires at a constant “drift velocity.”

The electrons are collected by sense wires which are read out by 16-channel amplifier/discriminator cards attached to the chamber supports. The discriminators are fed, via 16-channel ribbon cables, to CAEN 1190 TDCs [145] in a VXS crate in the detector huts. When the 1190s receive a pretrigger, they record the time of the last several hits⁶. The time between the pretrigger and the time at which the electron cloud hits a wire can be used to determine the distance at which the initial ionization occurred. Using this information from every wire plane in both chambers allows precise track reconstruction with residuals of $250\text{ }\mu\text{m}$ in the SHMS and $350\text{ }\mu\text{m}$ in the HMS.

⁵For a hit on an isolated drift chamber wire, it is impossible to know whether the ionized electrons came from the right or the left of the wire. This will be discussed further in the chapter on data analysis.

⁶The trigger and readout electronics will be discussed in more detail in the next section.

3.5.3 Threshold Cherenkov Counters

Threshold Cherenkov counters make use of a particle-dependent Cherenkov radiation threshold to discriminate between types of particles. A charged particle with mass m , velocity β , and 3-momentum p passing through a medium with index of refraction n will emit Cherenkov radiation if

$$\frac{c}{n} < \beta = \frac{p}{\sqrt{p^2 + m^2}} \quad (3.1)$$

or equivalently, as illustrated in figure 3-16,

$$1 - \frac{c}{n} > 1 - \beta = 1 - \frac{p}{\sqrt{p^2 + m^2}} \quad (3.2)$$

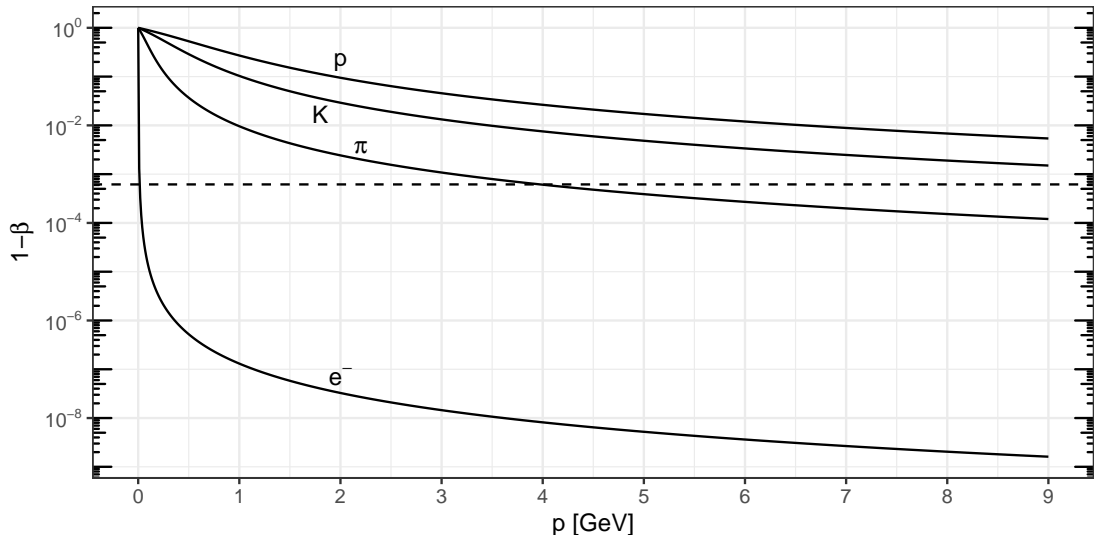


Figure 3-16: Value of $1 - \beta$ for various particles as a function of momentum. The horizontal line represents the Cherenkov threshold for C_4F_8O at a pressure of 0.45 atm, below which a particle will produce Cherenkov radiation.

Over a sufficiently narrow range of momenta, only some types of particles will emit Cherenkov radiation. For example, for a threshold Cherenkov counter filled with C_4F_8O at 0.45 atm, the presence or absence of Cherenkov radiation can be used to determine if the particle that generated a trigger is an electron or a hadron, provided the momentum range in question is below ~ 4 GeV. Given knowledge of the expected range of momenta an experiment requires and what types of backgrounds will need to be removed, one can pick an appropriate Cherenkov

medium based on its index of refraction. Further tuning of the threshold can be done by adjusting the pressure of the gas, making use of the fact that pressure is proportional to $n - 1$.

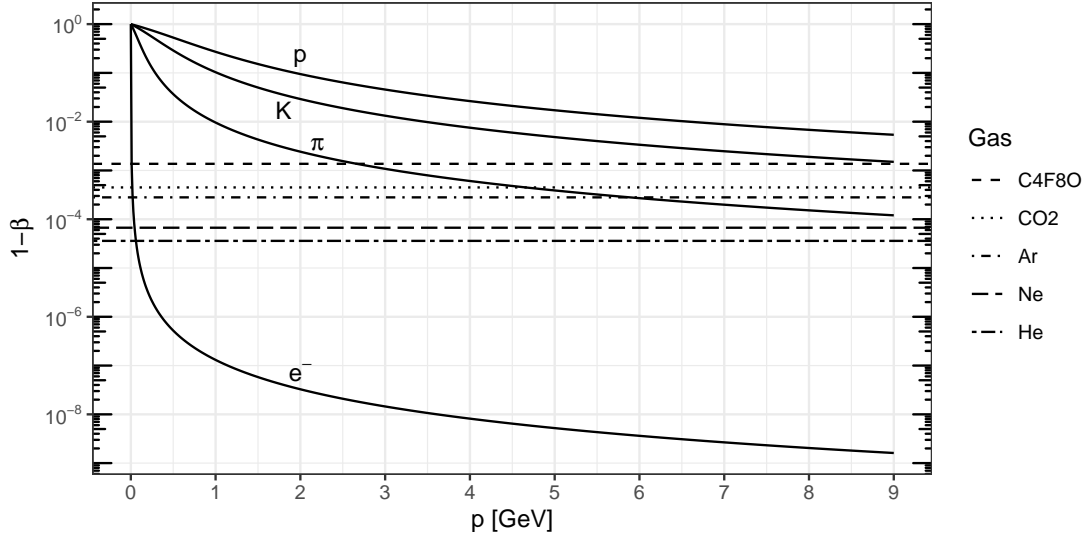


Figure 3-17: Value of $1 - \beta$ for various particles as a function of momentum. The horizontal lines represent the Cherenkov threshold for various gases at 1 atm, below which a particle will produce Cherenkov radiation.

Suppose a threshold Cherenkov detector has light-gathering efficiency $\epsilon_c(\lambda)$, a PMT with quantum efficiency $QE(\lambda)$, and is filled with a gas with transparency $G(\lambda)$ and index of refraction n . It can be shown [146] that by a particle of charge e passing through the detector with velocity β and path length L will generate $N_e = AL \left(1 - \frac{1}{\beta^2 n^2}\right)$ photoelectrons, where

$$A = 2\pi\alpha \int_{\lambda_1}^{\lambda_2} \epsilon_c(\lambda) QE(\lambda) G(\lambda) \frac{d\lambda}{\lambda^2}. \quad (3.3)$$

The gas Cherenkov detectors in the HMS and SHMS use spherical mirrors to focus Cherenkov radiation onto PMTs mounted on the back of the detector. The SHMS aerogel Cherenkov consists of an aerogel tray, covered in either GORE or Millipore diffusion materials [147], mounted between two columns of PMTs.

HMS Cherenkov

The HMS Cherenkov [148] is designed for electron-pion separation. During our runs, it was filled with C₄F₈O at 0.45 atm. After we had taken data, it was

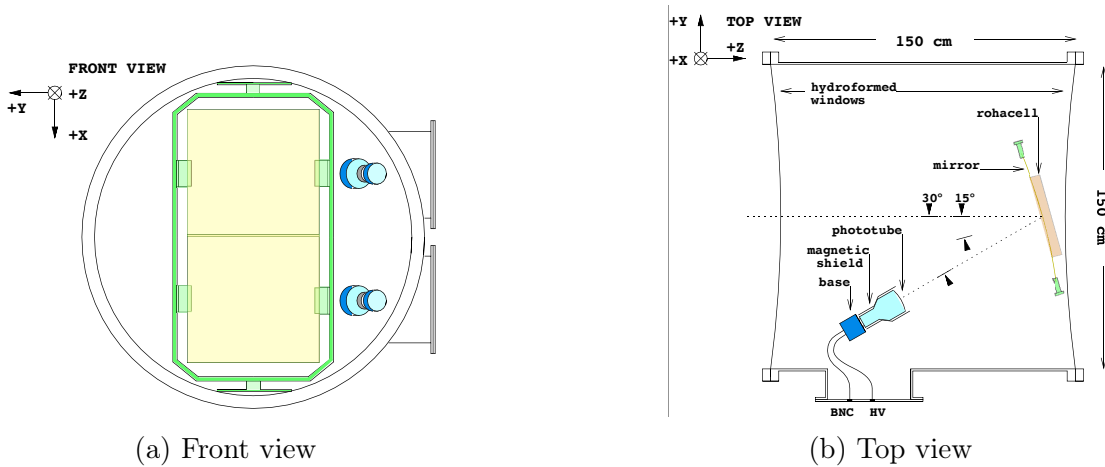


Figure 3-18: The HMS Cherenkov

discovered that the mirrors in the HMS Cherenkov had broken at some point before we began taking data. Analysis of this issue is presented in Section 4.7.2. Briefly, our production data are focused in the central region of the HMS acceptance and thus minimally affected by the broken mirrors.

SHMS Noble Gas Cherenkov

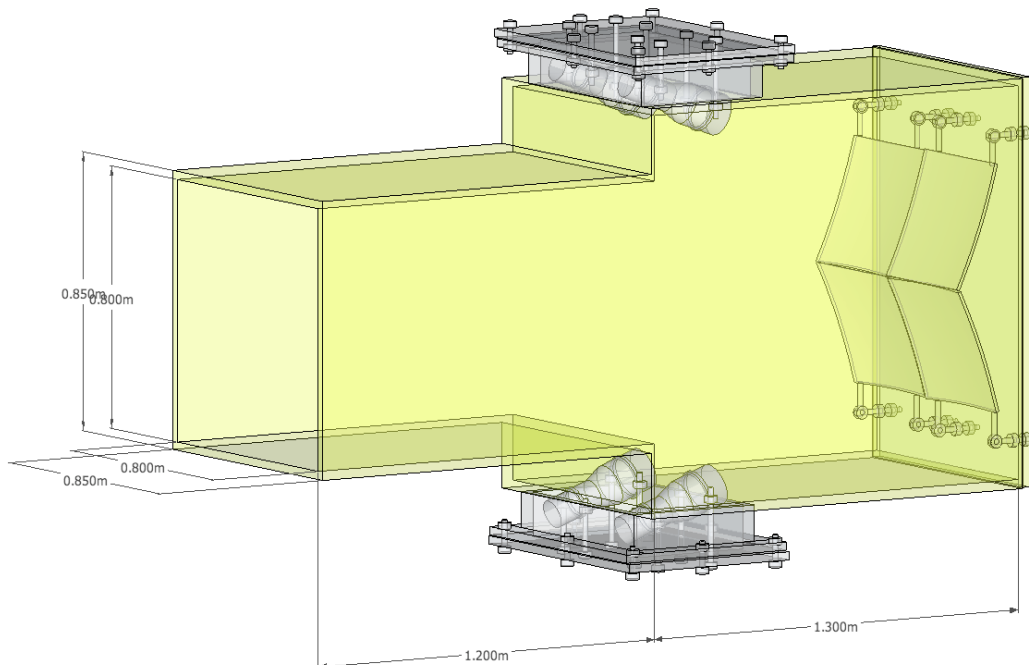


Figure 3-19: CAD rendering of the SHMS Noble Gas Cherenkov

The SHMS Noble Gas Cherenkov [146] is designed for e/pi separation. During our runs, it was filled with CO₂ at 1 atm.

SHMS Heavy Gas Cherenkov

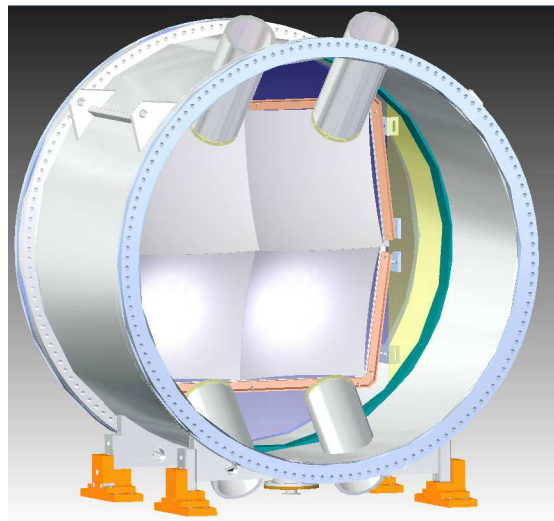


Figure 3-20: CAD rendering of the SHMS Heavy Gas Cherenkov

Designed for pi/K separation.

During our runs, it was filled with CO₂ at 1 atm.

SHMS Aerogel Cherenkov



Figure 3-21: A picture of the SHMS Aerogel Cherenkov

The SHMS Aerogel Cherenkov [147] was designed for K/p separation.

3.5.4 Calorimeters

A lead glass calorimeter provides another means for discriminating between electrons and hadrons. The calorimeters in both spectrometers consist of lead blocks with PMTs attached that collect light generated by electromagnetic showers. The electric field of the nuclei in the block will slow down a high energy electron passing through the block. The electron will radiate Bremsstrahlung photons, which will in turn generate positron-electron pairs that will also radiate photons, and so on. The resulting electromagnetic shower of photons, electrons, and positrons generates Cherenkov radiation that is collected by PMTs mounted on the ends of the lead glass blocks. The amount of light collected is proportional to the deposited energy. Electrons, positrons, and photons will deposit all of their energy. For the kinematics of E12-06-102, this is between 2 and 6 GeV. These particles will produce a peak centered around 1 in the distribution of the track-normalized energy deposition, E/p . A pion, whose mass is much greater than an electron's, will typically deposit about 300 MeV. A negative pion undergoing a charge-exchange reaction in the bulk of the calorimeter can produce a neutral pion which will decay into two photons, resulting in a significant fraction of energy being deposited. As a result, there is a large pion tail in the E/p distribution that extends up to 1. Heavier hadrons typically deposit no energy.

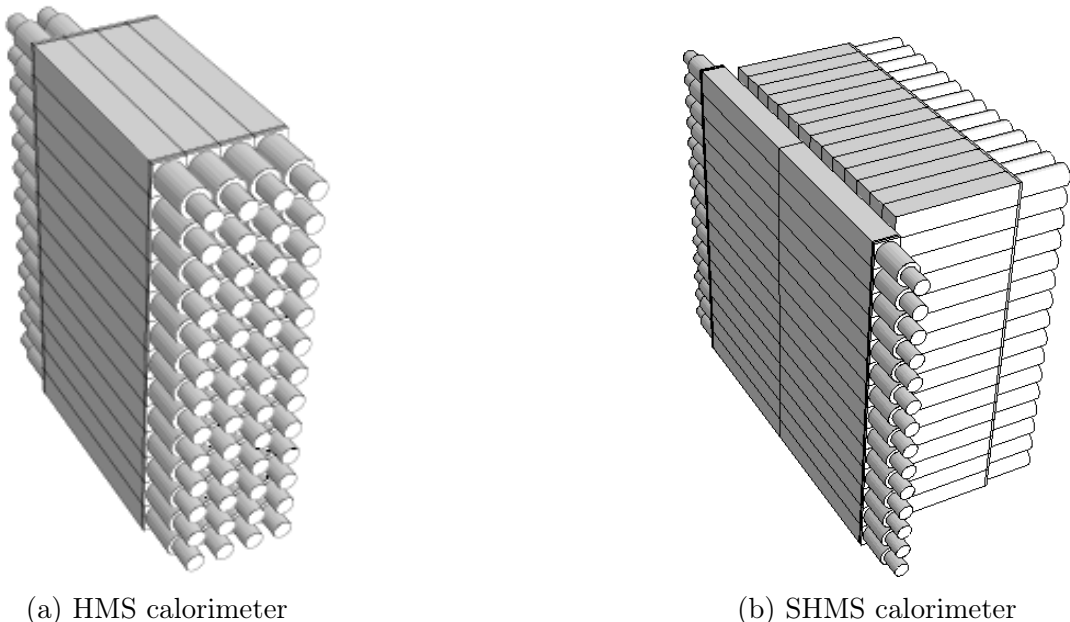


Figure 3-22: The HMS and SHMS calorimeters

HMS Calorimeter

The HMS calorimeter [149] consists of four rows of thirteen $10 \times 10 \times 70 \text{ cm}^3$ lead glass blocks. The total thickness is ~ 14.6 radiation lengths. The blocks are made of TF-1 type lead glass with an index of refraction of 1.65, radiation length 2.74 cm, and density 3.86 g cm^{-3} . Each block is wrapped in 25 μm thick aluminized Mylar and 40 μm thick Tedlar type film to block external light. The light generated in each block is collected by two Phillips XP3462B PMTs, one on each end.

SHMS Calorimeter

The SHMS calorimeter consists of a preshower and shower section. The preshower radiator consists of one layer of 28 TF-1 type lead glass blocks, identical to the HMS blocks, stacked in two columns of 14 blocks. The “fly eye” shower array consists of 224 modules from the decommissioned HERMES detector [150] stacked in 14 columns and 16 rows. The HERMES blocks are $8.9 \times 8.9 \times 50 \text{ cm}^3$ blocks of F-101 type lead glass with an index of refraction of 1.65, radiation length 2.78 cm, and density 3.86 g cm^{-3} . Each preshower block is read out by one Phillips XP3462B PMT, and each shower block by one Photonis XP3461 PMT.

3.6 Trigger and Data Acquisition Systems

The signals from each detector’s PMTs (or in the case of the drift chambers, each wire) are digitized by ADC250 [151] flash analog-to-digital converters (fADCs) or CAEN V1190 [145] time-to-digital converters (TDCs).

The HMS detector hut contains a VXS crate with TDCs that process signals from the HMS drift chambers. The SHMS detector hut contains a VXS crate with fADCs that process signals from the SHMS calorimeter’s preshower and shower PMTs, and a VME crate with TDCs that process signals from the SHMS drift chambers. The Counting Room contains TDCs and fADCs to process signals from all the other detectors, as well as sums of signals from other detectors. These sums form “pretrigger” signals that are sent to a Trigger Interface (TI) module which then distributes a specified trigger signal to synchronize readout of the fADCs and TDCs in every read-out controller (ROC). This analog trigger signal is called a

“Level 1 Accept,” or L1 for short. A copy of the Level 1 pretrigger is sent to every ROC which, when subtracted from the raw TDC time, improves timing resolution from ~ 25 ns to ~ 0.1 ns. Both spectrometers have a TI, allowing them to be run independently or in coincidence.

A broad overview of the SHMS trigger and readout system is given in [3-23](#). The HMS system is similar in structure, the largest differences being in the calorimeter signal chain.

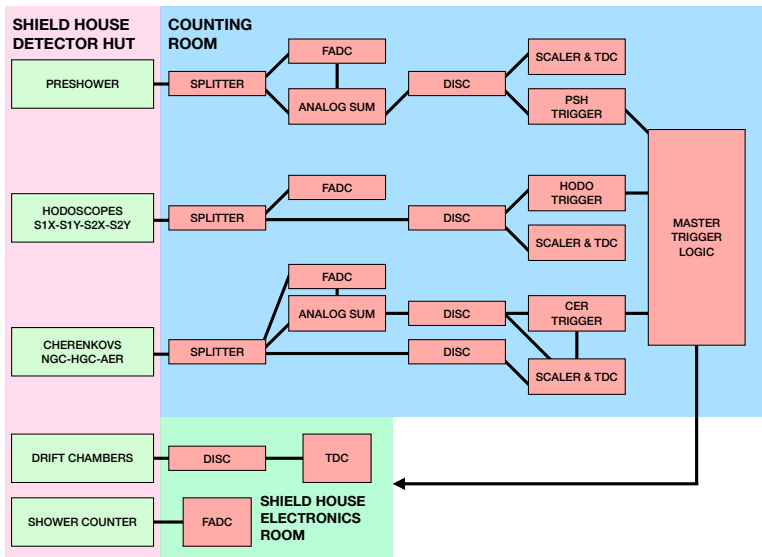


Figure 3-23: Schematic diagram of the trigger system. Adapted from H. Fenker and B. Sawatzky.

Every trigger and pretrigger described below is sent to TDCs to keep track of timing information necessary for event reconstruction, and scalers that count every trigger with negligible deadtime.

3.6.1 Pretriggers, TDC, and fADC Logic

Hodoscope

Each hodoscope consists of 4 planes of scintillator paddles, with a PMT mounted on both sides of each paddle. The signal from each PMT is sent to a passive splitter. One third of the signal amplitude is sent to an fADC, and the other two thirds are sent to a discriminator. The discriminator outputs are sent to daisy-chained TDCs and scalers, as well as a LeCroy 4564 logic unit. The logic unit computes a per-plane pretrigger by taking the AND of both sides’ N -fold ORs of each side’s

N PMTs. For instance, let $h1X+$ denote the 16-fold OR of the 16 PMTs on the left side of the 1X plane of the HMS hodoscope and similarly $h1X-$ denote the equivalent OR of the right hand side. Then the $h1X$ plane pretrigger is the AND of $h1X+$ and $h1X-$. The equations below describe the logic of each plane of the HMS and SHMS hodoscopes' pretriggers⁷.

$$h1X = h1X+ \text{ (16-fold OR)} \text{ AND } h1X- \text{ (16-fold OR)}$$

$$h1Y = h1Y+ \text{ (10-fold OR)} \text{ AND } h1Y- \text{ (10-fold OR)}$$

$$h2X = h2X+ \text{ (16-fold OR)} \text{ AND } h2X- \text{ (16-fold OR)}$$

$$h2Y = h2Y+ \text{ (10-fold OR)} \text{ AND } h2Y- \text{ (10-fold OR)}$$

$$p1X = p1X+ \text{ (13-fold OR)} \text{ AND } p1X- \text{ (13-fold OR)}$$

$$p1Y = p1Y+ \text{ (13-fold OR)} \text{ AND } p1Y- \text{ (13-fold OR)}$$

$$p2X = p2X+ \text{ (14-fold OR)} \text{ AND } p2X- \text{ (14-fold OR)}$$

$$p2Y = p2Y+ \text{ (21-fold OR)} \text{ AND } p2Y- \text{ (21-fold OR)}$$

These pretriggers are converted from ECL twisted-pair to NIM signals by sets of P/S model 7126 16-channel logic level translators [152]. The NIM pretrigger signals are converted to variable-width gates by sets of P/S model 752 logic units [153]. Sets of P/S Model 755 logic units [154] generate the following pretriggers for both spectrometers based on coincidences of hodoscope plane pretriggers:

- $S1 = 1X \text{ OR } 1Y$
- $S2 = 2X \text{ OR } 2Y$
- $\text{STOF} = S1 \text{ AND } S2$
- $\text{HODO 3/4} = \text{coincidence of at least 3 planes}$

⁷Because the SHMS 2Y plane has more PMTs than each logic unit has channels, each side's 21-fold OR is actually an OR of a 16-fold OR and a 5-fold OR.

Calorimeters

Both spectrometer's calorimeters consist of two (SHMS) to four (HMS) layers of long lead-glass blocks connected to PMTs on one or both sides.

The signals from the HMS calorimeter PMTs are read out in the Counting Room, where they pass through a passive 50:50 splitter, with one half of each signal sent to fADC inputs. The other half is sent to P/S model 740 analog sum modules [155] which generate sums for each side of each layer (hA+, hA-, hB+, hB-, hC, and hD⁸). A LeCroy model 428F [156] module sums both sides of the first two layers to form hA and hB. Each layer's sum is then sent to an fADC as well as a P/S model 715 discriminator [157] to form the following calorimeter pretriggers:

- hPreSH LO = $hA < -40\text{ mV}$
- hPreSH HI = $hA < -60\text{ mV}$
- hShower LO = $hA + hB + hC + hD < -45\text{ mV}$

The SHMS calorimeter shower counter PMTs are all sent directly to fADCs inside the electronics hut. As in the HMS, each SHMS preshower layer PMT's output passes through a passive 50:50 splitter, with half the signal amplitude sent to an fADC and the other half sent to analog sum modules that generate preshower LO/HI pretriggers.

Cherenkovs

All the threshold Cherenkov detectors in both spectrometers consist of some medium in (some types of) charged particles generate Cherenkov radiation in the visible spectrum and some number of PMTs that collect this light. The output of each PMT is read out in the Counting Room, where it passes through a passive 50:50 splitter. One half of the signal amplitude is sent to an fADC, and the other half is sent to a LeCroy 428F summing module [156]. This sum is sent to an fADC as well as to a P/S model 715 discriminator [157] to form a pretrigger for that Cherenkov

⁸The third and fourth layers of the HMS calorimeter only have PMTs connected to one side.

Other Pretriggers

Four other pretrigger signals are generated from combinations of pretrigger signals described above. They are as follows:

- EL-Hi = (HODO 3/4) AND (PreSH HI)
- EL-Lo = (Two of three from HODO 3/4, STOF, PreSH LO) AND (Cer)
- EL-Real = EL-Hi OR EL-Lo
- EL-Clean = EL-Hi AND EL-Lo

Electronic Dead Time Measurement (EDTM) Pulser

To estimate the deadtime due to all electronics involved in data acquisition, a pulser with a low frequency (3 Hz in our experiment) is inserted into the trigger logic. The EDTM pulser fires every trigger in the system, and is also sent to its own TDC and scaler channels. By comparing the number of accepted EDTM triggers to the number of EDTM trigger counts seen by the scaler, one can estimate deadtime. This process is discussed in more detail in Section [4.7.7](#).

3.6.2 Reference Times

The reference time for an event is an OR-ed version of pretrigger signals distributed to each fADC and TDC in every ROC. The TDC modules have two internal clocks, one with a 40 MHz cycle and one with a 10 GHz cycle. When a given detector signal is received by a TDC, the digitized time latches onto the leading edge of the 40 MHz cycle, yielding a timing resolution of ~ 25 ns. We feed a *reference time*, a copy of the pretrigger (common to all fADCs and TDCs in a given ROC), to the TDC which will latch onto the leading edge of the faster 10 GHz clock. The hcana analyzer subtracts the reference time from detectors' raw TDC times to yield a timing resolution of ~ 0.1 ns. This process is discussed in more detail in Section [4.2](#).

Chapter 4

Data Analysis

4.1 hcana

Hall C has developed a new analysis framework, hcana [158], written in C++ to replace ENGINE, the old analysis framework written in Fortran. hcana is an extension of the Hall A analyzer, Podd [159], a modular framework based on the CERN ROOT framework [160]. Event reconstruction or “replay” in hcana proceeds in the following order:

1. The analyzer unpacks hits stored as raw EVIO data and stores them in lists sorted by ROC, slot, and channel number. A text file containing a “detector map” associates these front-end electronics identifiers with a particular detector, plane/wire/PMT/etc., and type (ADC or TDC).
2. The `Decode()` method converts these lists of raw hits into physically meaningful ADC quantities (pulse amplitude, pulse time, pulse integral, pulse pedestal) and TDC times for every detector.
3. Tracking detectors run the `CoarseTrack()` method to generate a list of candidate tracks.
4. Non-tracking detectors run the `CoarseProcess()` method, placing fiducial cuts on ADC and TDC values to select “good” hits. This step also performs any relevant calculation that does not require accurate tracking information, such as calculating the number of photoelectrons collected by each PMT in a Cherenkov detector.

5. The analyzer then calculates precise tracking information for each event. All candidate tracks are transported from the focal plane to the target using the optics reconstruction matrix elements.
6. The best track among all candidate, the “golden track,” is selected using one of three methods called Simple, Prune, and Scin.
7. Non-tracking detectors run the `FineProcess()` method to calculate quantities that depend on accurate tracking information, such as the “track-normalized energy” deposited in the calorimeter, E/p .
8. Finally, physics modules that calculate quantities such as invariant mass W , momentum transfer Q^2 , and missing energy E_m are run.

After this event loop is run for all events of interest in a raw CODA file, TTrees containing reconstructed data are written to a ROOT file. hcana also allows the user to specify a set of one- and two-dimensional histograms to be generated for each run. Such standardized histograms are convenient for quality assurance and debugging problems during data acquisition. Replayed ROOT files can then be analyzed with further scripts written for the purpose of detector calibration or physics analysis.

The sections that follow in this chapter will describe the details of each step outlined in the list above.

4.2 Reference Time Cuts

Fig 4-1 illustrates the relationship between a detector signal and the internal clocks of the CAEN 1190 TDCs that determine the timing resolution of measurements in Hall C. An L1 pretrigger (see Section 3.6) that initiates read-out in a ROC latches onto the leading edge of the next cycle of an 1190’s 40 MHz clock. As a result, this digitized pretrigger time can only be known to have been received within the 25 ns window between that 40 MHz cycle and the previous cycle. Pretriggers also have an intrinsic 4 ns jitter¹, meaning that raw TDC signals can only be known to within \sim 29 ns. To improve the timing resolution, the DAQ sends a

¹A small, irregular variation in an otherwise periodic signal.

delayed copy of the pretrigger, called a *reference time*, to a TDC. The reference time latches onto the leading edge of the 1190's 10 GHz clock (accurate to 0.1 ns), and initiates read-out of the full TDC spectrum (a lookback window of a few μ s). All modules in a given ROC share the same reference time. Therefore, subtracting the raw TDC time (synced to the 40 MHz clock) from the reference time (synced to the 10 GHz clock), the timing resolution can be improved to approximately 0.1 ns. This reference time subtraction is performed offline during hcana replay.

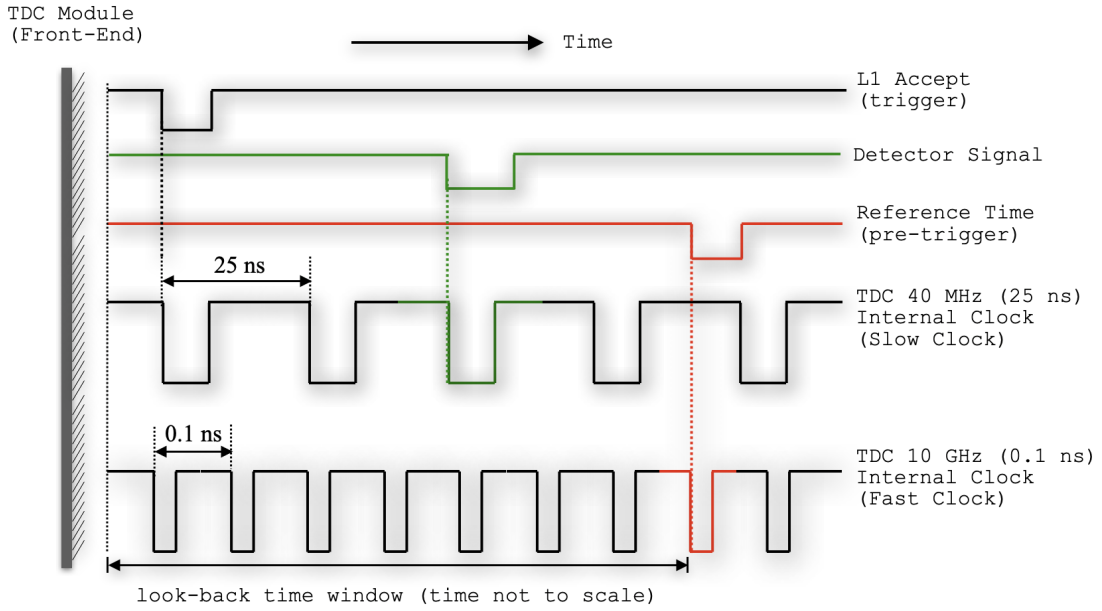


Figure 4-1: Scheme illustrating the synchronization of a detector signal with a CAEN 1190 TDC's internal 4 MHz and 10 GHz clocks. Figure reproduced from Carlos Yero's PhD thesis [161].

As shown in Fig 4-2, true physics events will lie within a range of approximately 300 raw TDC channels. Background events will have occurred earlier in the lookback window, and must be prevented from being chosen as the reference time. To accomplish this, hcana uses reference time cuts defined in the parameter files. Any hits outside the minimum and maximum TDC range will be ignored.

4.3 Detector Time Window Cuts

As with reference time selection, care must be taken to avoid background hits in the fADC spectra. The distribution of the differences between the fADC pulse times and reference-time-subtracted TDC times for a given PMT in a detector

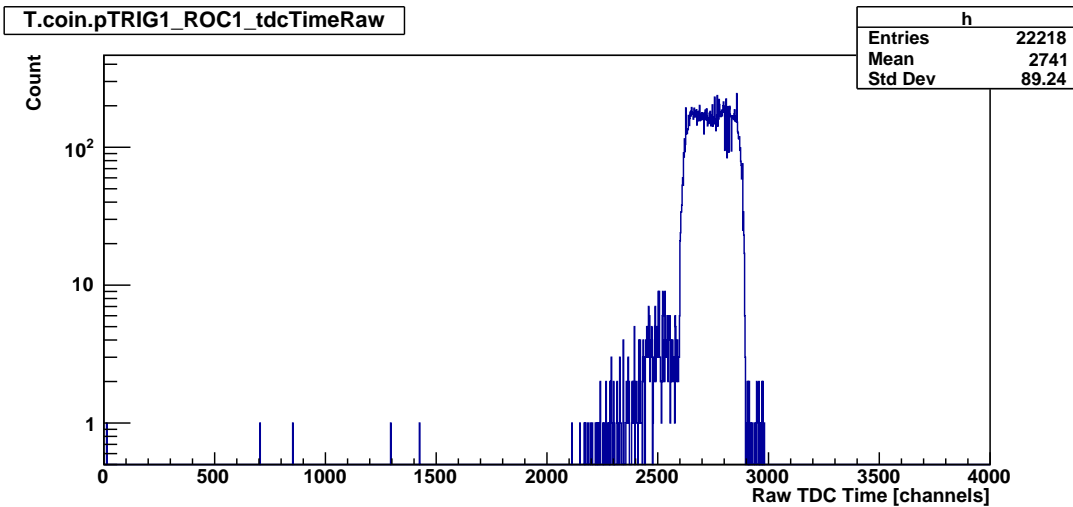


Figure 4-2: The raw TDC time spectrum in channels for the trigger formed by coincidence of three of four hodoscope planes in the SHMS. True physics events lie in the plateau from approximately 2600 to 2900 channels. Hits outside this plateau are background that will be ignored by hcana if the minimum and maximum cuts are set tightly around the plateau.

should be a narrow peak with a width determined by the resolutions of the TDCs and fADCs. Events far from this peak have TDC and fADC times that are not correlated, and can be assumed not to be associated with the current event. By placing lower and upper bounds on the difference between these times on a per-PMT basis, we can ensure that hcana will choose the correct fADC hits for every event. Representative histograms of these time differences are shown in Fig 4-3.

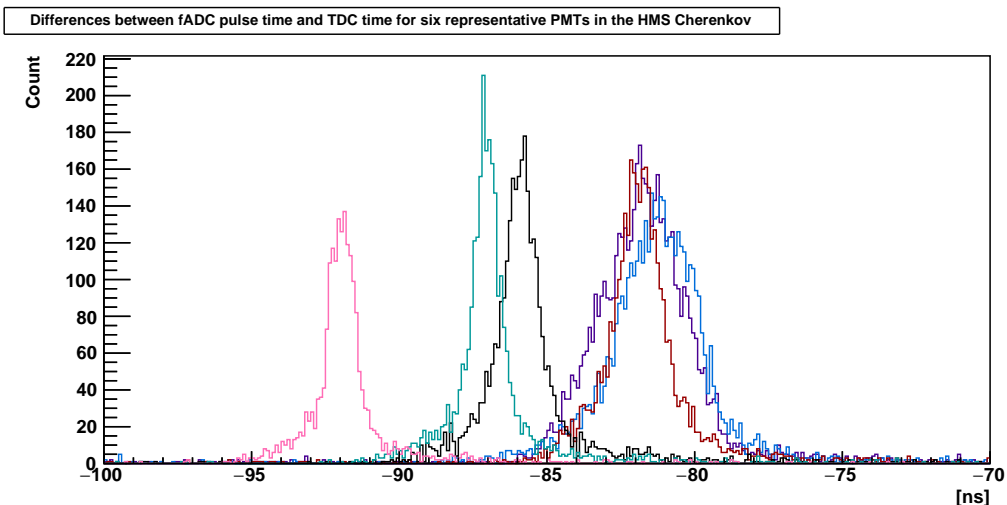


Figure 4-3: The difference between fADC pulse times and reference-time-subtracted TDC times for six representative PMTs on one side of one plane of the HMS calorimeter.

4.4 Detector Calibrations

4.4.1 Hodoscopes

The calibration procedure for the hodoscopes consists of determining a set of timing corrections applied to the raw times t_{raw} generated by discriminators fed into TDCs. The general form of a corrected TDC time for one end of a scintillator paddle is

$$t_{corr} = t_{raw} - t_{TW} - t_{cable} - t_{prop} - t_\lambda \quad (4.1)$$

- **Timewalk corrections t_{TW}**

Timewalk refers to the correlation between the amplitude of an analog signal fed into a leading-edge, fixed-threshold discriminator and the time the signal rises above the discriminator's threshold. As seen in Fig 4-4, pulses with a smaller amplitude cross a fixed threshold at later times despite starting at the same time.

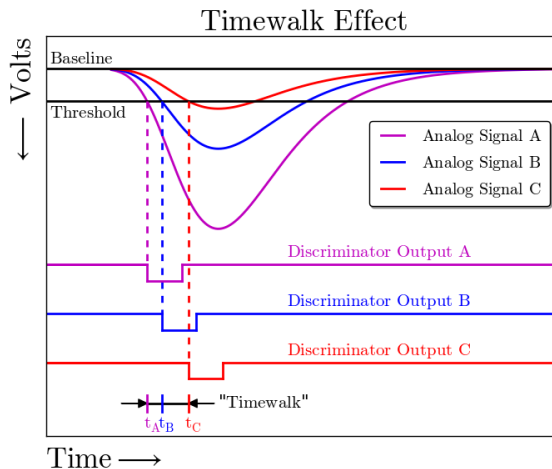


Figure 4-4: An illustration of the timewalk effect. Pulses with a smaller amplitude cross the fixed threshold at a later time. The TDCs in the Hall C DAQ are prone to this effect.

Fortunately, the fADCs are not prone to this effect so the pulse time recorded by an fADC can be used to correct the corresponding TDC time. The fADC pulse time is determined by a constant fraction discriminator (CFD) algorithm that finds the time, to a precision of 62.5 ps, at which the pulse reaches 50% of its maximum amplitude. This algorithm is illustrated in

Fig 4-5, and a comparison of pulse times of varying amplitudes is shown in Fig 4-6.

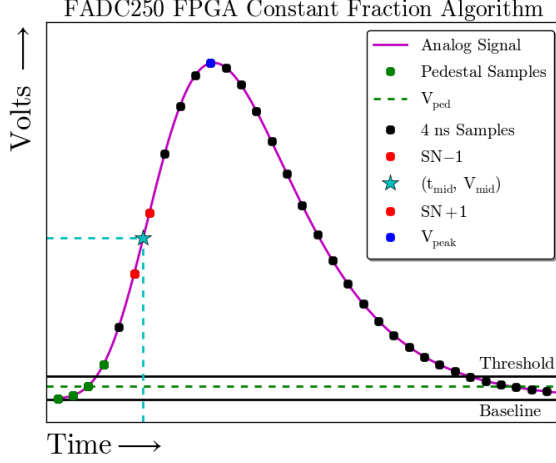


Figure 4-5: An illustration of the fADCs' CFD algorithm. The algorithm calculates the pedestal amplitude V_{ped} with a fixed-threshold discriminator. It then calculates the half-amplitude $V_{mid} = (V_{peak} - V_{ped})/2$ and determines which two samples $SN - 1$ and $SN + 1$ lie on either side of V_{mid} . The fADCs' coarse sampling rate is 250 MHz, yielding 4 ns between the two samples. This time is divided into 64 subsamples of 62.5 ps each, and the time t_{mid} corresponding to V_{mid} is found by linear interpolation..

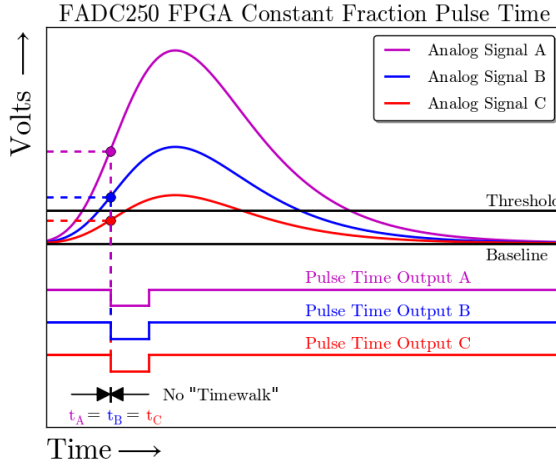


Figure 4-6: An illustration of the absence of timewalk in the fADCs' CFD algorithm.

A plot of the difference between raw TDC time and fADC pulse time versus fADC pulse amplitude can be fit to the form $t_{TW}(a) = c_1 + \frac{1}{TDC_{thr}}a^2$ where a is the pulse amplitude and TDC_{thr} is the TDC threshold (120 mV in this experiment). The per-PMT parameters c_1 and c_2 are extracted from a

calibration run with large statistics.

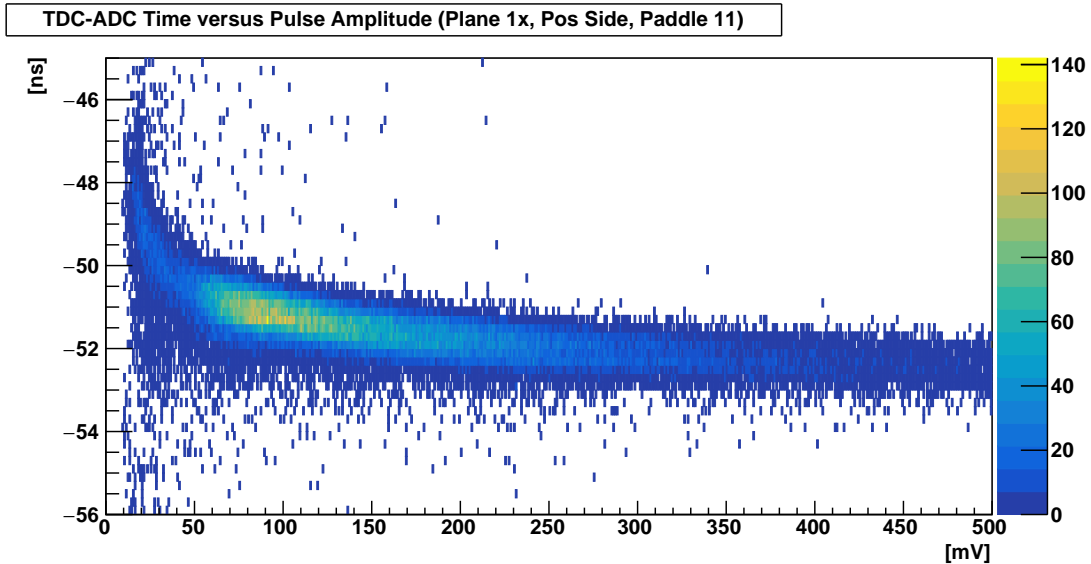


Figure 4-7: A two dimensional histogram showing the difference between TDC and fADC pulse times as a function of fADC pulse amplitude. As shown in Fig 4-4, smaller pulses cross a fixed threshold at a later time, leading to a delayed TDC time.

- **Cable/light propagation time** t_{cable} , t_{prop}

Signals from the hodoscope travel through BNC cables from the detector hut underground up to the electronics racks in the counting house above ground. Differences in cable propagation time between the opposite ends of the paddles need to be accounted for. The timewalk-corrected TDC times for the + and – sides of a paddle are the sum of the propagation time for the light through the paddle and the propagation time through the cables, $t^\pm = t_{prop}^\pm + t_{cable}^\pm$. The difference between the + and – sides' times should be proportional to the track's distance from the center of the paddle (i.e. the y coordinate for a horizontal paddle, x for a vertical paddle). If v is the speed of light in the paddle, this difference is $\Delta t = \frac{y}{v} + b$, where b is a parameter that captures the offset due to differences in cable propagation time. A linear fit of the time difference Δt versus track distance from the center of the paddle is used to extract the cable offset and light propagation speed for each paddle. The intercept b is the cable propagation time correction t_{cable}^\pm and the slope $1/v$ determines the light propagation time correction t_{prop}^\pm . For a horizontal paddle, $t_{prop}^\pm = (\pm L_\pm \pm y_{hit})$ where L_\pm is the y coordinate of

the ends of the paddle and y_{hit} is the y coordinate of the particle's track projected to the paddle's z position. The same formula holds for a vertical paddle, but using L_{\pm} in the x direction and x_{hit} at the paddle's z position.

- **Small perturbations t_λ**

This term corrects for small differences λ in timing between planes. Let t_i be the time, corrected for timewalk and propagation time, of a hit on a paddle in plane i , and D_{ij} be the distance between planes i and j . Then the difference between hits in these planes with small perturbations can be expressed as

$$(t_i + \lambda_i) - (t_j + \lambda_j) = \frac{D_{ij}}{v} \quad (4.2)$$

or equivalently, defining a term b_{ij} ,

$$\lambda_i - \lambda_j = \frac{D_{ij}}{v} - (t_i - t_j) \equiv b_{ij} \quad (4.3)$$

Generalizing this to all 6 combinations of differences between 4 planes, we can set up a system of linear equations with coefficients $c_i, j = \pm 1$ where i represents one of the 6 plane combinations and j is the “absolute” paddle number. Paddles are indexed with j from 1 to the total number of paddles in the 4 planes. In the HMS there are 52 total paddles, so the system of linear equations is

$$c_{1,1}\lambda_1 + c_{1,2}\lambda_2 + \cdots + c_{1,52}\lambda_{52} = b_{12} \quad (4.4)$$

$$c_{2,1}\lambda_1 + c_{2,2}\lambda_2 + \cdots + c_{2,52}\lambda_{52} = b_{13} \quad (4.5)$$

$$c_{3,1}\lambda_1 + c_{3,2}\lambda_2 + \cdots + c_{3,52}\lambda_{52} = b_{14} \quad (4.6)$$

$$c_{4,1}\lambda_1 + c_{4,2}\lambda_2 + \cdots + c_{4,52}\lambda_{52} = b_{23} \quad (4.7)$$

$$c_{5,1}\lambda_1 + c_{5,2}\lambda_2 + \cdots + c_{5,52}\lambda_{52} = b_{24} \quad (4.8)$$

$$c_{6,1}\lambda_1 + c_{6,2}\lambda_2 + \cdots + c_{6,52}\lambda_{52} = b_{34} \quad (4.9)$$

$$(4.10)$$

or in matrix notation

$$C\vec{\lambda} = \begin{bmatrix} c_{1,1} & c_{1,2} & \cdots & c_{1,52} \\ c_{2,1} & c_{2,2} & \cdots & c_{2,52} \\ c_{3,1} & c_{3,2} & \cdots & c_{3,52} \\ c_{4,1} & c_{4,2} & \cdots & c_{4,52} \\ c_{5,1} & c_{5,2} & \cdots & c_{5,52} \\ c_{6,1} & c_{6,2} & \cdots & c_{6,52} \end{bmatrix} \begin{bmatrix} \lambda_1 \\ \lambda_2 \\ \vdots \\ \lambda_{52} \end{bmatrix} = \begin{bmatrix} b_{12} \\ b_{13} \\ b_{14} \\ b_{23} \\ b_{24} \\ b_{34} \end{bmatrix} \quad (4.11)$$

Solving this for all λ s requires accumulating statistics from a run with many events k :

$$C\vec{\lambda} = \begin{bmatrix} \sum_k c_{1,1} & \sum_k c_{1,2} & \cdots & \sum_k c_{1,52} \\ \sum_k c_{2,1} & \sum_k c_{2,2} & \cdots & \sum_k c_{2,52} \\ \sum_k c_{3,1} & \sum_k c_{3,2} & \cdots & \sum_k c_{3,52} \\ \sum_k c_{4,1} & \sum_k c_{4,2} & \cdots & \sum_k c_{4,52} \\ \sum_k c_{5,1} & \sum_k c_{5,2} & \cdots & \sum_k c_{5,52} \\ \sum_k c_{6,1} & \sum_k c_{6,2} & \cdots & \sum_k c_{6,52} \end{bmatrix} \begin{bmatrix} \lambda_1 \\ \lambda_2 \\ \vdots \\ \lambda_{52} \end{bmatrix} = \begin{bmatrix} \sum_k b_{12} \\ \sum_k b_{13} \\ \sum_k b_{14} \\ \sum_k b_{23} \\ \sum_k b_{24} \\ \sum_k b_{34} \end{bmatrix} \quad (4.12)$$

hcana solves for $\vec{\lambda}$ using singular value decomposition, yielding a set of corrections $t_\lambda = \lambda_i$ for every paddle i .

4.4.2 Drift Chambers

When a charged particle passes through the drift chambers, it ionizes the gas filling the chamber. The electric field generated by the field wires causes the freed electrons to drift toward sense wires over a “drift time” t_D . The sense wires are read out by discriminators fed into TDC channels. Knowledge of which wires in each plane have been fired permits coarse track reconstruction. Finer resolution can be achieved by using the drift time to estimate a drift distance d_D , the distance from the wire at which the ionization occurred.

Assuming the events used for calibration illuminate the detector uniformly and that the drift velocity is uniform across the detector, the relationship between drift

distance and drift time t_D is

$$d_D(\tau = t_D) = \frac{\Delta}{2} \frac{\int_{t_0}^{t_D < t_{max}} F(\tau) d\tau}{\int_{t_0}^{t_{max}} F(\tau) d\tau} \quad (4.13)$$

where $F(\tau)$ is the distribution of drift times. The times t_0 and t_{max} are the minimum and maximum drift times, determined by the cell spacing and drift velocity. They are extracted from the distribution $F(\tau)$. The constant $\Delta/2$ ensures this expression respects the limiting cases of particles passing immediately adjacent to a sense wire or exactly between two sense wires.

The TDCs have a finite resolution, so these integrals are in reality actually sums over bins F_i with widths $\Delta\tau$,

$$d_D(\tau = t_D) = \frac{\Delta}{2} \frac{\sum_{i=0}^{n_{max} < N} F_i \Delta\tau}{\sum_{i=0}^N F_i \Delta\tau} \quad (4.14)$$

$$= \frac{\Delta}{2} \frac{1}{N} \sum_{i=0}^{n_{max}} F_i \quad (4.15)$$

where i is the bin index, n is the index of the bin in which drift time t_D lies, and N is the index of the maximum drift time.

The first step in calibrating the drift chambers is determining a t_0 for every wire. This is done by finding the point at which a linear fit of the lower range of the drift time spectrum to cross the x axis, as shown in Fig 4-8. If there are insufficient per-wire statistics to obtain a good fit, the distribution for all 16 wires connected to a card may be used instead to obtain a per-card t_0 .

The calibration script first generates a histogram of drift times with bins of width 1 ns and finds the bin in the histogram containing the maximum number of entries. A linear fit is then performed over the bins corresponding to 20–60% of the maximum bin content. The x-intercept of this fit yields t_0 , which can then be used to create a lookup table using equation 4.14. An example of the distribution of uncorrected and corrected drift times is shown in Fig 4-9.

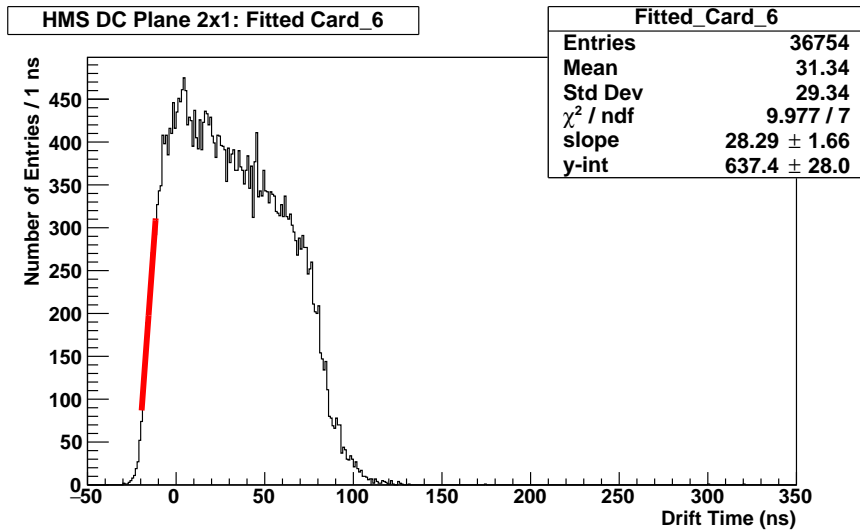


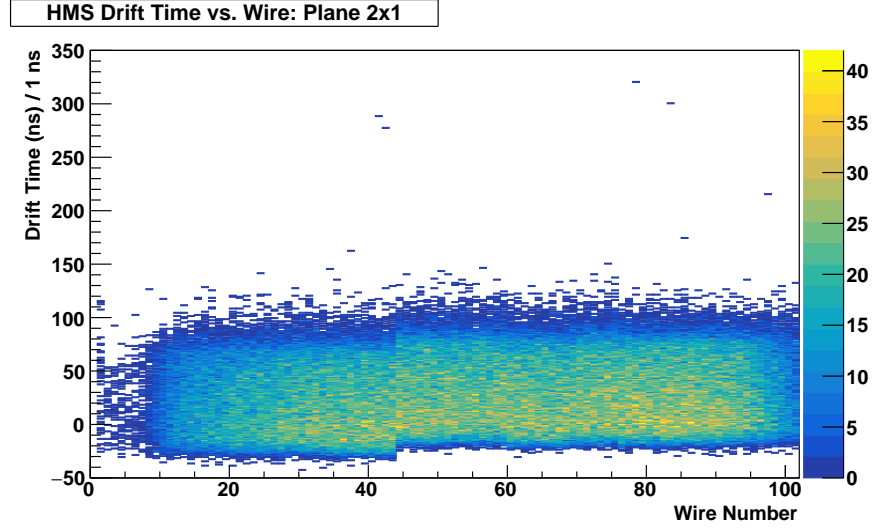
Figure 4-8: The distribution of drift times for one card in the HMS 2x1 plane. The red line is a linear fit to the range corresponding to 20–60% of the maximum bin content. The x-intercept of the fit is used as the offset t_0 for all wires in the card.

4.4.3 Cherenkovs

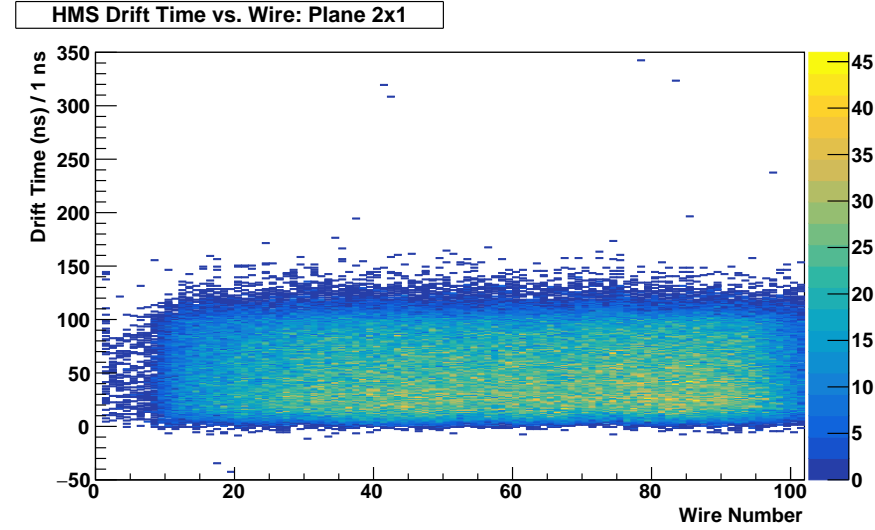
The calibration procedure for all threshold Cherenkov counters in both spectrometers involves extracting per-PMT conversion factors α_i to convert ADC pulse integrals to a number of photoelectrons. The number of photoelectrons collected by PMT i is $n_i = \alpha_i q_i$ where q_i is the pulse integral recorded for PMT i 's channel in the DAQ.

For the HMS Cherenkov, it is relatively straightforward to identify the single photoelectron peak in histograms of each PMT's pedestal-subtracted pulse integrals. This peak can be fit to a Gaussian with mean μ and standard deviation σ . The mean μ is the number of pC generated by one photoelectron. The conversion factor is then $\alpha_i = 1/\mu$.

Finding this peak for the SHMS Noble Gas Cherenkov has proved difficult, so a second method was developed. Events where an electron's Cherenkov radiation is focused on a single PMT are selected by cutting on calorimeter track-normalized energy approximately equal to 1, track position in the PMT's quadrant at the mirror plane, and low pulse integral in the other PMTs. The histograms of pulse integrals for these events are again fit with a Gaussian, from which the number of photoelectrons can be estimated to be $N_{PE} = (\mu/\sigma)^2$. The location of the single photoelectron peak in this histogram should then be $\mu/N_{PE} = \mu/(\mu/\sigma)^2 = \sigma^2/\mu$.



(a) Uncorrected drift times.



(b) Corrected drift times.

Figure 4-9: Two dimensional histograms of wire drift times for the HMS 2x1 plane, before (a) and after (b) t_0 correction.

The conversion factor is $\alpha_i = \mu/\sigma^2$.

4.4.4 Calorimeters

Energy deposited by particles in the calorimeters is reconstructed by converting ADC pulse integrals recorded for each PMT to the equivalent amount of energy converted into light collected by the PMTs. Accurate reconstruction requires accounting for both variations in PMT gain and attenuation as light propagates through the blocks. The PMTs were matched at the hardware level to have equal output amplitudes, so as to make the calorimeter pretrigger efficiencies as uniform

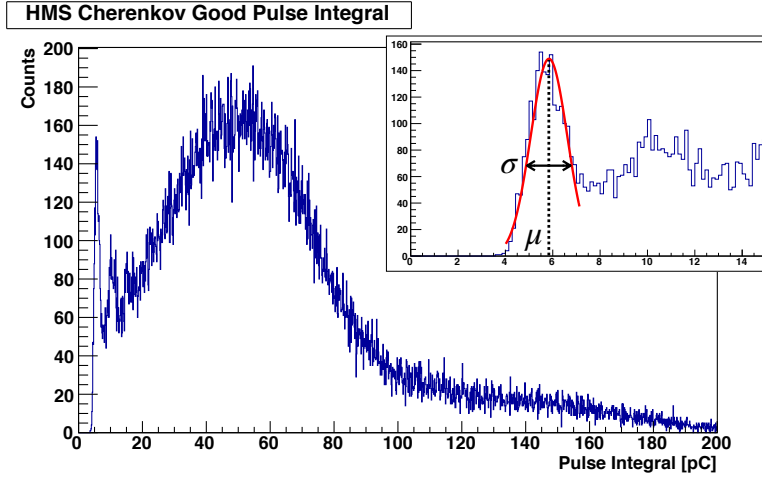


Figure 4-10: The distribution of pulse integrals in one PMT of the HMS Cherenkov. The single-photoelectron peak can be seen around 6 pC, the two-photoelectron peak can be faintly seen around 12 pC. The inset plot shows a Gaussian fit to the the single-photoelectron peak.

as possible over the spectrometers' acceptances. The energy e_i deposited in channel i is estimated by $e_i = \alpha_i q_i f(y)$ where α_i is the channel's calibration constant, q_i is the pulse integral recorded by the DAQ, and $f(y)$ is an attenuation correction.

hcana first converts pulse integrals to equivalent energy with a per-PMT conversion factor in the `CoarseProcess()` loop, and then in the `FineProcess()` loop applies an attenuation correction to each layer's reconstructed energy. This correction is a function of the track's horizontal y coordinate, so the blocks in the SHMS shower array, which run roughly parallel to the z coordinate, receive no attenuation correction.

The correction for blocks in HMS layers A and B, which have PMTs on both sides is:

$$f_{\pm}(y) = \frac{C \pm y}{C \pm \frac{y}{D}} \quad (4.16)$$

The correction for blocks in HMS layers C and D, which have PMTs on only one side, is:

$$f(y) = \frac{e^{\frac{y}{A}}}{1 + \frac{y^2}{B}} \quad (4.17)$$

The correction for blocks in the SHMS preshower layer is:

$$f(y) = \frac{1}{1 + \left(\frac{|y|}{A}\right)^B} \quad (4.18)$$

The parameters A , B , C , and D in the above expressions were determined based on measurements of light transmittance made with a spectrophotometer [149].

Determining the calibration coefficients is a constrained optimization problem [162, 163]. Let N be the number of PMTs in the calorimeter, $q = (q_1, \dots, q_N)^T$ their ADC pulse integrals, $\alpha = (\alpha_1, \dots, \alpha_N)^T$ their calibration constants, $e_0 = E(e)$ the mean of particle energies e obtained from the track reconstruction, and $q_0 = E(q)$ the mean ADC pulse integral. Then $e_R = \alpha^T q$ is the reconstructed particle energy. To determine α , the variance of the reconstructed energies with respect to the track energies should be minimized. That is, $E(e_R - e)^2$ should be minimized subject to the constraint $\alpha^T q_0 = e_0$.

The optimized calibration constants are

$$\alpha_C = \frac{e_0 - \alpha_U^T q_0}{q_0^T Q^{-1} q_0} Q^{-1} q_0 + \alpha_U \quad (4.19)$$

where $\alpha_U = Q^{-1} q_e$ are unconstrained calibration constants obtained from the correlation matrix $Q = E(qq^T)$ and $q_e = E(eq)$.

The distribution of track-normalized energy deposition for this experiment's data taken at $Q^2 = 8.0$ GeV with the liquid hydrogen target is shown in Fig 4-11. The red histogram represents events that did not fire the HMS Cherenkov. Pions should not fire the Cherenkov and should deposit very little of their energy in the calorimeter as a fraction of their momentum, which leads to the red distribution being skewed to the left in this figure. The blue histogram represents events that fired the HMS Cherenkov. Electrons should fire the Cherenkov and deposit all of their energy in the calorimeter, which leads to the peak around $E_{dep}/p = 1$. The blue events at low E_{dep}/p may be pions that "accidentally" fired the Cherenkov via knock-on electrons.

A two-dimensional histogram of HMS delta and track-normalized energy deposition is shown in Fig 4-12, illustrating the quality of the calibration. The blob around $E_{dep}/p = 1$ primarily contains electrons, and the blob at left contains pions.

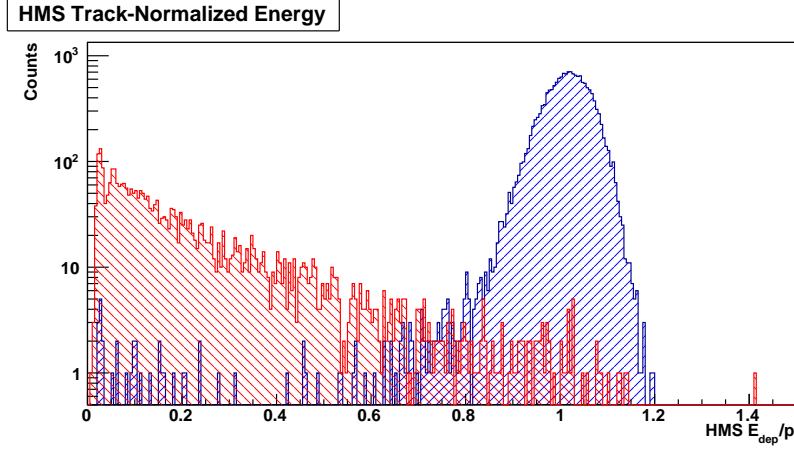


Figure 4-11: Track-normalized energy deposition for this experiment’s $Q^2 = 8.0 \text{ GeV}$ hydrogen data. The blue (red) histogram represents events that did (did not) fire the HMS Cherenkov.

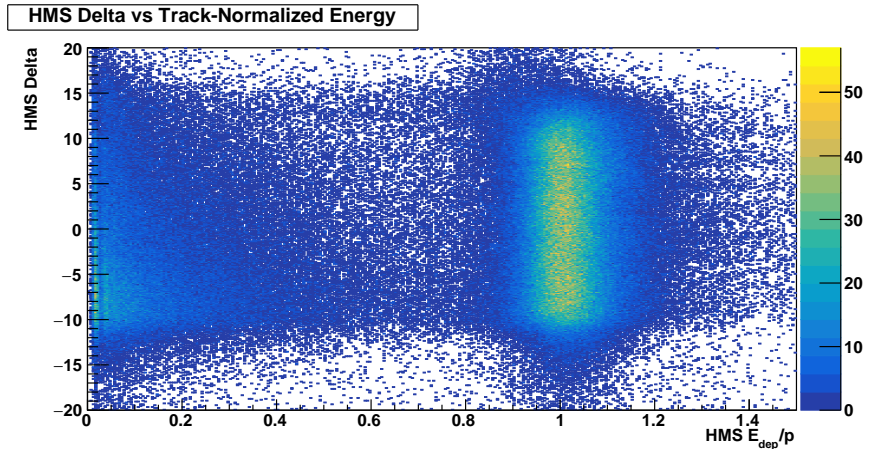


Figure 4-12: A two-dimensional histogram of HMS delta versus track-normalized energy deposition in the HMS calorimeter.

4.5 Tracking Algorithm

The hcana tracking algorithm fits a trajectory to the position of hits recorded by the drift chamber sense wires. As discussed in Section 4.4.2, the transverse distance between a sense wire and a particle passing by it can be precisely estimated by converting a reference-time-subtracted TDC time to a drift distance. Based on a single hit, it is impossible to tell whether the particle passed by on the left or right side of the wire. This ambiguity is resolved by looking at nearby pairs of planes that have identical wire orientation and spacing, but with cells displaced by half a cell.

In each drift chamber, hits that are close “enough” to each other are grouped

into *space points*. The hits in each space point are fit to create *stubs*, halves of a complete track. Stubs in both chambers are paired to form candidate tracks that are saved for further cleaning if the paired stubs are collinear “enough.”

In the event that multiple track candidates are found for an event, two options for selecting the best track (referred to as the *golden track*) exist. The simplest method selects the track with the lowest χ^2 value. The other method, referred to as *pruning*, involves a series of quality assurance tests that reject suboptimal tracks. If none of the tracks pass all the tests, this method defaults to selecting the track with the lowest χ^2 .

4.6 Optics

4.6.1 Target Variable Reconstruction Algorithm

Reconstructing the target variables $\delta_{tar} = \Delta p/p_0$, x'_{tar} , y_{tar} , and y'_{tar} is an iterative process that makes use of optimized optics matrices and polynomial combinations of x_{tar} and focal plane variables x_{fp} , x'_{fp} , y_{fp} , and y'_{fp} .

$$x'_{tar} = \sum_{ijklm} X'_{ijklm} x_{fp}^i x'_{fp}^j y_{fp}^k y'_{fp}^l x_{tar}^m \quad (4.20)$$

$$y_{tar} = \sum_{ijklm} Y_{ijklm} x_{fp}^i x'_{fp}^j y_{fp}^k y'_{fp}^l x_{tar}^m \quad (4.21)$$

$$y'_{tar} = \sum_{ijklm} Y'_{ijklm} x_{fp}^i x'_{fp}^j y_{fp}^k y'_{fp}^l x_{tar}^m \quad (4.22)$$

$$\delta_{tar} = \sum_{ijklm} D_{ijklm} x_{fp}^i x'_{fp}^j y_{fp}^k y'_{fp}^l x_{tar}^m \quad (4.23)$$

This iterative process entails the following steps:

1. Estimate x_{tar} from BPM and fast raster.
2. Use optics matrices to estimate y_{tar} , x_{tar} , y'_{tar} .
3. Correct these estimates for mispointing.
4. Use the calculations outlined below to obtain a new estimate of x_{tar} .

5. Return to Step 2 for some number of iterations, typically 6 or 7.

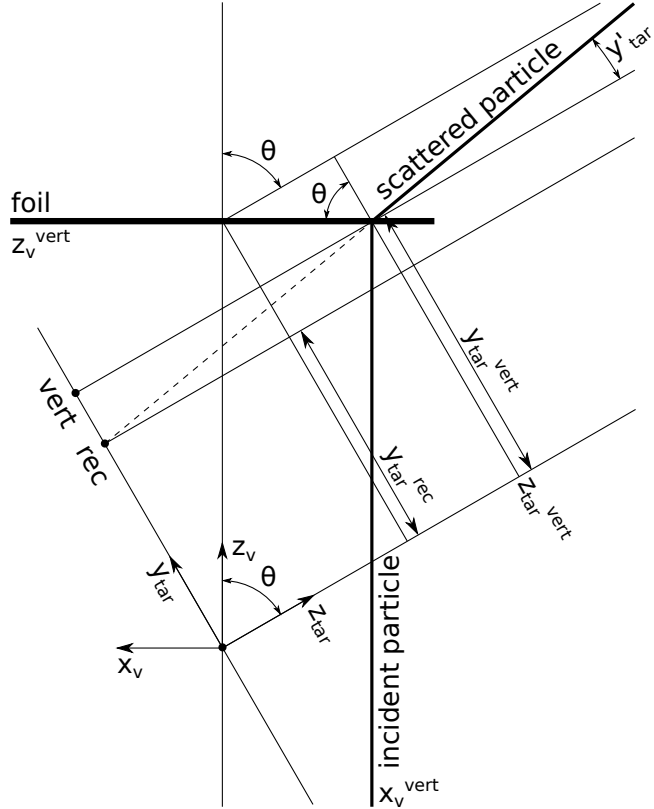


Figure 4-13: Coordinate systems and distances relevant to reconstruction. The coordinates with subscript v are in the target coordinate system, and the coordinates with subscript tar are reconstructed coordinates in the spectrometer coordinate system. The label “vert” marks the projection of the interaction vertex onto the spectrometer coordinate system. The label “rec” marks the reconstructed point calculated by the optics matrices using equation 4.20. Figure reproduced from Ref [164].

To derive the optics equations, consider Fig 4-13 and assume for now that the labeled distances are all known. Assume, as a first estimate, that the x_{tar}^{vert} coordinate in the spectrometer coordinate system is given by the BPM and fast raster measurements

$$x_{tar}^{vert} = -y^{beam} = -(y_0^{beam} - y_{fr}) \quad (4.24)$$

The reconstructed y_{tar}^{rec} coordinate in the spectrometer coordinate system is

$$y_{tar}^{rec} = y_{tar}^{vert} - \frac{dy}{dz} z_{tar}^{vert} = y_{tar}^{vert} - y'_{tar} z_{tar}^{vert} \quad (4.25)$$

The vertex coordinates in the spectrometer coordinate system can be obtained with a simple rotation from the target coordinate system

$$y_{tar}^{vert} = z_v^{vert} \sin \theta + x_v^{vert} \cos \theta \quad (4.26)$$

$$z_{tar}^{vert} = z_v^{vert} \cos \theta - x_v^{vert} \sin \theta \quad (4.27)$$

The x_v^{vert} and y_v^{vert} coordinates in the target coordinate system are given by the BPM and fast raster measurements²

$$x_v^{vert} = -x^{beam} = -(y_0^{beam} - x_{fr}) \quad (4.28)$$

$$y_v^{vert} = y^{beam} = y_0^{beam} - y_{fr} \quad (4.29)$$

Plugging equations 4.26 into equation 4.25 and solving for z_v^{vert} ,

$$y_{tar}^{rec} = (z_v^{vert} \sin \theta + x_v^{vert} \cos \theta) - y'_{tar}(z_v^{vert} \cos \theta - y_v^{vert} \sin \theta) \quad (4.30)$$

$$= (\sin \theta - y'_{tar} \cos \theta)z_v^{vert} + (\cos \theta + y'_{tar} \sin \theta)x_v^{vert} \quad (4.31)$$

$$= (\sin \theta - y'_{tar} \cos \theta)z_v^{vert} - (\cos \theta + y'_{tar} \sin \theta)x^{beam} \quad (4.32)$$

$$z_v^{vert} = \frac{y_{tar}^{rec} + x^{beam}(\cos \theta + y'_{tar} \sin \theta)}{\sin \theta - y'_{tar} \cos \theta}. \quad (4.33)$$

The above then provides a new estimate of x_{tar}^{rec}

$$x_{tar}^{rec} = x_{tar}^{vert} - x'_{tar}z_{tar}^{vert} - x^{off} \quad (4.34)$$

4.6.2 Reconstruction Matrix Optimization

The general process for optimizing optics matrix elements is outlined in Ref [164]. The optimization problem is an underdetermined residual sum of squares minimization problem, solved using singular value decomposition (SVD). The goal is to minimize the difference between “true” and reconstructed values of x'_{tar} , y_{tar} , and y'_{tar} . The data used for this process are taken using a sieve slit collimator and an optics target with three thin carbon foils spaced along the z axis.

²Recall that these use a right-handed coordinate system

The “true” values, denoted below with a hat, are determined in a two step process. First, each event is associated with a particular foil. The three peaks in a histogram of z_v^{vert} are fit with Gaussians, and events within $1 - 3\sigma$ of each peak are assigned that peak’s mean value z^{foil} for their true \hat{z}_v^{vert} position.

Then, a 2D histogram of y^{sieve} versus x^{sieve} positions is filled by projecting the events to the sieve position z^{sieve} . Gaussians are fit to the x and y projections of this histogram to estimate the locations of the rows and columns in the sieve pattern. Individual sieve holes containing at least 50 events within $1 - 2\sigma$ of their estimated x and y position have their projections fit again. The mean of these fits, x^{hole} and y^{hole} , are assigned as the “true” values for events whose projected positions at the sieve lie within these holes. An example histogram illustrating this process for SHMS run 1808 is shown in Fig 4-14.

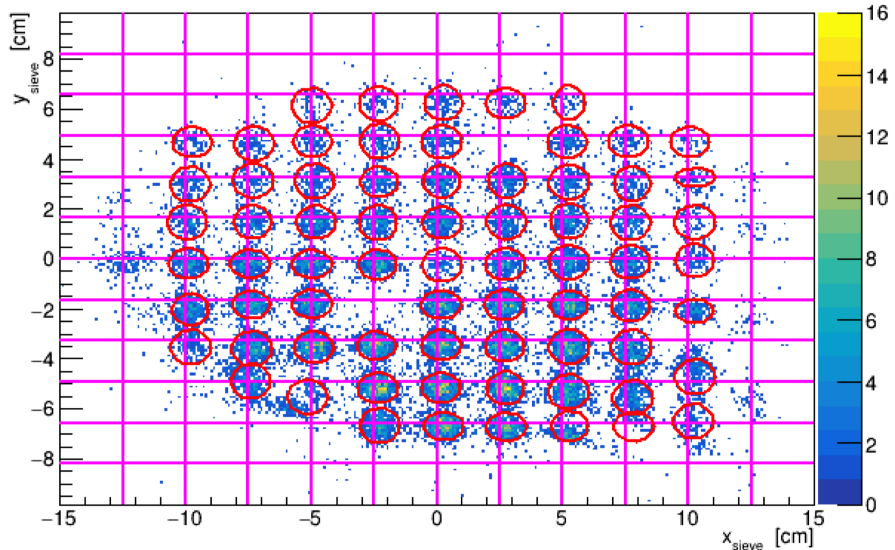


Figure 4-14: A 2D histogram of SHMS track positions projected to the sieve. Data were taken with three-foil optics target. Circles in red represent the Gaussians fits to holes with sufficient statistics. The intersections of the magenta grid represents the true locations of the sieve holes.

These values, combined with information from the BCMs and fast raster, are used to calculate the “true” values below.

$$\hat{x}_{tar}^{vert} = -y^{beam} \quad (4.35)$$

$$\hat{y}_{tar}^{vert} = z^{foil} \sin \theta + x^{beam} \cos \theta \quad (4.36)$$

$$\hat{z}_{tar}^{vert} = z^{foil} \cos \theta - x^{beam} \sin \theta \quad (4.37)$$

$$\hat{x}'_{tar}^{vert} = \frac{x^{hole} - \hat{x}_{tar}^{vert}}{z^{sieve} - \hat{z}_{tar}^{vert}} \quad (4.38)$$

$$\hat{y}'_{tar}^{vert} = \frac{y^{hole} - \hat{y}_{tar}^{vert}}{z^{sieve} - \hat{z}_{tar}^{vert}} \quad (4.39)$$

Consider a particular event e . Let o_e be one of the target variables x' , y , or y' for this event, \hat{o}_e the “true” value of the variable, and o_e^{rec} the estimate reconstructed from the corresponding optics matrix O_{ijklm} . For a matrix O_{ijklm} , the residual sum of squares RSS is

$$RSS = \sum_e (\hat{o}_e - o_e^{rec})^2 \quad (4.40)$$

$$= \sum_e \left(\hat{o}_e - \sum_{ijklm} O_{ijklm} x_{fp}^i x_{fp}'^j y_{fp}^k y_{fp}'^l x_{tar}^m \right)^2 \quad (4.41)$$

Minimizing RSS , the derivative with respect to matrix elements $O_{\bar{i}\bar{j}\bar{k}\bar{l}\bar{m}}$ for all combinations of particular indices $\bar{i}, \bar{j}, \bar{k}, \bar{l}$, and \bar{m} should be zero.

$$\frac{dRSS}{dO_{\bar{i}\bar{j}\bar{k}\bar{l}\bar{m}}} = -2 \sum_e \left(\hat{o}_e - \sum_{ijklm} O_{ijklm} x_{fp}^i x_{fp}'^j y_{fp}^k y_{fp}'^l x_{tar}^m \right) x_{fp}^{\bar{i}} x_{fp}'^{\bar{j}} y_{fp}^{\bar{k}} y_{fp}'^{\bar{l}} x_{tar}^{\bar{m}} = 0 \quad (4.42)$$

For compactness of notation, let

$$n = (i, j, k, l, m) \quad (4.43)$$

$$\lambda_n = x_{fp}^i x_{fp}'^j y_{fp}^k y_{fp}'^l x_{tar}^m \quad (4.44)$$

$$\Lambda^e = \sum_n O_n \lambda_n^e \quad (4.45)$$

The collinearity of x_{tar} and x'_{tar} makes optimization of matrix elements with non-zero powers of x_{tar} difficult. Previous efforts to fit these terms from data have produced worse results, so these elements are set to zero during the optimiza-

tion steps. For reconstruction, they are taken from a COSY [165] model of the spectrometer magnets.

With that in mind, note that Λ^e can be separated into parts that are dependent on and independent of x_{tar} , $\Lambda^e = \Lambda_{ind}^e + \Lambda_{dep}^e$ by limiting the sums to include either only indices $n' \in \text{ind}$ with zero powers of x_{tar} or only indices $n'' \in \text{dep}$ with nonzero powers of x_{tar} . Rewriting the condition for minimizing RSS with these definitions,

$$\begin{aligned} 0 &= \sum_e (\hat{o}_e - \Lambda^e) \lambda_{\bar{n}} \\ &= \sum_e (\hat{o}_e - \Lambda_{dep}^e - \Lambda_{ind}^e) \lambda_{\bar{n}} \end{aligned} \quad (4.46)$$

$$\begin{aligned} \sum_e (\hat{o}_e - \Lambda_{dep}^e) \lambda_{\bar{n}} &= \sum_e \Lambda_{ind}^e \lambda_{\bar{n}} \\ &= \sum_e \sum_{n \in \text{ind}} O_n \lambda_n \lambda_{\bar{n}} \\ &= \sum_{n \in \text{ind}} O_n \sum_e \lambda_n \lambda_{\bar{n}} \end{aligned} \quad (4.47)$$

There is one equation of this form for each x_{tar} -independent term indexed by \bar{n} . Together, they can be written in matrix notation

$$\vec{b} = A \vec{x} \quad (4.48)$$

where the matrix and vector elements are

$$A_{ij} = \sum_e \lambda_i \lambda_j \quad (4.49)$$

$$x_i = O_i \quad (4.50)$$

$$b_i = \sum_e (\hat{o}_e - \Lambda_{dep}^e) \lambda_i \quad (4.51)$$

and i and j are both abbreviations of the full set of indices as defined in equation 4.43. This is now a well-posed problem that can be solved using SVD. Recall that the terms included in this optimization step are only the x_{tar} -independent

terms. After SVD, the x_{tar} -dependent terms from COSY are reintroduced to form the full matrix elements used in reconstruction.

Appendix B contains figures comparing track information and physics quantities reconstructed from data and from SIMC.

4.7 Efficiency

In general, the efficiency of a given detector system is estimated by using information from other systems to select a set of “clean” events that can reasonably be expected to produce a signal in that particular system. Let N^{should} be the number of events selected by a cut C^{should} that should show a signal in detector D , and N^{did} be the subset of those events that pass a cut $C^{did} = C^{should} \wedge C^D$, where C^D is an additional cut on information from the detector D under consideration and \wedge represents the logical operation *and*. Then the efficiency of D is $\epsilon^D = N^{did}/N^{should}$.

4.7.1 HMS Calorimeter

A set of electrons that should have normalized track energy deposition approximately equal to one are selected using the cuts in Table 4.1.

Table 4.1: List of cuts used to estimate HMS Calorimeter efficiency.

	Variables	Cut
C^{should}	HMS Cherenkov NPE	H.cer.npeSum>0
	δ_{HMS}	-10.0 < H.gtr.dp && H.gtr.dp < 10.0
	β_{HMS}	0.8 < H.gtr.beta && H.gtr.beta < 1.2
	Good hodoscope time	H.hod.goodstarttime==1
$C^{HC_{Cal}}$	HMS Calorimeter Energy	0.8 < H.cal.etottracknorm && H.cal.etottracknorm < 1.15

Events are divided into δ bins of width 5 and efficiencies $\epsilon_i = N_i^{did}/N_i^{should}$ are calculated for each bin. A 95% confidence interval for each bin’s estimated efficiency is obtained using the Clopper-Pearson method. A weight $w_i = 1/\sigma_i^2$ for each bin is assigned, where σ_i is the larger of differences between ϵ_i and the upper

and lower CI bounds. Then the weighted efficiency is

$$\epsilon = \frac{\sum_i w_i \epsilon_i}{\sum_j w_j} \quad (4.52)$$

with uncertainty

$$\sigma_\epsilon = \frac{1}{\sqrt{\sum_i w_i}} \quad (4.53)$$

4.7.2 HMS Cherenkov

A set of electrons that should fire the Cherenkov are selected using the cuts in Table 4.2. A weighted efficiency is calculated as discussed in Section 4.7.1

Table 4.2: List of cuts used to estimate HMS Cherenkov efficiency.

Variables	Cut
HMS Calorimeter Energy	$0.8 < \text{H.cal.etcottracknorm} \&& \text{H.cal.etcottracknorm} < 1.15$
C^{should}	δ_{HMS}
	$-10.0 < \text{H.gtr.dp} \&& \text{H.gtr.dp} < 10.0$
	β_{HMS}
	$0.8 < \text{H.gtr.beta} \&& \text{H.gtr.beta} < 1.2$
	Good hodoscope time
	$\text{H.hod.goodstarttime} == 1$
C^{HCer}	HMS Cherenkov NPE
	$\text{H.cer.npeSum} > 0$

After we had taken data, it was discovered that the mirrors in the HMS Cherenkov had broken at some point before we started taking data. Fig 4-16 shows the distributions of tracks projected to the HMS mirrors for events that should and did fire the Cherenkov. The broken regions visible in Fig 4-15 correspond to the regions in Fig 4-17 with decreased efficiency.

Data shown in these figures are from defocused HMS run 1327. Because the magnets were defocused, reconstruction of the particles' momenta was not possible, so one cannot use the track-normalized energy deposition to select electrons that should fire the Cherenkov. For this reason, the energy deposition divided by the spectrometer's central momentum (a less precise version of track-normalized energy deposition) was used. A defocused run has the advantage of illuminating the spectrometer's entire acceptance, allowing a full characterization of which regions of the acceptance are negatively affected by the broken mirrors.

Fig 4-18 and Fig 4-19 show the distribution of track positions at the HMS Cherenkov mirrors for all events that should fire the Cherenkov in our production

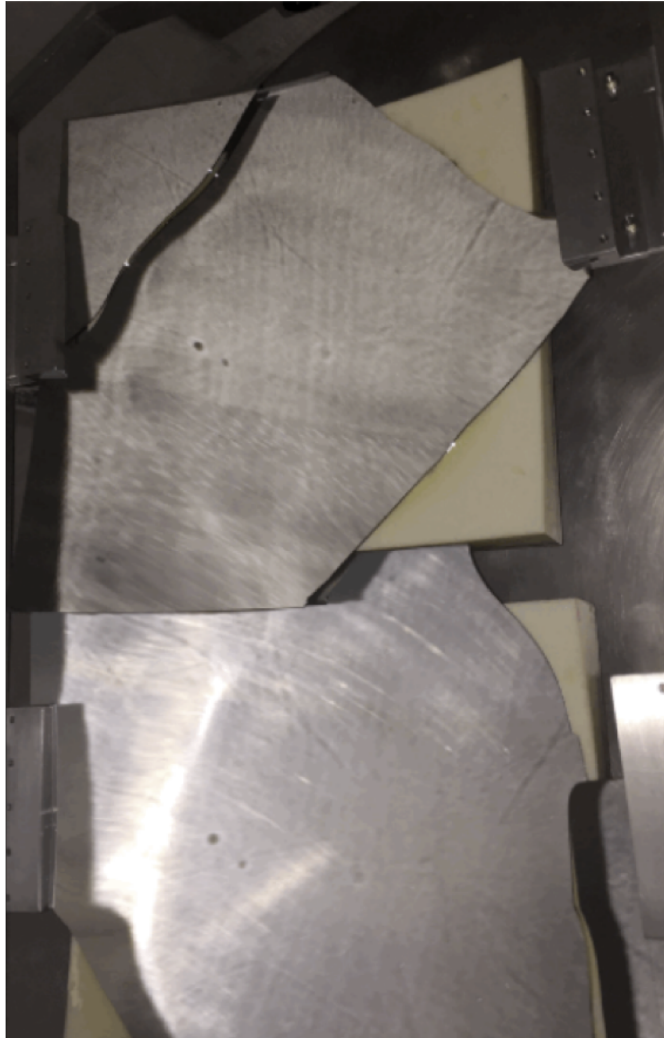


Figure 4-15: A picture of the broken HMS Cherenkov mirrors taken after the detector was removed from the hut for repair. The mirrors' Rohacell supports are visible where portions of the mirrors have broken off.

$Q^2 = 8.0 \text{ GeV}^2$ data. This sample is selected using the same C^{should} cut defined in Table 4.2 used to estimate the detector's efficiency. Because the vast majority of our events lie in the central region of the acceptance that is unaffected by the broken mirrors, it is sufficient to include this effect as part of the overall efficiency estimate for this detector.

4.7.3 SHMS Noble Gas Cherenkov

The SHMS Noble Gas Cherenkov was used as a pion veto. The SHMS central momenta used in this experiment range from 5.122 to 8.505 GeV. The pion threshold in this detector is 4.65 GeV while the proton threshold is 30 GeV, well above the range of the SHMS magnets. A set of protons that should not fire

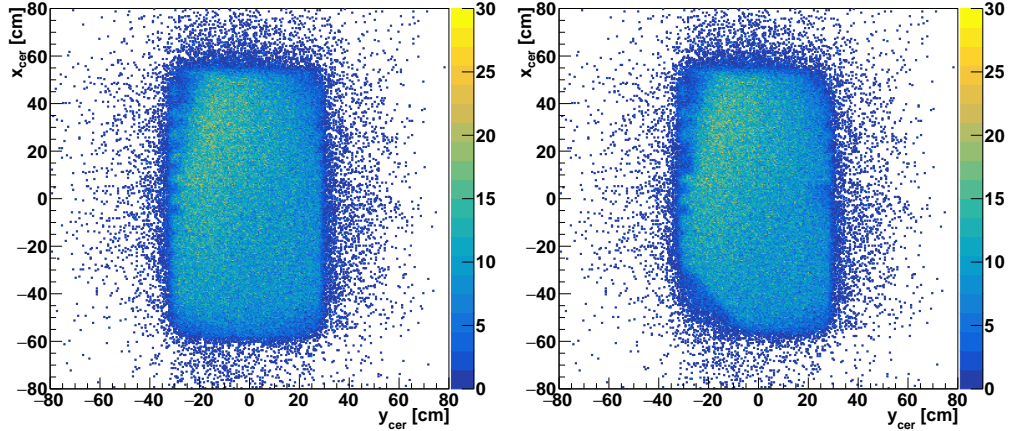


Figure 4-16: The distribution of tracks projected to the HMS Cherenkov mirrors for events that should (left) and did (right) fire the Cherenkov. Data shown are from defocused HMS run 1327. Events that should fire were selected by requiring the energy deposition in the HMS calorimeter normalized to the HMS central momentum to be between 0.9 and 1.1. No cuts were placed on β or δ .

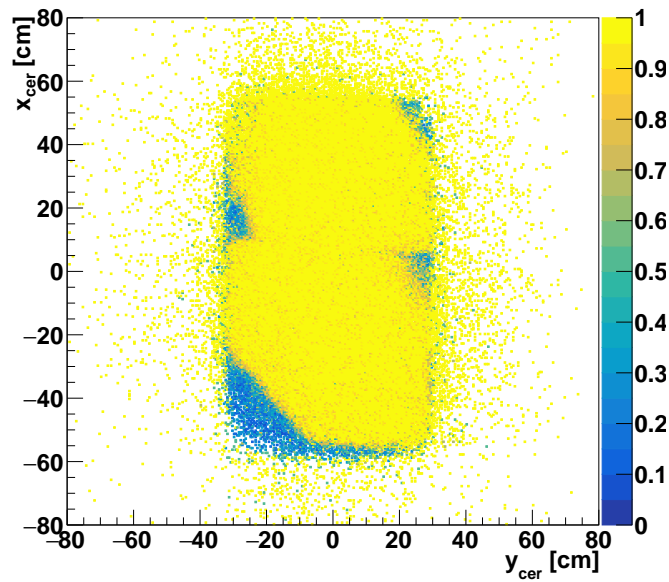


Figure 4-17: The efficiency of the HMS Cherenkov, binned by track position projected to the Cherenkov mirrors. The regions most affected by the broken mirrors are at large negative x and y , large positive x and y , and on the edges near the center of the dispersive direction x .

the Cherenkov are selected using the cuts in Table 4.3. A weighted efficiency is calculated as discussed in Section 4.7.1

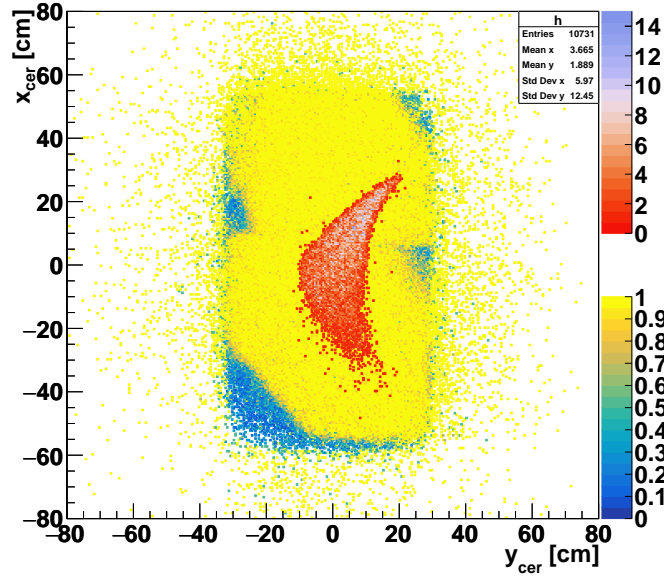


Figure 4-18: The distribution of tracks projected to the HMS Cherenkov mirrors for our $Q^2 = 8.0 \text{ GeV}^2 H(e, e'p)$ data is shown in red and lavender on top of the efficiency as a function of position in blue and yellow.

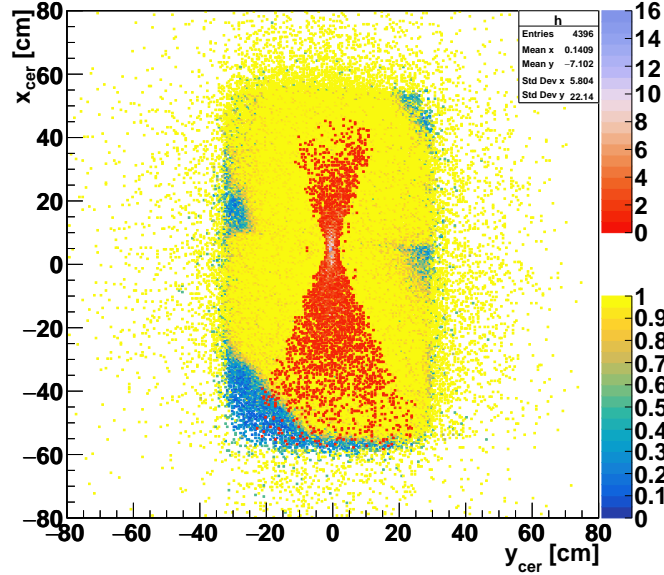


Figure 4-19: The distribution of tracks projected to the HMS Cherenkov mirrors for our $Q^2 = 8.0 \text{ GeV}^2 {}^{12}\text{C}(e, e'p)$ data is shown in red and lavender on top of the efficiency as a function of position in blue and yellow.

4.7.4 Tracking

The tracking efficiency ϵ_{track} is the probability of hcana reconstructing track based on signals with drift chamber wires when a particle passes through the

Table 4.3: List of cuts used to estimate SHMS Noble Gas Cherenkov efficiency.

	Variables	Cut
C^{should}	δ_{SHMS}	$-10.0 < P.gtr.dp \&\& P.gtr.dp < 10.0$
	β_{SHMS}	$P.gtr.\beta < 1.4$
	Good hodoscope time	$P.hod.goodstarttime==1$
C^{PCer}	SHMS Cherenkov NPE	$P.ngcer.npeSum<0.1$

spectrometer. The set of cuts used to select such events are listed in Tables 4.4 and 4.5. Events that should almost certainly have a good track candidate have a reasonable value of β estimated from time of flight and hits in hodoscope paddles in the “fiducial region” near the center of the acceptance. They will also not have “too many” drift chamber hits; particles in such events may have grazed the edge of dipole window, creating an electromagnetic shower, preventing hcana from reconstructing the track accurately.

The number of events with multiple candidate tracks in the HMS was small, so the efficiency can be estimated by taken N^{did} to be the number of events that pass the cut $C^{should} \wedge C^{HTrack}$. To correct for the larger amount of multitrack events in the SHMS, the *did* condition was adjusted to ensure that the golden track is located in a central region of the acceptance and resulted in a reasonable focal plane time. Multitrack events were also not counted if they have “too many” hits on negative side ADCs. With this modification, the numerator in the SHMS tracking efficiency is the number of events that pass the cut $C^{should} \wedge (C^{PMultipleTrack} \vee C^{PSingleTrack})$, where \vee represents the logical operation *or*.

4.7.5 Luminosity Scan

At high beam currents and energies, energy deposition in liquid cryotargets cause localized boiling. This causes local drops in density which decrease measured charge-normalized yields from what would be expected for a liquid target with constant density. A beam current-dependent *target boiling correction* can be extracted with a luminosity scan, which consists of measuring charge-normalized yields over a range of beam currents with the same spectrometer settings. A linear fit of the drop in yield with increased current provides a correction that can be used with production data at any beam current.

Table 4.4: List of cuts used to estimate HMS tracking efficiency.

Variables	Cut
Fiducial cut	H.hod.goodscinhit==1
$\beta_{notrack}$	$0.5 < \text{H.hod.betanotrack} \&\& \text{H.hod.betanotrack} < 1.4$
C^{should}	$(\text{H.dc.1x1.nhit} + \text{H.dc.1u2.nhit} + \text{H.dc.1u1.nhit} + \text{H.dc.1v1.nhit} + \text{H.dc.1x2.nhit} + \text{H.dc.1v2.nhit}) < 35$
Few hits in DC 2	$(\text{H.dc.2x1.nhit} + \text{H.dc.2u2.nhit} + \text{H.dc.2u1.nhit} + \text{H.dc.2v1.nhit} + \text{H.dc.2x2.nhit} + \text{H.dc.2v2.nhit}) < 35$
SHMS Cherenkov NPE	P.ngcer.npeSum<0.1
HMS Cherenkov NPE	H.cer.npeSum>0
$C^{HTtrack}$	At least one track found H.dc.ntrack>0

Table 4.6 lists the HMS and SHMS singles runs used to study target boiling. These runs were taken immediately before and after this experiment. Both the HMS and SHMS were set at scattering angles of 25° and central momenta of 4.4 GeV to collect electrons scattered from hydrogen and carbon targets.

The average of the normalized slopes and intercepts of the fits to SHMS and HMS hydrogen runs was used as a correction to the production hydrogen yields of the form

$$f_{boil}(I_{mean}) = 1 - 0.000385I_{mean} \quad (4.54)$$

where I_{mean} is the mean beam current during the run whose yield is to be corrected.

The slopes of fits to carbon yields were consistent with zero, as should be the case for a solid target; if the yields are appropriately corrected for rate-dependent effects (i.e. deadtime and detector efficiencies) the yield should be independent of current. The variation in carbon yields from the luminosity scan was used as an estimate of the systematic uncertainty due to deadtime and detector efficiencies.

4.7.6 Trigger

Let P_i be the efficiency of the i th hodoscope plane in one spectrometer. This efficiency is estimated by taking tracks that point to the center of the plane's paddles and counting how many times the paddle actually fires. Because the triggers used in this experiment were formed by the coincidence of three of four hodoscope planes,

Table 4.5: List of cuts used to estimate SHMS tracking efficiency.

Variables	Cut
Fiducial cut	P.hod.goodscinhit==1
Good hodoscope time	P.hod.goodstarttime==1
$\beta_{notrack}$	P.hod.betanotrack < 1.2
C^{should}	Few hits in DC 1 (P.dc.1x1.nhit + P.dc.1u2.nhit + P.dc.1u1.nhit + P.dc.1v1.nhit + P.dc.1x2.nhit + P.dc.1v2.nhit) < 25
	Few hits in DC 2 (P.dc.2x1.nhit + P.dc.2u2.nhit + P.dc.2u1.nhit + P.dc.2v1.nhit + P.dc.2x2.nhit + P.dc.2v2.nhit) < 25
$C^{PSingleTrack}$	SHMS Cherenkov NPE P.ngcer.npeSum<0.1
	HMS Cherenkov NPE H.cer.npeSum>0
$C^{PMultipleTrack}$	One track found P.dc.ntrack==1
	More than one track found P.dc.ntrack > 1
	Few hits on negative side ADCs P.hod.1x.totNumGoodNegAdcHits<5 && P.hod.1y.totNumGoodNegAdcHits<5 && P.hod.2x.totNumGoodNegAdcHits<5 && P.hod.2y.totNumGoodNegAdcHits<5
	Good focal plane time -10 < P.hod.1x.fptime && P.hod.1x.fptime < 50 && -10 < P.hod.1y.fptime && P.hod.1y.fptime < 50 && -10 < P.hod.2x.fptime && P.hod.2x.fptime < 50 && -10 < P.hod.2y.fptime && P.hod.2y.fptime < 50
	δ -15 < P.gtr.dp && P.gtr.dp < 15
y_{tar}	-5 < P.gtr.y && P.gtr.y < 5
x'_{tar}	-0.2 < P.gtr.th && P.gtr.th < 0.2
y'_{tar}	-0.2 < P.gtr.ph && P.gtr.ph < 0.2

the trigger efficiency is given by the product of the spectrometers' individual 3/4 efficiencies,

$$\epsilon_{hodo} = P_{3/4} = P_1 P_2 P_3 P_4 + P_1 P_2 P_3 (1 - P_4) + P_1 P_2 (1 - P_3) P_4 \quad (4.55)$$

$$+ P_1 (1 - P_2) P_3 P_4 + (1 - P_1) P_2 P_3 P_4 \quad (4.56)$$

This calculation is carried out by the THcHodoscope::TrackEff() method in hcana and saved in the text report output saved when a run is replayed.

Table 4.6: List of runs used to study target boiling and the corresponding nominal beam currents.

Target	Current [μA]	SHMS run	HMS run
LH_2	10	3210	2078, 2080
	20	3211	2081
	35	3212, 3213	2082, 2083
	45	3214	2084
	55	3215	2085
	70	3207	2076
	80	3206	2075
Aluminum Dummy	40	3226	2096
$1.5\% \ ^{12}C$	60	3223	2093
	50	3224	2094
	35	3225	2095

4.7.7 Livetime

When a trigger is accepted, the DAQ system is unable to accept additional triggers for a time determined by the gate widths of front end electronics and the time it takes for CODA to write the event to disk. The time during which the DAQ is unable to accept another event is referred to as deadtime. The inverse concept, livetime, refers to the total time that the DAQ is *not* occupied by processing incoming triggers. The total livetime TLT is a correction applied to the charge normalized yield to account for events that are missed because of this phenomenon.

The EDTM (see Section 3.6.1) pulser allows an estimate of the total livetime in a given run. It sends regular pulses at a low frequency (3 Hz in our experiment) at the trigger logic level in the counting house. By comparing the number of triggers that are accepted by the DAQ to the number of pulses that are counted by the EDTM scaler, we can estimate the total livetime as

$$TLT = \frac{N_{EDTM,accepted}}{N_{EDTM,scaler}} \quad (4.57)$$

where $N_{EDTM,accepted}$ is the number of events with a non-zero hit in the EDTM TDC spectrum and $N_{EDTM,scaler}$ is the total number of EDTM triggers counted by the EDTM scaler.

Because livetime should be dependent on trigger rate and the trigger rates vary between our kinematic settings, we calculate a per-run livetime to correct

each run's yield. Moreover, the EDTM system was not functional when we took our first set of data for Q^2 of 8 GeV 2 . To estimate the livetime for these data, we performed a linear fit of the other kinematics' TLT dependence on SHMS 3/4 trigger rate and used this fit to estimate the livetime for the $Q^2=8\text{ GeV}^2$ runs.

The computer livetime can be estimated as

$$CLT = \frac{N_{phys,accepted} - N_{EDTM,accepted}}{N_{phys,scaler} - N_{EDTM,scaler}} \quad (4.58)$$

The computer livetime for our data is negligible because CODA was configured to only take coincidence events, whose rates were all quite low (below 6 Hz) for all our kinematics.

4.8 Proton Absorption

Because protons are strongly interacting particles, they may undergo a nuclear reaction as they pass through the SHMS before forming an SHMS 3/4 trigger. The corresponding electron in the HMS will have formed an HMS 3/4 trigger, but the “missing” SHMS 3/4 will lead to a missing coincidence trigger. As result, the total coincidence yield will be underestimated by some amount. The proton absorption A is the percentage of protons that, in this manner, fail to form a coincidence trigger.

A theoretical estimate of the absorption can be obtained by considering the proton's mean free path in the materials along its path through the SHMS. Suppose a material is made up of components with atomic weights A_i , mass density ρ_i , and total cross section $\sigma_{tot,i}$. The nuclear collision length is $\lambda_T = \sum_i A_i / (N_A \rho_i \sigma_{tot,i})$. The nuclear interaction length λ_I is similarly defined, subtracting the elastic and quasielastic cross sections from $\sigma_{tot,i}$. Because the elastic cross section is peaked in the forward direction, and will thus remove few protons from the spectrometer's acceptance, we use the average $\bar{\lambda}$ of λ_T and λ_I as our estimate of the mean free path. Our theoretical prediction of the absorption is $A_{pred} = 1 - e^{-\sum_i X_i / \bar{\lambda}_i}$ where X_i is the thickness of each material in the proton's path. Table 4.7 lists the properties of relevant materials in the SHMS. Nuclear collision and interaction lengths are taken from Ref [166]. Based on this table, we estimate the absorption

to be $A_{pred} = 8.56\%$.

Table 4.7: Summary of materials in the SHMS that contribute to proton absorption.

System	Component	Material	Thickness (cm)	Density (g cm ⁻³)	X (g cm ⁻²)	λ_T^a (g cm ⁻²)	λ_I^a (g cm ⁻²)	$\bar{\lambda}$ (g cm ⁻²)	$X/\bar{\lambda}$ (10 ⁻³)
Target and Magnets	LH2	LH2	5.00	0.07	0.35	42.80	52.00	47.40	7.38
	Scattering chamber	Al	0.01	2.7	0.03429	69.70	107.20	88.45	0.39
	Air	Air	30.00	0.001	0.03675	61.30	90.10	75.70	0.49
	HB entrance	Al	0.03	2.7	0.06858	69.70	107.20	88.45	0.78
	Dipole exit	Al	0.05	2.7	0.13716	69.70	107.20	88.45	1.55
Noble Gas Cherenkov	Entrance window	Tedlar	0.01	1.3	0.0066	61.70	90.30	76.00	0.087
	Gas	CO ₂ 1.0 atm	200.00	0.002	0.396	60.70	88.90	74.80	5.29
	Mirror	SiO ₂	0.30	2.2	0.66	65.20	97.80	81.50	8.10
	Mirror support	Rohacell	1.80	0.11	0.198	-	-	70.00	2.83
	Exit window	Tedlar	0.01	1.3	0.0066	61.70	90.30	76.00	0.087
Drift Chambers	Entrance window	Mylar	0.00254	1.39	0.00353	58.90	84.90	71.90	0.049
	Gas	50/50 Ethane/Ar	3.81	0.002	0.00587	68.60	101.00	84.80	0.069
	Field wire ^b	W	0.00483	2.7	0.01303	69.80	108.00	88.90	0.147
	Sense wire ^b	Be/Cu	0.00030	19.3	0.00582	110.00	185.00	147.50	0.040
	Kapton in wire and cathode planes	Kapton	0.18	1.42	0.25248	59.20	85.50	72.35	3.49
Hodoscope	Exit window	Mylar	0.00254	1.39	0.00353	58.90	84.90	71.90	0.049
	Scintillator plane (x2.25)	PVT	1.13	1.032	1.16100	57.30	81.30	69.30	16.8
Heavy Gas Cherenkov	Entrance window	Al	0.10	2.7	0.27	69.70	107.20	88.45	3.05
	Gas	CO ₂ 1.0 atm	104.44	0.002	0.20679	60.70	88.90	74.80	2.76
	Mirror	SiO ₂	0.30	2.2	0.66	65.20	97.80	81.50	8.10
	Exit window	Al	0.10	2.7	0.27	69.70	107.20	88.45	3.05
Aerogel Cherenkov	Entrance window	Al	0.13	2.699	0.35086	69.70	107.20	88.45	3.97
	Aerogel	Aerogel	9.00	0.143	1.28571	65.00	97.30	81.15	15.8
	Air	Air	17.10	0.001	0.02103	61.30	90.10	75.70	0.28
	Exit window	Al	0.16	2.7	0.43200	69.70	107.20	88.45	4.88
Total									89.5

^aNuclear interaction and collision lengths taken from PDG [166].

^bThe thicknesses of the wires are “effective” thicknesses, determined by the wire radii and cell spacings described in subsection 3.5.2. This effective thickness of a single wire plane is the average thickness of a wire with radius r repeated in a lattice of cell width w, seen by a particle whose position in the XY plane is random. This effective thickness is $\pi r^2/w$.

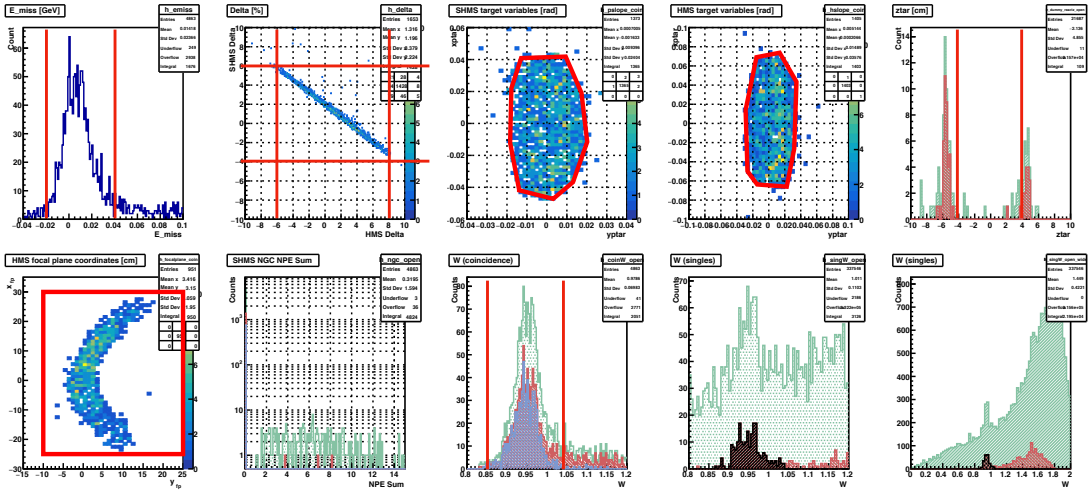


Figure 4-20: Histograms of the quantities used to guide the selection of cuts for selecting $H(e, e'p)$ events to estimate proton absorption. The data shown are from this experiment’s $Q^2 = 11.5 \text{ GeV}^2$ data taken with the hydrogen target. The two right histograms on the bottom row are singles data, and the others are coincidence data. The red lines and contours indicate the cuts used. The green histograms represent the data with no cuts applied. The red histograms represent the data with cuts applied on information obtained from the HMS only. The blue histogram represents the data with both HMS and SHMS cuts. The black histogram represents the final cut on W for singles data.

Using the charge-normalized yields, Y_{coin} and Y_{sing} , from coincidence and HMS singles $H(e, e'p)$ runs, we can measure the proton absorption $A_{\text{exp}} = 1 - Y_{\text{coin}}/Y_{\text{sing}}$. With a tight cut on spectrometer acceptance and invariant mass W and correcting for detector efficiencies and deadtime, Y_{sing} should be an accurate count of all electrons that participated in elastic scattering. In contrast, Y_{coin} , even with the same cuts and corrections, will have underestimated the “true” yield; some portion of the electrons detected in the HMS will have corresponding protons that did not form a 3/4 trigger in the SHMS because they were absorbed. Using our $Q^2 = 11.5 \text{ GeV}^2$ runs and the cuts listed in Table 4.8, we estimate a proton absorption of $A_{\text{exp}} = 8.83 \pm 0.69\%$. The uncertainty quoted here is only statistical—an estimate of the systematic uncertainty and a final revised absorption value were obtained from a cut study described below.

These cuts were selected by an iterative process of plotting a sequence of histograms, each of which is plotted with a cut determined by the preceding his-

Table 4.8: List of cuts used in proton absorption estimate.

Variables	Cut
HMS PID	$H.\text{cer.npeSum} > 1 \ \&\& 0.90 < H.\text{cal.etottracknorm} \ \&\& H.\text{cal.etottracknorm} < 1.10$
E_{miss}	$-0.02 < P.\text{kin.secondary.emiss} \ \&\& P.\text{kin.secondary.emiss} < 0.04$
δ_{HMS}	$-6.0 < H.\text{gtr.dp} \ \&\& H.\text{gtr.dp} < 8.0$
x'_{tar}, y'_{tar}	Graphical cut on HMS xptar and yptar shown in Fig 4-20
z_{tar}	$\text{abs}(H.\text{react.z}) < 3$
y_{tar}	$\text{abs}(H.\text{gtr.y}) < 2$
x_{fp}	$-25 < H.\text{dc.x}[0] \ \&\& H.\text{dc.x}[0] < 30$
y_{fp}	$-10 < H.\text{dc.y}[0] \ \&\& H.\text{dc.y}[0] < 25$
W	$0.85 < H.\text{kin.W} \ \&\& H.\text{kin.W} < 1.04$

tograms in the sequence. The relevant histograms are shown in Fig 4-20. The process can be summarized as follows:

1. Plot E_{miss} for $H(e, e'p)$ data using HMS Cherenkov and calorimeter cuts to select electrons. Select a cut around the peak of this distribution.
2. Plot SHMS and HMS delta for $H(e, e'p)$ data using that E_{miss} cut and the HMS PID cuts. Select a cut on both.
3. Plot HMS and SHMS x'_{tar} vs y'_{tar} for $H(e, e'p)$ data using all prior cuts. Place a tight graphical cut on this distribution.
4. Plot z_{tar} and y_{tar} for singles dummy data using cuts on HMS delta x'_{tar} , and y'_{tar} . Place cuts on z_{tar} and y_{tar} to remove events from the walls of the cell.
5. Plot HMS x_{fp} vs y_{fp} for $H(e, e'p)$ data using all prior cuts. Place a loose cut on this focal plane distribution.
6. Define a subset of “HMS-only” cuts from the full set of cuts “coincidence” cuts selected so far.
7. Examine the distributions of W and SHMS Noble Gas Cherenkov NPE sum. Ensure that the HMS-only cuts are able to reproduce the W distribution plotted using coincidence cuts. Ensure that there are not a significant number of pions showing up as non-zero entries in the SHMS Noble Gas Cherenkov NPE sum distribution.
8. Using these HMS-only cuts, calculate the yields from coincidence and HMS singles $H(e, e'p)$ data.

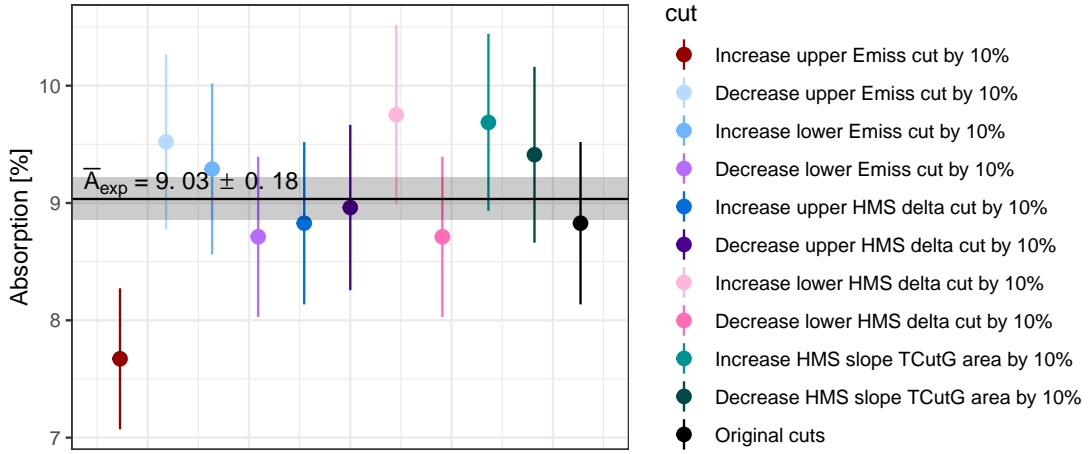


Figure 4-21: Values of absorption estimated with 10% variations on cuts used to select $H(e, e'p)$ events.

To estimate the systematic uncertainty of this measurement, we varied the limits of the following cuts by $\pm 10\%$: E_{miss} , HMS delta, HMS x'_{tar} and y'_{tar} . The absorption values for each of these variations are shown in Fig 4-21 along with the mean and standard deviation of these estimates. We use the mean value of these variations, $\bar{A}_{exp} = 9.03 \pm 0.71\%$, as our final estimate of the proton absorption, where the uncertainty is the quadrature sum of the systematic and statistical uncertainties. Note that the theoretical estimate of absorption $A_{pred} = 8.56\%$ is within the uncertainty in this measurement.

While there are significant variations in proton-nucleus cross sections below 1 GeV, these cross sections reach plateaus around 1 GeV that have been measured up to the TeV range. An incomplete catalog of hadron-nucleus cross section measurements can be found in Refs [167, 168, 169, 170, 171, 172, 173].

Because these cross sections and thus the free path lengths are independent of proton momentum over the range we studied (approximately 4 to 10 GeV), there is no momentum dependence in either our estimate or measurement of proton absorption in the SHMS. Therefore any uncertainty in proton absorption will only contribute to the magnitude of measured transparencies, and not the presence or absence of a rise in transparency with Q^2 characteristic of the onset of CT.

4.9 Coincidence Time

The *coincidence time* is the difference between the trigger time recorded by one spectrometer and the trigger time recorded by the other spectrometer. The TDC times recorded in Hall C are precise enough that a histogram of coincidence times will show a series of peaks separated by 2 ns, reflecting the CEBAF beam bunching structure. In addition, a given pair of spectrometer central momenta will show different types of scattering events (e.g. ep , $e\pi^+$, $\pi^-\pi^+$, ...) lying in different coincidence time peaks; the differing particle masses result in differing velocities for a given momentum.

Given single arm TDC trigger times t^H and t^P and coincidence TDC trigger time t^{coin} , the uncorrected coincidence time is

$$t_{uncorrected}^{coin} = t^H - t^P - t^{coin} \quad (4.59)$$

Using the particles' velocities, models of the spectrometers' optics, and surveys of Hall C, these times are corrected for the additional time it takes a particle not traveling along the central ray of a spectrometer. Given x'_{tar} in mrad and δ in percent, the additional length traveled is given by

$$\Delta L^P = 0.11 * x'_{tar}^P * 1000 + 0.057 * \delta^P / 100 \quad (4.60)$$

$$\Delta L^H = 0.12 * x'_{tar}^H * 1000 + 0.17 * \delta^H / 100 \quad (4.61)$$

Let v be a particle's velocity³, $L^{P(H)}$ the length of the the central ray of the SHMS (HMS), $\Delta L^{P(H)}$ the additional length traveled beyond the central ray, $\langle t_{hodostart}^{P(H)} \rangle$ the hodoscope start time, and $t_{fp}^{P(H)}$ the focal plane time. Then the SHMS (HMS) correction $\Delta t^{P(H)}$ is

$$\Delta t^P = \frac{L^P}{v} + \frac{\Delta L^P}{v} + (\langle t_{hodostart}^P \rangle - t_{fp}^P) \quad (4.62)$$

$$\Delta t^H = \frac{L^H}{v} + \frac{\Delta L^H}{v} + (\langle t_{hodostart}^H \rangle - t_{fp}^H) \quad (4.63)$$

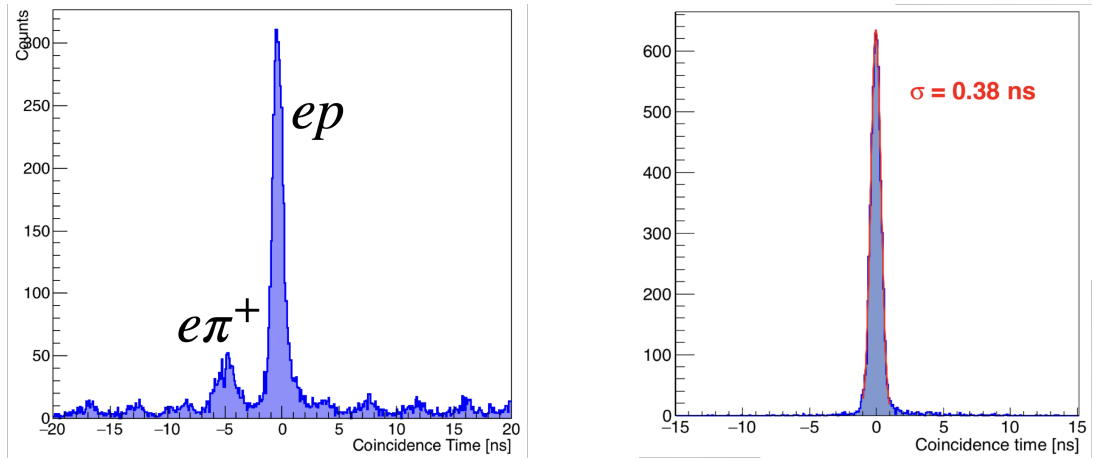
³Given reconstructed momentum p , a particle has velocity $\beta = v/c = p/\sqrt{p^2 + m^2}$.

The corrected coincidence time is

$$t_{corrected}^{coin} = (t^P - \Delta t^P) - (t^H - \Delta t^H) - t_{offset} \quad (4.64)$$

where t_{offset} is an offset due to signal propagation times which can be corrected for in PARAM files if desired. Strictly speaking, this is not necessary, because one identifies the location of the true coincidence peak in the coincidence time spectrum and places cuts around this value, whether or not it's centered at zero.

Coincidence time distributions for two runs are shown in Fig 4-22. The distribution on the left comes from a run with large backgrounds, which result in numerous peaks in coincidence time. A large peak corresponding to true ep coincidences can be seen near 0 ns, and a smaller peak corresponding to $e\pi^+$ coincidences to the left near -5 ns. The smaller peaks separated by 4 ns are accidental coincidences coming from other beam bunches. The distribution on the right is a typical run from this experiment and shows negligible contributions from accidental coincidences.



(a) To coincidence time distribution for a run taken specifically to observe the structure caused by different coincidence types.

(b) The coincidence time distribution for a typical production run is very clean, with negligible accidental coincidences.

Figure 4-22: The distribution of coincidence times for two runs.

4.10 Event Selection

Several cuts were placed to select true ep coincidences in the analysis of $^{12}C(e, e'p)$ and $H(e, e'p)$ data. They are listed in Tables 4.9 and 4.10. Most of the cuts are identical for the two targets—the only difference is the limits of cuts placed on E_{miss} and p_{miss} . The cuts on delta in both spectrometers ensure that the events used are in a central region of momentum acceptance with acceptable optics reconstruction. Cuts on normalized calorimeter energy and Cherenkov photoelectrons select electrons in the HMS and remove negatively charged pions. Similarly, the noble gas Cherenkov in the SHMS acts as a pion-veto to limit SHMS events to protons. The cuts on E_{miss} and p_{miss} were selected for consistency with prior measurements and to keep the center of mass energy below the threshold for pion creation.

Table 4.9: List of cuts used to select clean $H(e, e'p)$ events.

Variables	Cut
HMS Calorimeter Energy	$0.8 < H.cal.etottracknorm \&\& H.cal.etottracknorm < 1.15$
HMS Cherenkov NPE	$H.cer.npeSum > 0$
SHMS NG Cherenkov Veto	$P.ngcer.npeSum < 0.1$
δ_{HMS}	$-8.0 < H.gtr.dp \&\& H.gtr.dp < 8.0$
δ_{SHMS}	$-10.0 < P.gtr.dp \&\& P.gtr.dp < 15.0$
β_{HMS}	$0.6 < H.gtr.beta \&\& H.gtr.beta < 1.4$
β_{SHMS}	$0.8 < P.gtr.beta \&\& P.gtr.beta < 1.4$
E_{miss}	$P.kin.secondary.emiss < 0.1$
p_{miss}	$\text{abs}(P.kin.secondary.pmiss) < 0.1$
p_{miss}	$-0.1 < P.kin.secondary.pmiss \&\& P.kin.secondary.pmiss < 0.1$
Good hodoscope times	$H.hod.goodstarttime == 1 \&\& P.hod.goodstarttime == 1$

Table 4.10: List of cuts used to select clean $^{12}C(e, e'p)$ events.

Variables	Cut
HMS Calorimeter Energy	$0.8 < H.cal.etottracknorm \&\& H.cal.etottracknorm < 1.15$
HMS Cherenkov NPE	$H.cer.npeSum > 0$
SHMS NG Cherenkov Veto	$P.ngcer.npeSum < 0.1$
δ_{HMS}	$-8.0 < H.gtr.dp \&\& H.gtr.dp < 8.0$
δ_{SHMS}	$-10.0 < P.gtr.dp \&\& P.gtr.dp < 15.0$
β_{HMS}	$0.6 < H.gtr.beta \&\& H.gtr.beta < 1.4$
β_{SHMS}	$0.8 < P.gtr.beta \&\& P.gtr.beta < 1.4$
E_{miss}	$P.kin.secondary.emiss < 0.08$
p_{miss}	$-0.3 < P.kin.secondary.pmiss \&\& P.kin.secondary.pmiss < 0.3$
Good hodoscope times	$H.hod.goodstarttime == 1 \&\& P.hod.goodstarttime == 1$

4.11 Charge-normalized Yield

Experimental yields Y for each kinematic setting were corrected using kinematic-specific efficiencies ϵ (PID, tracking, hodoscope), and total electronic livetimes TLT . Due to limited statistics, the same proton absorption correction A , calculated using $Q^2 = 11.5 \text{ GeV}^2$ data, was used for all kinematics. The same LH2 boiling correction for current I in μA , $f_{boil}(I) = 1 - 0.000385I$ was used for all hydrogen runs.

The corrected experimental yield for each kinematic setting was obtained using

$$Y_{exp} = \frac{N_{coin}}{Q} \frac{f_{boil}(I)}{(1 - A) * TLT} [\epsilon_{track}\epsilon_{cer}\epsilon_{cal}\epsilon_{hodo}]_{HMS}^{-1} [\epsilon_{track}\epsilon_{cer}\epsilon_{hodo}]_{SHMS}^{-1} \quad (4.65)$$

The carbon yields in both data and simulation were integrated over the the region $E_{miss} < 0.08 \text{ GeV}$ and $|\vec{p}_{miss}| < 0.3 \text{ GeV}$; this cut removes any accidental coincidences from pions in the SHMS. Nucleon-nucleon short-range correlations shift the single particle strength to higher p_{miss} than predicted by the independent particle shell model (IPSM) spectral functions used by SIMC (see Appendix A). To correct for this, a correction factor of 1.11 ± 0.03 [18] is applied to the simulation yields. This correction is the ratio of the values of the integral $\int d^3p dE_m S(E_m, \vec{p}_m)$ calculated for IPSM and correlated [174] spectral functions. These cuts and correction factor were the same as the ones used in previous experiments measuring nuclear transparency for $^{12}\text{C}(e, e'p)$. This choice was made in the interest of consistency and ease of comparing these new results with the prior data.

Chapter 5

Results

5.1 Missing Energy and Missing Momentum

Figures 5-1 through 5-8 compare distributions of physics quantities measured in experiment (in blue) and from simulation (in red). These figures' panels show invariant mass W (top left), missing energy E_m (top right), missing momentum \vec{p}_m (bottom left), and p_{mz} , the component of missing momentum parallel to the 3-momentum transfer \vec{q} (bottom right). Similar comparisons of target variables are contained in Appendix .

The shapes of the missing energy spectra for $H(e, e'p)$ data disagree in the region between 0 and ~ 50 MeV because SIMC does not include any smearing of reconstructed momenta that results from the spectrometers' finite resolution. To obtain our transparency measurements for $H(e, e'p)$ we integrate these distributions over $E_m < 100$ MeV, so this distortion does not affect our results.

The tail of the missing momentum distributions above 300 MeV is lower in simulation than experiment. This is likely because short range correlations [175] drive nucleons to higher missing momenta than is accounted for by the spectral functions used in SIMC. For $^{12}C(e, e'p)$ we integrate the yield over the $\vec{p} < 300$ MeV region so our transparency measurements are insensitive to the divergence above this limit.

Fig 5-9 compares the E_m distributions for $^{12}C(e, e'p)$ measured in experiment (blue) to the results of SIMC simulations that either include (red) or do not include (black) radiative corrections. Note that the high energy tail of the distributions is

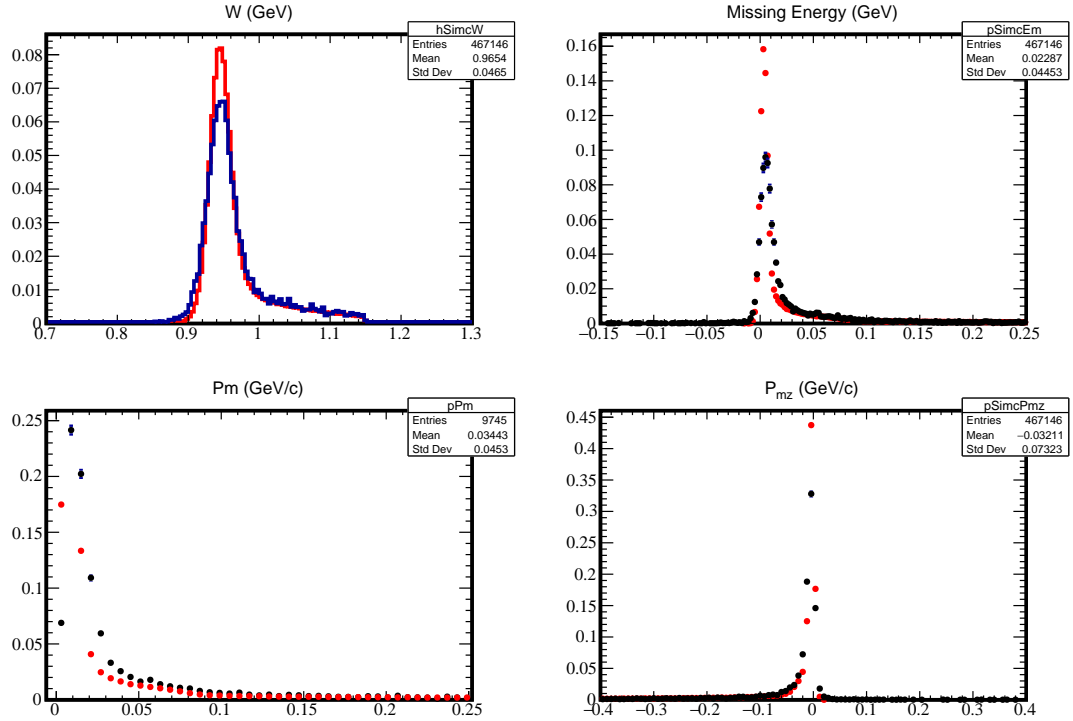


Figure 5-1: Experimental (in blue) and Monte Carlo (in red) distributions of reconstructed physics quantities for the LH_2 target at $Q^2 = 8.0 \text{ GeV}^2$.

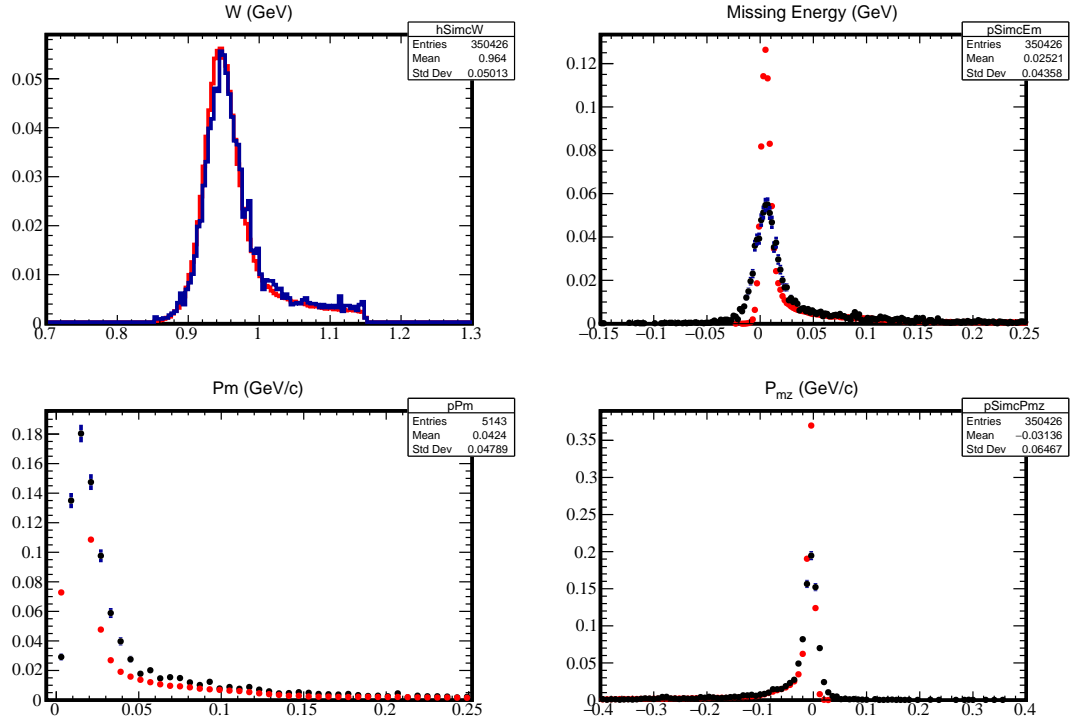


Figure 5-2: Experimental (in blue) and Monte Carlo (in red) distributions of reconstructed physics quantities for the LH_2 target at $Q^2 = 9.5 \text{ GeV}^2$.

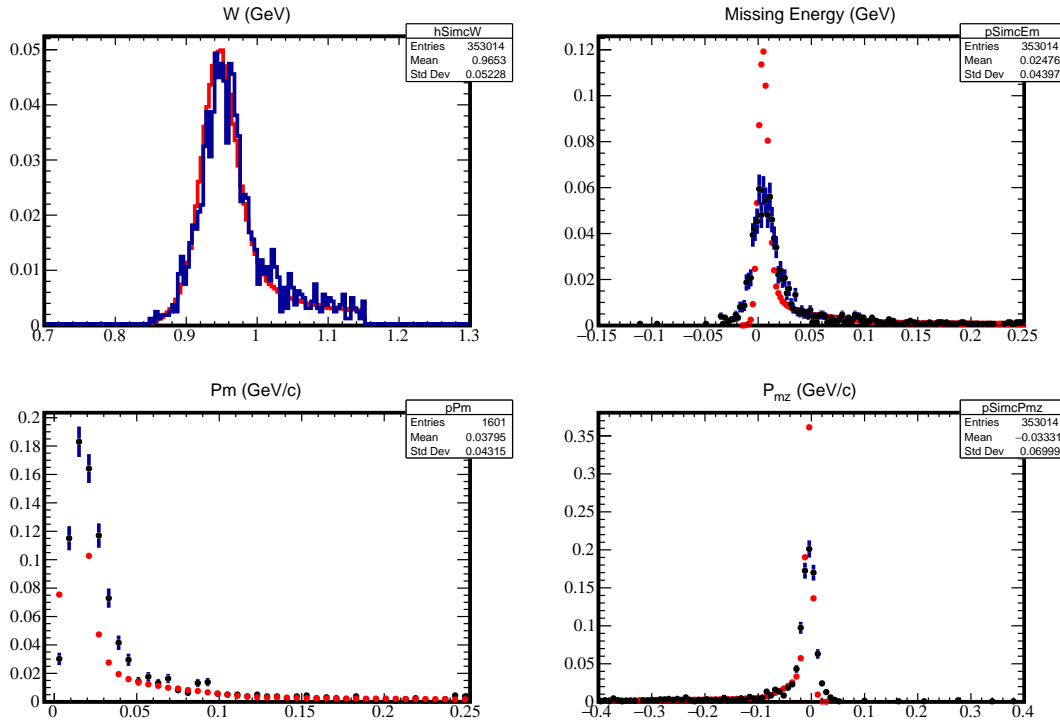


Figure 5-3: Experimental (in blue) and Monte Carlo (in red) distributions of reconstructed physics quantities for the LH_2 target at $Q^2 = 11.5 \text{ GeV}^2$.

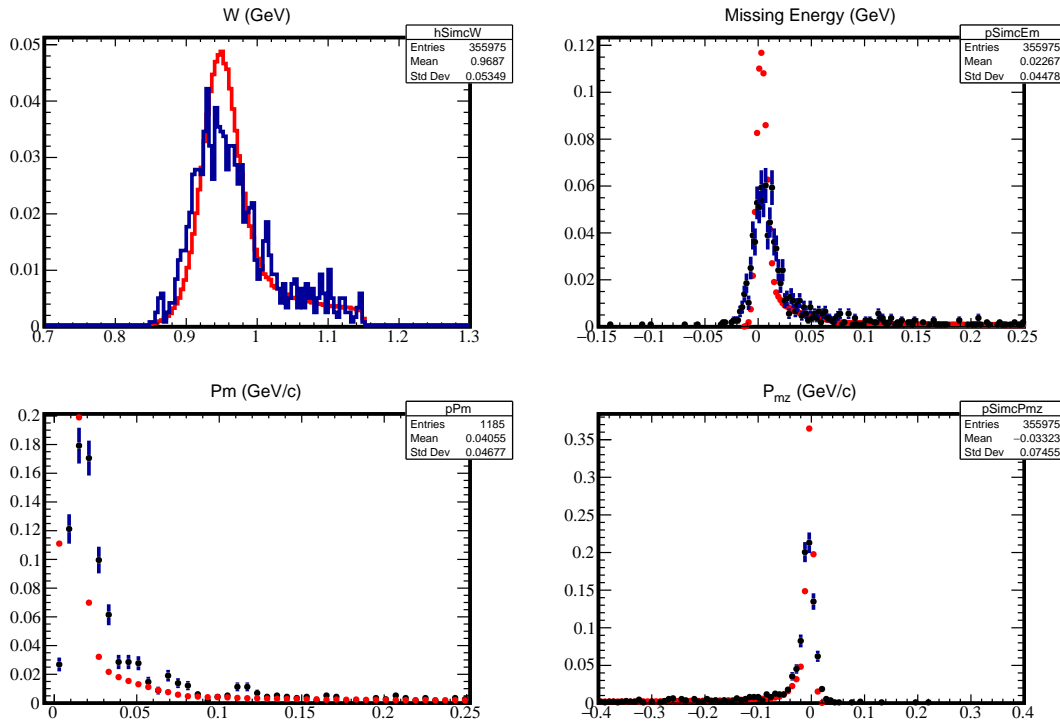


Figure 5-4: Experimental (in blue) and Monte Carlo (in red) distributions of reconstructed physics quantities for the LH_2 target at $Q^2 = 14.2 \text{ GeV}^2$.

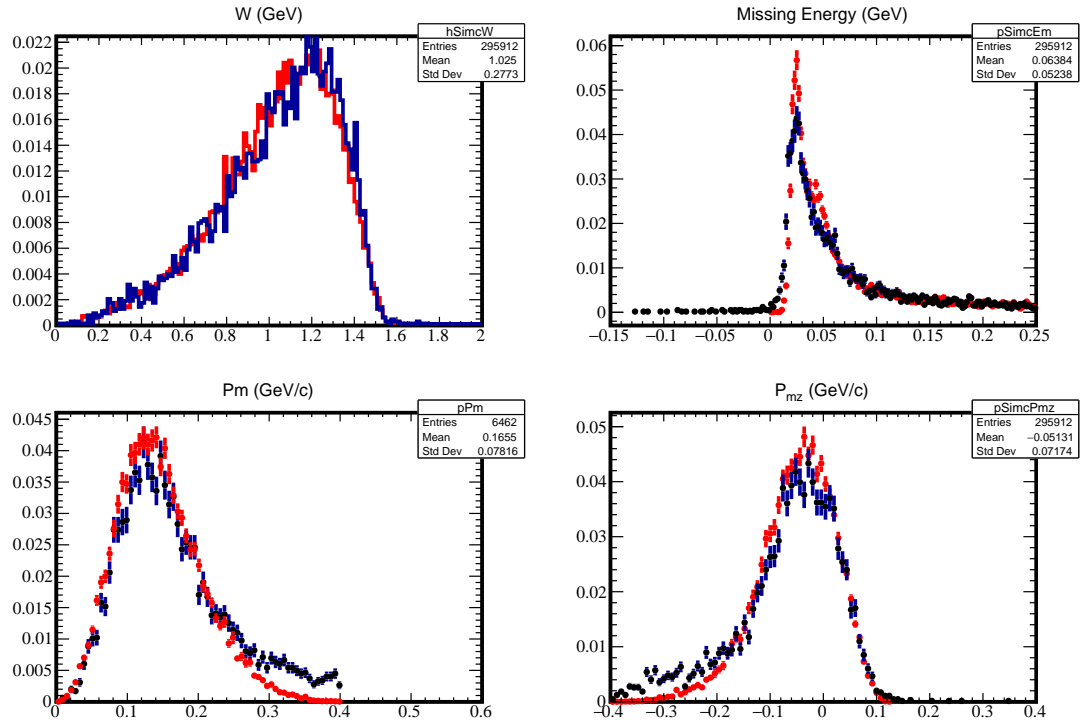


Figure 5-5: Experimental (in blue) and Monte Carlo (in red) distributions of reconstructed physics quantities for the ^{12}C target at $Q^2 = 8.0 \text{ GeV}^2$.

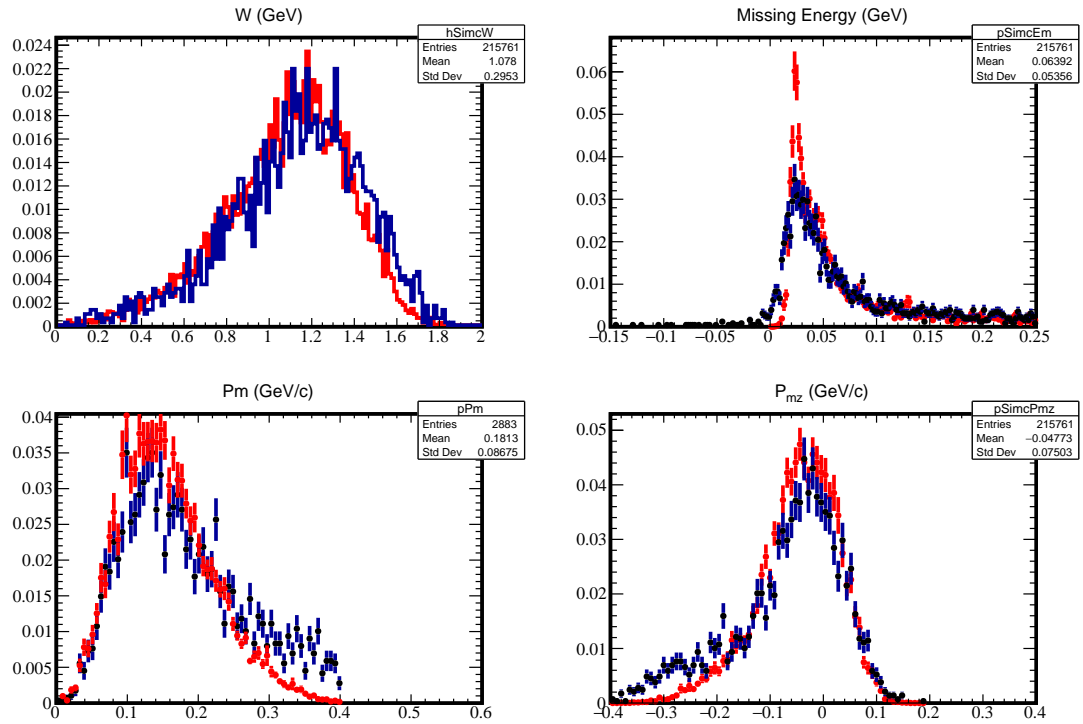


Figure 5-6: Experimental (in blue) and Monte Carlo (in red) distributions of reconstructed physics quantities for the ^{12}C target at $Q^2 = 9.5 \text{ GeV}^2$.

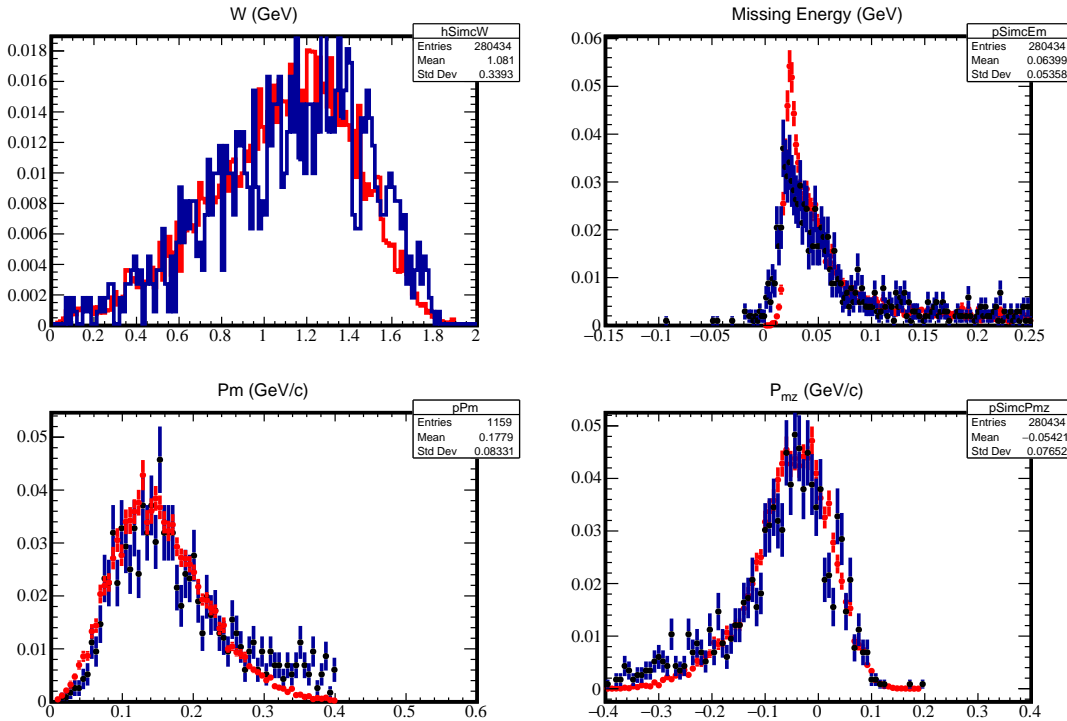


Figure 5-7: Experimental (in blue) and Monte Carlo (in red) distributions of reconstructed physics quantities for the ^{12}C target at $Q^2 = 11.5 \text{ GeV}^2$.

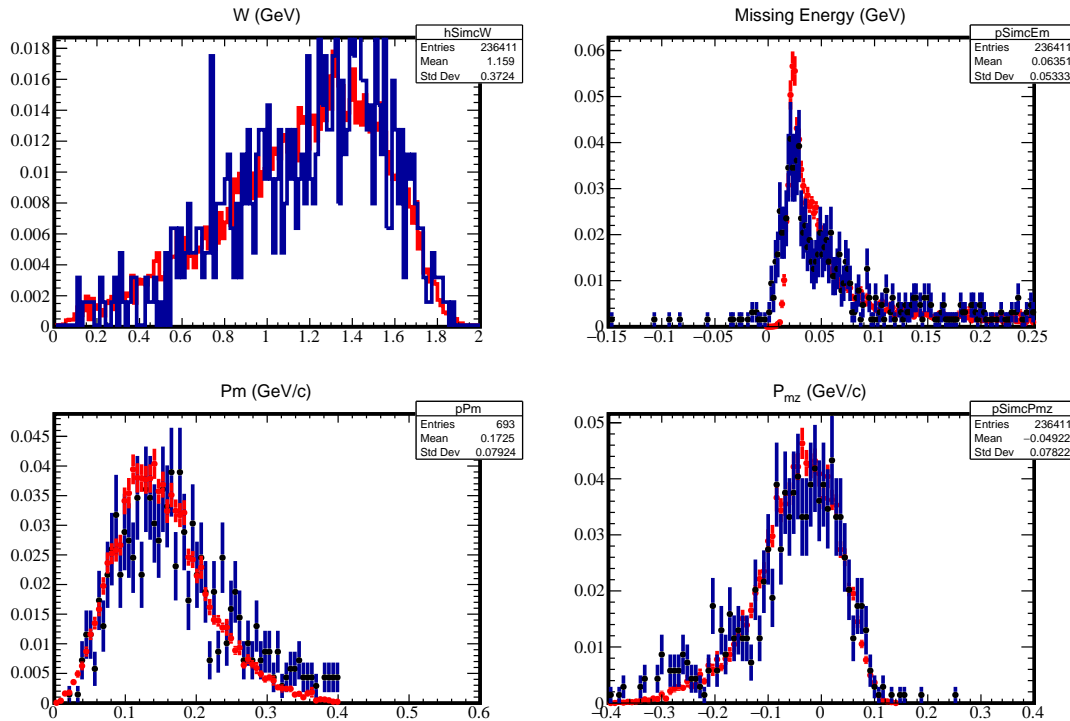


Figure 5-8: Experimental (in blue) and Monte Carlo (in red) distributions of reconstructed physics quantities for the ^{12}C target at $Q^2 = 14.2 \text{ GeV}^2$.

only accurately modeled with the inclusion of radiative effects. The disagreement at lower values can be attributed to the spectrometers' finite resolutions. The green lines indicate the region of E_m integrated over to calculate nuclear transparency T .

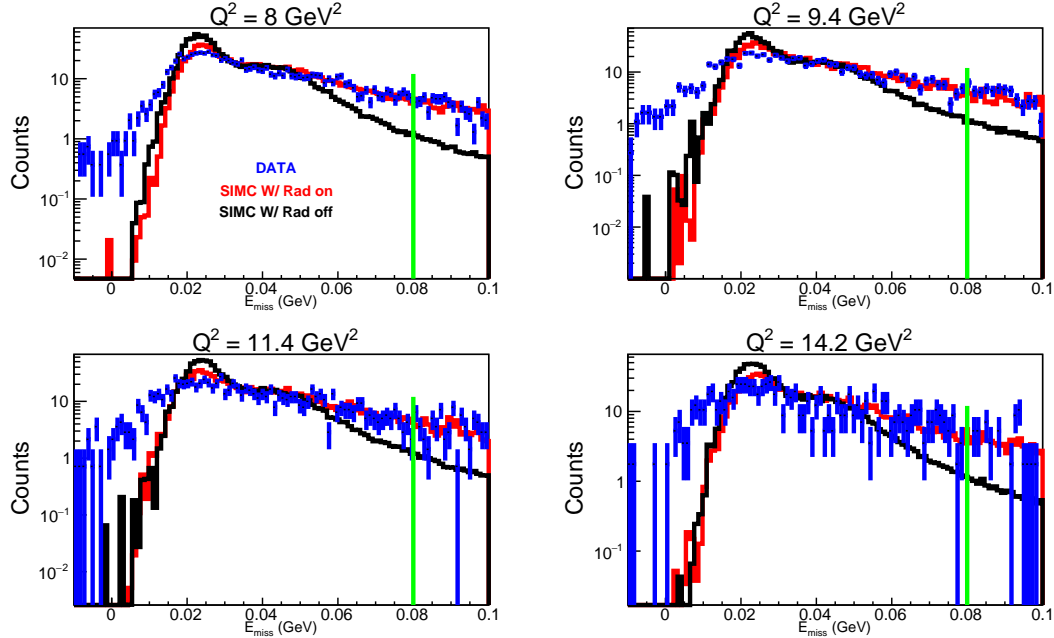


Figure 5-9: Distributions of missing energy E_m measured in experiment (blue) and from Monte Carlo with (red) and without (black) radiative corrections. Data are for $^{12}\text{C}(e, e'p)$.

5.2 Nuclear Transparency

The nuclear transparency was extracted as the ratio of the experimental yield to the simulated PWIA yield from SIMC over the phase space volume V defined by the limits $E_m < 80 \text{ MeV}$ and $|\vec{p}_{\text{miss}}| < 300 \text{ MeV}$ for $^{12}\text{C}(e, e'p)$ and $E_m < 100 \text{ MeV}$ and $|\vec{p}_{\text{miss}}| < 100 \text{ MeV}$ for $H(e, e'p)$.

$$T(Q^2) = \frac{\int_V d^3 p_m dE_m Y_{\text{exp}}(E_m, \vec{p}_m)}{\int_V d^3 p_m dE_m Y_{\text{PWIA}}(E_m, \vec{p}_m)} \quad (5.1)$$

The nuclear transparency measured as a function of Q^2 for $H(e, e'p)$ is shown in Fig 5-10. This elastic scattering process has no final state interactions and should be accurately modeled by the PWIA as implemented in SIMC. The ratio T should thus be equal to one for each point, and these measurements are consistent with

$T = 1$ well within the statistical and systematic uncertainty. This indicates that the Monte Carlo simulation in SIMC accurately models the scattering process and that both the spectrometers and hcana are accurately reconstructing physics quantities.

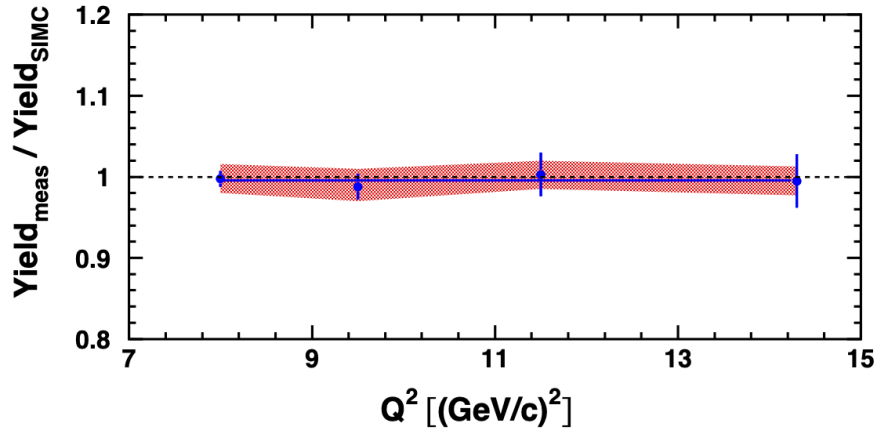


Figure 5-10: Nuclear transparency for $H(e, e'p)$ as a function of momentum transfer. The error bars represent statistical uncertainty and the shaded band represents the 4.0% systematic uncertainty.

The nuclear transparency measured as a function of Q^2 for $^{12}C(e, e'p)$ is shown in Fig 5-10 along with previous measurements. Our measurements from 8–14.2 GeV 2 are consistent with conventional multiple scattering calculations [32] and do not support the onset of color transparency.

5.2.1 Systematic Uncertainty

Table 5.1 lists the major sources of systematic uncertainty in our measurements of nuclear transparency.

The systematic uncertainty due to spectrometer acceptance was estimated by taking the average of the bin-wise difference between the normalized missing momentum spectra for data and simulation.

The uncertainty due to event selection was estimated by varying the limits of the cuts listed in Tables 4.9 and 4.10 by $\pm 10\%$ one at a time and calculating the corresponding percentage change in measured transparency. The quadrature sum of these variations was used as the systematic uncertainty. The uncertainty due to livetime and the detector efficiencies was determined from a set of luminosity scans taken with the ^{12}C target. The charge-normalized yield from these scans for each

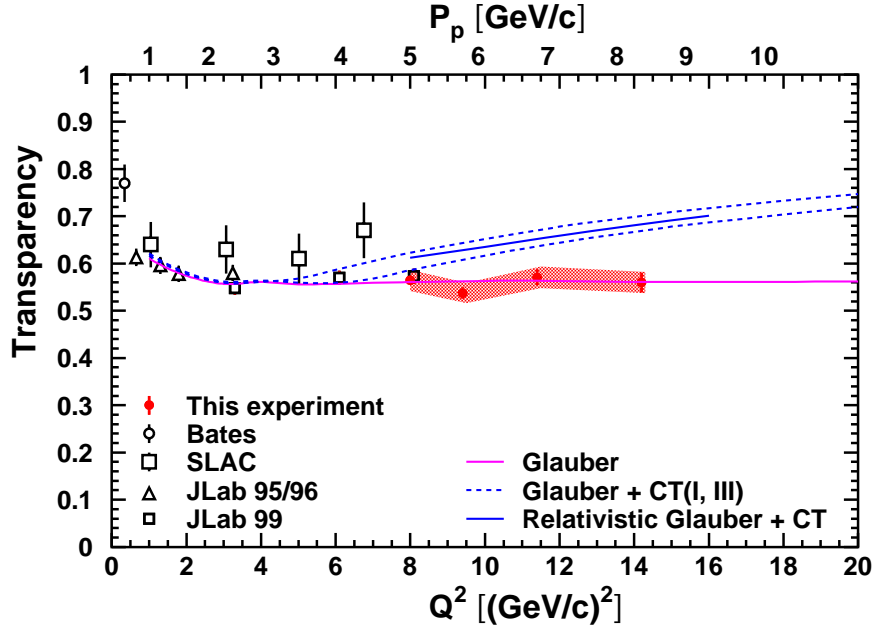


Figure 5-11: Nuclear transparency for $^{12}\text{C}(e, e'p)$ as a function of momentum transfer. The results of this experiment, E12-06-107, are shown in red along with previous measurements in open shapes. The error bars represent statistical uncertainty and the shaded band represents the 4.0% systematic uncertainty. The magenta line is the prediction of a Glauber model that does not include CT [32]. The dashed lines represent predictions, for two choices of parameters, of a model including CT [38]. The solid line represents the prediction of a relativistic Glauber model that includes CT [41].

spectrometer was found to be independent of the beam current within statistical uncertainties. The average variation in the normalized yield vs beam current was recorded as the systematic uncertainty (0.5%). The normalization uncertainty due to the free ep cross section used in SIMC is 1.8% [176]. The uncertainty due to target thickness is taken from the JLab target group's measurements. The uncertainty in measured charge was estimated to be 1% by varying the minimum beam current cut used by hcana to calculate each run's average current. The uncertainty in proton absorption is taken from the cut-variation study discussed in section 4.8. The uncertainty in tracking efficiency was estimated from the average variation in tracking efficiency when using three independent criteria to select events that should and did form a track.

The uncertainty due to radiative corrections arises from the tails of the E_m distributions generated by SIMC; it was estimated by varying the E_m limit used to calculate T .

Table 5.1: Systematic uncertainties in our measurements of nuclear transparency. Q^2 -dependent uncertainties are averaged over all kinematic settings. The total uncertainty is the quadrature sum of the individual contributions.

Source	Q^2 -dependent uncertainty (%)
Spectrometer acceptance	2.6
Event selection	1.4
Tracking efficiency	0.5
Radiative corrections	1.0
Live time & detector efficiency	0.5
Source	Normalization uncertainty (%)
Free ep cross section	1.8
Target thickness	0.5
Beam charge	1.0
Proton absorption	1.2
Total	4.0

Chapter 6

Summary and Conclusion

Using the upgraded 12 GeV CEBAF beam at JLab, coincidence $(e, e'p)$ data were taken with 1H and ${}^{12}C$ targets for Q^2 values between 8.0 and 14.2 GeV^2 . Nuclear transparencies were extracted for each kinematic point by taking the ratio of charge-normalized yields from experiment to yields from Monte Carlo PWIA simulation. The transparency measured at the lowest kinematic point at $Q^2 = 8.0 \text{ GeV}^2$ agrees with prior measurements at JLab. The Q^2 -dependence of the measured transparencies is consistent with traditional Glauber multiple scattering theory and does not show an onset of color transparency in ${}^{12}C(e, e'p)$ up to $Q^2 = 14.2 \text{ GeV}^2$. Given the onset of CT's connection to factorization theorems, this result may be troubling for efforts to study baryon GPDs.

As discussed in Sec 2.1, Brodsky and de Téramond [64] use light-front holographic QCD to derive an expression for a PLCs transverse size as a function of twist τ and Q^2 . Their calculations suggest that the onset of CT in ${}^{12}C(e, e'p)$ may be higher than what can currently be probed in Hall C, perhaps not occurring until $Q^2 \sim 20 \text{ GeV}^2$.

Using the same framework, Caplow-Munro and Miller [177] demonstrate that expansion effects are not sufficiently large enough to credit final state interactions with the absence of CT in this experiment's measurements. If a PLC were formed, it should have remained small as it exited the nucleus. The lack of a rise in transparency then suggests that a PLC was not formed, and that the proton's electromagnetic form factor is dominated at large momentum by the Feynman

mechanism¹ rather than a PLC.

Experiments at JLab in the near future will include color transparency studies in ρ (Hall B) and π (Hall C) electroproduction, and π photoproduction in Hall D. A future ~ 20 GeV upgrade to the CEBAF accelerator is possible [179]. Replacing the highest-energy recirculating arcs with Fixed Field Alternating Gradient arcs would allow 6–7 additional beam passes through the existing CEBAF SRF cavities, yielding a beam with nearly double the present maximum energy. With this upgrade, a future experiment could revisit the results of this experiment and probe a range of Q^2 that Brodsky et al. suggest may finally show the onset of color transparency.

¹In the Feynman mechanism, a single quark carrying a large portion of a hadron's momentum absorbs the entire momentum transfer Q [178].

Appendix A

SIMC

A.1 Spectral Functions

The spectral functions used in SIMC are based on the independent particle shell model (IPSM), which assumes nucleons occupy shells with quantum numbers n, l, j , similar to the model of electron orbitals in atomic physics. In this model, the spectral function can be factored into a sum of per-shell energy and momentum distributions

$$S(E_m, \vec{p}_m) = \sum_i N_i \|\varphi_i(\vec{p})\|^2 L_i(E_m) \quad (\text{A.1})$$

where N_i is the occupation number of the i th shell, $\varphi_i(\vec{p})$ is the bound state wavefunction, and $L_i(E_m)$ is an energy profile.

The energy profile of each nuclear shell i with binding energy E_i is given by a Lorentzian with finite width Γ_i that accounts for the finite lifetime of the one-hole state.

$$L_i(E) = \frac{1}{\pi} \frac{\Gamma_i/2}{(E - E_i)^2 + \Gamma_i^2/4} \quad (\text{A.2})$$

The separation energy E cannot be less than the minimum proton removal energy $E_{min} = m_p + m_{A-1} - m_A$, so these profiles are cut off below E_{min} and normalized to ensure the spectroscopic sum rule, Equation 1.5, is obeyed.

$$L_i(E) = \begin{cases} L_i(E)/ \int_{E_{min}}^{\infty} L_i(E) dE & \text{if } E \geq E_{min} \\ 0 & \text{if } E < E_{min} \end{cases} \quad (\text{A.3})$$

The wavefunctions $\varphi_i(\vec{p})$ are Fourier transforms of solutions $\psi(\vec{r})$ to the Schroedinger equation with a potential given by the sum of a Woods-Saxon potential $-V_0 f(\vec{r})$, Coulomb potential $V_C(r)$, and spin-orbit coupling,

$$V(\vec{r}) = -V_0 f(r) + V_C(r) + V_{SO} \left(\frac{\hbar}{m_\pi c} \right)^2 \frac{2}{r} \frac{df}{dr} \vec{l} \cdot \vec{s} \quad (\text{A.4})$$

The Woods-Saxon potential is characterized by depth V_0 , radius $R_0 = r_0(A - 1)^{1/3}$, and diffuseness a parameters and a form given by a Fermi-Dirac distribution

$$f(r) = \frac{1}{1 + e^{\frac{r-R_0}{a}}} \quad (\text{A.5})$$

The Coulomb potential is that of a uniform sphere of radius $R_c = r_c(A - 1)^{1/3}$.

The model parameters were obtained from fits to the Saclay measurements [29, 27] of the ^{12}C spectral functions. The wavefunctions were obtained using the method described in Ref [180, 181, 182].

Short range nucleon-nucleon correlations push protons to higher missing energy and momentum than accounted for by the IPSM. Without correcting for this, simulated yields would be artificially large. Assuming this leads to a uniform suppression of the spectral function below the Fermi momentum, the spectral functions can be corrected by a constant factor, assuming one consistently works in the same volume V_m of (E_m, \vec{p}_m) phase space. Given spectral functions S_{SRC} , that include the effects of short range correlations, the correction is given by

$$\frac{\int_{V_m} S_{IPSM}(E_m, \vec{p}_m) dE_m d^3 p_m}{\int_{V_m} S_{SRC}(E_m, \vec{p}_m) dE_m d^3 p_m} \quad (\text{A.6})$$

A.2 Coulomb Corrections

Coulomb distortions of the PWIA model arise from electromagnetic interactions between the beam electron and target nucleus, modifying the momentum transfer and incoming/outgoing momenta of the electron.

The energy required to bring an electron from infinity to a position \vec{r} inside a

nucleus with $Z - 1$ protons is

$$\Delta E(\vec{r}) = f_C(|\vec{r}|) \left[\alpha \frac{(Z-1)}{R_0} \right] \quad (\text{A.7})$$

where $\vec{r} = 0$ is the center of the nucleus, α is the fine structure constant, and $R_0 = 1.1A^{1/3} + 0.86A^{-1/3}$ is the radius of the nucleus.

SIMC uses the prescription described in Ref [183], which takes this energy to be

$$\Delta E = \frac{f(Z-1)\alpha}{R_0} \quad (\text{A.8})$$

where the factor f is of order 1; SIMC uses $f = 1.125$.

Assuming the incoming electron is not deflected, its initial momentum at the interaction vertex becomes

$$(\vec{p}_e)_v = \vec{p}_e(1 + \Delta E/p_e) \quad (\text{A.9})$$

This value is used to calculate the momentum transfer

$$\vec{q} = (\vec{p}'_e)_v - (\vec{p}_e)_v \quad (\text{A.10})$$

and opposite correction is applied to the outgoing electron momentum,

$$\vec{p}_e = (\vec{p}'_e)(1 - \Delta E/(p'_e)_v) \quad (\text{A.11})$$

A.3 Radiative Corrections

The method for radiative corrections in SIMC is based on the work of Mo and Tsai [184]. The full derivation by Makins et. al [185, 17] for coincidence elastic and quasielastic scattering done is quite lengthy. What follows in this section is an overview of the main results. In brief, SIMC calculates vertex corrections and the energy radiated as internal and external Bremsstrahlung, modifies the simulated particles' vertex 4-momenta accordingly, and applies a weight to the event.

A.3.1 Internal Bremsstrahlung

The cross section for scattering an electron into a solid angle $d\Omega_e$ accompanied by the emission of a single photon with momentum in the range $d^3\omega$ is

$$\frac{d\sigma}{d\Omega_e d^3\omega} = \frac{d\sigma^{(1)}}{d\Omega_e} \Big|_{ep} \frac{-\alpha}{4\pi^2(\omega^0)^2} \left[\frac{k'}{\omega \cdot k'} - \frac{p'}{\omega \cdot p'} - \frac{k}{\omega \cdot k} + \frac{p}{\omega \cdot p} \right]^2 \quad (\text{A.12})$$

$$= \frac{d\sigma^{(1)}}{d\Omega_e} \Big|_{ep} \frac{A(\hat{\omega})}{\omega^0} \quad (\text{A.13})$$

where $\frac{d\sigma^{(1)}}{d\Omega_e} \Big|_{ep}$ is the single-photon exchange ep cross section, and $A(\hat{\omega})$ is the angular distribution of single photon Bremsstrahlung. The kinematic terms on the right hand side come from the amplitudes given by the Feynman diagrams in Fig A-1

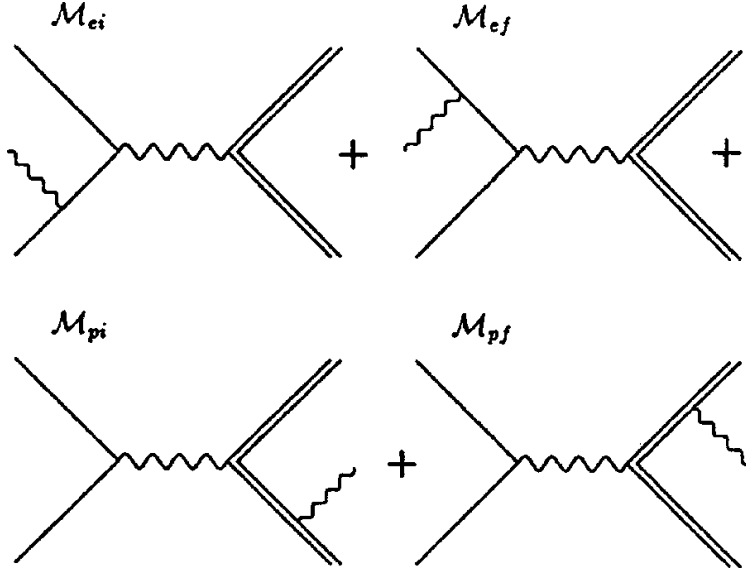


Figure A-1: Figure reproduced from Ref [185].

Let

$$B(p_i, p_j, \Delta E_m) = \int_0^{\Delta E_m} d^3\omega \frac{1}{8\pi^2\omega^0} \frac{p_i \cdot p_j}{(\omega \cdot p_i)(\omega \cdot p_j)} \quad (\text{A.14})$$

and

$$\lambda = \int d\Omega_\gamma A(\hat{\omega}) \quad (\text{A.15})$$

Allowing the emission of multiple Bremsstrahlung photons, with a total energy E_{tot} ,

$$\frac{d\sigma}{d\Omega_e d^3\omega} = \frac{d\sigma^{(1)}}{d\Omega_e} \Big|_{ep} (1 - \sigma_{hard})(-\delta'_{soft}(E_{tot})e^{-\delta_{soft}(E_{tot})}F(\lambda)) \quad (\text{A.16})$$

where $F(\lambda) = \frac{e^{-C\lambda}}{\Gamma(1+\lambda)}$ and C is the Euler-Mascheroni constant.

The contribution from one photon Bremsstrahlung is

$$\delta_{soft}(\Delta E_m) = 2\alpha \sum_{i,j} \Theta(p_i)\Theta(p_j)\bar{B}(p_i, p_j, \Delta E_m) \quad (\text{A.17})$$

where $\bar{B}(p_i, p_j, \Delta E_m)$ is $B(p_i, p_j, \Delta E_m)$ without the infrared divergent term p_i is one of k, k', p, p' and $\Theta(p_i)$ is the sign function.

The contribution from one-loop diagrams is

$$\delta_{hard} = 2\alpha \left[-\frac{3}{4\pi} \log\left(\frac{-q^2}{m_e^2}\right) + \frac{1}{\pi} - \sum_i \delta_i^{vp}(q^2) \right] \quad (\text{A.18})$$

where

$$\delta_i^{vp} = \frac{1}{3\pi} \left(-\frac{5}{3} - \frac{4m_i^2}{q^2} + \left(1 + \frac{2m_i^2}{q^2}\right) \sqrt{1 - \frac{4m_i^2}{q^2}} \log \left[\frac{\sqrt{1 - \frac{4m_i^2}{q^2}} + 1}{\sqrt{1 - \frac{4m_i^2}{q^2}} - 1} \right] \right) \quad (\text{A.19})$$

is the vacuum polarization correction due to flavor i of leptons and light quarks of flavor i .

As shown in Fig A-2, the single photon angular distribution is peaked around the directions of the incoming and outgoing electron, and this focus increases with momentum transfer Q^2 . A broad peak in the direction of the scattered proton also becomes more defined with increasing Q^2 . The *peaking approximation* consists of dividing the total energy radiated in Bremsstrahlung into three photons of energy E_e , $E_{e'}$, and $E_{p'}$ that travel in the directions \hat{k} of the incoming electron, \hat{k}' of the outgoing electron, and \hat{p}' of the outgoing proton. The angular distribution $A(\hat{\omega})$ then becomes

$$A_{peaking}(\hat{\omega}) = \lambda_e \delta(\hat{\omega} - \hat{k}) + \lambda_{e'} \delta(\hat{\omega} - \hat{k}') + \lambda_{p'} \delta(\hat{\omega} - \hat{p}') \quad (\text{A.20})$$

The form of these λ_i terms can be found by breaking up the angular distribution $A(\hat{\omega})$ into three terms—one due to electron, one due to the proton, and one with

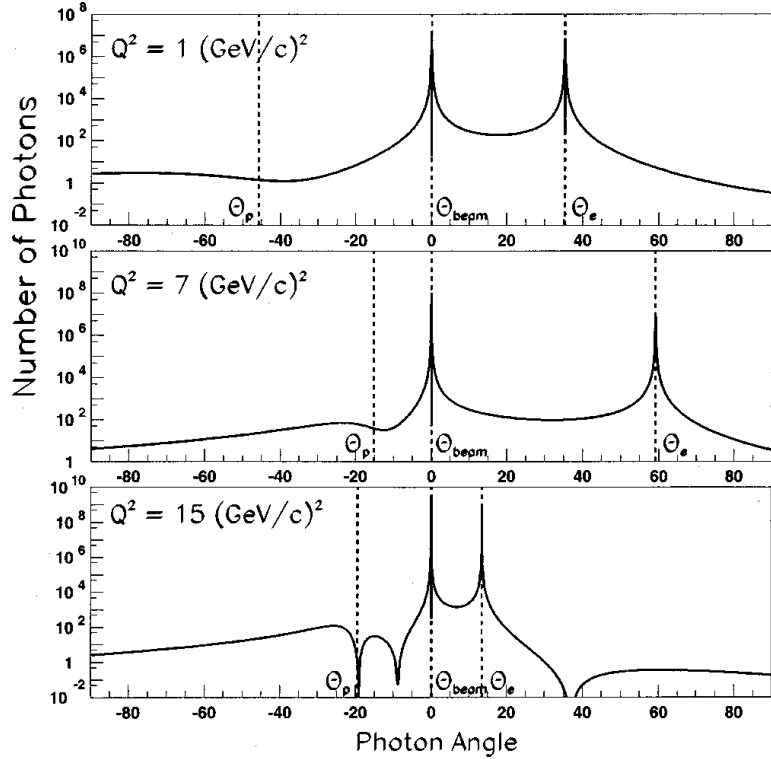


Figure A-2: The angular distribution of first order single photon Bremsstrahlung for three values of momentum transfer Q^2 . The photon angle, given in degrees, is measured with respect to the direction of the incoming beam electron. The directions θ_e and θ_p of the scattered electron and proton are indicated by dotted lines. Figure reproduced from Ref [185].

the cross terms

$$A(\hat{\omega}) = -\frac{\alpha(\omega^0)^2}{4\pi^2} \left[\left(\frac{k'}{\omega \cdot k'} - \frac{k}{\omega \cdot k} \right)^2 + \left(\frac{p'}{\omega \cdot p'} - \frac{p}{\omega \cdot p} \right)^2 - 2 \left(\frac{k'}{\omega \cdot k'} - \frac{k}{\omega \cdot k} \right) \left(\frac{p'}{\omega \cdot p'} - \frac{p}{\omega \cdot p} \right) \right] \quad (\text{A.21})$$

By expanding each of these terms in the polar coordinate θ , making approximations about their asymptotic behavior near and away from the peaks, and finally

integrating them, one can distribute their contents among the three directions

$$\lambda_e = \frac{\alpha}{\pi} \left[\log \left(\frac{4k^2}{m_e^2} \right) + 2 \log \left(\frac{k}{k'} \right) + \log \left(\frac{1 - \cos\theta_e}{2} \right) - 1 \right] \quad (\text{A.22})$$

$$\lambda_{e'} = \frac{\alpha}{\pi} \left[\log \left(\frac{4k'^2}{m_e^2} \right) + 2 \log \left(\frac{k}{k'} \right) + \log \left(\frac{1 - \cos\theta_e}{2} \right) - 1 \right] \quad (\text{A.23})$$

$$\lambda_{p'} = \frac{\alpha}{\pi} \left[\frac{p'^0}{|\vec{p}|} \log \left(\frac{p'^0 + |\vec{p}|}{p'^0 - |\vec{p}|} \right) - 2 \right] \quad (\text{A.24})$$

Generalizing to multiphoton Bremsstrahlung,

$$\frac{d\sigma}{d\Omega_e dE_e dE_{e'} dE_{p'}} = \frac{d\sigma^{(1)}}{d\Omega_e} \Big|_{ep} (1 - \delta_{hard}) \quad (\text{A.25})$$

$$\times \frac{\lambda_e \lambda_{e'} \lambda_{p'}}{(kk')^{\lambda_e/2} (kk')^{\lambda_{e'}/2} (m_p p'^0)^{\lambda_{p'}/2}} \quad (\text{A.26})$$

$$\times \frac{1}{E_e^{1-\lambda_e} E_{e'}^{1-\lambda_{e'}} E_{p'}^{1-\lambda_{p'}}} \quad (\text{A.27})$$

A.3.2 External Bremsstrahlung

External Bremsstrahlung refers to the emission of photons in the fields of nuclei other than the nucleus participating in the primary scattering. The proton emits a negligible amount of such radiation, but the electron will experience these losses as it travels through various materials¹

Early [186] provides a numerical solution for the probability that an electron with momentum k radiates a total energy E^{ext} while traveling through t radiation lengths of material with atomic number Z ,

$$\frac{1}{\Gamma(1+bt)} \frac{bt}{E^{ext}} \left(\frac{E^{ext}}{k} \right)^{bt} \Phi^{ext} \left(\frac{E^{ext}}{k} \right) \quad (\text{A.28})$$

where b is a parameter expressing the Z dependence,

$$b = \frac{1}{9} \left(12 + \frac{Z+1}{ZL_1 + L_2} \right) \quad (\text{A.29})$$

where $L_1 = \ln 184.15 - \frac{1}{3} \ln Z$ and $L_2 = \ln 1194 - \frac{2}{3} \ln Z$. The function Φ^{ext} is a correction for large photon energies. For the incoming electron, SIMC uses the

¹SIMC calculates external Bremsstrahlung for the region between the target chamber entrance window and the spectrometer entrance windows. Energy loss and multiple scattering are the dominant corrections in the magnets and detectors.

approximate form

$$\Phi_e^{ext} \left(\frac{E_e}{k} \right) = 1 - \frac{bt}{bt - \lambda_e} \frac{E_e}{k} \quad (\text{A.30})$$

SIMC combines the internal and external Bremsstrahlung into three photon energies E_e , $E_{e'}$, and $E_{p'}$

$$\frac{d\sigma}{d\Omega_e dE_e dE_{e'} dE_{p'}} = \frac{d\sigma}{d\Omega_e} \Big|_{ep} (1 - \delta_{hard}) \quad (\text{A.31})$$

$$\times \frac{1}{\Gamma(1 + bt_e)} \frac{bt_e + \lambda_e}{k^{bt_e} (kk')^{\lambda_e/2}} \frac{1}{E_e^{1-\lambda_e-bt_e}} \quad (\text{A.32})$$

$$\times \frac{1}{\Gamma(1 + bt_{e'})} \frac{bt_{e'} + \lambda_{e'}}{k^{bt_{e'}} (kk')^{\lambda_{e'}/2}} \frac{1}{E_{e'}^{1-\lambda_{e'}-bt_{e'}}} \quad (\text{A.33})$$

$$\times \frac{\lambda_{p'}}{(m_p p')^{\lambda_{p'}/2}} \frac{1}{E_{p'}^{1-\lambda_{p'}}} \quad (\text{A.34})$$

Using the energy distributions contained in this expression, SIMC generates the radiated energy based on the limits E_{min} and E_{max} imposed by the model spectral functions, spectrometer acceptances, and randomly generated initial and final 4-momenta of particles participating in scattering. These energies are then subtracted from the particles' vertex energies.

Then, SIMC generates a weight W_{rad}^{event} for the event based on the probabilities of emitting energies E_i , where i is one of e , e' , and p' . The first contribution to this weight, $W_{rad}^{soft} = W_{rad}^e W_{rad}^{e'} W_{rad}^{p'}$, is due to Bremsstrahlung, where

$$W_{rad}^e = \frac{1}{\Gamma(1 + bt_e)} \frac{1}{k^{bt_e} (kk')^{\lambda_e/2}} \left((E_{max}^e)^{bt+\lambda_e} - (E_{max}^e)^{bt+\lambda_e} \right) \quad (\text{A.35})$$

$$W_{rad}^{e'} = \frac{1}{\Gamma(1 + bt_{e'})} \frac{1}{k^{bt_{e'}} (kk')^{\lambda_{e'}/2}} \left((E_{max}^{e'})^{bt+\lambda_{e'}} - (E_{max}^{e'})^{bt+\lambda_{e'}} \right) \quad (\text{A.36})$$

$$W_{rad}^{p'} = \frac{1}{(m_p p')^{\lambda_{p'}/2}} \left((E_{max}^{p'})^{\lambda_{p'}} - (E_{max}^{p'})^{\lambda_{p'}} \right) \quad (\text{A.37})$$

The second contribution $\Phi^{ext} = \Phi_e^{ext} \Phi_{e'}^{ext}$ is due to external radiation. The final contribution $(1 - \delta_{hard})$ is due to vertex corrections. Altogether, the weight from radiative corrections is

$$W_{rad} = W_{rad}^{soft} \Phi^{ext} (1 - \delta_{hard}) \quad (\text{A.38})$$

A.4 Multiple Scattering

When recoiling protons, incoming electrons and scattered electrons travel through materials, they deviate from their original paths after scattering elastically off the nuclei that compose the material. SIMC includes a list of the effective thickness in radiation lengths t_{eff} of every material a particle passes through. As the simulated particle with momentum p passes through each material, a rescattering angle θ is calculated using the approximation of Molière's multiple scattering theory given in Equation (6) of Ref [187],

$$\theta = \frac{E_s}{p\beta} \sqrt{t_{eff}} \left[1 + \epsilon \log_{10} \left(\frac{t_{eff}}{\beta^2} \right) \right] \quad (\text{A.39})$$

where $E_s = 13.6 \text{ MeV}$ and $\epsilon = 0.088$ are parameters taken from fits to multiple scattering measurements taken at Fermilab [188]. These measurements were taken with incident pions, kaons, and protons at momenta between 50 and 200 GeV on hydrogen, beryllium, carbon, aluminum, copper, tin, and lead targets.

A.5 Energy Loss

Inelastic collisions with the atomic electrons of a material, resulting in ionization or excitation, are responsible for a particle's energy loss as it travels through the material. Energy loss in MeV is determined by the Bethe-Bloch formula, the implementation of which can currently be found in `enerloss_new.f`.

$$E_{loss} = K \frac{Z}{A} \frac{t}{\beta^2} \left[1.063 + \log \left(\frac{m_e}{I^2} \right) + 2 \log(\gamma\beta) - \beta^2 + \log \left(K \frac{Z}{A} \frac{t}{\beta^2} \right) - \delta \right] \quad (\text{A.40})$$

where $K = 0.1536 \times 10^{-3} \text{ cm}^2 \text{ g}^{-1}$, t is the thickness of the material in g cm^{-2} , Z and A are the effective atomic number and weight of the material, $I = 16Z^{0.9} \text{ eV}$ is the estimated ionization energy of the material, and δ is a momentum-dependent density effect correction.

The density effect arises from the fact that a charged particle will polarize the atoms in the material along its path. Electrons in atoms far from this path will be shielded and contribute less to the total energy loss. The magnitude of this effect

is greater at larger momenta.

Appendix B

Comparison of Experimental and Monte Carlo Distributions

This appendix compares the distributions of reconstructed target quantities measured in experiment to those generated by SIMC. Error bars are statistical only and the distributions are normalized to each other.

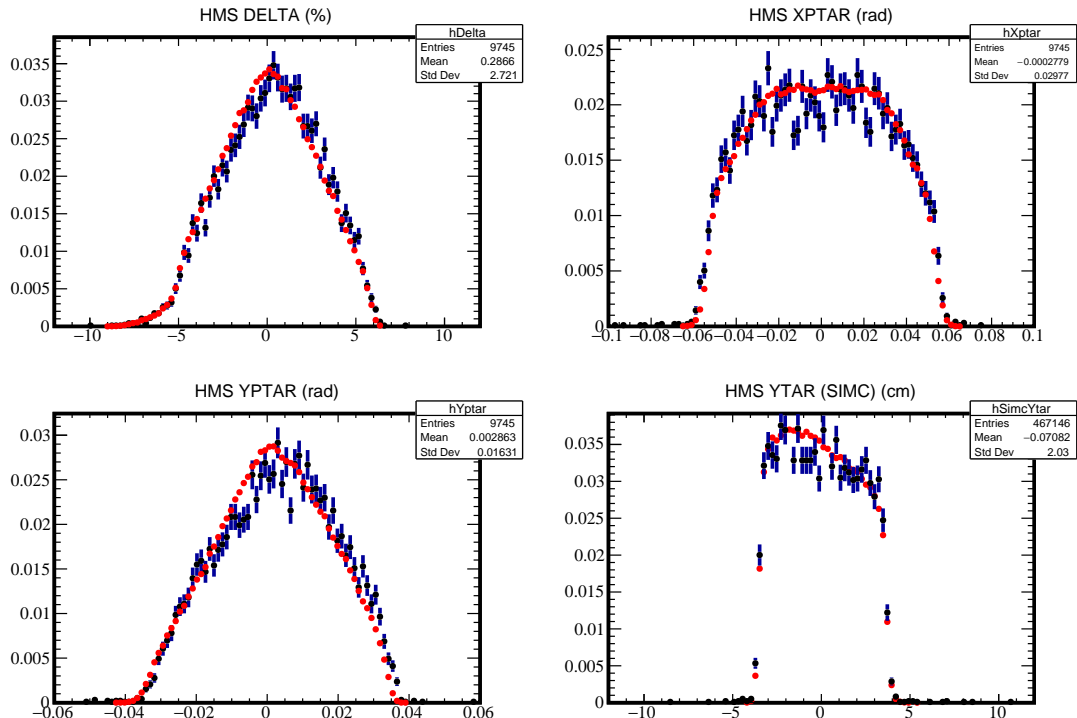


Figure B-1: Experimental (in blue) and Monte Carlo (in red) distributions of target quantities reconstructed from the HMS for the LH_2 target at $Q^2 = 8.0 \text{ GeV}^2$.

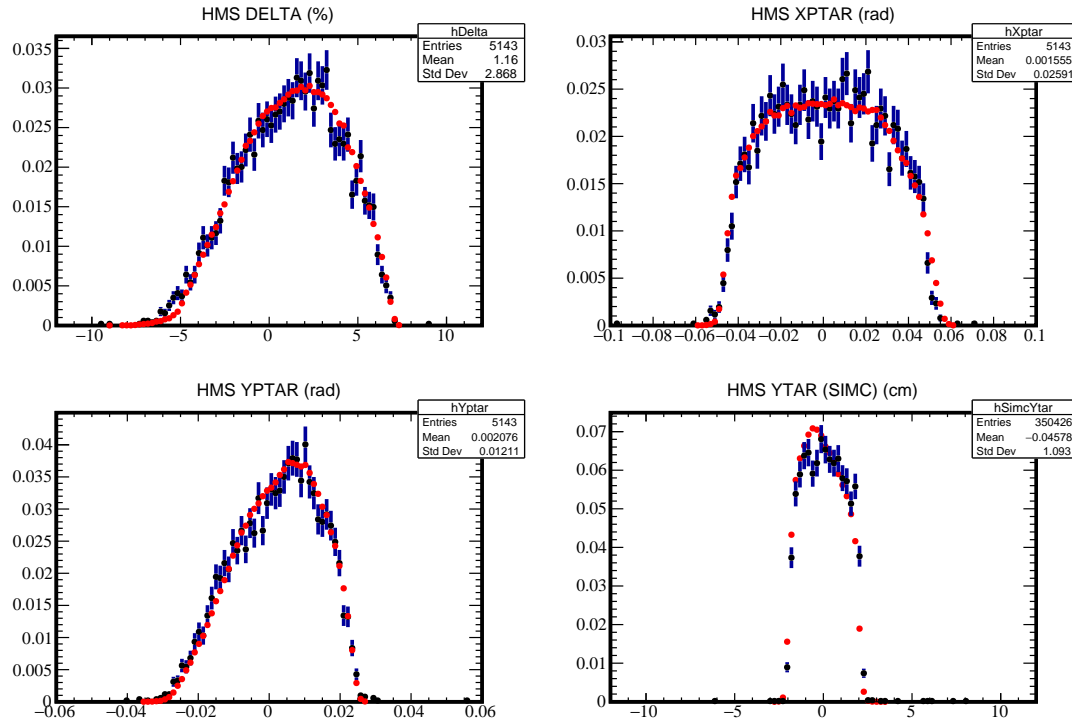


Figure B-2: Experimental (in blue) and Monte Carlo (in red) distributions of target quantities reconstructed from the HMS for the LH_2 target at $Q^2 = 9.5 \text{ GeV}^2$.

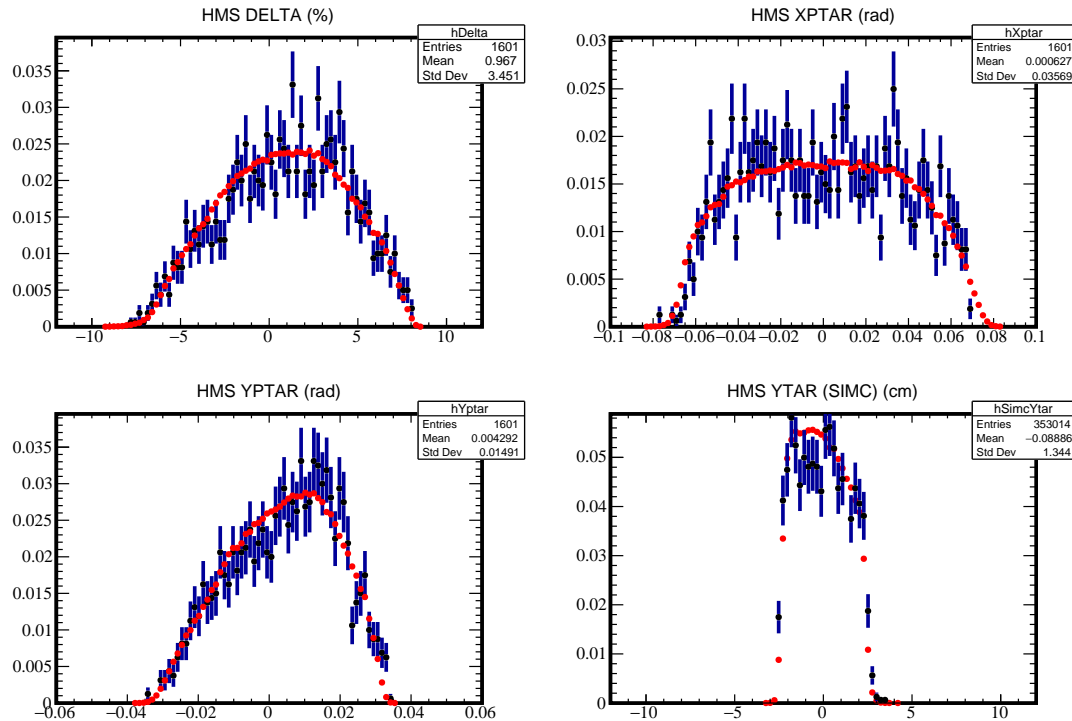


Figure B-3: Experimental (in blue) and Monte Carlo (in red) distributions of target quantities reconstructed from the HMS for the LH_2 target at $Q^2 = 11.5 \text{ GeV}^2$.

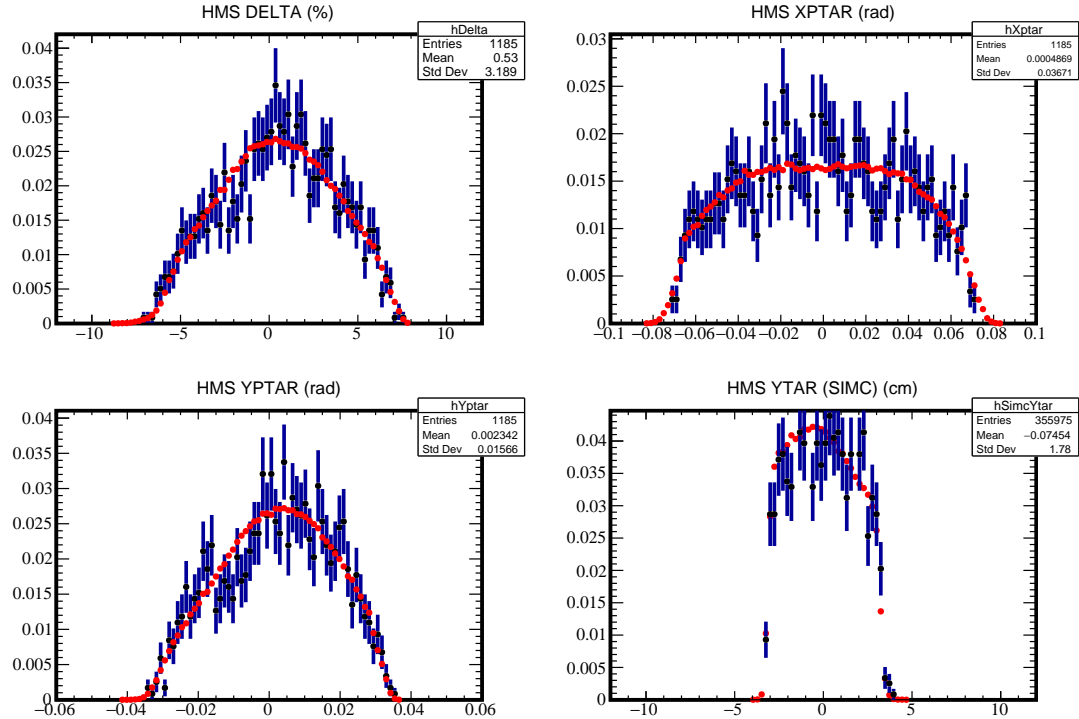


Figure B-4: Experimental (in blue) and Monte Carlo (in red) distributions of target quantities reconstructed from the HMS for the LH_2 target at $Q^2 = 14.2 \text{ GeV}^2$.

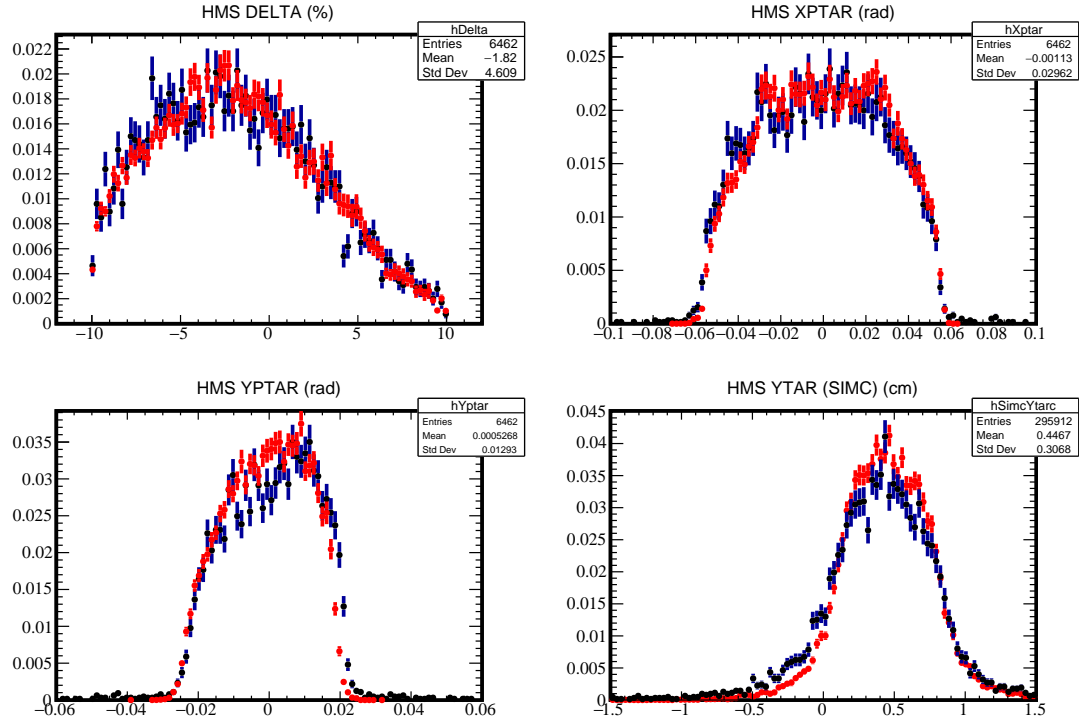


Figure B-5: Experimental (in blue) and Monte Carlo (in red) distributions of target quantities reconstructed from the HMS for the ^{12}C target at $Q^2 = 8.0 \text{ GeV}^2$.

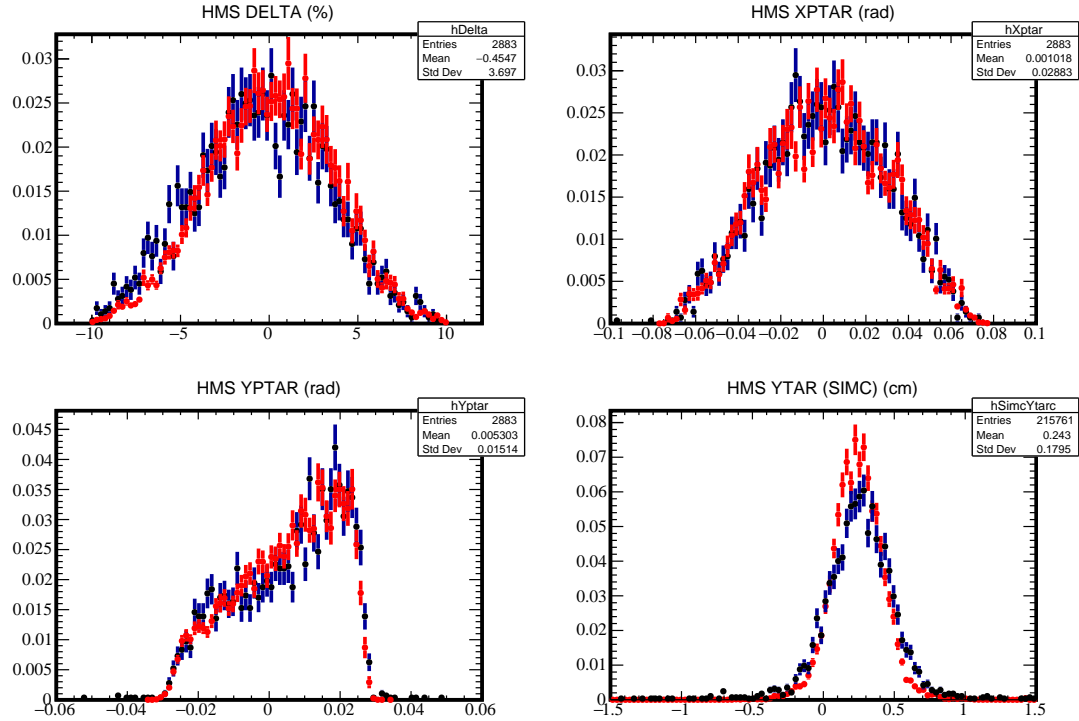


Figure B-6: Experimental (in blue) and Monte Carlo (in red) distributions of target quantities reconstructed from the HMS for the ^{12}C target at $Q^2 = 9.5 \text{ GeV}^2$.

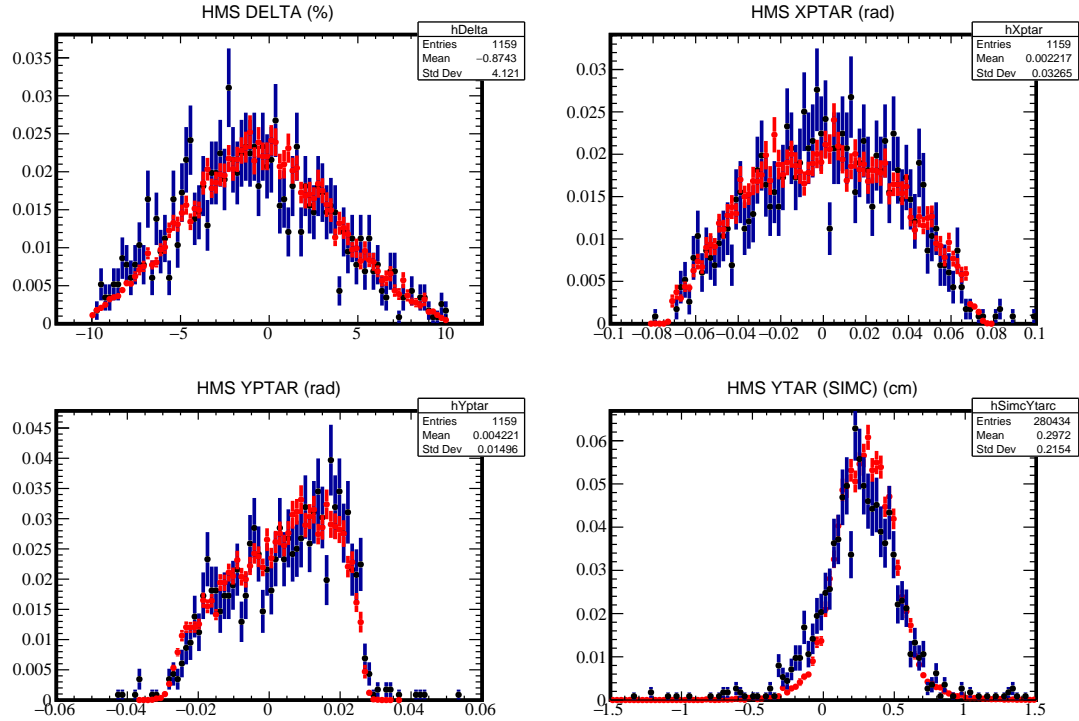


Figure B-7: Experimental (in blue) and Monte Carlo (in red) distributions of target quantities reconstructed from the HMS for the ^{12}C target at $Q^2 = 11.5 \text{ GeV}^2$.

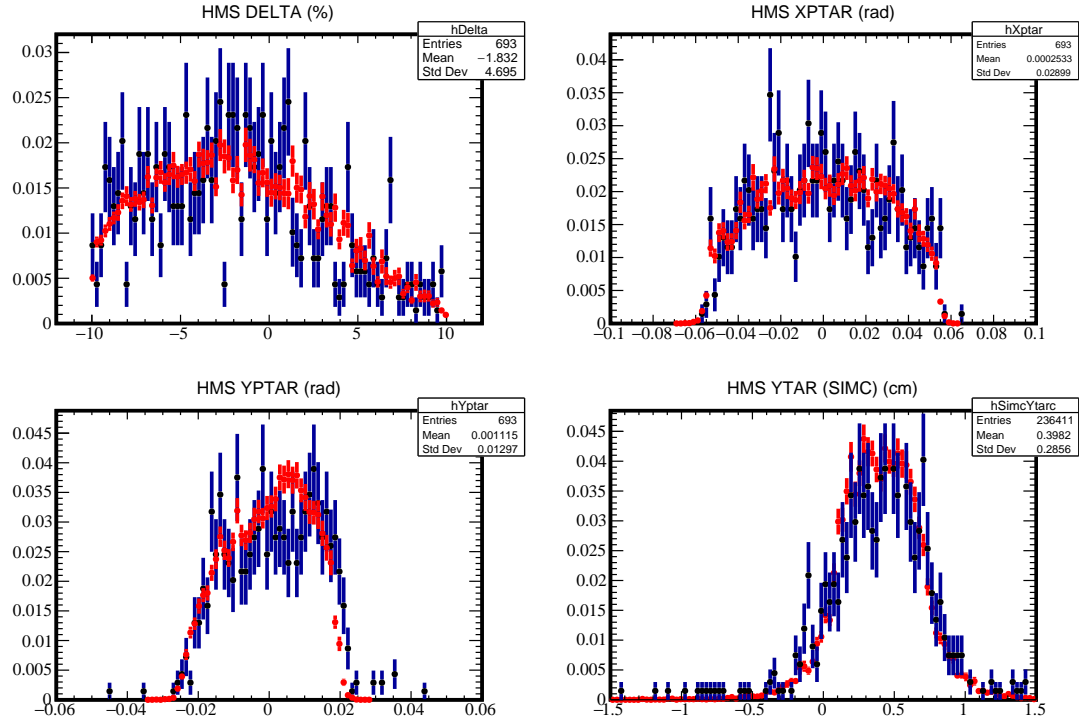


Figure B-8: Experimental (in blue) and Monte Carlo (in red) distributions of target quantities reconstructed from the HMS for the ^{12}C target at $Q^2 = 14.2 \text{ GeV}^2$.

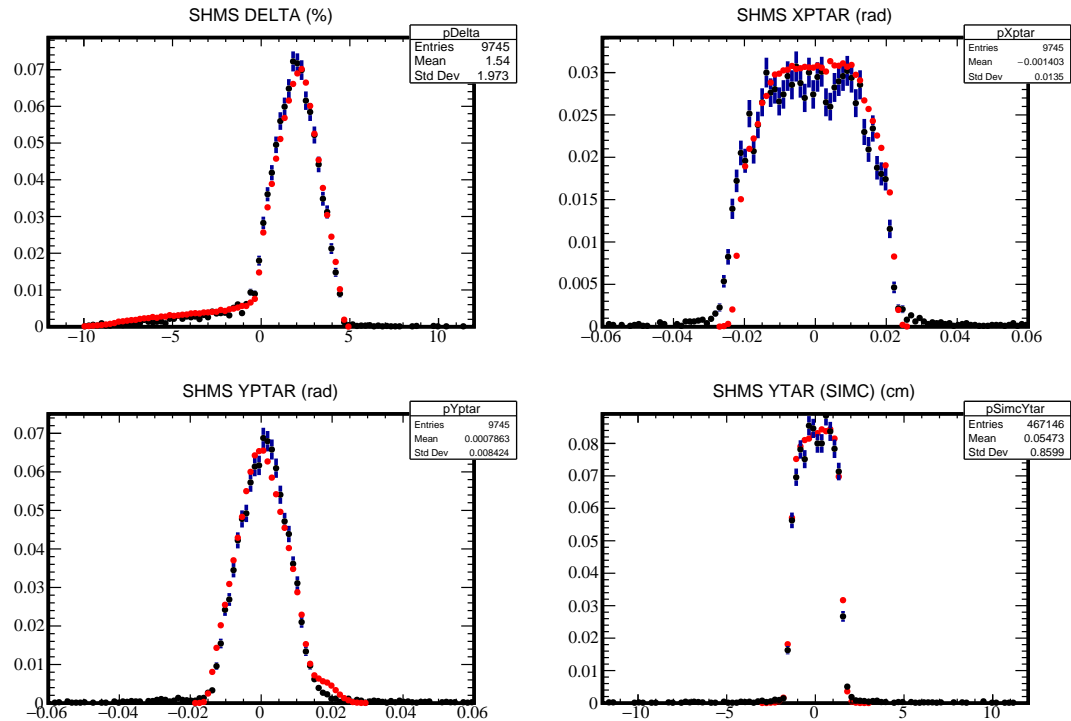


Figure B-9: Experimental (in blue) and Monte Carlo (in red) distributions of target quantities reconstructed from the SHMS for the LH_2 target at $Q^2 = 8.0 \text{ GeV}^2$.

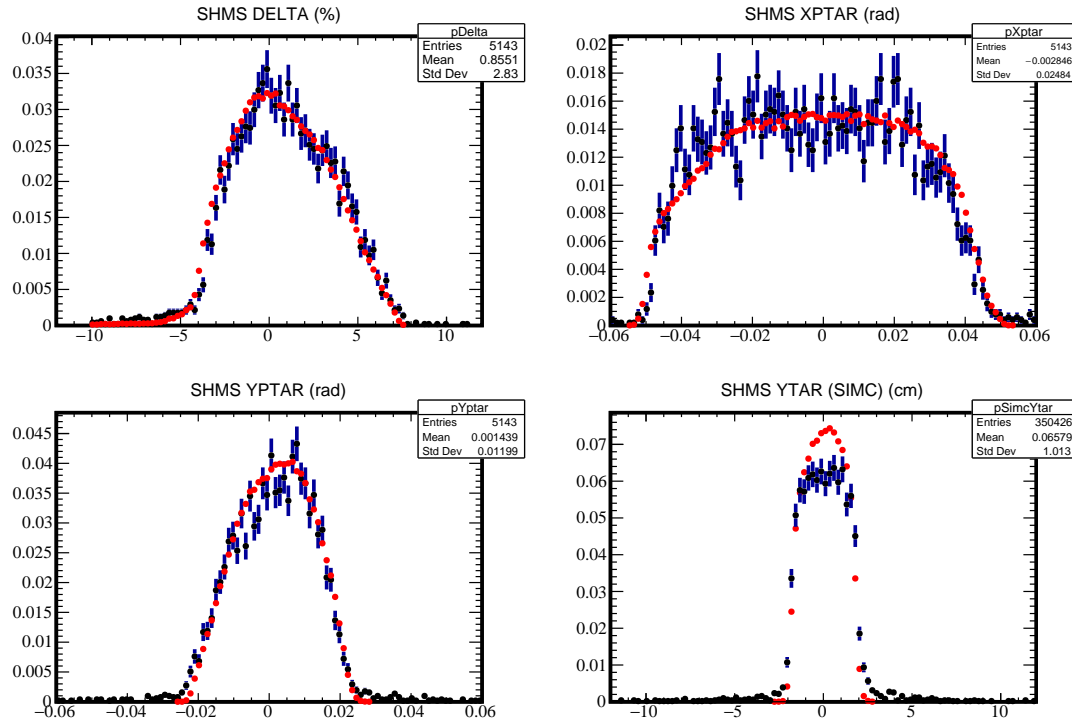


Figure B-10: Experimental (in blue) and Monte Carlo (in red) distributions of target quantities reconstructed from the SHMS for the LH_2 target at $Q^2 = 9.5 \text{ GeV}^2$.

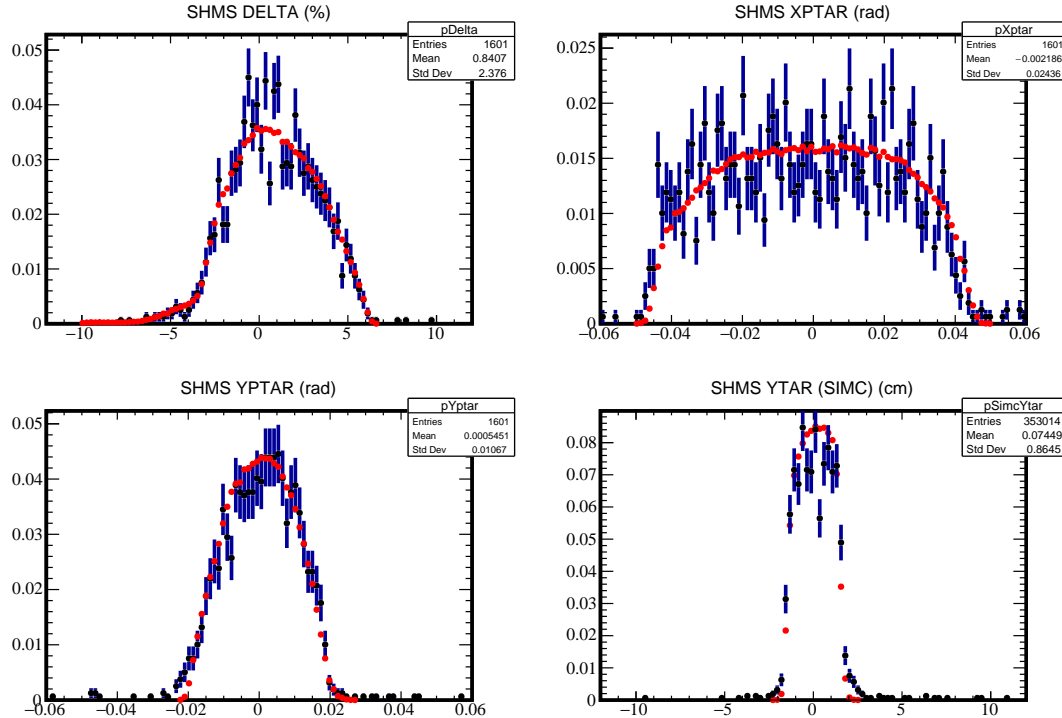


Figure B-11: Experimental (in blue) and Monte Carlo (in red) distributions of target quantities reconstructed from the SHMS for the LH_2 target at $Q^2 = 11.5 \text{ GeV}^2$.

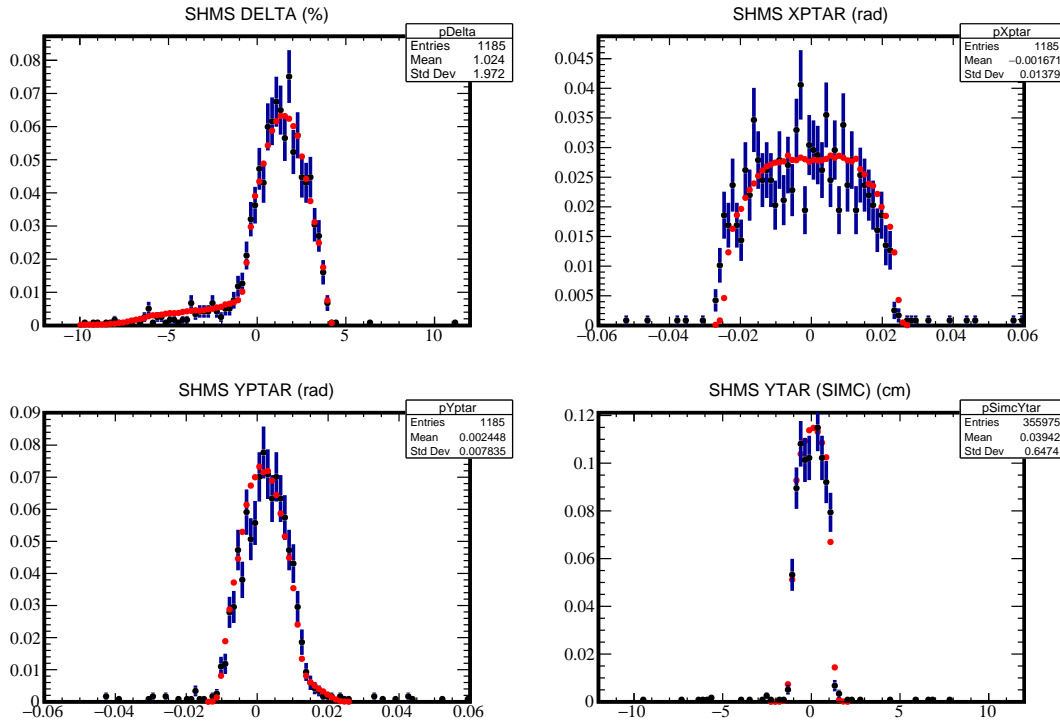


Figure B-12: Experimental (in blue) and Monte Carlo (in red) distributions of target quantities reconstructed from the SHMS for the LH_2 target at $Q^2 = 14.2 \text{ GeV}^2$.

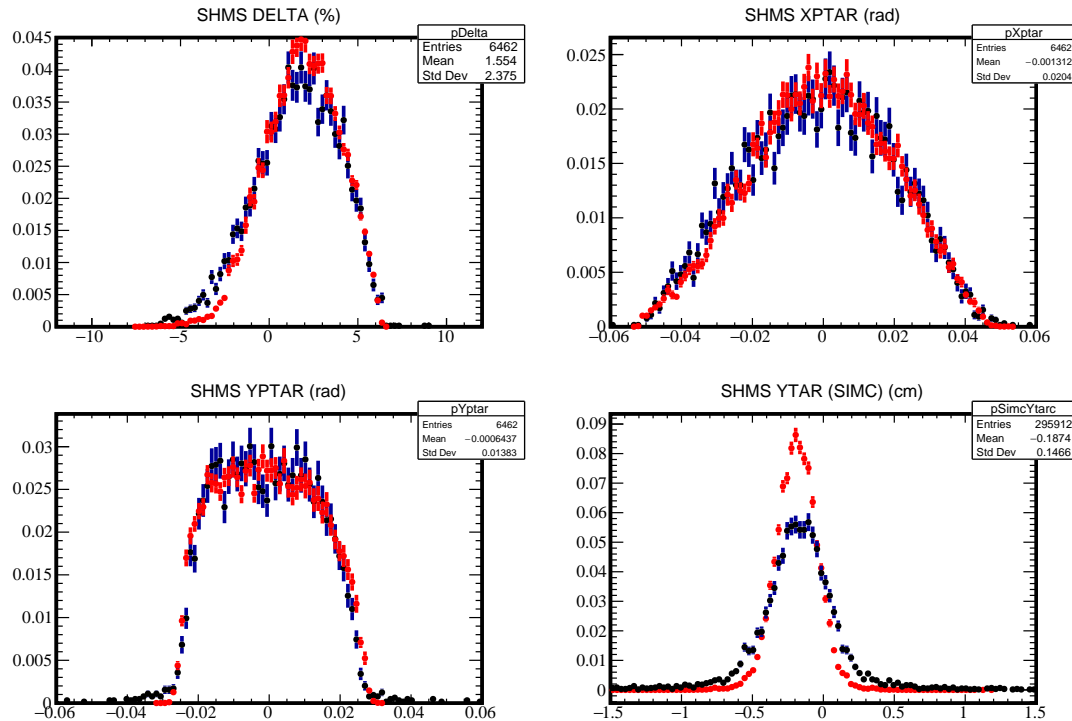


Figure B-13: Experimental (in blue) and Monte Carlo (in red) distributions of target quantities reconstructed from the SHMS for the ^{12}C target at $Q^2 = 8.0 \text{ GeV}^2$.

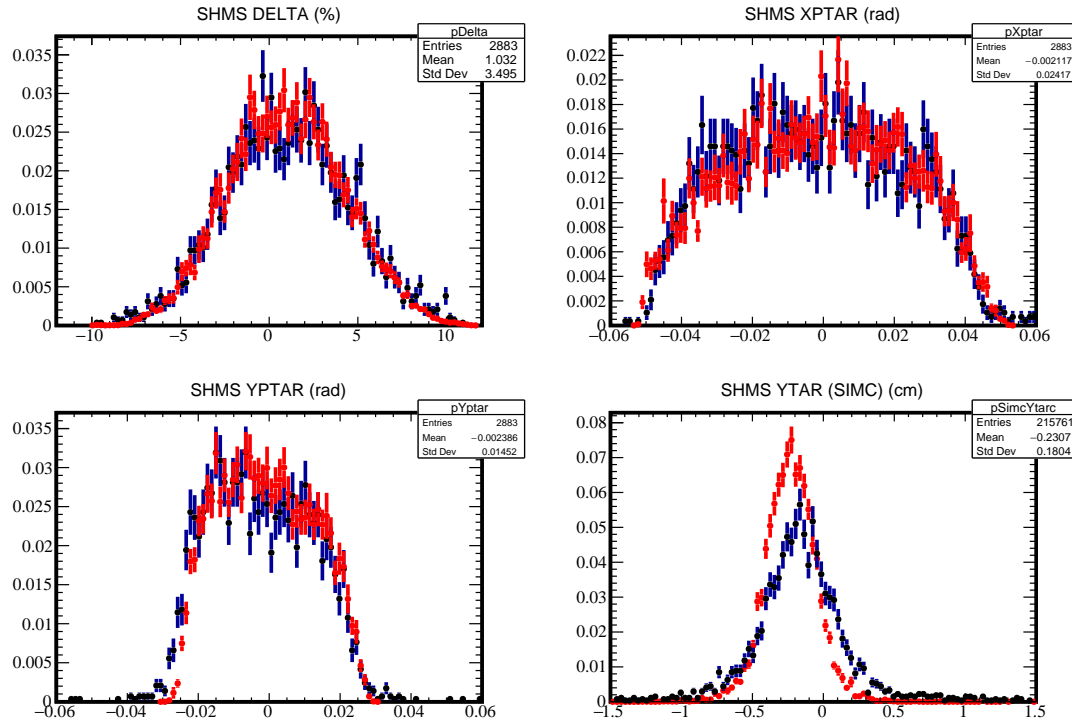


Figure B-14: Experimental (in blue) and Monte Carlo (in red) distributions of target quantities reconstructed from the SHMS for the ^{12}C target at $Q^2 = 9.5 \text{ GeV}^2$.

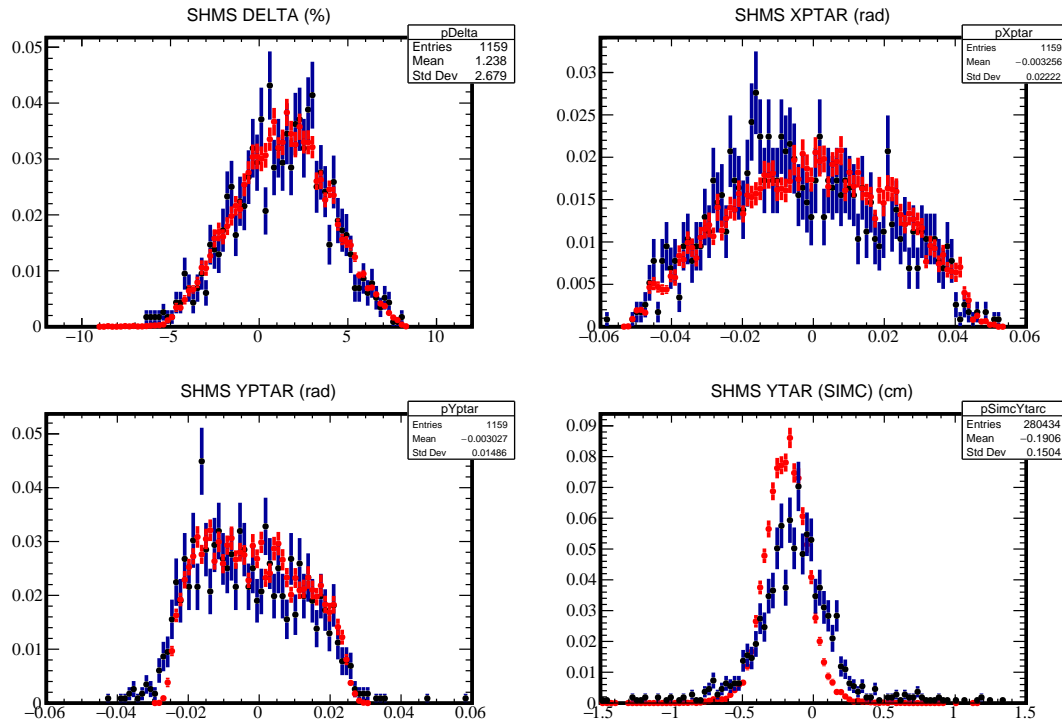


Figure B-15: Experimental (in blue) and Monte Carlo (in red) distributions of target quantities reconstructed from the SHMS for the ^{12}C target at $Q^2 = 11.5 \text{ GeV}^2$.

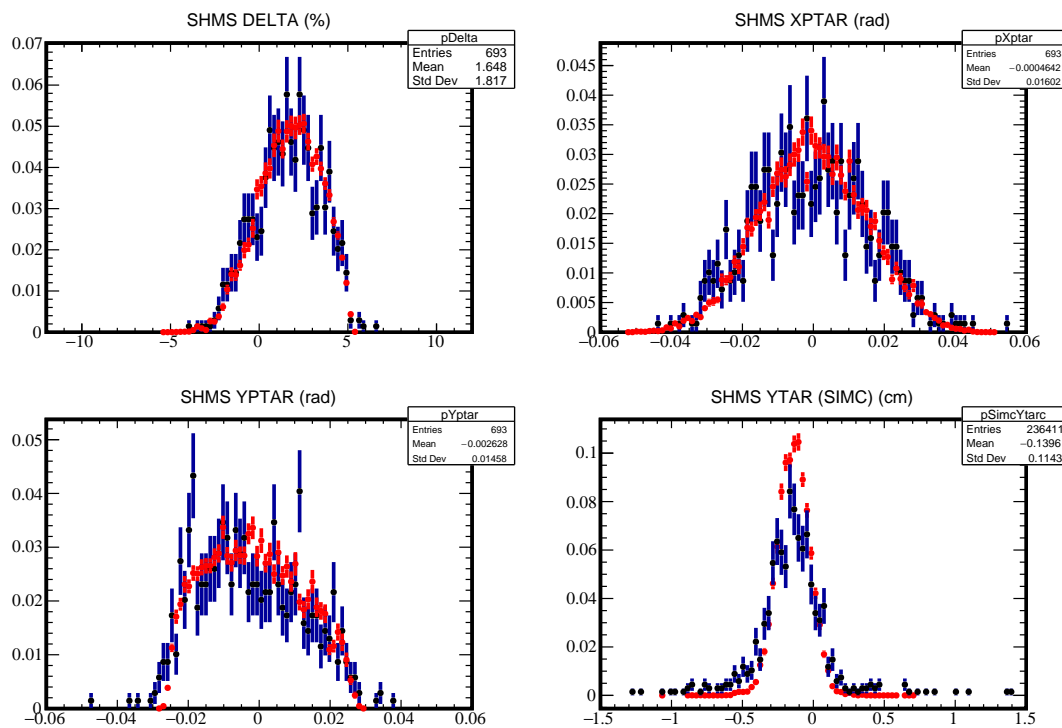


Figure B-16: Experimental (in blue) and Monte Carlo (in red) distributions of target quantities reconstructed from the SHMS for the ^{12}C target at $Q^2 = 14.2 \text{ GeV}^2$.

Bibliography

- [1] S. Berryman. Ancient Atomism. In E. N. Zalta, editor, *The Stanford Encyclopedia of Philosophy*. Metaphysics Research Lab, Stanford University, Winter 2016 edition, 2016. [1](#)
- [2] N. Huggett. Zeno’s Paradoxes. In E. N. Zalta, editor, *The Stanford Encyclopedia of Philosophy*. Metaphysics Research Lab, Stanford University, Winter 2019 edition, 2019. [1](#)
- [3] R. Brown. XXVII. A brief account of microscopical observations made in the months of June, July and August 1827, on the particles contained in the pollen of plants; and on the general existence of active molecules in organic and inorganic bodies. *The Philosophical Magazine*, 4(21):161–173, 1828. doi:10.1080/14786442808674769. URL <https://doi.org/10.1080/14786442808674769>. [2](#)
- [4] A. Einstein. Über die von der molekularkinetischen Theorie der Wärme geforderte Bewegung von in ruhenden Flüssigkeiten suspendierten Teilchen. *Annalen der Physik*, 322(8):549–560, January 1905. doi:10.1002/andp.19053220806. [2](#)
- [5] NobelPrize.org. Jean Baptiste Perrin – Biographical. URL <https://www.nobelprize.org/prizes/physics/1926/perrin>. [2](#)
- [6] E. Rutherford. The scattering of α and β particles by matter and the structure of the atom. *The London, Edinburgh, and Dublin Philosophical Magazine and Journal of Science*, 21(125):669–688, 1911. [2](#)
- [7] Wikimedia Commons. Standard Model of Elementary Particles, 2019. URL https://commons.wikimedia.org/wiki/File:Standard_Model_of_Elementary_Particles.svg. File: Standard Model of Elementary Particles.svg. [ix](#), [3](#)
- [8] B. Frois. The new frontiers of electron scattering at intermediate energy. *Nuclear Physics A*, 434:57–83, 1985. ISSN 0375-9474. doi:[https://doi.org/10.1016/0375-9474\(85\)90492-0](https://doi.org/10.1016/0375-9474(85)90492-0). URL <https://www.sciencedirect.com/science/article/pii/0375947485904920>. [5](#)
- [9] R. J. Glauber. High-Energy Collision Theory. *Lectures in Theoretical Physics*, I:315, 1959. [6](#), [12](#)
- [10] A. H. Mueller. Topics in High-Energy Perturbative QCD Including Interactions with Nuclear Matter. In *17th Rencontres de Moriond on Elementary*

- Particle Physics: I. Electroweak Interactions and Grand Unified Theories*, pages 13–43. 1982. URL <https://inspirehep.net/literature/181065>. 6, 24
- [11] S. J. Brodsky, et al. Breakdown of QCD Factorization Theorems for Inclusive Reactions. In *XIII International Symposium on Multiparticle Dynamics*, pages 841–854. 8 1982. URL <https://inspirehep.net/literature/179397>. 6, 24
 - [12] A. S. Carroll, et al. Nuclear Transparency to Large-Angle pp Elastic Scattering. *Phys. Rev. Lett.*, 61:1698–1701, Oct 1988. doi:10.1103/PhysRevLett.61.1698. URL <https://link.aps.org/doi/10.1103/PhysRevLett.61.1698>. 7, 35
 - [13] I. Mardor, et al. Nuclear Transparency in Large Momentum Transfer Quasielastic Scattering. *Phys. Rev. Lett.*, 81:5085–5088, Dec 1998. doi:10.1103/PhysRevLett.81.5085. URL <https://link.aps.org/doi/10.1103/PhysRevLett.81.5085>. 7, 35
 - [14] A. Leksanov, et al. Energy Dependence of Nuclear Transparency in C ($p, 2p$) Scattering. *Phys. Rev. Lett.*, 87:212301, Nov 2001. doi:10.1103/PhysRevLett.87.212301. URL <https://link.aps.org/doi/10.1103/PhysRevLett.87.212301>. 7, 35
 - [15] J. Aclander, et al. Nuclear transparency in $90^\circ_{\text{c.m.}}$ quasielastic $A(p, 2p)$ reactions. *Phys. Rev. C*, 70:015208, Jul 2004. doi:10.1103/PhysRevC.70.015208. URL <https://link.aps.org/doi/10.1103/PhysRevC.70.015208>. 7, 35, 36
 - [16] G. Garino, et al. Proton propagation in nuclei studied in the (e,e'p) reaction. *Phys. Rev. C*, 45:780–790, Feb 1992. doi:10.1103/PhysRevC.45.780. URL <https://link.aps.org/doi/10.1103/PhysRevC.45.780>. 7, 14, 16, 22, 38
 - [17] N. C. R. Makins, et al. Momentum transfer dependence of nuclear transparency from the quasielastic $^{12}\text{C}(\text{e}, \text{e}'\text{p})$ reaction. *Phys. Rev. Lett.*, 72:1986–1989, Mar 1994. doi:10.1103/PhysRevLett.72.1986. URL <https://link.aps.org/doi/10.1103/PhysRevLett.72.1986>. 7, 16, 21, 22, 38, 127
 - [18] T. O'Neill, et al. A-dependence of nuclear transparency in quasielastic $A(\text{e}, \text{e}'\text{p})$ at high Q2. *Physics Letters B*, 351(1):87–92, 1995. ISSN 0370-2693. doi:[https://doi.org/10.1016/0370-2693\(95\)00362-O](https://doi.org/10.1016/0370-2693(95)00362-O). URL <https://www.sciencedirect.com/science/article/pii/0370269395003620>. 7, 16, 22, 38, 113
 - [19] D. Abbott, et al. Quasifree ($e, e' p$) Reactions and Proton Propagation in Nuclei. *Phys. Rev. Lett.*, 80:5072–5076, Jun 1998. doi:10.1103/PhysRevLett.80.5072. URL <https://link.aps.org/doi/10.1103/PhysRevLett.80.5072>. 7, 14, 16, 22, 38
 - [20] K. Garrow, et al. Nuclear transparency from quasielastic $A(e, e' p)$ reactions up to $Q^2 = 8.1(\text{GeV}/c)^2$. *Phys. Rev. C*, 66:044613, Oct 2002.

- doi:10.1103/PhysRevC.66.044613. URL <https://link.aps.org/doi/10.1103/PhysRevC.66.044613>. 7, 14, 16, 22, 38
- [21] D. Rohe, et al. Nuclear transparency from quasielastic $^{12}\text{C}(e, e' p)$. *Phys. Rev. C*, 72:054602, Nov 2005. doi:10.1103/PhysRevC.72.054602. URL <https://link.aps.org/doi/10.1103/PhysRevC.72.054602>. 7, 11, 14, 16, 22, 38
- [22] B. Clasie, et al. Measurement of Nuclear Transparency for the $A(e, e' \pi^+)$ Reaction. *Phys. Rev. Lett.*, 99:242502, Dec 2007. doi:10.1103/PhysRevLett.99.242502. URL <https://link.aps.org/doi/10.1103/PhysRevLett.99.242502>. x, 7, 39, 40
- [23] X. Qian, et al. Experimental study of the $A(e, e' \pi^+)$ reaction on ^1H , ^2H , ^{12}C , ^{27}Al , ^{63}Cu , and ^{197}Au . *Phys. Rev. C*, 81:055209, May 2010. doi:10.1103/PhysRevC.81.055209. URL <https://link.aps.org/doi/10.1103/PhysRevC.81.055209>. x, 7, 39, 40
- [24] Particle Data Group, et al. Review of Particle Physics. *Progress of Theoretical and Experimental Physics*, 2020(8), 08 2020. ISSN 2050-3911. doi:10.1093/ptep/ptaa104. URL <https://doi.org/10.1093/ptep/ptaa104.083C01>. 8
- [25] A. Dieperink et al. Knock-out processes and removal energies. *Annual Review of Nuclear Science*, 25(1):1–26, 1975. 10
- [26] T. De Forest. Off-shell electron-nucleon cross sections: The impulse approximation. *Nuclear Physics A*, 392(2):232–248, 1983. ISSN 0375-9474. doi:[https://doi.org/10.1016/0375-9474\(83\)90124-0](https://doi.org/10.1016/0375-9474(83)90124-0). URL <https://www.sciencedirect.com/science/article/pii/0375947483901240>. 10, 11
- [27] S. Frullani, et al. Single particle properties of nuclei through $(e, e' p)$ reactions. *Advances in Nuclear Physics*, 14, 1984. 10, 18, 126
- [28] A. Dieperink, et al. Quasi-elastic electron scattering on ^3He . *Physics Letters B*, 63(3):261–264, 1976. ISSN 0370-2693. doi:[https://doi.org/10.1016/0370-2693\(76\)90258-6](https://doi.org/10.1016/0370-2693(76)90258-6). URL <https://www.sciencedirect.com/science/article/pii/0370269376902586>. 11
- [29] J. Mougey, et al. Quasi-free $(e, e' p)$ scattering on ^{12}C , ^{28}Si , ^{40}Ca and ^{58}Ni . *Nuclear Physics A*, 262(3):461–492, 1976. ISSN 0375-9474. doi:[https://doi.org/10.1016/0375-9474\(76\)90510-8](https://doi.org/10.1016/0375-9474(76)90510-8). URL <https://www.sciencedirect.com/science/article/pii/0375947476905108>. 11, 126
- [30] O. Benhar, et al. Final state interactions in $^4\text{He}(e, e' p)^3\text{H}$ at large proton energy. *Nuclear Physics A*, 673(1):241–255, 2000. ISSN 0375-9474. doi:[https://doi.org/10.1016/S0375-9474\(00\)00126-3](https://doi.org/10.1016/S0375-9474(00)00126-3). URL <https://www.sciencedirect.com/science/article/pii/S0375947400001263>. 11
- [31] R. Schiavilla, et al. RB Wiringa, S. Fantoni. *Nucl. Phys. A*, 473:267, 1987. 14, 15

- [32] V. R. Pandharipande et al. Nuclear transparency to intermediate-energy nucleons from (e,e'p) reactions. *Phys. Rev. C*, 45:791–798, Feb 1992. doi:10.1103/PhysRevC.45.791. URL <https://link.aps.org/doi/10.1103/PhysRevC.45.791>. 14, 16, 22, 38, 120, 121
- [33] I. Lagaris et al. Phenomenological two-nucleon interaction operator. *Nuclear Physics A*, 359(2):331–348, 1981. ISSN 0375-9474. doi:[https://doi.org/10.1016/0375-9474\(81\)90240-2](https://doi.org/10.1016/0375-9474(81)90240-2). URL <https://www.sciencedirect.com/science/article/pii/0375947481902402>. 14
- [34] I. Lagaris et al. Variational calculations of realistic models of nuclear matter. *Nuclear Physics A*, 359(2):349–364, 1981. ISSN 0375-9474. doi:[https://doi.org/10.1016/0375-9474\(81\)90241-4](https://doi.org/10.1016/0375-9474(81)90241-4). URL <https://www.sciencedirect.com/science/article/pii/0375947481902414>. 14
- [35] R. B. Wiringa. Single-particle potential in dense nuclear matter. *Phys. Rev. C*, 38:2967–2970, Dec 1988. doi:10.1103/PhysRevC.38.2967. URL <https://link.aps.org/doi/10.1103/PhysRevC.38.2967>. 14
- [36] B. Friedman et al. The single particle potential in nuclear matter. *Physics Letters B*, 100(3):205–208, 1981. ISSN 0370-2693. doi:[https://doi.org/10.1016/0370-2693\(81\)90317-8](https://doi.org/10.1016/0370-2693(81)90317-8). URL <https://www.sciencedirect.com/science/article/pii/0370269381903178>. 14
- [37] R. Arndt, et al. Nucleon-nucleon scattering analyses. II. Neutron-proton scattering from 0 to 425 MeV and proton-proton scattering from 1 to 500 MeV. *Physical Review C*, 15(3):1002, 1977. 14
- [38] L. L. Frankfurt, et al. Correlation effects in nuclear transparency. *Phys. Rev. C*, 51:3435–3444, Jun 1995. doi:10.1103/PhysRevC.51.3435. URL <https://link.aps.org/doi/10.1103/PhysRevC.51.3435>. ix, 16, 19, 22, 121
- [39] G. R. Farrar, et al. Transparency in Nuclear Quasiexclusive Processes with Large Momentum Transfer. *Phys. Rev. Lett.*, 61:686–689, Aug 1988. doi:10.1103/PhysRevLett.61.686. URL <https://link.aps.org/doi/10.1103/PhysRevLett.61.686>. 16, 17, 27, 28, 39, 40, 41, 45
- [40] W. Cosyn, et al. Color transparency and short-range correlations in exclusive pion photo- and electroproduction from nuclei. *Phys. Rev. C*, 77:034602, Mar 2008. doi:10.1103/PhysRevC.77.034602. URL <https://link.aps.org/doi/10.1103/PhysRevC.77.034602>. x, 16, 22, 40
- [41] W. Cosyn, et al. Nuclear transparencies from photoinduced pion production. *Phys. Rev. C*, 74:062201, Dec 2006. doi:10.1103/PhysRevC.74.062201. URL <https://link.aps.org/doi/10.1103/PhysRevC.74.062201>. 16, 22, 39, 42, 121
- [42] J. Ryckebusch, et al. Relativistic formulation of Glauber theory for A(e,e'p) reactions. *Nuclear Physics A*, 728(1):226–250, 2003. ISSN 0375-9474. doi:<https://doi.org/10.1016/j.nuclphysa.2003.08.022>. URL <https://www.sciencedirect.com/science/article/pii/S0375947403017123>. 17, 19

- [43] S. Frankel, et al. Extracting nuclear transparency from p,2p-A and e,e'p-A cross sections. *Nuclear Physics A*, 580(4):595–613, 1994. ISSN 0375-9474. doi:[https://doi.org/10.1016/0375-9474\(94\)90783-8](https://doi.org/10.1016/0375-9474(94)90783-8). URL <https://www.sciencedirect.com/science/article/pii/0375947494907838>. 17
- [44] JLab Hall C Collaboration. GitHub - JeffersonLab/simc_gfortran. URL https://github.com/JeffersonLab/simc_gfortran. 21
- [45] JLab Hall C Collaboration. SIMC Monte Carlo - HallCWiki. URL https://hallcweb.jlab.org/wiki/index.php/SIMC_Monte_Carlo. 21
- [46] D. Perkins. Ionization at the origin of electron Pairs, and the lifetime of the neutral pion. *Philosophical Magazine Series 1*, 46:1146–1148, 1955. doi: <https://doi.org/10.1080/14786441008521131>. 24
- [47] P. Fowler et al. LXVIII. Measurement of ionization in nuclear emulsions. *The London, Edinburgh, and Dublin Philosophical Magazine and Journal of Science*, 46(377):587–610, 1955. doi:10.1080/14786440608521107. URL <https://doi.org/10.1080/14786440608521107>. 24
- [48] W. Wolter et al. Ionization at the origin of an electron pair of very high energy. *Il Nuovo Cimento (1955-1965)*, 4(3):648–650, 1956. 24
- [49] J. Iwadare. Suppression effect of the ionization produced by electron-positron pairs of extremely high energy. *The Philosophical Magazine: A Journal of Theoretical Experimental and Applied Physics*, 3(31):680–691, 1958. doi:10.1080/14786435808237003. URL <https://doi.org/10.1080/14786435808237003>. 24
- [50] A. A. Varfolomeev, et al. Ionization along the Tracks of High-Energy Electron-Positron Pairs. *Journal of Experimental and Theoretical Physics*, 36(3):707–717, 1959. URL <http://www.jetp.ac.ru/cgi-bin/e/index/r/36/3/p707?a=list>. 24
- [51] I. P. Zieliński. On the possibility of the electronic measurement of the King-Perkins-Chudakov effect for electron pairs using a multilayer silicon detector. *Nuclear Instruments and Methods in Physics Research Section A: Accelerators, Spectrometers, Detectors and Associated Equipment*, 238(2):562 – 563, 1985. ISSN 0168-9002. doi:[https://doi.org/10.1016/0168-9002\(85\)90502-9](https://doi.org/10.1016/0168-9002(85)90502-9). URL <https://www.sciencedirect.com/science/article/pii/0168900285905029>. 24
- [52] J. Bjorken. Hadron Final States in Deep Inelastic Processes. *Lect. Notes Phys.*, 56:93, 1976. 24
- [53] L. Frankfurt, et al. Color transparency phenomenon and nuclear physics. Technical report, P00001036, 1992. URL <https://inspirehep.net/literature/333065>. 25
- [54] S. Brodsky, et al. Hadronic wave functions at short distances and the operator product expansion. *Physics Letters B*, 91(2):239 – 244, 1980. ISSN 0370-2693. doi:[https://doi.org/10.1016/0370-2693\(80\)90441-4](https://doi.org/10.1016/0370-2693(80)90441-4). URL <https://www.sciencedirect.com/science/article/pii/0370269380904414>. 25

- [55] G. P. Lepage et al. Exclusive processes in perturbative quantum chromodynamics. *Phys. Rev. D*, 22:2157–2198, Nov 1980. doi:10.1103/PhysRevD.22.2157. URL <https://link.aps.org/doi/10.1103/PhysRevD.22.2157>. 25, 32, 36
- [56] N. Isgur et al. Asymptopia in High Q^{**2} Exclusive Processes in QCD. *Phys. Rev. Lett.*, 52:1080, 1984. doi:10.1103/PhysRevLett.52.1080. 25
- [57] N. Isgur et al. The Applicability of Perturbative QCD to Exclusive Processes. *Nucl. Phys. B*, 317:526–572, 1989. doi:10.1016/0550-3213(89)90532-4. 25
- [58] N. Isgur et al. Perturbative QCD in exclusive processes. *Phys. Lett. B*, 217:535–538, 1989. doi:10.1016/0370-2693(89)90092-0. 25
- [59] F. E. Low. Model of the bare Pomeron. *Phys. Rev. D*, 12:163–173, Jul 1975. doi:10.1103/PhysRevD.12.163. URL <https://link.aps.org/doi/10.1103/PhysRevD.12.163>. 25
- [60] S. Nussinov. Colored-Quark Version of Some Hadronic Puzzles. *Phys. Rev. Lett.*, 34:1286–1289, May 1975. doi:10.1103/PhysRevLett.34.1286. URL <https://link.aps.org/doi/10.1103/PhysRevLett.34.1286>. 25
- [61] S. Nussinov. Perturbative recipe for quark-gluon theories and some of its applications. *Phys. Rev. D*, 14:246–257, Jul 1976. doi:10.1103/PhysRevD.14.246. URL <https://link.aps.org/doi/10.1103/PhysRevD.14.246>. 25
- [62] J. F. Gunion et al. Quark-counting and hadron-size effects for total cross sections. *Phys. Rev. D*, 15:2617–2621, May 1977. doi:10.1103/PhysRevD.15.2617. URL <https://link.aps.org/doi/10.1103/PhysRevD.15.2617>. 25
- [63] S. J. Brodsky, et al. Light-front holographic QCD and emerging confinement. *Physics Reports*, 584:1–105, 2015. ISSN 0370-1573. doi:<https://doi.org/10.1016/j.physrep.2015.05.001>. URL <https://www.sciencedirect.com/science/article/pii/S0370157315002306>. Light-front holographic QCD and emerging confinement. 26
- [64] S. J. Brodsky et al. The Onset of Color Transparency in Holographic Light-Front QCD, 2021. URL <https://indico.jlab.org/event/437/contributions/8362/>. The Future of Color Transparency and Hadronization Studies at Jefferson Lab and Beyond. 26, 27, 123
- [65] B. Jennings et al. On color transparency. *Physics Letters B*, 236(2):209 – 213, 1990. ISSN 0370-2693. doi:[https://doi.org/10.1016/0370-2693\(90\)90830-Y](https://doi.org/10.1016/0370-2693(90)90830-Y). URL <https://www.sciencedirect.com/science/article/pii/037026939090830Y>. 28
- [66] B. K. Jennings et al. Energy dependence of color transparency. *Phys. Rev. D*, 44:692–703, Aug 1991. doi:10.1103/PhysRevD.44.692. URL <https://link.aps.org/doi/10.1103/PhysRevD.44.692>. 28

- [67] B. K. Jennings et al. Realistic hadronic matrix element approach to color transparency. *Phys. Rev. Lett.*, 69:3619–3622, Dec 1992. doi:10.1103/PhysRevLett.69.3619. URL <https://link.aps.org/doi/10.1103/PhysRevLett.69.3619>. 28
- [68] S. J. Brodsky, et al. Diffractive lepto production of vector mesons in QCD. *Phys. Rev. D*, 50:3134–3144, Sep 1994. doi:10.1103/PhysRevD.50.3134. URL <https://link.aps.org/doi/10.1103/PhysRevD.50.3134>. 29, 31, 34
- [69] J. C. Collins, et al. Factorization for hard exclusive electroproduction of mesons in QCD. *Phys. Rev. D*, 56:2982–3006, Sep 1997. doi:10.1103/PhysRevD.56.2982. URL <https://link.aps.org/doi/10.1103/PhysRevD.56.2982>. 29, 30
- [70] L. L. Frankfurt, et al. Hard exclusive pseudoscalar meson electroproduction and spin structure of the nucleon. *Phys. Rev. D*, 60:014010, Jun 1999. doi:10.1103/PhysRevD.60.014010. URL <https://link.aps.org/doi/10.1103/PhysRevD.60.014010>. 29
- [71] M. Diehl, et al. Probing Partonic Structure in $\gamma^*\gamma \rightarrow \pi\pi$ near Threshold. *Phys. Rev. Lett.*, 81:1782–1785, Aug 1998. doi:10.1103/PhysRevLett.81.1782. URL <https://link.aps.org/doi/10.1103/PhysRevLett.81.1782>. 29
- [72] M. Strikman. QCD Factorization theorems for DIS exclusive processes and inclusive diffraction: New probes of hadrons and nuclei. *Nuclear Physics A*, 663-664:64c – 73c, 2000. ISSN 0375-9474. doi:[https://doi.org/10.1016/S0375-9474\(99\)00573-4](https://doi.org/10.1016/S0375-9474(99)00573-4). URL <http://www.sciencedirect.com/science/article/pii/S0375947499005734>. 29
- [73] X. Ji. Gauge-Invariant Decomposition of Nucleon Spin. *Phys. Rev. Lett.*, 78:610–613, Jan 1997. doi:10.1103/PhysRevLett.78.610. URL <https://link.aps.org/doi/10.1103/PhysRevLett.78.610>. 29
- [74] X. Ji. Deeply virtual Compton scattering. *Phys. Rev. D*, 55:7114–7125, Jun 1997. doi:10.1103/PhysRevD.55.7114. URL <https://link.aps.org/doi/10.1103/PhysRevD.55.7114>. 29
- [75] A. Radyushkin. Scaling limit of deeply virtual compton scattering. *Physics Letters B*, 380(3):417 – 425, 1996. ISSN 0370-2693. doi:[https://doi.org/10.1016/0370-2693\(96\)00528-X](https://doi.org/10.1016/0370-2693(96)00528-X). URL <http://www.sciencedirect.com/science/article/pii/037026939600528X>. 29
- [76] A. V. Radyushkin. Nonforward parton distributions. *Phys. Rev. D*, 56:5524–5557, Nov 1997. doi:10.1103/PhysRevD.56.5524. URL <https://link.aps.org/doi/10.1103/PhysRevD.56.5524>. 29
- [77] J. C. Collins, et al. Proof of Factorization for Exclusive Deep-Inelastic Processes. *Low x Physics*, Jun 1998. doi:10.1142/9789814447256_0041. URL http://dx.doi.org/10.1142/9789814447256_0041. 29

- [78] D. Dutta et al. The search for the onset of color transparency: A status report. *Int. J. Mod. Phys.*, E21:1230004, 2012. doi:10.1142/S0218301312300044. 30, 47
- [79] L. Mankiewicz et al. Remarks on exclusive electroproduction of transversely polarized vector mesons. *Phys. Rev. D*, 61:074013, Feb 2000. doi:10.1103/PhysRevD.61.074013. URL <https://link.aps.org/doi/10.1103/PhysRevD.61.074013>. 30
- [80] B. Blättel, et al. How transparent are hadrons to pions? *Phys. Rev. Lett.*, 70:896–899, Feb 1993. doi:10.1103/PhysRevLett.70.896. URL <https://link.aps.org/doi/10.1103/PhysRevLett.70.896>. 31
- [81] L. Frankfurt, et al. Coherent nuclear diffractive production of mini-jets — illuminating color transparency. *Physics Letters B*, 304(1):1 – 7, 1993. ISSN 0370-2693. doi:[https://doi.org/10.1016/0370-2693\(93\)91390-9](https://doi.org/10.1016/0370-2693(93)91390-9). URL <http://www.sciencedirect.com/science/article/pii/0370269393913909>. 31, 32, 33
- [82] L. L. Frankfurt, et al. Perturbative Pion Wave Function in Coherent Pion-Nucleon Di-Jet Production. *Found. Phys.*, 30:533–542, April 2000. doi:10.1023/A:1003616828027. URL <https://link.springer.com/article/10.1023/A:1003616828027>. 31
- [83] L. Frankfurt, et al. Coherent QCD phenomena in the coherent pion-nucleon and pion-nucleus production of two jets at high relative momenta. *Phys. Rev. D*, 65:094015, May 2002. doi:10.1103/PhysRevD.65.094015. URL <https://link.aps.org/doi/10.1103/PhysRevD.65.094015>. 31
- [84] L. Frankfurt, et al. Hard diffractive electroproduction of vector mesons in QCD. *Phys. Rev. D*, 54:3194–3215, Sep 1996. doi:10.1103/PhysRevD.54.3194. URL <https://link.aps.org/doi/10.1103/PhysRevD.54.3194>. 31
- [85] M. D. Sokoloff, et al. Experimental Study of the A Dependence of $\frac{J}{\psi}$ Photoproduction. *Phys. Rev. Lett.*, 57:3003–3006, Dec 1986. doi:10.1103/PhysRevLett.57.3003. URL <https://link.aps.org/doi/10.1103/PhysRevLett.57.3003>. 31
- [86] T. H. Bauer, et al. The hadronic properties of the photon in high-energy interactions. *Rev. Mod. Phys.*, 50:261–436, Apr 1978. doi:10.1103/RevModPhys.50.261. URL <https://link.aps.org/doi/10.1103/RevModPhys.50.261>. 31
- [87] G. A. Miller, et al. Pion transverse charge density from timelike form factor data. *Phys. Rev. D*, 83:013006, Jan 2011. doi:10.1103/PhysRevD.83.013006. URL <https://link.aps.org/doi/10.1103/PhysRevD.83.013006>. ix, 32, 33
- [88] E. M. Aitala, et al. Direct Measurement of the Pion Valence-Quark Momentum Distribution, the Pion Light-Cone Wave Function Squared. *Phys. Rev. Lett.*, 86:4768–4772, May 2001. doi:10.1103/PhysRevLett.86.4768. URL <https://link.aps.org/doi/10.1103/PhysRevLett.86.4768>. 32

- [89] E. M. Aitala, et al. Observation of Color-Transparency in Diffractive Dissociation of Pions. *Phys. Rev. Lett.*, 86:4773–4777, May 2001. doi:10.1103/PhysRevLett.86.4773. URL <https://link.aps.org/doi/10.1103/PhysRevLett.86.4773>. 32
- [90] M. Zielinski, et al. Three pion production on nuclei at 200 GeV. *Zeitschrift für Physik C Particles and Fields*, 16(3):197–204, 1983. 33
- [91] S. Chekanov, et al. Exclusive electroproduction of J/ψ mesons at HERA. *Nuclear Physics B*, 695(1):3 – 37, 2004. ISSN 0550-3213. doi:<https://doi.org/10.1016/j.nuclphysb.2004.06.034>. URL <http://www.sciencedirect.com/science/article/pii/S0550321304004274>. 34
- [92] ZEUS Collaboration. Exclusive ρ_0 production in deep inelastic scattering at HERA. *PMC Physics A*, 1:6, 2007. ISSN 1754-0410. doi:10.1186/1754-0410-1-6. URL <http://dx.doi.org/10.1186/1754-0410-1-6>. 34
- [93] L. Frankfurt, et al. Coherent QCD phenomena in the coherent pion-nucleon and pion-nucleus production of two jets at high relative momenta. *Czech. J. Phys.*, 55:B675, 2005. URL <https://arxiv.org/abs/hep-ph/0412260>. 34
- [94] L. Frankfurt, et al. Diffractive heavy quarkonium photoproduction and electroproduction in QCD. *Phys. Rev. D*, 57:512–526, Jan 1998. doi:10.1103/PhysRevD.57.512. URL <https://link.aps.org/doi/10.1103/PhysRevD.57.512>. 34
- [95] J. P. Ralston et al. Fluctuating proton size and oscillating color transparency. *Phys. Rev. Lett.*, 61:1823–1826, Oct 1988. doi:10.1103/PhysRevLett.61.1823. URL <https://link.aps.org/doi/10.1103/PhysRevLett.61.1823>. 35
- [96] B. Pire et al. Fixed angle elastic scattering and the chromo-Coulomb phase shift. *Physics Letters B*, 117(3):233 – 237, 1982. ISSN 0370-2693. doi:[https://doi.org/10.1016/0370-2693\(82\)90553-6](https://doi.org/10.1016/0370-2693(82)90553-6). URL <http://www.sciencedirect.com/science/article/pii/0370269382905536>. 36, 37
- [97] J. P. Ralston et al. Oscillatory Scaling Violations and the Quantum Chromodynamic Coulomb Phase. *Phys. Rev. Lett.*, 49:1605–1608, Nov 1982. doi:10.1103/PhysRevLett.49.1605. URL <https://link.aps.org/doi/10.1103/PhysRevLett.49.1605>. 36
- [98] A. Sen. Asymptotic behavior of the fixed-angle on-shell quark scattering amplitudes in non-Abelian gauge theories. *Phys. Rev. D*, 28:860–875, Aug 1983. doi:10.1103/PhysRevD.28.860. URL <https://link.aps.org/doi/10.1103/PhysRevD.28.860>. 36
- [99] S. J. Brodsky et al. Scaling Laws at Large Transverse Momentum. *Phys. Rev. Lett.*, 31:1153–1156, Oct 1973. doi:10.1103/PhysRevLett.31.1153. URL <https://link.aps.org/doi/10.1103/PhysRevLett.31.1153>. 36
- [100] S. J. Brodsky et al. Scaling laws for large-momentum-transfer processes. *Phys. Rev. D*, 11:1309–1330, Mar 1975. doi:10.1103/PhysRevD.11.1309. URL <https://link.aps.org/doi/10.1103/PhysRevD.11.1309>. 36

- [101] V. A. Matveev, et al. Automodellism in the large-angle elastic scattering and structure of hadrons. *Lett. Nuovo Cim.*, 7(15):719–723, 8 1973. doi: 10.1007/BF02728133. URL <https://www.osti.gov/biblio/4452246>. 36
- [102] P. V. Landshoff. Model for elastic scattering at wide angle. *Phys. Rev. D*, 10:1024–1030, Aug 1974. doi:10.1103/PhysRevD.10.1024. URL <https://link.aps.org/doi/10.1103/PhysRevD.10.1024>. 36
- [103] P. V. Landshoff et al. Higher-order QCD corrections to exclusive processes: The multiple scattering mechanism. *Zeitschrift für Physik C Particles and Fields*, 6(1):69–75, 1980. 36
- [104] A. H. Mueller. Perturbative QCD at High-Energies. *Phys. Rept.*, 73:237, 1981. doi:10.1016/0370-1573(81)90030-2. 36
- [105] D. Sivers, et al. Large transverse momentum processes. *Physics Reports*, 23(1):1 – 121, 1976. ISSN 0370-1573. doi:[https://doi.org/10.1016/0370-1573\(76\)90015-6](https://doi.org/10.1016/0370-1573(76)90015-6). URL <http://www.sciencedirect.com/science/article/pii/0370157376900156>. 37
- [106] S. J. Brodsky et al. Spin Correlations, QCD Color Transparency, and Heavy-Quark Thresholds in Proton-Proton Scattering. *Phys. Rev. Lett.*, 60:1924–1927, May 1988. doi:10.1103/PhysRevLett.60.1924. URL <https://link.aps.org/doi/10.1103/PhysRevLett.60.1924>. 37
- [107] B. Van Overmeire et al. A relativistic framework to determine the nuclear transparency from A(p,2p) reactions. *Physics Letters B*, 644(5):304–310, 2007. ISSN 0370-2693. doi:<https://doi.org/10.1016/j.physletb.2006.11.060>. URL <http://www.sciencedirect.com/science/article/pii/S0370269306015140>. 37
- [108] D. Dutta, et al. Nuclear transparency with the $\gamma \xrightarrow{n} \pi^- p$ process in ${}^4\text{He}$. *Phys. Rev. C*, 68:021001, Aug 2003. doi:10.1103/PhysRevC.68.021001. URL <https://link.aps.org/doi/10.1103/PhysRevC.68.021001>. 38
- [109] A. Arriaga, et al. Three-body correlations in few-body nuclei. *Phys. Rev. C*, 52:2362–2368, Nov 1995. doi:10.1103/PhysRevC.52.2362. URL <https://link.aps.org/doi/10.1103/PhysRevC.52.2362>. 38, 39
- [110] A. Larson, et al. Pionic color transparency. *Phys. Rev. C*, 74:018201, Jul 2006. doi:10.1103/PhysRevC.74.018201. URL <https://link.aps.org/doi/10.1103/PhysRevC.74.018201>. x, 39, 40, 42
- [111] M. M. Kaskulov, et al. Deeply inelastic pions in the exclusive reaction $p(e, e' \pi^+)n$ above the resonance region. *Phys. Rev. D*, 78:114022, Dec 2008. doi:10.1103/PhysRevD.78.114022. URL <https://link.aps.org/doi/10.1103/PhysRevD.78.114022>. x, 40, 41, 45
- [112] M. M. Kaskulov, et al. Pionic transparency in semi-exclusive electro-production off nuclei. *Phys. Rev. C*, 79:015207, Jan 2009. doi:10.1103/PhysRevC.79.015207. URL <https://link.aps.org/doi/10.1103/PhysRevC.79.015207>. x, 40, 41

- [113] M. Kaskulov et al. Resonance–parton duality in (e,e') off nucleons. *Progress in Particle and Nuclear Physics*, 67(2):194–199, 2012. ISSN 0146-6410. doi:<https://doi.org/10.1016/j.ppnp.2011.12.017>. URL <https://www.sciencedirect.com/science/article/pii/S0146641011001347>. From Quarks and Gluons to Hadrons and Nuclei. [x](#), [40](#), [41](#)
- [114] B. Andersson, et al. Parton fragmentation and string dynamics. *Physics Reports*, 97(2):31–145, 1983. ISSN 0370-1573. doi:[https://doi.org/10.1016/0370-1573\(83\)90080-7](https://doi.org/10.1016/0370-1573(83)90080-7). URL <https://www.sciencedirect.com/science/article/pii/0370157383900807>. [41](#)
- [115] K. Gallmeister et al. Space–time picture of fragmentation in Pythia/Jetset for HERMES and RHIC. *Physics Letters B*, 630(1):40–48, 2005. ISSN 0370-2693. doi:<https://doi.org/10.1016/j.physletb.2005.08.135>. URL <https://www.sciencedirect.com/science/article/pii/S0370269305012955>. [41](#)
- [116] M. R. Adams, et al. Measurement of Nuclear Transparencies from Exclusive ρ^0 Meson Production in Muon-Nucleus Scattering at 470 GeV. *Phys. Rev. Lett.*, 74:1525–1529, Feb 1995. doi:[10.1103/PhysRevLett.74.1525](https://doi.org/10.1103/PhysRevLett.74.1525). URL <https://link.aps.org/doi/10.1103/PhysRevLett.74.1525>. [42](#), [43](#), [44](#)
- [117] M. Arneodo, et al. Exclusive ρ^0 and ϕ muoproduction at large Q². *Nucl. Phys. B*, 429(3), 1994. doi:[https://doi.org/10.1016/0550-3213\(94\)90152-X](https://doi.org/10.1016/0550-3213(94)90152-X). URL <https://www.sciencedirect.com/science/article/pii/055032139490152X>. [42](#), [43](#)
- [118] K. Ackerstaff, et al. Observation of a Coherence Length Effect in Exclusive ρ^0 Electroproduction. *Phys. Rev. Lett.*, 82:3025–3029, Apr 1999. doi:[10.1103/PhysRevLett.82.3025](https://doi.org/10.1103/PhysRevLett.82.3025). URL <https://link.aps.org/doi/10.1103/PhysRevLett.82.3025>. [43](#), [44](#)
- [119] G. McClellan, et al. Incoherent Photoproduction of ρ^0 Mesons From Complex Nuclei and Comparison with Vector-Dominance Predictions. *Phys. Rev. Lett.*, 23:554–556, Sep 1969. doi:[10.1103/PhysRevLett.23.554](https://doi.org/10.1103/PhysRevLett.23.554). URL <https://link.aps.org/doi/10.1103/PhysRevLett.23.554>. [44](#)
- [120] J. Hüfner, et al. Glauber multiple scattering theory for the photoproduction of vector mesons off nuclei and the role of the coherence length. *Physics Letters B*, 383(3):362–366, 1996. [44](#)
- [121] A. Airapetian, et al. Q^2 Dependence of Nuclear Transparency for Exclusive ρ^0 Production. *Phys. Rev. Lett.*, 90:052501, Feb 2003. doi:[10.1103/PhysRevLett.90.052501](https://doi.org/10.1103/PhysRevLett.90.052501). URL <https://link.aps.org/doi/10.1103/PhysRevLett.90.052501>. [43](#)
- [122] B. Z. Kopeliovich, et al. Color transparency versus quantum coherence in electroproduction of vector mesons off nuclei. *Phys. Rev. C*, 65:035201, Feb 2002. doi:[10.1103/PhysRevC.65.035201](https://doi.org/10.1103/PhysRevC.65.035201). URL <https://link.aps.org/doi/10.1103/PhysRevC.65.035201>. [45](#)

- [123] L. El Fassi, et al. Evidence for the onset of color transparency in ρ^0 electro-production off nuclei. *Physics Letters B*, 712(4):326–330, 2012. ISSN 0370-2693. doi:<https://doi.org/10.1016/j.physletb.2012.05.019>. URL <https://www.sciencedirect.com/science/article/pii/S0370269312005369>. 45, 46, 47
- [124] L. Frankfurt, et al. Color transparency in semi-inclusive electroproduction of ρ mesons. *Phys. Rev. C*, 78:015208, Jul 2008. doi:10.1103/PhysRevC.78.015208. URL <https://link.aps.org/doi/10.1103/PhysRevC.78.015208>. 45, 46, 47
- [125] K. Gallmeister, et al. Color transparency in hadronic attenuation of ρ^0 mesons. *Phys. Rev. C*, 83:015201, Jan 2011. doi:10.1103/PhysRevC.83.015201. URL <https://link.aps.org/doi/10.1103/PhysRevC.83.015201>. 45, 46, 47
- [126] B. Z. Kopeliovich, et al. Color transparency in electroproduction of the ρ meson at low energies. *Phys. Rev. C*, 76:015205, Jul 2007. doi:10.1103/PhysRevC.76.015205. URL <https://link.aps.org/doi/10.1103/PhysRevC.76.015205>. 46, 47
- [127] D. Dutta, et al. Color transparency: Past, present and future. *Progress in Particle and Nuclear Physics*, 69:1–27, Mar 2013. ISSN 0146-6410. doi:10.1016/j.ppnp.2012.11.001. URL <http://dx.doi.org/10.1016/j.ppnp.2012.11.001>. 47
- [128] R. Kazimi, et al. Operational Results of Simultaneous Four-Beam Delivery at Jefferson Lab. In *10th International Particle Accelerator Conference*, page WEPMP053. 2019. doi:10.18429/JACoW-IPAC2019-WEPMP053. 48
- [129] C. Yan et al. Superharp: A Wire scanner with absolute position readout for beam energy measurement at CEBAF. *Nucl. Instrum. Meth. A*, 365:261–267, 1995. doi:10.1016/0168-9002(95)00505-6. 51
- [130] K. Unser. The Parametric current transformer: A Beam current monitor developed for LEP. *AIP Conf. Proc.*, 252:266–275, 1992. doi:10.1063/1.42124. 52
- [131] Hall C Staff and Users. *Jefferson Lab Hall C Standard Equipment Manual*, Nov 2019. URL <https://hallcweb.jlab.org/safety-docs/current/Standard-Equipment-Manual.pdf>. <https://hallcweb.jlab.org/safety-docs/current/Standard-Equipment-Manual.pdf>. 52, 59, 60
- [132] C. Yan, et al. Linear beam raster for cryogenic targets. *Nuclear Instruments and Methods in Physics Research Section A: Accelerators, Spectrometers, Detectors and Associated Equipment*, 539(1):1 – 15, 2005. ISSN 0168-9002. doi:<https://doi.org/10.1016/j.nima.2004.09.034>. URL <https://www.sciencedirect.com/science/article/pii/S0168900204021874>. 53
- [133] D. Meekins. *Hall C Cryogenic Target Stack*, August 2016. URL https://userweb.jlab.org/~smithg/target/Qweak/TGTDrawings_Dec2017.pdf.

https://userweb.jlab.org/~smithg/target/Qweak/TGTDrawings_Dec2017.pdf. 54

- [134] H. Szumila-Vance. *Commissioning the HMS optics in the 2017-2018 run period*, Dec 2018. URL <https://hallcweb.jlab.org/doc-private>ShowDocument?docid=998>. 58
- [135] H. Szumila-Vance. *Notes on the SHMS optics in the 2017-18 run period*, Feb 2019. URL <https://hallcweb.jlab.org/doc-private>ShowDocument?docid=1007>. 58
- [136] Saint-Gobain. *BC404*. URL <https://www.crystals.saint-gobain.com/products/bc400-bc404>. <https://www.crystals.saint-gobain.com/products/bc400-bc404>. 60
- [137] G. Niculescu, et al. *SHMS Hodoscope Scintillator Detectors*, July 2016. URL https://hallcweb.jlab.org/document/howtos/shms_scintillator_hodoscope.pdf. https://hallcweb.jlab.org/document/howtos/shms_scintillator_hodoscope.pdf. 60
- [138] Rexon. *RP-408*. URL <https://www.rexon.com/RP408.htm>. <https://www.rexon.com/RP408.htm>. 60
- [139] J. Wilson. *Quartz Hodoscope: Assembly, Calibration, and Data Analysis*, 2014. URL <https://hallcweb.jlab.org/doc-private>ShowDocument?docid=806>. <https://hallcweb.jlab.org/doc-private>ShowDocument?docid=806>. 60
- [140] W. R. Leo. *Techniques for nuclear and particle physics experiments: a how-to approach; 2nd ed.* Springer, Berlin, 1994. doi:10.1007/978-3-642-57920-2. URL <https://cds.cern.ch/record/302344>. 60, 61
- [141] S. Malace. *Operating voltages for HMS scintillators*, March 2017. URL https://hallcweb.jlab.org/DocDB/0008/000834/001/table_data_hv_update17.pdf. https://hallcweb.jlab.org/DocDB/0008/000834/001/table_data_hv_update17.pdf. 62
- [142] S. Malace. *Operating voltages for SHMS scintillators*, March 2017. URL https://hallcweb.jlab.org/DocDB/0008/000821/001/shms_table_data_hv.pdf. https://hallcweb.jlab.org/DocDB/0008/000821/001/shms_table_data_hv.pdf. 62
- [143] S. Malace. *Operating voltages for SHMS quartz plane*, March 2017. URL https://hallcweb.jlab.org/DocDB/0008/000826/001/shms_quartz_table_data_hv.pdf. https://hallcweb.jlab.org/DocDB/0008/000826/001/shms_quartz_table_data_hv.pdf. 62
- [144] E. Christy, et al. *Hall C Reference: SHMS Drift Chambers*, December 2016. URL https://hallcweb.jlab.org/document/howtos/shms_drift_chambers.pdf. https://hallcweb.jlab.org/document/howtos/shms_drift_chambers.pdf. 62

- [145] CAEN. *CAEN 1190 User Manual*, August 2011. URL https://coda.jlab.org/drupal/system/files/pdfs/HardwareManual/CAEN/V1190_REV10.pdf. 64, 70
- [146] D. Day. *Preliminary Design Report for the SHMS Noble Gas Čerenkov*, Dec 2017. URL <https://hallcweb.jlab.org/DocDB/0009/000933/001/shms-cerv6.pdf>. <https://hallcweb.jlab.org/DocDB/0009/000933/001/shms-cerv6.pdf>. 66, 68
- [147] T. Horn, et al. The Aerogel Čerenkov detector for the SHMS magnetic spectrometer in Hall C at Jefferson Lab. *Nuclear Instruments and Methods in Physics Research Section A: Accelerators, Spectrometers, Detectors and Associated Equipment*, 842:28 – 47, 2017. ISSN 0168-9002. doi:<https://doi.org/10.1016/j.nima.2016.10.039>. URL <http://www.sciencedirect.com/science/article/pii/S0168900216310774>. 66, 68
- [148] C. Cothran, et al. A threshold gas Čerenkov detector for CEBAF’s Hall C high momentum spectrometer. *Bulletin of the American Physical Society*, 40(2), 4 1995. 66
- [149] H. Mkrtchyan, et al. The lead-glass electromagnetic calorimeters for the magnetic spectrometers in Hall C at Jefferson Lab. *Nuclear Instruments and Methods in Physics Research Section A: Accelerators, Spectrometers, Detectors and Associated Equipment*, 719:85 – 100, 2013. ISSN 0168-9002. doi:<https://doi.org/10.1016/j.nima.2013.03.070>. URL <http://www.sciencedirect.com/science/article/pii/S0168900213004154>. 70, 88
- [150] H. Avakian et al. Performance of the electromagnetic calorimeter of the HERMES experiment. *Nucl. Instrum. Meth. A*, 417:69–78, 1998. doi:[10.1016/S0168-9002\(98\)00540-3](https://doi.org/10.1016/S0168-9002(98)00540-3). 70
- [151] H. Dong. *Description and Instructions for the Firmware of Processing FPGA of the ADC250 Boards Version 0x0C0D*, February 2017. URL https://coda.jlab.org/drupal/system/files/pdfs/HardwareManual/fADC250/FADC250_Processing_FPGA_Firmware_ver_0xC0D_Description_Instructions.pdf. 70
- [152] Phillips Scientific. *16 Channel Logic Level Translator CAMAC Model 7126*, March 1997. URL <http://www.phillipsscientific.com/pdf/7126ds.pdf>. 72
- [153] Phillips Scientific. *Quad Two-fold Logic Unit NIM Model 752*, July 1996. URL <http://www.phillipsscientific.com/pdf/752ds.pdf>. 72
- [154] Phillips Scientific. *Quad Majority Logic Unit NIM Model 755*, July 1996. URL <http://www.phillipsscientific.com/pdf/755ds.pdf>. 72
- [155] Phillips Scientific. *Quad Liner/Logic Fan-In/Out NIM Model 740*, January 1996. URL <http://www.phillipsscientific.com/pdf/740ds.pdf>. 73
- [156] LeCroy. *Quad Linear Fan-In/Fan-Out Model 428F*, September 1995. URL <https://teledynelecroy.com/lrs/dsheets/428.htm>. 73

- [157] Phillips Scientific. *Constant Fraction Timing Discriminator NIM Model 715*, January 1996. URL <http://www.phillipsscientific.com/pdf/715ds.pdf>. 73
- [158] JLab Hall C Collaboration. GitHub - JeffersonLab/hcana. URL <https://github.com/JeffersonLab/hcana>. 75
- [159] JLab Hall A Collaboration. GitHub - JeffersonLab/analyzer. URL <https://github.com/JeffersonLab/analyzer>. 75
- [160] R. Brun et al. ROOT: An object oriented data analysis framework. *Nucl. Instrum. Meth. A*, 389:81–86, 1997. doi:10.1016/S0168-9002(97)00048-X. 75
- [161] C. Yero. *Cross Section Measurements of Deuteron Electro-Disintegration at Very High Recoil Momenta and Large 4-Momentum Transfers (Q₂)*. Ph.D. thesis, Florida International University, 7 2020. URL https://misportal.jlab.org/ul/publications/view_pub.cfm?pub_id=16338. 77
- [162] T. Amatuni. On the calibration of segmented full absorption calorimeters. 88
- [163] V. Tadevosyan et al. HMS Calorimeter in HCANA: Recent progress. URL https://hallaweb.jlab.org/data_reduc/AnaWork2015/HMS_Calorimeter_in_HCANA.pdf. 88
- [164] J. Bericic. Notes on HMS_optics, Mar 2017. URL https://hallcweb.jlab.org/DocDB/0008/000849/001/HMS_optics_notes.pdf. 91, 92
- [165] K. Makino et al. COSY INFINITY Version 9. *Nuclear Instruments and Methods in Physics Research Section A: Accelerators, Spectrometers, Detectors and Associated Equipment*, 558(1):346–350, 2006. ISSN 0168-9002. doi:<https://doi.org/10.1016/j.nima.2005.11.109>. URL <https://www.sciencedirect.com/science/article/pii/S0168900205021522>. Proceedings of the 8th International Computational Accelerator Physics Conference. 95
- [166] D. Groom. AtomicNuclearProperties, Feb 2011. URL <https://pdg.lbl.gov/2018/AtomicNuclearProperties/>. <https://pdg.lbl.gov/2018/AtomicNuclearProperties/>. 105, 106
- [167] A. Carroll, et al. Absorption cross section of $\pi\pm$, $K\pm$, p and \bar{p} on nuclei between 60 and 280 GeV/c. *Physics Letters B*, 80(3):319–322, 1979. ISSN 0370-2693. doi:[https://doi.org/10.1016/0370-2693\(79\)90226-0](https://doi.org/10.1016/0370-2693(79)90226-0). URL <https://www.sciencedirect.com/science/article/pii/0370269379902260>. 109
- [168] N. Kwong et al. The energy dependence of nuclear reaction cross sections. *Physics Letters B*, 146(6):370–374, 1984. ISSN 0370-2693. doi:[https://doi.org/10.1016/0370-2693\(84\)90141-2](https://doi.org/10.1016/0370-2693(84)90141-2). URL <https://www.sciencedirect.com/science/article/pii/0370269384901412>. 109

- [169] S. Denisov, et al. Absorption cross sections for pions, kaons, protons and antiprotons on complex nuclei in the 6 to 60 GeV/c momentum range. *Nuclear Physics B*, 61:62–76, 1973. ISSN 0550-3213. doi:[https://doi.org/10.1016/0550-3213\(73\)90351-9](https://doi.org/10.1016/0550-3213(73)90351-9). URL <https://www.sciencedirect.com/science/article/pii/0550321373903519>. 109
- [170] L. Ray. Proton-nucleus total cross sections in the intermediate energy range. *Phys. Rev. C*, 20:1857–1872, Nov 1979. doi:[10.1103/PhysRevC.20.1857](https://doi.org/10.1103/PhysRevC.20.1857). URL <https://link.aps.org/doi/10.1103/PhysRevC.20.1857>. 109
- [171] H. P. Wellisch et al. Total reaction cross section calculations in proton-nucleus scattering. *Phys. Rev. C*, 54:1329–1332, Sep 1996. doi:[10.1103/PhysRevC.54.1329](https://doi.org/10.1103/PhysRevC.54.1329). URL <https://link.aps.org/doi/10.1103/PhysRevC.54.1329>. 109
- [172] J. R. Letaw, et al. Proton-nucleus total inelastic cross sections - an empirical formula for E greater than 10 MeV. *The Astrophysical Journal Supplement Series*, 51:271–275, March 1983. doi:[10.1086/190849](https://doi.org/10.1086/190849). 109
- [173] A. Kohama, et al. Energy and Mass-Number Dependence of Hadron–Nucleus Total Reaction Cross Sections. *Journal of the Physical Society of Japan*, 85(9):094201, 2016. doi:[10.7566/JPSJ.85.094201](https://doi.org/10.7566/JPSJ.85.094201). URL <https://doi.org/10.7566/JPSJ.85.094201>. 109
- [174] J. W. Van Orden, et al. Short-range correlations and the nuclear momentum density distribution for ^{16}O . *Phys. Rev. C*, 21:2628–2631, Jun 1980. doi:[10.1103/PhysRevC.21.2628](https://doi.org/10.1103/PhysRevC.21.2628). URL <https://link.aps.org/doi/10.1103/PhysRevC.21.2628>. 113
- [175] N. Fomin, et al. New Results on Short-Range Correlations in Nuclei. *Annual Review of Nuclear and Particle Science*, 67(1):129–159, 2017. doi:[10.1146/annurev-nucl-102115-044939](https://doi.org/10.1146/annurev-nucl-102115-044939). URL <https://doi.org/10.1146/annurev-nucl-102115-044939>. 114
- [176] P. E. Bosted. Empirical fit to the nucleon electromagnetic form factors. *Phys. Rev. C*, 51:409–411, Jan 1995. doi:[10.1103/PhysRevC.51.409](https://doi.org/10.1103/PhysRevC.51.409). URL <https://link.aps.org/doi/10.1103/PhysRevC.51.409>. 121
- [177] O. Caplow-Munro et al. Color transparency and the proton form factor: Evidence for the Feynman mechanism. *Phys. Rev. C*, 104:L012201, Jul 2021. doi:[10.1103/PhysRevC.104.L012201](https://doi.org/10.1103/PhysRevC.104.L012201). URL <https://link.aps.org/doi/10.1103/PhysRevC.104.L012201>. 123
- [178] S. D. Drell et al. Connection of Elastic Electromagnetic Nucleon Form Factors at Large Q^2 and Deep Inelastic Structure Functions Near Threshold. *Phys. Rev. Lett.*, 24:181–186, Jan 1970. doi:[10.1103/PhysRevLett.24.181](https://doi.org/10.1103/PhysRevLett.24.181). URL <https://link.aps.org/doi/10.1103/PhysRevLett.24.181>. 124
- [179] A. Bogacz. Future Nuclear Physics Machines at JLAB: 24 GeV CE-BAF and a 54 GeV Site Filler, Dec 2020. URL <https://www.jlab.org/accelerator-seminar-alex-bogacz-remote>. JLab Accelerator Seminar. 124

- [180] C. Giusti et al. Separation of structure functions and electron distortion in quasifree ($e, e' p$) reactions. *Nuclear Physics A*, 485(3-4):461–480, 1988. [126](#)
- [181] C. Giusti et al. Electron distortion in quasifree ($e, e' p$) reactions. *Nuclear Physics A*, 473(4):717–735, 1987. [126](#)
- [182] H. Blok et al. Electron-Scattering Form Factors and Nuclear Transition Densities. In *Computational Nuclear Physics 1*, pages 190–205. Springer, 1991. [126](#)
- [183] A. Aste, et al. Coulomb distortion of relativistic electrons in the nuclear electrostatic field. *The European Physical Journal A-Hadrons and Nuclei*, 26(2):167–178, 2005. [127](#)
- [184] L. W. Mo et al. Radiative corrections to elastic and inelastic ep and np scattering. *Reviews of Modern Physics*, 41(1):205, 1969. [127](#)
- [185] R. Ent, et al. Radiative corrections for $(e, e' p)$ reactions at GeV energies. *Phys. Rev. C*, 64:054610, Oct 2001. doi:[10.1103/PhysRevC.64.054610](https://doi.org/10.1103/PhysRevC.64.054610). URL <https://link.aps.org/doi/10.1103/PhysRevC.64.054610>. [xiv](#), [127](#), [128](#), [130](#)
- [186] R. Early. Numerical solution of the electron diffusion equation. *Nuclear Instruments and Methods*, 109(1):93–100, 1973. ISSN 0029-554X. doi:[https://doi.org/10.1016/0029-554X\(73\)90454-0](https://doi.org/10.1016/0029-554X(73)90454-0). URL <https://www.sciencedirect.com/science/article/pii/0029554X73904540>. [131](#)
- [187] G. R. Lynch et al. Approximations to multiple Coulomb scattering. *Nuclear Instruments and Methods in Physics Research Section B: Beam Interactions with Materials and Atoms*, 58(1):6–10, 1991. ISSN 0168-583X. doi:[https://doi.org/10.1016/0168-583X\(91\)95671-Y](https://doi.org/10.1016/0168-583X(91)95671-Y). URL <https://www.sciencedirect.com/science/article/pii/0168583X9195671Y>. [133](#)
- [188] G. Shen, et al. Measurement of multiple scattering at 50 to 200 GeV/c. *Phys. Rev. D*, 20:1584–1588, Oct 1979. doi:[10.1103/PhysRevD.20.1584](https://doi.org/10.1103/PhysRevD.20.1584). URL <https://link.aps.org/doi/10.1103/PhysRevD.20.1584>. [133](#)